THE UNIVERSITY *of* EDINBURGH

Differential Cross Section Measurements in H→WW and Prospects of Observing H→b$\bar{\text{b}}$ in Future LHC Runs at the ATLAS Detector

Paul Glaysher

Doctor of Philosophy
The University of Edinburgh
June 2016

Abstract

The highly celebrated discovery of a new particle with a mass of 125 GeV in proton-proton collisions by the ATLAS and CMS experiments at the CERN Large Hadron Collider in 2012 has been shown to be compatible with the Standard Model description of the Higgs boson. However, in order to fully verify the Standard Model nature of the Higgs boson, most of its properties still remain to be measured. Such measurements include differential cross section measurements, which are shown here for the H→WW decay channel and the coupling of the Higgs boson to bottom quarks, for which a study of future prospects is presented.

Differential fiducial cross section measurements of the Higgs boson were performed in the $\mathrm{H} \to \mathrm{WW}^* \to \ell\nu\ell\nu$ channel at the ATLAS detector with 20 fb^{-1} of $\sqrt{s} = 8$ TeV collision data. For Higgs bosons produced by gluon-gluon fusion, the cross section is measured as a function of kinematic variables, including transverse momentum and rapidity of the Higgs boson, as well as the number of jets associated with the Higgs event. The obtained distributions are unfolded to a fiducial volume using a two-dimensional iterative Bayesian algorithm. The measured fiducial differential cross sections are compared to predictions from Monte Carlo generators. The total cross section measured in the fiducial volume defined by the charged lepton and neutrino kinematic properties is 36.0 ± 9.7 fb. Additionally the jet-veto efficiency in the fiducial volume is extracted from the differential cross sections.

An analysis is presented of Higgs boson production and decay into bottom quarks in association with a vector boson at the ATLAS detector for the future high-luminosity LHC with proton-proton collisions at $\sqrt{s} = 14$ TeV. The vector bosons are reconstructed from Z→ $\ell^+\ell^-$ or W→ $\ell\nu$ final states, where ℓ is an electron or muon. The analysis uses generator-level Monte Carlo samples to which efficiency and resolution smearing functions are applied. These reproduce the expected resolution of the upgraded ATLAS detector for the foreseen amount of pile-up

due to multiple overlapping proton-proton collisions. The analysis of the ZH($\rightarrow$ $\ell^+\ell^- b\bar{b}$) channel is presented and results are combined with the WH($\rightarrow$ $\ell\nu b\bar{b}$) channel from a corresponding study. For an integrated luminosity of 300 fb^{-1} using an average pile-up of 60, the expected significance is 3.9 σ with an expected error on the signal strength of 25%. Likewise, for 3000 fb^{-1} using an average pile-up of 140 the expected significance is 8.8 σ, and the error on the signal strength is expected to be about 15%.

Lay summary

The Large Hadron Collider at CERN (European Organisation for Nuclear Research) is the largest particle accelerator ever built. In a 27 km circular tunnel the LHC collides protons at high energies in the hope to produce particles that have not been observed before. The highlight of the LHC programme as of now is the discovery of the Higgs boson in 2012. The existence of the Higgs boson was predicted in the 1960s and is a crucial component in the theory explaining why fundamental particles have mass. Following the theoretical formulation, it would take about 50 years and multiple generations of particle accelerators to verify its existence.

The Higgs boson was discovered independently at two of the major particle detectors at the LHC, the ATLAS and CMS experiments. These detectors measure millions of collisions every second and continue to study the Higgs boson and search for new phenomena. Most Higgs boson properties remain to be measured. This thesis discusses two types of Higgs boson property measurements at the ATLAS detector.

The Higgs boson itself cannot be detected directly and its presence in a collision is established by measuring its decay products. The Higgs boson decays to different well-understood particles at rates predicted by the theory.

By measuring the Higgs boson decaying to W bosons, the Higgs boson production rate was determined. Spectra of the production rate as a function of measurable quantities of the Higgs boson were obtained, describing the underlying properties of the Higgs boson. Such include momentum and angular distributions. Particular care was taken to correct the measured spectra for detector inefficiencies, limited resolution and acceptance, for better comparison with theory predictions. The measurements were compared to state of the art theoretical simulations, which were found to be in good agreement.

Secondly, a key outstanding observation is the decay of the Higgs boson to bottom quarks. The predicted decay rate to bottom quarks is relatively high but the production of background processes with identical signatures is a factor of 10^7 more likely. Extracting the signal from this large background is difficult. This challenging task requires a vastly larger dataset than currently obtained. To increase the rate at which data is collected, the LHC will undergo multiple upgrades. So will the detector to deal with higher data rates and radiation levels. A simulation study was conducted to estimate the sensitivity to the Higgs boson to bottom quarks decay in light of increased statistics, higher collision energy and an upgraded detector in future LHC running. Special considerations were made for the number of overlapping collisions, called event pile-up. Pile-up is expected to increase significantly compared to current conditions and has a major impact on the performance of correctly reconstructing particles in the detector.

Declaration

I declare that this thesis was composed by myself, that the work contained herein is my own except where explicitly stated otherwise in the text, and that this work has not been submitted for any other degree or professional qualification except as specified.

Parts of this work have been published in [1] and [2].

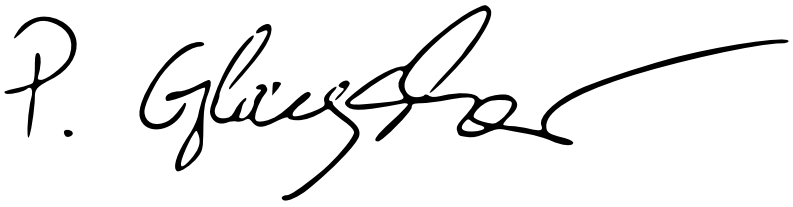

(*Paul Glaysher, June 2016*)

Acknowledgements

I would like to thank all who made my time at the University of Edinburgh and CERN as enjoyable as it was:

I would like to express my sincere gratitude to my supervisor, Victoria Martin, for the continuous support of my research and the completion of this thesis. I appreciate all her efforts that made my time as a PhD student productive and rewarding.

Special thanks goes to Corrinne Mills, for the opportunity to closely work with her. I have greatly benefited from her guidance, insight and motivation.

Flavia Dias, for being a good colleague and friend.

Kathrin Becker, Chris Hays, Li Yuan, Chris Delitzsch and Reina C. C. Toro, with whom it was a true pleasure to work with.

Olivier Arnaez and Aleandro Nisati, for their support when things got tricky.

Stephan Eisenhardt and Andreas Korn, for the great experience in the lab.

Ben Wynne and Yanyan Gao, for all the help, advice and laughs.

Dianne Ferguson, Tim Bristow, Sebastian Olivares and Jack Medley, for their companionship on this journey.

I wish to express my appreciation of the support I received in the past:

David Newbold, Jaap Velthuis and Erika Garutti, for their encouragement to pursue a PhD.

Michael Rode, for his encouragement to study physics.

I also thank my ever-supportive friends and family: my brother, mum and grandparents, and above all Christin, for always believing in me. A final word of thanks to Grampam, for his infectious enthusiasm for physics and life itself.

Contents

Chapter 1

Introduction

The discovery of the Higgs boson by the ATLAS and CMS collaborations at the Large Hadron Collider (LHC) in 2012 was a triumph for experimental and theoretical particle physics [3, 4]. After a 40 year long search the Higgs boson solves a long standing shortfall of the Standard Model (SM) of particle physics [5–7]. It confirms the existence of an associated Higgs field which explains electroweak symmetry breaking as a mechanism to generate massive vector bosons [8–12], as well as fermion masses via Yukawa coupling.

Following the discovery, initial measurements of the Higgs boson confirm that it is compatible with the Standard Model description [13–17]. Further measurements are however needed to fully verify the SM nature of the Higgs boson. These include precision measurements of the Higgs boson kinematic properties and its couplings to SM particles.

This thesis presents measurements of differential cross section measurements in the $H \rightarrow WW$ decay channel and a simulation study of the yet to be observed Higgs boson coupling to bottom quarks.

The ATLAS and CMS detectors first measured the Higgs boson in proton-proton collisions at the LHC with a centre of mass energy of 7 and 8 TeV, in the period of 2010-2012 referred to as Run 1 of the LHC. The combined dataset amounts to 25 fb^{-1} of integrated luminosity. After a long shutdown, the LHC came back online in 2015, colliding protons near the design energy of 14 TeV. The LHC will continue operations until 2023 with a continuous increase in collision rate, delivering a total of 300 fb^{-1}. A major upgrade to the High Luminosity LHC

will produce up to 10 times higher collision rate compared to the nominal LHC design, which will deliver 3000 fb^{-1} by approximately 2035.

The ATLAS Run 1 dataset allows for initial measurement of the Higgs boson including differential cross sections. Differential cross section measurements are a direct, and near model independent, method of testing the compatibility of the Higgs boson with the SM. Although statistically limited in comparison to measurements from future LHC runs, these results will provide unique constrains for 8 TeV collisions. The observation of $\text{H} \rightarrow \text{WW}$ was made in 2014 [18]. This decay channel provides a sample with a high yield of Higgs boson candidates to perform differential cross section measurements. Higgs boson production by gluon fusion was measured by the author in the $\text{H} \rightarrow \text{WW}$ decay channel as a function of kinematic observables in the final state. Such measurements are sensitive to QCD and PDF models of the gluon fusion process and comparisons to theory predictions are made by *unfolding* the results to correct for detector effects.

The coupling of the Higgs boson to vector boson pairs is well established, but coupling to fermions has only been observed in the decay to τ-leptons [19]. A vital outstanding measurement is the decay of the Higgs boson to quarks. Although indirect evidence of top quark coupling can be inferred from the top-quark loop in $gg \rightarrow \text{H}$ production, the most suited channel to directly measure quark couplings is in the decay to bottom quarks due to the large branching ratio of 58%.

The $\text{H} \rightarrow b\bar{b}$ channel suffers however from large backgrounds, produced by strong interactions. In order to discriminate the $\text{H}\rightarrow b\bar{b}$ decay from the background, the associated production with a W or Z boson is considered, instead of the dominant gluon fusion production mode. This trade-off of production rate for a cleaner signal means the prohibitively large QCD background can be rejected, in particular for events where the associated vector boson decays leptonically.

A sensitivity study is presented for the observation of $\text{VH}, \text{H} \rightarrow b\bar{b}$ in future LHC runs. Results are shown for the 300 and 3000 fb^{-1} milestones. Results for the Z boson channel were produced by the author and are presented in combination with corresponding results of the W boson channel produced by collaborators.

Chapter 2 summarises the importance of the Higgs mechanism within the Standard Model. Electroweak theory, and the necessity of electroweak symmetry breaking to explain the mass of the W and Z bosons, is presented. Spontaneous symmetry breaking is introduced by the Higgs mechanism which leads to the

generation of a massive scalar Higgs boson. Lastly, the coupling of fermions to the Higgs field is presented.

Higgs boson phenomenology at the LHC is discussed in **Chapter 3**, including production and decay modes. The WW and $b\bar{b}$ decay modes of interest in this thesis are highlighted.

Chapter 4 gives an overview of the underlying principles used to simulate Higgs boson and background events at the LHC. Numerical Monte Carlo simulation is used to simulate particles produced in proton-proton collisions. Parton Distribution Functions provide the momentum fractions of the colliding partons and fixed order calculations of the matrix element model the hard scatter. Lastly the detector response is simulated. Particular focus is given to the simulation of low energy QCD emissions and the importance of resummation techniques in perturbative QCD calculations. Predictions from such calculations are later compared to differential cross section measurements from the $gg \to \mathrm{H} \to \mathrm{WW} \to \mathrm{e}\nu\mu\nu$ channel.

Chapter 5 gives an overview of the experimental setup of the LHC and the ATLAS detector during the Run 1 data period with 7 and 8 TeV. The individual sub-systems of the ATLAS detector and their role in particle identification and reconstruction are described in detail. Definitions of reconstructed *physics objects* are given.

A series of upgrades to the LHC and the ATLAS detector are planned over the next 10 years, as shown in **Chapter 6**. The upgrades to the LHC accelerator complex will result in a significant increase in the collision rate. Going beyond the original design parameters of the LHC, an upgrade to the High Luminosity LHC (HL-LHC) will provide about 10 times higher collision rate than initially envisioned. Higher collisions, and thus data rates, will allow the LHC experiments to study very rare processes and signatures with a low signal to background ratio. The upgrade is motivated by the search for new phenomena, such as supersymmetry or dark matter, and also precision measurements including Higgs boson properties.

A higher collision rate poses multiple challenges for the operation of the ATLAS detector. Firstly, high radiation levels cause damage to the sensors. The performance of the silicon sensor near the interaction point in particular degrades with time and a radiation hard replacement must be installed which can survive higher radiation levels. The impact of radiation damage to the ATLAS

Semiconductor Tracker was evaluated at the end of Run 1, by determining the change in depletion voltage. The results are given in **Appendix C**.

Secondly, an increase in event pile-up, the number of simultaneous overlapping collisions, degrades the track reconstruction performance. To counteract the impact of pile-up, the upgraded silicon sensors will be of higher granularity and less susceptible to radiation damage. Results from testing of the new front-end readout chip for the silicon pixel upgrade are given in **Appendix D**.

Detector inefficiencies and resolution effects mean that measured quantities do not fully reflect the underlying process. A method to correct the $H \to WW$ measurements for this difference, called *unfolding* is discussed in **Chapter 7**. Unfolding allows for an extrapolation to a defined fiducial volume, a particle-level description with similar selection requirements as the measurements. The complexity of the $H \to WW$ measurement requires the use of Bayesian iterative unfolding.

Chapter 8 describes the $H \to WW$ differential measurements using the ATLAS Run 1 8 TeV data. The analysis closely follows the strategy of the analysis that led to the observation of $H \to WW$ decays [18], the results of which are summarised. Modifications with respect to the reference analysis are discussed. The dominant $gg \to H \to WW \to e\nu\mu\nu$ channel is chosen to construct differential cross sections. The Higgs boson signal is obtained by subtracting the background estimation from the data after an event selection is applied. The application of the unfolding strategy is presented alongside the treatment of statistical and systematic uncertainties which are also extrapolated to the fiducial volume.

Chapter 9 presents the prospects of measuring $H \to b\bar{b}$ in future LHC runs. The analysis follows the Run 1 $H \to b\bar{b}$ search strategy [20], from which most analysis considerations are adopted. The $WH \to \ell\nu b\bar{b}$ and $ZH \to \ell\ell b\bar{b}$ channels are considered individually and as a combination. An upgraded ATLAS detector is considered, by applying parametrised response functions to particle level data, which scale as a function of pile-up. The sensitivity is computed from a likelihood fit, with different scenarios of systematic uncertainties.

An overall summary and conclusion is given in **Chapter 10**, including an outlook for future LHC runs.

Chapter 2

Theoretical Motivation

The Standard Model (SM) of particle physics describes fundamental particles and their interactions. It describes the universe in terms of fundamental matter particles, *fermions*, and force carriers, *bosons*. The SM is the culmination of achievements in theoretical and experimental physics in the 20th century. Its description of a wide range of phenomena has been experimentally verified to a high degree of precision.

Described by the electroweak force, weak interactions are mediated by the $W^{\pm}$ and Z bosons, which are measured to have masses of approximately 80 and 91 GeV [21]. In contrast to experimental findings, the underlying symmetry of the theory however dictates that these particles have zero mass. By introducing the Higgs mechanism of electroweak symmetry breaking, the dynamic generation of massive $W^{\pm}$ and Z bosons is possible. This mechanism also predicts the existence of a massive scalar particle, the Higgs boson. The discovery of the Higgs boson at the LHC in 2012 was a major breakthrough underlining the success of the SM. In Section 2.1 a brief introduction to the SM is given, outlining the particle content and interactions, with more detail on the Electroweak force in Section 2.2. Section 2.3 describes electroweak symmetry breaking and the Higgs mechanism.

2.1 The Standard Model of Particle Physics

The SM is a gauge quantum field theory describing interactions of elementary particles [5–7]. The particle properties of the theory are determined by conser-

vation rules expressed as symmetries that must be obeyed by the Lagrangian. That is, the Lagrangian of the SM is invariant under transformations expressed as symmetry groups. Describing the strong, weak and electromagnetic forces the SM is invariant under local transformations of the SU(3) $\times$ SU(2) $\times$ U(1) gauge groups respectively. Furthermore, as required by special relativity, the theory is invariant under global transformations of the Poincaré group, leaving it identical in all inertial reference frames.

Following Noether's theorem [22], each gauge group of the SM couples to a conserved current and is thus related to a force of nature, mediated by one or more bosons.

Quantum Electrodynamics (QED) obeys the symmetry of the U(1) group. It describes the observed electromagnetic interaction and is mediated by the photon, γ, which couples to electric charge. It has been shown that the electromagnetic and weak interactions are manifestations of the same underlying force, the unified electroweak (EW) force [23–25]. In this sense U(1) QED group is thus the unbroken remainder of a combined SU(2)$\times$U(1) electroweak group. The weak interactions of the SU(2)$\times$U(1) group are mediated by the massive $W^{\pm}$ and Z bosons, which in the same way as the photon arise as a mixture of the underlying gauge fields, detailed in Section 2.2.

Quantum chromodynamics (QCD) underlies the symmetry of the special unitary group group SU(3) [26]; it represents the strong interaction between eight gluons and particles with colour charge. The generators of SU(3) are given by eight 3×3 Gell-Mann matrices, a generalisation of Pauli matrices [27].

The gauge bosons of the strong and weak interactions experience self-interactions, a consequence of these gauge groups being non-Abelian [28].

The particle content of the SM is presented in Figure 2.1. The fermions are half-integer spin particles and are categorised into quarks and leptons, according to their charges under the different forces. Quarks undergo interactions of the strong, electromagnetic and weak force, while charged leptons only experience the electromagnetic and weak force (in the case of the electrically neutral neutrino only the weak force). Quarks and leptons are grouped into three generations. Muon and tau particles are the heavier generations of the electron, for example. Massive fermions decay to lighter generations, which means that only the first generation of fermions form stable matter. Individual quarks are also not stable, with a short interaction time they form bound states as colour neutral hadrons.

Each fermion also has a corresponding anti-particle, with opposite additive quantum numbers but the same mass.

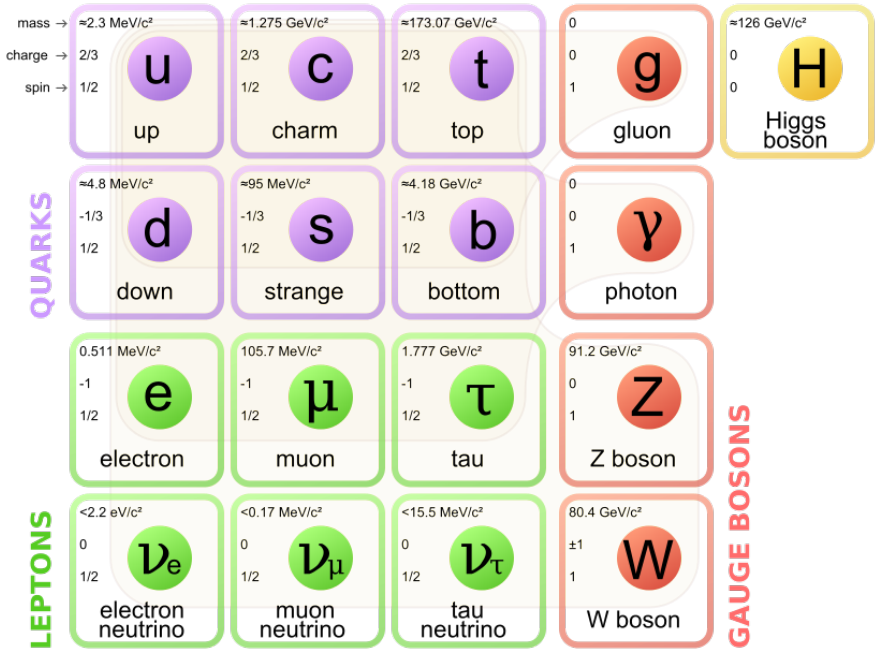

Figure 2.1 All particles of the SM, showing three generations of fermions, the gauge bosons and the Higgs boson, from Wikimedia Commons based on Ref. [21].

2.2 Electroweak Interactions

An early theory of weak interactions by Fermi [29], explained muon decay and nuclear β-decay via four-point lepton interactions with a Fermi coupling constant of G_F. Although adequate at describing low energy phenomena, the theory leads to unitary-violating[1] cross sections at energies greater than ∼300 GeV [30]. This motivated the introduction of charged vector bosons, $\mathrm{W}^{\pm}$, as mediators of the weak interaction. Unlike the electromagnetic interactions mediated by the massless photon, the $\mathrm{W}^{\pm}$ must be massive to accommodate the short range of the weak interaction. The propagator, the interaction probability amplitude, is then suppressed by the $\mathrm{W}^{\pm}$ boson mass m^2_{W}. For coupling to a vector boson with strength g, the propagator then is given by $g/(p^2 - m^2_{\mathrm{W}})$, where p is the momentum of the mediating $\mathrm{W}^{\pm}$, which solves the problem of large cross sections

[1] Unitarity requires the scattering amplitude to be finite. The accessible phase-space however increases with available energy and the high-energy regime can produce infinite cross sections due to large, non-renormalisable amplitudes.

at high energies violating unitarity. In the low energy limit, the propagator relates to the Fermi coupling as $G_F \sim g/m_{\mathrm{W}}^2$, recovering the Fermi description.

The difficulty in unifying the electromagnetic and weak force is illustrated by the fact that QED has a vectorial symmetry structure whereas the discovery of parity[2] violation in cobalt-60 β-decays [31] showed weak interactions to obey axial-vector symmetry (V-A) symmetry [32]. Likewise, the photon is massless, while the $\mathrm{W}^{\pm}$ bosons were found to be massive, despite the inherent requirement of massless vector bosons in the description of electroweak theory at the time. Also, the measurements of massive fermions stood in conflict with the chiral symmetry of the weak interactions requiring massless fermions.

Unification of the weak and electromagnetic forces was achieved by Glashow and Weinberg [5, 6] with a $\mathrm{SU(2)_L \times U(1)_Y}$ group, containing three $(\mathrm{W}_\mu^1, \mathrm{W}_\mu^2, \mathrm{W}_\mu^3)$ and one B_μ gauge fields. Fermion fields are expressed in terms of left-handed (L) and right-handed (R) chiral components. Specifically, left-handed leptons form doublets $\boldsymbol{\ell}_{\mathrm{L}}$ of $\mathrm{SU(2)_L}$ while right-handed leptons are singlets ℓ_{R}. The charged weak currents are thus purely left-handed. Under electroweak theory, fermions have two quantum numbers: the weak isospin T and the hypercharge Y. $\mathrm{SU(2)_L}$ describes the coupling of left-handed fermions and right-handed anti-fermions to T. This restriction reflects the V-A symmetry of the weak sector. $\mathrm{U(1)_Y}$ describes the coupling of all fermions to Y corresponding to a vectorial symmetry. Subsequently, the electric charge Q is expressed as a combination of the third component of the isospin T_3 and Y, as

$$Q = T_3 + Y/2. \tag{2.1}$$

An overview of fermion charges is given in Figure 2.2.

The $\mathrm{W}_\mu^{\mathrm{j}}$ fields couple to T with strength g, the gauge coupling of the U(1) symmetry related to electromagnetism. The B_μ field couples to Y with strength g', the gauge coupling of the SU(2) symmetry related to the weak interaction. Critically, the $\mathrm{W}_\mu^{\mathrm{j}}$ only couples to left-handed L chiral particles, thus explaining the V-A nature of weak interactions alongside the vector nature of QED. The physical gauge fields of $\mathrm{SU(2)_L \times U(1)_Y}$ arise from the mixing of $\mathrm{W}_\mu^{\mathrm{j}}$ and B_μ as:

$$\mathrm{W}_\mu^{\pm} = (\mathrm{W}_\mu^1 \mp i\mathrm{W}_\mu^2)/\sqrt{2} \tag{2.2}$$

[2]Parity describes the invariance of an interaction under sign change of spatial coordinates.

			T	T_3	Y	Q
$\begin{pmatrix}\nu_e\\ e\end{pmatrix}_{\mathrm{L}}$	$\begin{pmatrix}\nu_\mu\\ \mu\end{pmatrix}_{\mathrm{L}}$	$\begin{pmatrix}\nu_\tau\\ \tau\end{pmatrix}_{\mathrm{L}}$	$\frac{1}{2}$ $\frac{1}{2}$	$+\frac{1}{2}$ $-\frac{1}{2}$	-1 -1	0 -1
e_{R}	μ_{R}	τ_{R}	0	0	-2	-1
$\begin{pmatrix}u\\ d\end{pmatrix}_{\mathrm{L}}$	$\begin{pmatrix}c\\ s\end{pmatrix}_{\mathrm{L}}$	$\begin{pmatrix}t\\ b\end{pmatrix}_{\mathrm{L}}$	$\frac{1}{2}$ $\frac{1}{2}$	$+\frac{1}{2}$ $-\frac{1}{2}$	$+\frac{1}{3}$ $+\frac{1}{3}$	$+\frac{2}{3}$ $-\frac{1}{3}$
u_{R}	c_{R}	t_{R}	0	0	$+\frac{4}{3}$	$+\frac{2}{3}$
d_{R}	s_{R}	b_{R}	0	0	$-\frac{2}{3}$	$-\frac{1}{3}$

Figure 2.2 Fermion charges for left-handed doublets and right-handed singlets, based on Ref. [21]. The total weak isospin T, its third component T_3, the weak hypercharge Y and the electric charge Q. The corresponding anti-fermions have inverted charges.

$$\mathrm{Z}_\mu = \mathrm{W}^3_\mu \cos\theta_{\mathrm{W}} - \mathrm{B}_\mu \sin\theta_{\mathrm{W}}, \tag{2.3}$$

$$\mathrm{A}_\mu = \mathrm{W}^3_\mu \sin\theta_{\mathrm{W}} + \mathrm{B}_\mu \cos\theta_{\mathrm{W}}, \tag{2.4}$$

where

$$\cos\theta_{\mathrm{W}} = g/\sqrt{g^2+g'^2} \;\; and \;\; \sin\theta_{\mathrm{W}} = g'/\sqrt{g^2+g'^2}. \tag{2.5}$$

These correspond to the observed $\mathrm{W}^\pm$, neutral Z boson and the photon γ. The W and Z masses are related by the Weinberg angle θ_W [27]:

$$m_{\mathrm{Z}} = \frac{m_{\mathrm{W}}}{\cos\theta_{\mathrm{W}}}. \tag{2.6}$$

The $\mathrm{SU(2)_L \times U(1)_Y}$ theory thus incorporates fermions in left-handed SU(2) doublets and right-handed SU(2) singlets which interact with $\mathrm{W}^\pm$, Z and γ bosons, as well as gauge boson self interactions due to the non-Abelian EW group structure. Interactions are given by the $\mathrm{W}^\pm$ boson coupling to weak isospin T with strength g, and the vectorial, c_V, and axial, c_A, coupling of the Z boson with strength $g/\cos\theta_{\mathrm{W}}$, as given by Equation 2.7. The photon couples to Q with strength $e = g\,\sin\theta_{\mathrm{W}}$

$$c_V = T_3 - 2Q\sin^2\theta_{\mathrm{W}}, \quad c_A = T_3 \tag{2.7}$$

The Langrangian of the $SU(2)_L \times U(1)_Y$ group is given by

$$\mathcal{L} = -\frac{1}{4}W_j^{\mu\nu}W^j_{\mu\nu} - \frac{1}{4}B^{\mu\nu}B_{\mu\nu} \tag{2.8}$$

Despite the successful unification of the weak and electromagnetic force, the theory still predicts massless W and Z bosons. By spontaneously breaking the symmetry in the form of the Higgs mechanism, massive gauge bosons can be generated.

2.3 Higgs Mechanism

Spontaneous symmetry breaking (SSB) describes a theory that is symmetric under a transformation but its vacuum state is not. In particle physics SSB occurs when a field assumes a non-zero vacuum expectation value, in violation of the underlying symmetry. An example of this is given by a complex scalar field, ϕ, and the Lagrangian

$$\mathcal{L} = (\partial_\mu \phi^\dagger)(\partial^\mu \phi) + \mu^2 \phi^\dagger \phi - \lambda(\phi^\dagger \phi)^2 \tag{2.9}$$

which has a positive value of μ^2 and λ. Under these conditions the Lagrangian potential follows the shape of a sombrero hat or the bottom of a wine bottle, as seen in Figure 2.3. First a toy case with only a U(1) symmetry is considered, resulting in a massive photon field A_μ. A Lagrangian as in Equation 2.9 is invariant under global U(1) rotational transformation of type $\phi \rightarrow e^{-i\theta}\phi$, but has infinite degenerate vacuum values of $\phi = \mu e^{-i\theta}/\sqrt{2\lambda}$, for an azimuthal angle θ, representing an arbitrary phase shift. Once a randomly chosen vacuum state is assumed the rotational symmetry of U(1) no longer holds, resulting in SSB.

According to the Goldstone theorem, SSB of a continuous local symmetry will generate a massless scalar Nambu-Goldstone boson [34]. The local symmetry is characterised by transformations which depend on the position x in phase space. Radial $h(x)$ and azimuthal $\theta(x)$ excitations of the vacuum, with vacuum energy $v = \mu/\sqrt{\lambda}$ can be described the field

$$\phi(x) = \frac{1}{\sqrt{2}}(v + h(x))e^{-i\theta(x)/v} \tag{2.10}$$

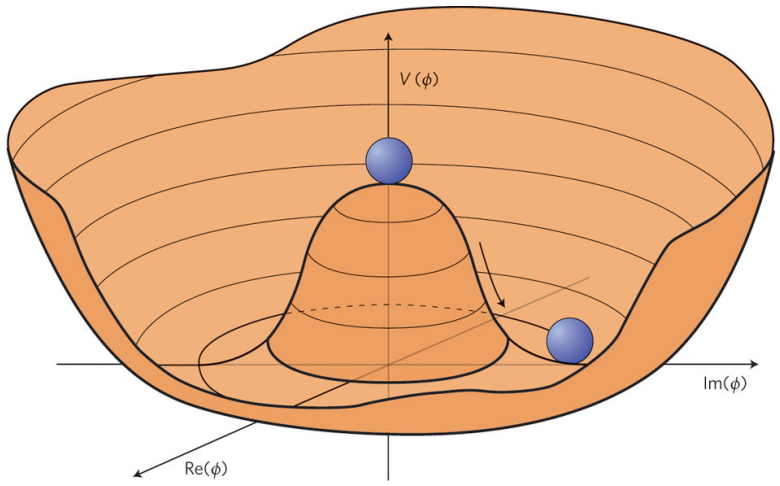

Figure 2.3 Lagrangian potential with non-zero vacuum state. In fact, vacuum state is arbitrarily chosen from infinite number of choices when falling into the vacuum state. This leads to spontaneous symmetry breaking. Fluctuations in the azimuthal direction around the vertical axis correspond to a Nambu-Goldstone boson, while excitations in the radial direction give rise to a massive Higgs boson [33].

and equation 2.9 becomes

$$\mathcal{L} = \tfrac{1}{2}\partial_\mu\theta\,\partial^\mu\theta + \tfrac{1}{2}\partial_\mu h\,\partial^\mu h - \mu^2 h^2 + ... \tag{2.11}$$

where the constant terms corresponding to neither mass nor kinetic energy, are omitted. From Equation 2.11 one can identify a massless Nambu-Goldstone boson in the θ mode and an additional massive boson in the h mode, with mass $\sqrt{2}\mu$, which will be associated with the Higgs boson.

For a global symmetry the Goldstone theorem predicts an additional massless scalar boson which was not experimentally observed. However, under SSB of continuous local symmetry, the Nambu-Goldstone bosons are remarkably 'absorbed' by the gauge bosons. The additional degrees of freedom the gauge bosons assume give them mass, by what is known as the Higgs mechanism [8–12].

This can be seen when considering a Lagrangian for a U(1) gauge theory with a sombrero hat potential

$$\mathcal{L} = (D_\mu\phi)^\dagger(D^\mu\phi) - \tfrac{1}{4}F_{\mu\nu}F^{\mu\nu} + \mu^2\phi^\dagger\phi - \lambda(\phi^\dagger\phi)^2 \tag{2.12}$$

where $D_\mu = \partial_\mu + iqA_\mu$ is the covariant derivative and $F_{\mu\nu} = \partial_\mu A_\nu - \partial_\nu A_\mu$ is the electromagnetic field tensor. Such Lagrangian is invariant under local U(1)

transformations for a gauge transformation of the potential $A_\mu \to A_\mu + \frac{1}{q}\partial_\mu \alpha(x)$ and $\phi \to \phi e^{i\alpha}$. One can choose to set $\alpha(x) = -\theta(x)/v$, absorbing the θ mode into the photon field $A_\mu \to A_\mu - \frac{1}{qv}\partial_\mu \theta(x)$. By absorbing the θ-mode, the excitations of the vacuum are thus given by

$$\phi(x) = \tfrac{1}{\sqrt{2}}(v + h(x)) \tag{2.13}$$

and the Langragian from Equation 2.12 can be written as

$$\mathcal{L} = \tfrac{1}{2}q^2v^2\mathrm{A}_\mu\mathrm{A}^\mu - \tfrac{1}{4}\mathrm{F}_{\mu\nu}\mathrm{F}^{\mu\nu} + \tfrac{1}{2}\partial_\mu h \partial^\mu h - \mu^2 h^2 + ... \tag{2.14}$$

where static terms are again omitted. The Nambu-Goldstone boson is now absorbed by the A_μ field giving it mass qv and we are still left with a massive Higgs boson, h. The Higgs boson is a by-product of the Higgs mechanism, which also generates a massive A_μ field.

Parallels can be drawn to other phenomena where the U(1) symmetry is spontaneously broken, giving mass to the photon. In superconductors for example, QED is spontaneously broken, giving the photon mass [35, 36] which leads to the Meissner effect [37]. The resultant bosonic field from lattice vibrations is given by a Bose-Einstein condensate of bound electrons in the form of a Cooper pair [38]. The similarity of Cooper pairs and the Higgs boson has motivated speculations that the Higgs boson is a composite particle [39].

The given case of SSB for a U(1) symmetry corresponding to QED needs to be extended to the non-Abelian SU(2) × U(1) group to include the SU(2) fields $\mathrm{W}^\pm$ and Z [40]. For a SU(2) × U(1) gauge theory the Lagrangian from Equation 2.11 has a potential given by

$$\mathcal{L} = (D_\mu\phi)^\dagger(D^\mu\phi) - \tfrac{1}{4}F_{\mu\nu}F^{\mu\nu} - \tfrac{1}{4}G_{\mu\nu}G^{\mu\nu} + \mu^2\phi^\dagger\phi - \lambda(\phi^\dagger\phi)^2 \tag{2.15}$$

with the covariant derivative $D_\mu = \partial_\mu + \frac{i}{2}g\vec{\sigma}\cdot\vec{\mathrm{W}}_\mu + \frac{i}{2}g\text{'}Y\mathrm{B}_\mu$ and field tensors $F_{\mu\nu} = \partial_\mu\mathrm{W}_\nu - \partial_\nu\mathrm{W}_\mu - g\mathrm{W}_\mu\mathrm{W}_\nu$ and $G_{\mu\nu} = \partial_\mu\mathrm{B}_\nu - \partial_\nu\mathrm{B}_\mu$. The Pauli spin matrices, $\vec{\sigma}$, are the generators of SU(2). Here we consider ϕ, a SU(2) doublet of complex scalar fields

$$\phi = \begin{pmatrix}\phi^+\\ \phi^-\end{pmatrix} = \frac{1}{\sqrt{2}}\begin{pmatrix}\phi_1 + i\phi_2\\ \phi_3 + i\phi_4\end{pmatrix} \tag{2.16}$$

As before there are infinite degenerate vacuum states satisfying $\phi_1^2+\phi_2^2+\phi_3^2+\phi_4^2 = v^2$. Just as for the U(1) case of the Higgs mechanism, the gauge absorbs

the additional ϕ modes, resulting in small perturbations around the vacuum expectation

$$\phi = \frac{1}{\sqrt{2}} \begin{pmatrix} 0 \\ v + h(x) \end{pmatrix} \tag{2.17}$$

and the Lagrangian from Equation 2.15 can be written as

$$\mathcal{L} = \tfrac{1}{8} g^2 v^2 \mathrm{W}_\mu \mathrm{W}^\mu - \tfrac{1}{4} F_{\mu\nu} F^{\mu\nu} + \tfrac{1}{8} v^2 g'^2 \mathrm{B}_\mu \mathrm{B}^\mu - \tfrac{1}{4} v^2 g g' \mathrm{B}_\mu \mathrm{W}_3^\mu - \tfrac{1}{4} \mathrm{G}_{\mu\nu} \mathrm{G}^{\mu\nu} + \tfrac{1}{2} \partial_\mu h \partial^\mu h - \mu^2 h^2 + ... \tag{2.18}$$

or

$$\mathcal{L} = \tfrac{1}{4} g^2 v^2 \, \mathrm{W}_\mu^+ \mathrm{W}^{-\mu} - \tfrac{1}{2} (\partial_\mu \mathrm{W}_\nu^+ - \partial_\nu \mathrm{W}_\mu^+)(\partial^\mu \mathrm{W}^{-\nu} - \partial^\nu \mathrm{W}^{-\mu}) + \tfrac{1}{8} v^2 (g^2 + g'^2) \mathrm{Z}_\mu \mathrm{Z}^\mu - \tfrac{1}{4} (\partial_\mu \mathrm{Z}_\nu - \partial_\nu \mathrm{Z}_\mu)(\partial^\mu \mathrm{Z}^\nu - \partial^\nu \mathrm{Z}^\mu) - \tfrac{1}{4} F_{\mu\nu} F^{\mu\nu} + \tfrac{1}{2} \partial_\mu h \, \partial^\mu h - \mu^2 h^2 + ... \tag{2.19}$$

The $W^\pm$ bosons acquire a mass of $gv/2$, the Z boson acquires a mass of $v\sqrt{g^2 + g'^2}/2$. By equation 2.5 the relationship $m_\mathrm{W} = m_\mathrm{Z} \cos\theta_\mathrm{W}$ was predicted and later verified. As before, all Nambu-Goldstone bosons are absorbed and a Higgs boson of mass $\mu/\sqrt{2}$ is generated as a by-product of SSB. But no prediction on the Higgs boson mass is given by the theory as μ is a free parameter, which made its experimental verification difficult.

Finally, Yukawa couplings were incorporated into Electroweak theory to allow for fermion masses. For the example of an electron SU(2) doublet $\boldsymbol{e}_\mathrm{L}$,

$$\boldsymbol{e}_L = \begin{pmatrix} e_\mathrm{L} \\ \nu_{e\,\mathrm{L}} \end{pmatrix}, \tag{2.20}$$

its coupling to the Higgs doublet ϕ as in Equation 2.17 leads to a Lagrangian density of

$$\mathcal{L} = -g_e (\bar{\boldsymbol{e}}_\mathrm{L} \phi \, e_\mathrm{R} + \bar{e}_\mathrm{R} \phi^\dagger \boldsymbol{e}_\mathrm{L}). \tag{2.21}$$

Here g_e is the electron Yukawa coupling strength and e_R is the right-handed electron singlet. The coupling to the vacuum state of the Higgs potential and the coupling to the Higgs boson can expressed in the following expansion

$$\mathcal{L} = -\frac{g_e \, v}{\sqrt{2}} \big(\bar{e}_\mathrm{L} e_\mathrm{R} + \bar{e}_\mathrm{R} e_\mathrm{L}\big) - \frac{g_e}{\sqrt{2}} \big(\bar{e}_\mathrm{L} h \, e_\mathrm{R} + \bar{e}_\mathrm{R} h \, e_\mathrm{L}\big). \tag{2.22}$$

The first term represents the electron mass m_e equivalent to $g_e v/\sqrt{2}$ and the second term corresponds to the coupling of the electron to the Higgs boson,

which is proportional to m_e/v. This result, illustrated for the simpler case of the electron, also holds for other fermion couplings[3] including quarks, where the coupling constant g_e must be replaced by a more general fermion coupling constant g_{F} which is proportional to m_{F}.

The discovery of the Higgs boson at the LHC, as discussed in the following Chapter experimentally confirms the presented mechanisms of vector boson and fermion mass generation. Detailed measurements of its interactions with gauge bosons are presented and its interactions with fermions are tested.

[3]It can be seen that the neutrino masses are predicted to be zero, due to the fact that there is no right-handed neutrino field in the theory. The observation of neutrino oscillations [41] however suggest a non-zero mass difference between the neutrino families.

Chapter 3

The Higgs boson at the LHC

In 2012 the ATLAS and CMS collaborations announced the discovery of a new particle, which was consistent with the long sought-after Higgs boson [42]. Since the observation of a new particle by the ATLAS [3] and CMS [4] collaborations in the search for the Standard Model (SM) Higgs boson [43–48], the mass, spin, charge conjugation and parity of the new particle have been measured by both collaborations [15–17]. The mass of the new particle has been measured to be $m_{\mathrm{H}} = 125.09 \pm 0.24$ GeV [15] by combining ATLAS and CMS measurements. The strengths of the couplings between the new particle and the gauge bosons and fermions have also been explored [13, 14]. In all cases the results are consistent with SM predictions, as shown in Figure 3.1.

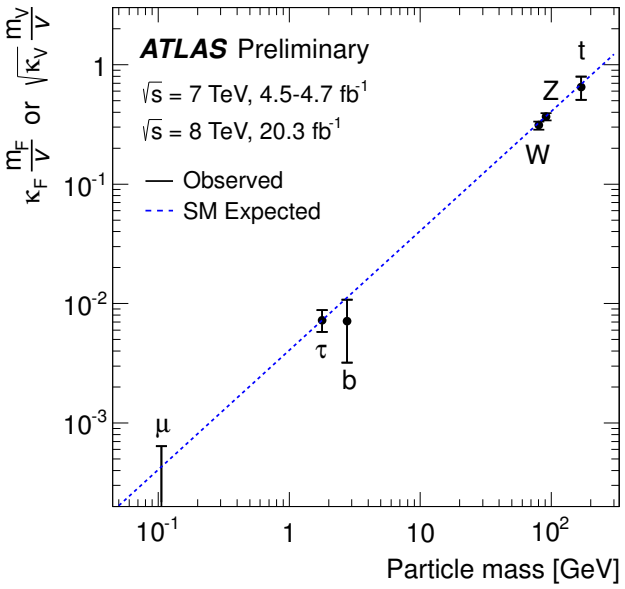

Figure 3.1 Higgs boson coupling strength scale factors for bosons and fermions as a function of the particle mass, assuming a SM Higgs boson with a mass of 125.36 GeV [49]. The dashed line indicates the predicted mass dependence for the SM Higgs boson. κ_F or κ_V is the ratio of measured to SM predicted cross section times branching ratio of the Higgs coupling to fermions or vector bosons.

3.1 Higgs Boson Production

The SM Higgs boson couples directly to all massive SM particles, with a coupling strength that depends on the mass of the particle. For gauge boson and fermion couplings the coupling strength scales quadratically and linearly respectively,

$$g_{\mathrm{HVV}} \propto \frac{m_{\mathrm{V}}^2}{v}, \quad g_{\mathrm{HFF}} \propto \frac{m_{\mathrm{F}}}{v}, \tag{3.1}$$

as displayed by Equations 2.19 & 2.22. Therefore, the dominant Higgs boson production modes involve the top quark, and the $\mathrm{W}^{\pm}$ and Z bosons. Couplings to massless gluons and photons is only possible via intermediate loops, containing virtual massive particles. The dominant Higgs boson production mechanisms for proton-proton collisions at the LHC are shown in Figure 3.2. The proton constituents are comparably light and the Higgs boson is primarily produced through heavy mediators, e.g. a $t\bar{t}$ loop. The cross sections of the most important production mechanisms with 8 TeV proton-proton collisions are given in Table 3.1.

Gluon-gluon fusion (ggF) is the dominant production mode of the Higgs boson

Process	Cross section in fb
ggF	19.27 ± 2.01
VBF	1.58 ± 0.04
WH	0.70 ± 0.02
ZH	0.42 ± 0.02
ttH	0.13 ± 0.02
bbH	0.20 ± 0.03

Table 3.1 Predicted Higgs boson production cross section in femto barns (fb) at the LHC for 8 TeV proton-proton collisions, for a Higgs boson with mass of 125 GeV. Values are given for NNLO QCD and NLO EW precision [50].

at the LHC, shown in Figure 3.2(a). Two incoming gluons g from two colliding protons interact via a loop process mediated by a quark. The heavy top quark t is the dominant mediator as the coupling to the Higgs boson scales with fermion mass. The dominant ggF production cross section is given by the strong coupling in $g \to t\bar{t}$ and large Yukawa coupling in $t\bar{t} \to$ H.

Vector boson fusion (VBF) is the second most common production mechanism,shown in Figure 3.2(b). Under VBF two incoming quarks each radiate either two oppositely charged W bosons or two Z bosons, which fuse to form a Higgs boson. The initial quarks undergo a large momentum transfer and form energetic jets, in the forward direction, close to the proton beam-line. VBF is thus characterised by events with two associated hadronic jets.

Associated production of a Higgs boson with a vector boson (VH), also called 'Higgsstrahlung', is the third most likely production mode, shown in Figure 3.2(c). An incoming quark q and anti-quark $\bar{q}$ scatter to form a W or Z boson which then radiates a Higgs boson. VH production is suppressed over the previous mechanisms due to the high mass of the vector boson that needs to be generated in addition to the Higgs boson. Further suppression arises from the relatively weak coupling of $q\bar{q} \to$ W/Z.

Finally, associated production (ttH , bbH) with a $t\bar{t}$ or $b\bar{b}$ pair, shown in Figure 3.2(d). It is similar to the ggF process, except that instead of a closed virtual quark loop the quarks are two real outgoing particles, measurable in the final state. The production of heavy quarks means this mode is highly kinematically suppressed over ggF.

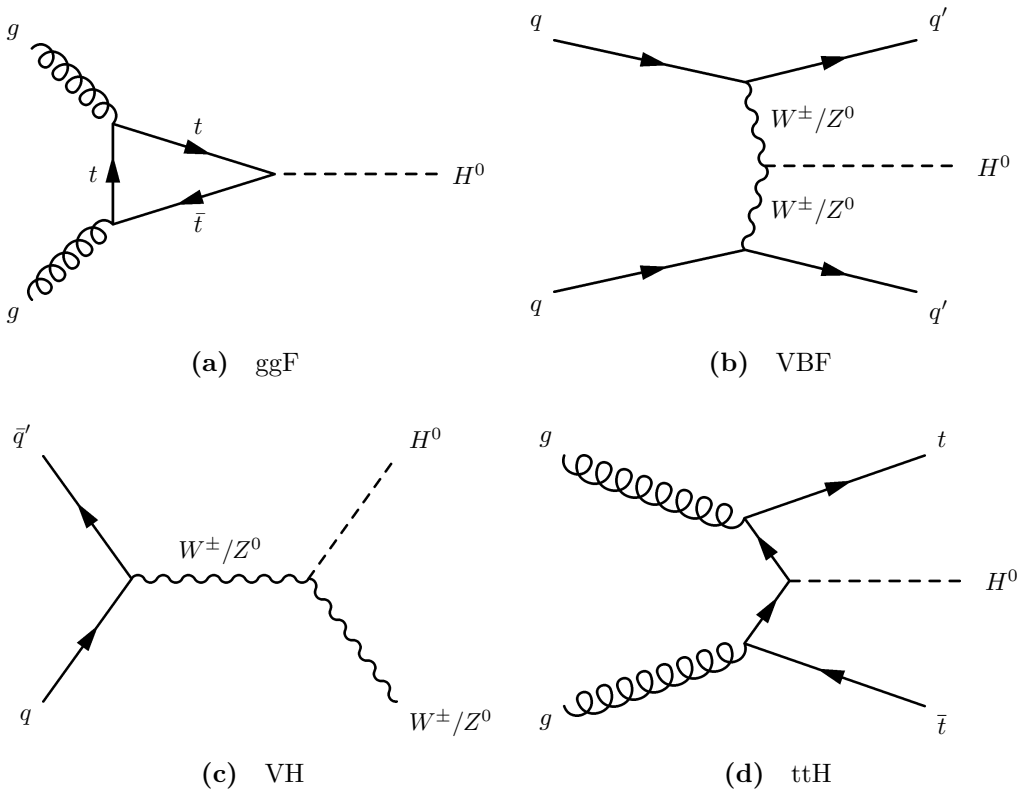

(a) ggF **(b)** VBF

(c) VH **(d)** ttH

Figure 3.2 Feynman diagrams of the dominant Higgs boson production mechanisms at the LHC. (a) gluon-gluon fusion, (b) vector boson fusion, (c) Higgsstrahlung and (d) $t\bar{t}$ associated production.

3.2 Higgs Boson Decays

For a mass of 125 GeV the Higgs boson is expected to have a very short lifetime of $1.6 \cdot 10^{-22}$ s, with an experimental upper bound of $1.9 \cdot 10^{-13}$ s [51]. It is therefore never observed directly, but rather from various decay products. Although the Higgs boson mass is not predicted by the theory, decay branching ratios are predicted as a function of the Higgs boson mass. In general it is kinematically required to have $m_H > m_A + m_B$ for a $H \to A + B$ decay, but 'off-shell' processes are allowed, yet suppressed, where this condition is violated. An example of this is given by the $H \to WW^*$ channel. Decay modes involving massless particles are mediated via loops of massive (electrically or colour) charged particles. The dominant branching ratios of a 125 GeV Higgs boson are given in Figure 3.3.

Differentiating between a Higgs boson signal and other processes with identical final state signatures, called background, is the main challenge in performing Higgs boson measurements. Different Higgs boson decay modes have different background compositions, and sensitivity is enhanced by studying each decay channel independently. The discovery of the Higgs boson in 2012 was based on the ZZ, $\gamma\gamma$ and WW decay channels [3, 4]. The first observation to fermion decays was later seen in $H \to \tau\tau$ decays [52, 53].

The properties of the WW and $b\bar{b}$ channels which are considered in this thesis are highlighted below.

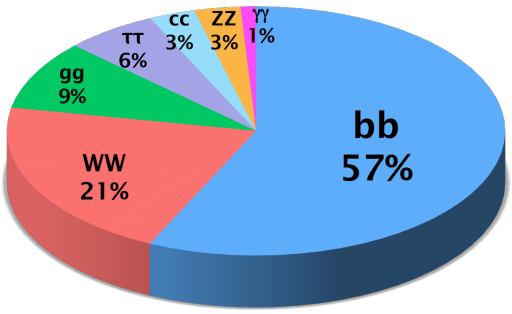

Figure 3.3 Predicted branching ratios of the Higgs boson for $m_H = 125$ GeV.

3.2.1 The H→WW* Channel

The H → WW* channel has the second largest branching ratio of all SM 125 GeV Higgs boson decays. This decay is only kinematically allowed when one of the W bosons is off-shell, denoted as W*. The W boson decays hadronically W → qq', 67.6% of the time. The leptonic decay rate, W → $\ell\nu$, is 10.8% per lepton flavour [54]. The H → WW* channel thus produces $qqqq$, $\ell\nu qq$ and $\ell\nu\ell\nu$ final states. The fully leptonic H → WW* → $\ell\nu\ell\nu$ decay is characterised by two oppositely charged final stated leptons and has the highest signal to background ratio of the three decay modes. The reconstruction of a measured H → WW → e$\nu\mu\nu$ candidate event is shown in Figure 3.4.

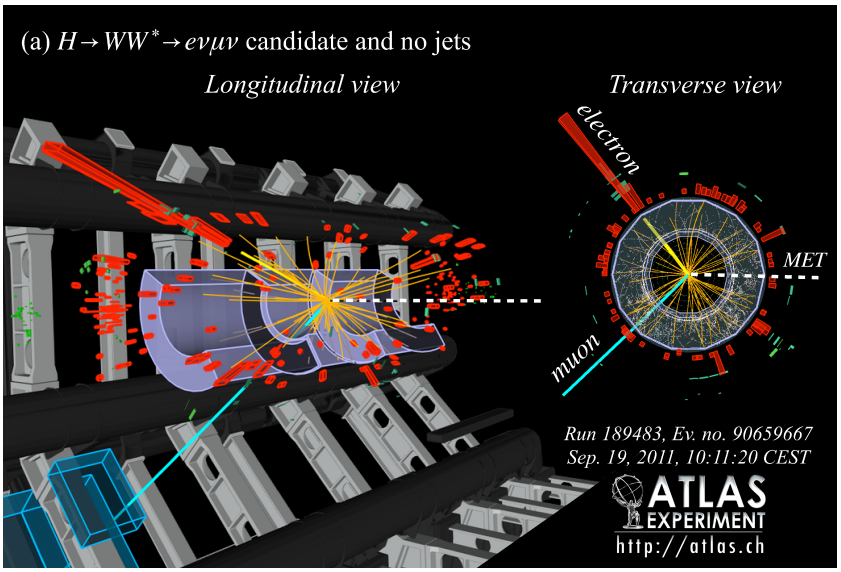

Figure 3.4 Event display of a H → WW → e$\nu\mu\nu$ candidate with no additional jets, produced by ggF. The neutrinos are represented by missing transverse momentum (E_T^{miss}, dotted line) that balances the electron and muon momenta. The properties of the shown event are $p_T^e = 33$ GeV, $p_T^\mu = 24$ GeV, $m_{e\mu} = 48$ GeV, $\Delta\phi_{e\mu} = 1.7$, $p_T^{miss} = 37$ GeV, and transverse mass $m_T = 98$ GeV [55].

3.2.2 The H → b$\bar{\text{b}}$ Channel

The H→ $b\bar{b}$ channel has the largest branching ratio of all SM 125 GeV Higgs boson decays. This channel suffers from an overwhelming background of directly produced b-jets, which has a 10^7 times larger cross section than the ggF produced Higgs boson for 8 TeV collisions. The signal to noise is however greatly enhanced

by focusing the experiment search to the VH production mode in which the associated vector boson decays leptonically, which provides an effective method of background rejection. In the case of ZH production, the most useful channels are given by Z boson decays to two oppositely charged electrons or muons, or to two neutrinos. The branching ratio of $Z \to \nu\bar{\nu}$ decays is 20%, while $Z \to \ell\ell$ has a branching ratio of 3.4% per lepton family. The reconstruction of a measured $ZH \to e^+e^-b\bar{b}$ candidate event is shown in Figure 3.5.

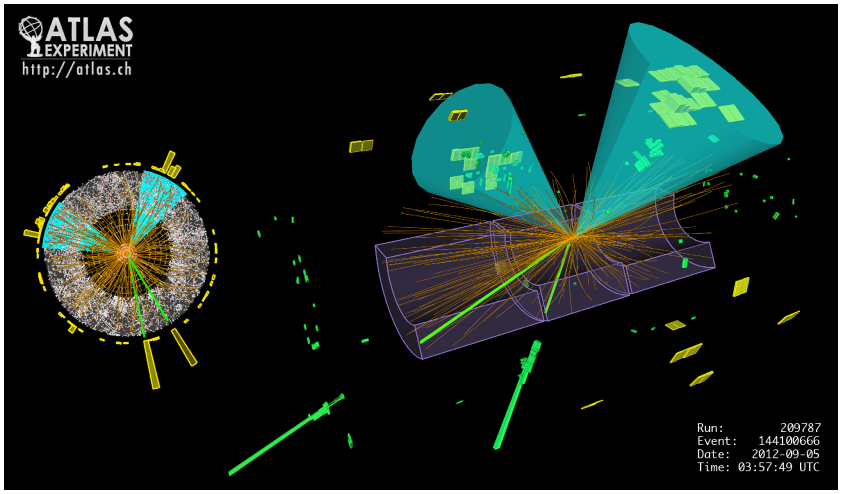

Figure 3.5 Display of a Higgs boson candidate event with two selected leptons. The two identified b-jets have transverse momenta of 70 GeV and 65 GeV, respectively, with an invariant mass of 122 GeV. The identified electrons have transverse momenta of 63 GeV and 54 GeV, respectively, resulting in a transverse momentum of the Z boson candidate of 115 GeV [56].

Chapter 4

Simulation of LHC Particle Interactions

Simulation of signal and background processes are an important ingredient to any analysis conducted at the LHC. The Higgs boson search relies on modelling background well in order to measure an excess in data over the simulated background expectation. Numerical results from Monte Carlo simulation are obtained by repeated random sampling of variables from probability distributions based on phase-space integrations of matrix element calculations. Monte Carlo (MC) data production is performed in four stages: colliding partons, hard interaction process, showering model of quark hadronisation and the detector response. Simulated data samples are constructed separately for all background processes and signal hypotheses, which are then compared to measured data. The modelling of quantum chromodynamics is a key element in describing production and decay process at the LHC.

4.1 Quantum Chromodynamics

QCD describes the strong interaction of coloured particles, quarks and gluons. The modelling of QCD is governed by two important features, namely *confinement* and *asymptotic freedom*. Confinement describes the phenomenon that quarks do not exist in isolation but rather form colourless compound hadrons [57]. At small distances, as within a hadron however, the constituent

partons experience a low interaction strength and have a high degree of freedom to move independently of each other, referred to as asymptotic freedom. Both features relate to the running of the strong coupling constant. The strong coupling constant of QCD α_s and its dependence on Q is shown in Figure 4.1.

The running of the coupling constant reflects the fact that the strength of the strong force changes with the energy scale Q of the interaction. For small scales, corresponding to large distances, the coupling is large and the theory is non-perturbative. In this low energy region the principle of confinement dominates [57]. For high scales, corresponding to small distances, α_s is small and the process behaves according to asymptotic freedom [58].

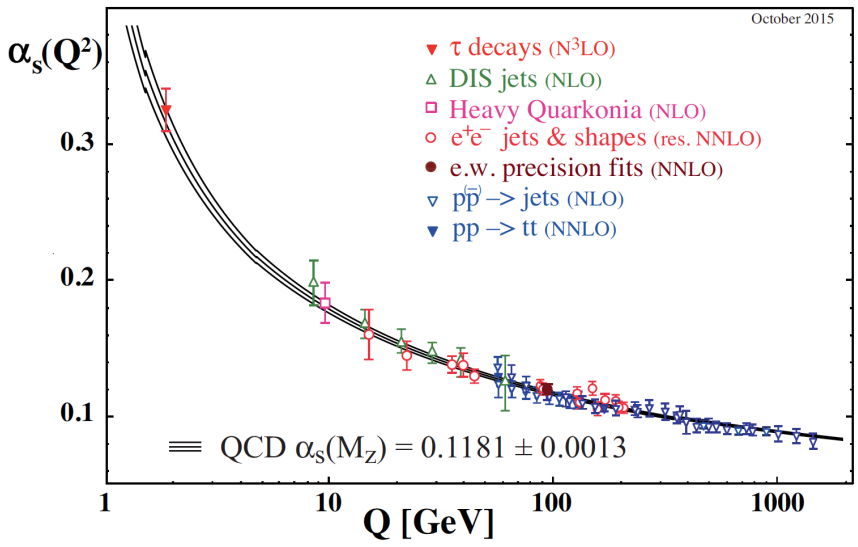

Figure 4.1 Running of the strong coupling constant α_s as a function of the energy scale Q [59]. The shape of the running is predicted by the SU(3) theory but the level must be determined by experiment for fixed values of Q. The world average of α_s measured at the energy scale of the Z boson mass is given.

UV divergences in loop integrals can occur in the theory of QCD. These divergences are compensated for by *renormalisation*. An unphysical and arbitrary *renormalisation scale* μ_R is chosen [60], by which otherwise divergent energies are separated. Above μ_R, loops are renormalised and below μ_R, loops are calculated in perturbation theory. The value of μ_R is typically chosen to be equal to the factorisation scale μ_F, see Section 4.2, satisfying the relation of $Q/2 < \mu_R,\, \mu_F < 2\,Q$ [60].

4.2 Parton Distribution Functions

In proton-proton collisions at the LHC interactions between the proton constituents occur. These constituents, called partons, are either one of the three valence-quarks (uud) or spontaneously produced non-valence quark-anti-quark pairs and gluons that arise from the strong interaction between the valence quarks. The parton distribution functions (PDF) describe the momentum distribution of partons within a proton [61]. A PDF gives the probability of a given parton flavour to assume a momentum fraction x of the total proton momentum for a energy scale Q. Due to the non-perturbative QCD description of the strong interaction between partons inside a hadron and the limitations in current lattice QCD calculations, PDFs cannot be predicted directly. PDFs are therefore obtained from parametrisations of parton models to experimental data collected at collider experiments and fixed target experiments, most crucially in deep inelastic scattering for example at the DESY electron-proton collider HERA [62].

Since measurements are only possible for certain Q^2 scales, it is necessary to extrapolate to the regime of interest. This evolution is described by the DGLAP [63, 64] equations which calculate the probability of a parton assuming a momentum fraction x, $f(x, Q^2)$, for any Q^2 where the strong coupling constant $\alpha_s(Q^2)$ is known. An example of the MSTW2008 PDF set is given in Figure 4.2, where the probability density distributions of different partons of particular momentum fractions for fixed values of Q^2 are shown.

Following the QCD factorisation theorem [66], the PDFs are used as weights for the incoming momenta of the hard process. It states that the hard scatter can be treated independently from soft pertubative emissions. The boundary defining which emissions are treated as part of the hard scatter and which are described by the PDF is given by a factorisation scale μ_F. The choice of μ_F, which is proportional to Q, can be a large source of uncertainty in the modelling a of process.

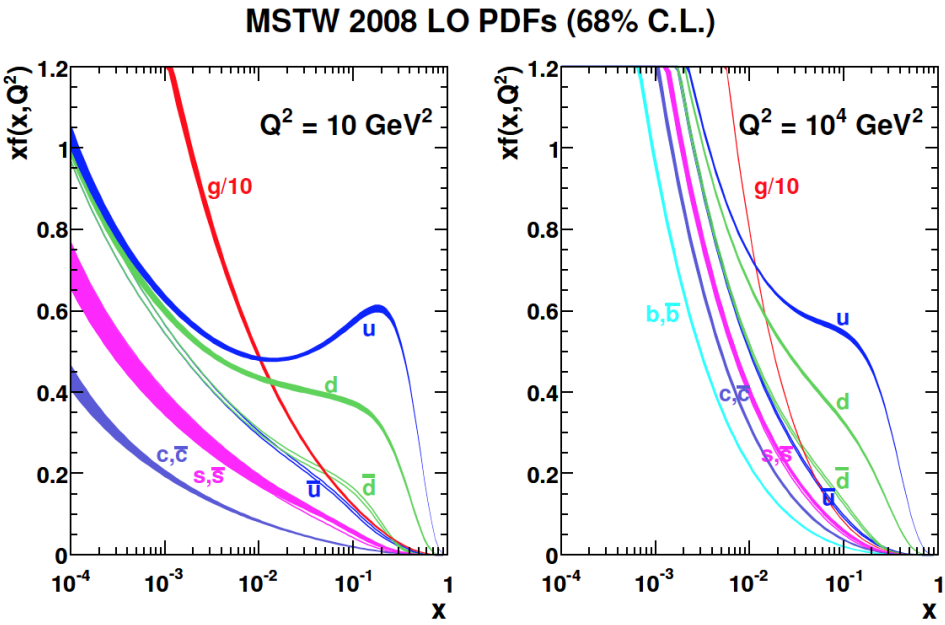

Figure 4.2 Example of leading order parton distribution functions from the MSTW2008 PDF set [65] for protons. Momentum fraction x is weighted by its PDF value $f(x, Q^2)$ for fixed values of Q^2. The bands indicate 68% confidence level uncertainties. The right-hand PDF evaluated at $Q = 100$ GeV corresponds roughly to the Higgs boson mass.

4.3 Perturbative QCD

Interesting collision interactions involve high momentum transfer and thus high momentum partons that are asymptotically free. Therefore, parton level cross sections σ can be computed as perturbative series in α_s

$$\sigma = \sum_{m=0}^{n\to\infty} \alpha_s(Q^2)^{k+m}\sigma(m). \tag{4.1}$$

Here k denotes the number of QCD vertices at leading order and $\sigma(m)$ is the cross section contribution of order m. Such series converges since typically $\alpha_s < 1$. In practice calculations are made to fixed order n ($n \neq \infty$), either $n = 0$ (LO), $n = 1$ (NLO) or $n = 2$ (NNLO). For fixed order calculations there is a residual dependence on the renormalisation scale μ_R and factorisation scale μ_F. The residual term from missing higher order contributions is of order α_s^{k+n+1} and its size is indirectly established by varying μ_R and μ_F, as the physical cross section is independent of the scales choices. The dependence of the residual term on the scale choices constitutes a theory uncertainty on the calculation.

Fixed order calculations of converging series are a good tool to calculate cross sections. Additional soft emissions from the hard scatter process however can cause non-perturbative behaviour of the series. In such cases resummation techniques are required.

4.4 QCD Resummation

The cross sections of exclusive processes are calculated for a subset of the total phase space. Differential cross sections for example are calculated in independent steps for each bin of the distribution. In this case it is not given that higher order terms are necessarily decreasing in size for all individual regions of phase space. Resummation accounts for a logarithmically enhanced subset of terms at each order of the perturbative series.

The quark-quark scattering cross section for example is enhanced by the emission of a low momentum gluon. The contribution depends on the logarithm of the difference in the energy scale Q of the hard scatter and the scale of the soft emission Q_1. The terms of the perturbative series are modified as $\alpha_s^{k+m} L^{2m}$ where $L \sim \ln(Q_1/Q)$. Given the additional gluon emission the series assumes the schematic form

$$\sigma \sim \alpha_s^k \Big[\alpha_s \big(L^2 + L + 1\big) + \alpha_s^2 \big(L^4 + L^3 + L^2 + L + 1\big) + \mathcal{O}\big(\alpha_s^3 L^6\big) \Big] \tag{4.2}$$

For soft emissions Q_1 is small compared to Q and the probability of emission approaches 1, resulting in $\alpha_s L^2 \approx 1$. Thus the logarithmic contribution exceeds the suppression of α_s with increasing order m and the series is no longer perturbative in α_s. A similar argument holds for collinear emissions, where the angle of the emission approaches zero.

Cross section calculations involving large logarithmic contributions need to be *resummed*. Resummation refers to the re-ordering of terms defining which contributions are considered for a fixed order calculation. Before the perturbative series was ordered in powers of α_s and the leading terms were considered for a fixed order calculation. Under resummation the series is ordered by powers of $\alpha_s L^2$, taking into account logarithmic enhancement from additional soft or collinear emissions. Calculations up to the order of $\alpha_s^{k+m} L^{2m}$ are referred to as leading logarithms (LL) while $\alpha_s^{k+m} L^{2m-1}$ terms are next-to-leading logarithms (NLL).

The measured cross sections in Section 8.12 are compared to theoretical predictions. Most of these are calculated at NNLO and NNLL precision. For calculations at NNLO+NNLL, terms of both α_s and $\alpha_s L^2$ are summed, while removing potential double-counting.

Typically, soft or collinear emission is simulated by a parton shower model which includes a resummation procedure. A showering model generates emissions from an outgoing parton, which consequentially loses energy and approaches the non-perturbative confinement region. The showering models described later typically calculate emissions at NNLL order.

4.5 Matrix Element

The first stage of simulating particle interactions is the calculation of the matrix element, which describes the transition of an initial to a final state via a mediator. The matrix element describes the initial scattering without subsequent decays of the outgoing particles, known as the *hard process*. Feynman diagrams are used to describe these processes; the leading oner ones for quark-quark scattering are shown in Figure 4.3. The interaction amplitude is given by the matrix element, $\mathcal{M}$, which is calculated from the features of the diagram: the incoming and outgoing momenta as well as the couplings of the interaction vertices. Following the Feynman rules [67], the matrix element for the process of quark scattering via gluon exchange shown in Figure 4.3a is

$$\mathcal{M} = \frac{g_s^2}{q^2} \frac{\lambda_{ij}^a \lambda_{lk}^a}{4} \Big[\bar{u}_j \gamma^\mu u_i\Big] \Big[\bar{v}_k \gamma_\mu v_l\Big] \tag{4.3}$$

expressed at Leading Order (LO), with the Dirac matrices γ^μ. Here q is the gluon momentum, a is the colour index of the gluon (1 to 8), i, j, k, l are the quark colours (1,2,3) and λ^a is the Gell-Mann matrix, with implicit sums over all indices. The interaction strength is given by the coupling constant of the strong force, g_s.

Diagrams with additional vertices to the hard-scatter process are called Next-to-Leading Order (NLO). Besides the LO diagram of Figure 4.3a, other diagrams with the same initial and final state can be constructed, containing additional internally closed loops, as in Figures 4.4a&b. Likewise, additional emissions producing measurable quantities can occur, as in Figure 4.4c. In practice the

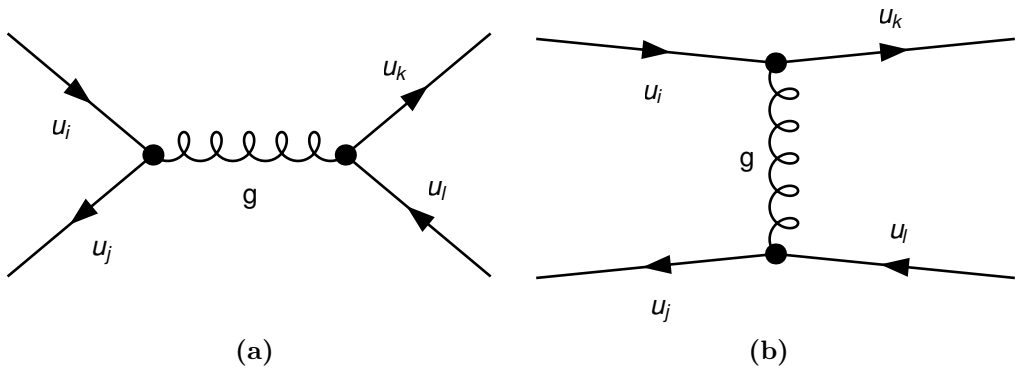

Figure 4.3 Example of quark scattering via the exchange of a gluon in the (a) space-channel and (b) time-channel. In coming quarks are labelled as u_i and u_j, the final state quarks are labelled as u_k and u_l.

matrix element $\mathcal{M}$ is calculated from the sum of the LO process and NLO corrections. The number of additional diagrams grows factorially with ascending order of the series expansion describing $\mathcal{M}$, making NNLO or higher order calculations complex and computationally expensive. With the exception of *soft* QCD processes with low momentum transfer, the amplitude of higher order contributions decreases, suppressed by additional factors of the coupling constant α_s. Thus a truncated series expansion approach is a legitimate description of interactions and estimates the impact of higher order calculations as corrections to the LO diagram.

The matrix element $\mathcal{M}$ is the transition amplitude of incoming (i) to final state (f) particles. The kinematically allowed density of states is given by the initial and final momenta of p_i and p_f. For a simplified case where the in-going and out-going particles have equal and opposite momenta and $\mathcal{M}$ is independent of the momenta p_i and p_f, the cross section σ for two body inelastic scattering from Figure 4.3 can be expressed as [68]

$$\frac{d\sigma}{d\Omega} = \frac{1}{64\pi^2 s}\frac{|p_f|}{|p_i|}|\mathcal{M}|^2\,, \tag{4.4}$$

where Ω is the solid angle. The centre-of mass energy $\sqrt{s}$ results from the sum of energies of the two incoming particles, as $s = (E_1 + E_2)^2$, in the centre-of-mass frame. The momenta $p_{i,f}$ are given in the centre-of-mass frame. $\mathcal{M}$ is computed from Equation 4.3 where the average over all initial spin states and the sum over all out-going momentum states is taken. In the analysis presented in this thesis (Chapters 8 & 9), all signal and dominant background processes use cross sections calculated at NLO.

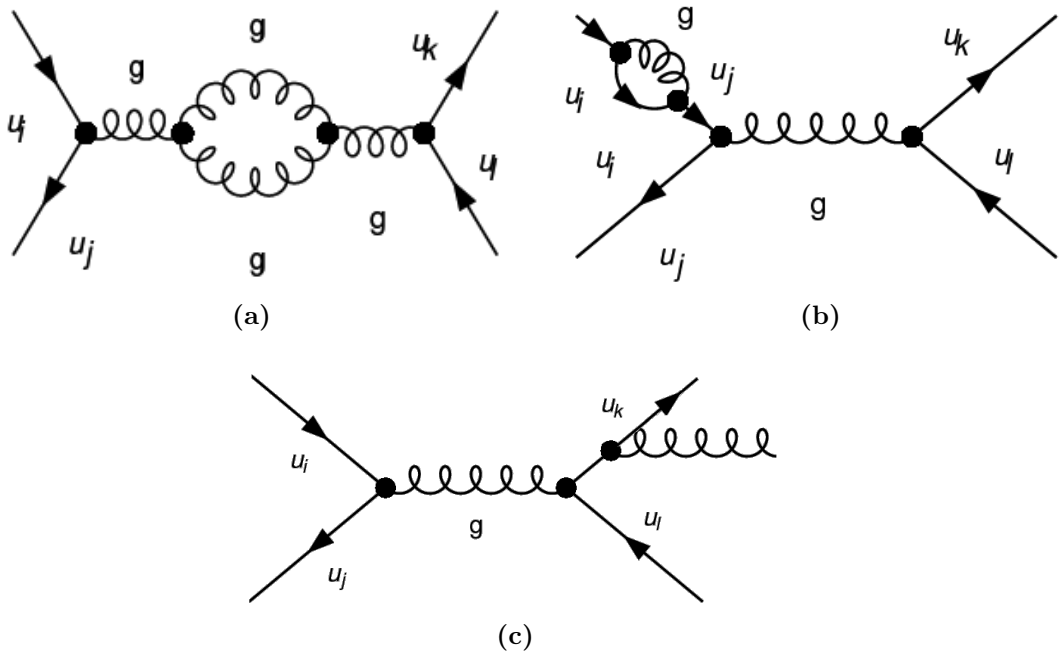

Figure 4.4 Small set of examples of Next-to-leading and Next-to-next-to-leading order diagrams. (a&b) NNLO diagrams with emission of a virtual gluon. (c) Next-to-leading order diagram with emission of an outgoing gluon.

The cross section is related to the rate dN/dt at which a process occurs by the instantaneous luminosity $\mathcal{L}$ of the collider

$$\frac{dN}{dt} = \mathcal{L}\sigma \tag{4.5}$$

and the differential cross section can be expressed as

$$\frac{d\sigma}{d\Omega} = \frac{1}{\mathcal{L}}\frac{dN}{d\Omega\, dt} \tag{4.6}$$

It is thus possible to calculate the rate of events from the matrix element for a given luminosity and phase space. This requires the incoming and outgoing particles to be well defined. In the case of the proton-proton collisions at the LHC, interactions occur between quarks and gluons carrying an unknown fraction of the proton energy. The initial state is thus not known and the distribution of p_i is given by the PDFs discussed in Section 4.2.

Likewise, the outgoing particles p_f are ill-defined in the case when they undergo subsequent decays or hadronisation, discussed in Section 4.6.

4.6 Hadronisation

The hard process, as described by the matrix element, is at the parton-level, which is not the observable final state. Due to the colour charge of the outgoing partons, additional gluons or quark antiquark pairs are emitted. This occurs above a hadronisation scale of about 1 GeV and the emissions are in the collinear direction forming a parton shower. This is simulated by randomly creating these emissions in a sequence whilst reducing the scale Q at each step using a perturbative QCD description. This model only holds for soft and collinear emissions. Hard wide-angle emissions must therefore be included into the original matrix element of the hard process.

Below the hadronisation scale of about 1 GeV, the shower constituents form colourless hadrons and QCD processes follow a non-perturbative description. This is simulated by one of two widely used phenomenological models, the cluster [69] or the string [70] model. The cluster model is used in the HERWIG [71] and SHERPA [72–76] generators, while the string model is implemented in the PYTHIA [77, 78] generator. Both models are shown in Figure 4.5.

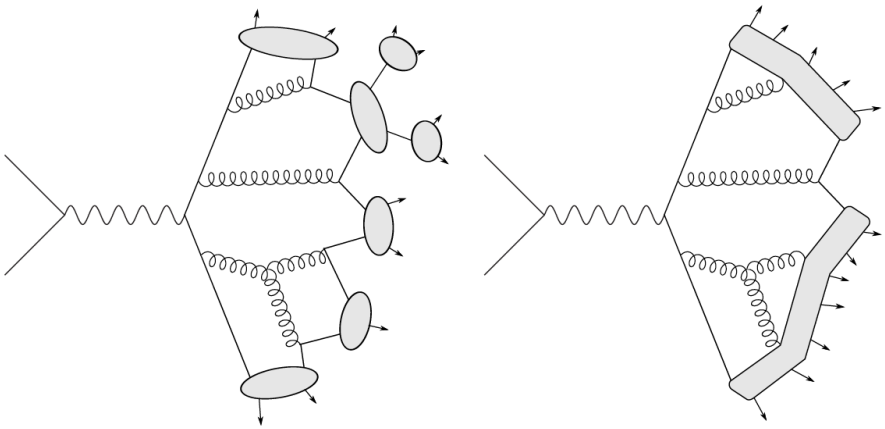

Figure 4.5 Cluster model (left) String model (right) of quark showering [69].

The **cluster model** relies on the concept of preconfinement [79] and treats the hadronic shower as a series of discrete $q\bar{q}$ pairs. Preconfinement states that colour-connected partons have a mass distribution that rapidly drops with high masses and is independent of the energy scale Q, while unassociated parton pairs are characterised by distinctly higher masses. Firstly, all outgoing or radiated gluons are split into $q\bar{q}$ pairs, then all $q\bar{q}$ pairs are combined to form colour-singlet clusters. If the mass of such cluster is above a typical threshold of 1 GeV [80], it

is split into two clusters, each containing a $q\bar{q}$ pair. This splitting is performed along the axis between both initial $q\bar{q}$ constituents. Clusters below the mass threshold are treated as excited mesons, which in turn decay to two hadrons. The final hadronisation step is performed according to the expected branching ratios. A weakness of the clustering model is its incorrect treatment of heavy initial clusters and an overestimate of baryon and heavy quark production [80].

The **string model** is a more continuous description of the hadronisation. Colour-connected $q\bar{q}$ pairs are considered and the potential between the partons is proportional to their distance. The potential is thought of as a virtual colour flux *string*. When the distance and thus the potential is sufficiently large, the string breaks and forms a new $q\bar{q}$ pair. Radiated gluons are treated as *kinks* of the strings, carrying momentum. For each string breaking vertex the resulting quark masses and momenta are set by Gaussian distributions. Baryons are formed by allowing the creation of di-quarks in string breaks.

Underlying event

Additional parton production that is not ascribed to the hard process or its showering arises from secondary interactions between remnant partons in the incoming protons. These produce additional soft partons which form the *underlying event* (UE). The UE consists of both the breakup of the beam remnants and multiple parton scattering, producing more than one distinct hard scatter. The modelling of the UE strongly relies on experimental constraints from minimum bias events. Minimum bias events are recorded with a low trigger threshold and therefore typically do not contain a hard scatter.

4.7 Detector Simulation

The final step in simulating LHC events is accounting for the detector response. The ATLAS detector is discussed in Chapter 5. In order to compare MC samples with data they are reconstructed taking into account detector inefficiencies and acceptance. A well understood model of the detector performance is thus needed. This includes a precise model of the material within the detector volume, the behaviour of all active media, signal generation and processing. Interactions of all generated final state particles with the detector material and its active

components are performed by the Geant4 package [81]. Energy depositions of particles passing through the active material are simulated and transformed into hits in the detector. Parametrisations for additional effects such as noise and event pile-up are considered. From the simulated detector hits, events are reconstructed using the same algorithms as applied to real collision data. Long lived particles with a lifetime of $c\tau > 10\,\text{mm}$ are considered stable by the MC generator and their decay is simulated by Geant4.

Detector simulation is highly resource intensive and takes longer to compute than the event generation or showering. In particular, the complex calorimeter of ATLAS requires a significant amount of time to simulate. The full detector simulation of a single $t\bar{t}$ event, for example, takes about 15 min of CPU time [82], subject to detector and data processing configurations.

4.8 Monte Carlo Generators

An overview of different generators used for the studies presented is given below. Event generators are used to model background and signal processes or provide estimates of theoretical uncertainties.

- **HERWIG** is a general purpose event generator for hard scatter modelling, describing the tree level process of two initial particles going to two final particles [71]. Higher multiplicity final states are simulated by the parton shower using the cluster model, including initial and final state radiation. It can simulate the underlying event, hadronisation and subsequent hadronic decays. Although HERWIG is only a LO generator with limited use as a standalone generator where accurate kinematic modelling is required, it is heavily used for its parton-shower algorithms.

- **PYTHIA** has strong similarity with HERWIG. A major difference arises in the way logarithmic enhancements are calculated. PYTHIA calculates the logarithm of the ratio of momenta of the particle at its soft emission, while HERWIG considers the angular separation between these. PYTHIA follows the string parton shower model [77, 78].

- **SHERPA** is a NLO multi-purpose event generator used for many final states, modelling the hard process, initial and final state radiation, as well as showering [72–76]. It is aimed at describing collision final states with

more than two partons. It uses the cluster model to merge hadronisation and showering.

- **POWHEG**, the Positive Weight Hardest Emission Generator, combines NLO QCD calculations with parton shower models, providing predictions for a wide range of signals, including the SM Higgs boson and background processes [78, 83, 84].
- **NNLOPS** Implementation of POWHEG with NNLO precision for Higgs boson plus additional jet production [85, 86].
- **MadGraph** Set of cross section calculations from Lagrangian definitions with parton shower matching. Versions such as MadGraph5_aMC@NLO provide next-to-leading order calculations [87–89].

Cross section calculators do not generate events, but provide precise calculations of total and differential cross sections. Such calculations are either used as corrections to event generators or comparisons to measurements.

- **HRes** is a dedicated tool for SM Higgs boson cross section calculations at NNLO in QCD perturbation theory and NNLL precision [90]. Predictions of the Higgs p_{T} spectra have comparatively small uncertainties. HRes is therefore used to reweight predictions made by other generators.
- **ST, BLPTW, STWZ, JetVHeto** Analytical ggF differential cross section calculations, at NNLO+NNLL precision [91–94].

MC data is primarily used for signal and background estimation or calibration of the detector. In Chapter 8 MC generators and cross section calculations are also used as a comparison to the H→WW fiducial differential cross section measurements. The H→ $b\bar{b}$ study in Chapter 9 makes predictions on the future sensitivity of this channel on the basis of MC data.

Chapter 5

The LHC and the ATLAS Experiment

The ATLAS (A Toroidal LHC Apparatus) detector is one of the 7 experiments at the Large Hadron Collider (LHC) at CERN, along side CMS (Compact Muon Solenoid), LHCb (Large Hadron Collider beauty), ALICE (LArge Ion Collider Experiment), LHCf (LHC forward), TOTEM (TOTal Elastic and diffractive cross section Measurement) and MoEDAL (Monopole and Exotics Detector at the LHC). ATLAS [95] and CMS [96] are the largest experiments, both are multi-purpose detectors capable of studying Standard Model processes, the Higgs boson as well as a wide range of beyond the Standard Model physics. LHCb [97] specialises in heavy flavour physics, investigating CP violation and searches for new physics in rare decays of hadrons containing bottom and charm quarks. ALICE [98] focuses on heavy ion collisions, to study QCD and the quark-gluon plasma at high energies and temperatures. The smaller experiments have more specific goals. LHCf [99] measures the neutral particle flux in the very forward region of the interaction point. TOTEM [100] is dedicated to measuring the total proton-proton cross section, and MoEDAL [101] searches for magnetic monopoles. The ATLAS experiment was proposed in 1994 and construction was completed in 2008. The ATLAS collaboration has roughly 3000 members from 175 institutions in 38 countries.

5.1 The Large Hadron Collider

The Large Hadron Collider (LHC) [102] is the biggest and most powerful particle collider ever built. Located at CERN, near Geneva on the French-Swiss border, the LHC is a circular collider with 27 km circumference, installed in the former LEP tunnel [103], approximately 100 m underground. The LHC is capable of colliding protons with a centre of mass energy of $\sqrt{s} = 14$ TeV and lead-ions with 2.76 TeV per nucleon. ATLAS is primarily concerned with proton collisions. The two counter-rotating beams travel in two separate beam pipes around the LHC and intersect at four interaction points, where the four main experiments are positioned. The protons are injected into the LHC by a chain of smaller accelerators as shown in Figure 5.1. First hydrogen atoms are stripped of their valence electrons, the remaining protons are then accelerated to 50 MeV in the linear accelerator LINAC2, followed by the circular Proton Synchrotron Booster (PBS), bringing the proton energy to 1.4 GeV. The Proton Synchrotron (PS) and Super Proton Synchrotron (SPS) boost the protons to 25 GeV and then 450 GeV before they are injected into the LHC. Throughout the acceleration steps the protons are arranged into bunches. The design [105] foresees 2808 bunches per beam, each containing approximately 10^{11} protons, and a bunch separations of 25 ns. The LHC acceleration is performed by 8 superconductive radio frequency (RF) cavities in each beam direction. The RF cavities boost and then maintain the proton energy with an oscillating EM field of 400 MHz, resulting in a maximum accelerating field of 5 MV/m. A total of 1232 superconducting dipole magnets are needed to bend the beams around the LHC ring. The superconducting state is achieved by cooling to 1.9 K with superfluid helium, necessary to support a current of 11700 A, corresponding to a magnetic field of 8.4 T [106] for the $\sqrt{s} = 14$ TeV configuration. Additionally, 392 superconducting quadrupole magnets focus and stabilise the beams. The first run of the LHC (Run 1), lasted from 2010 until 2012, during which the LHC operated at a centre of mass energy of $\sqrt{s} = 7$ TeV and $\sqrt{s} = 8$ TeV, with a bunch spacing of 50 ns.

5.1.1 Luminosity and Pile-up

To study rare processes a large dataset is needed, which is achieved by a high collision rate, quantified by the instantaneous luminosity, $\mathcal{L}$. The expected

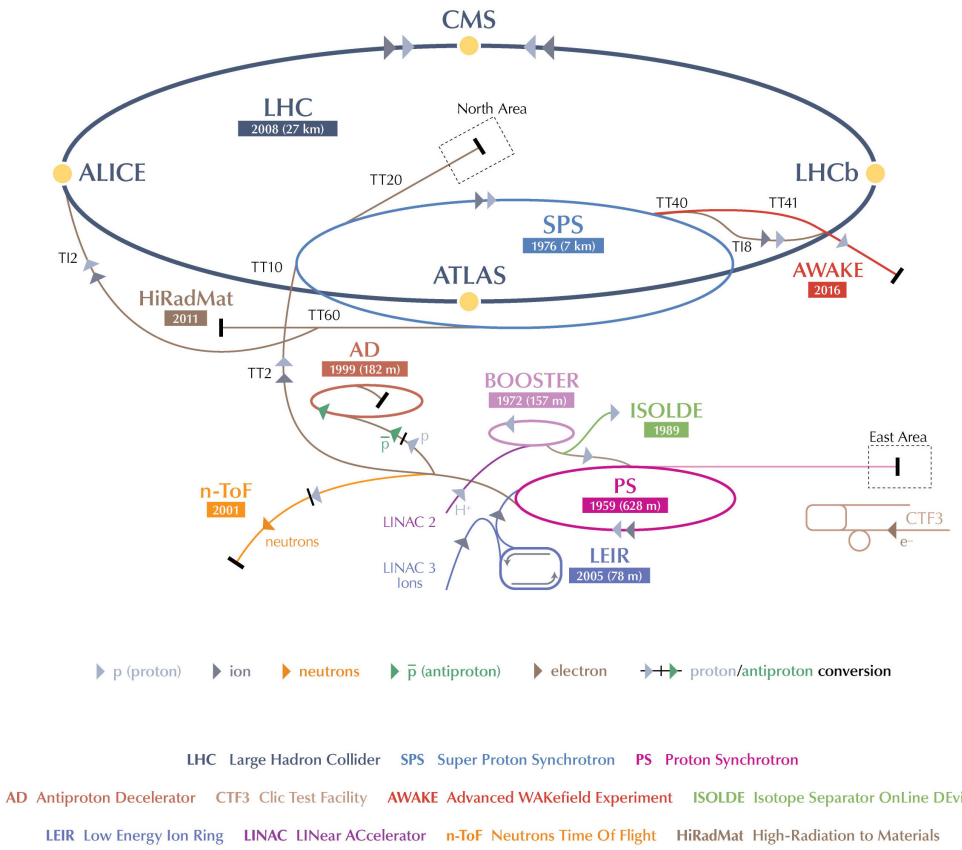

Figure 5.1 The LHC with the four major experiments are shown together with the accelerator complex that serves as an injector for the LHC [104].

number of events N_i for a process with a production cross section of σ_i is given by

$$N_i = \sigma_i \int \mathcal{L}\, dt, \tag{5.1}$$

which depends the time integrated luminosity. The instantaneous luminosity can be expressed in terms of beam parameters as

$$\mathcal{L} = \frac{N_b^2 n_b f_{rev}}{4\pi A_x A_y} F, \tag{5.2}$$

where N_b is the number of particles per bunch, n_b the number of bunch pairs per revolution, f_{rev} the beam revolution frequency, A_x and A_y represent the beam spread in x and y at the time of collision and F is a geometrical reduction factor due to the fact that the beams do not collide head-on but at a small angle.

The LHC design luminosity is $\mathcal{L} = 10^{34}\,\mathrm{cm}^{-2}\mathrm{s}^{-1}$, for a 25 ns bunch spacing of $n_b = 2808$ bunches and $f_{rev} = 11.2$ kHz. Each bunch containing 1.15×10^{11} protons with $A_x = A_y = 16.7\,\mu$m [102].

High luminosity comes at a price, namely additional simultaneous proton-proton interactions, called pile-up, resulting in the overlap of electronic signals from multiple interactions. With a cross section of σ_{inel}, the number of inelastic proton-proton interactions per bunch crossing is Poisson distributed, with a mean value of $\langle\mu\rangle$. $\mu > 1$ thus represents the existence of pile-up events in the collision. When a rare interesting event triggers the detector readout, the more common and uninteresting pile-up collisions will simultaneously be recorded, obscuring the interesting physics and degrading detector performance.

Increasing N_b or n_b results in higher luminosities but also raises the level of pile-up. Higher N_b produces more interactions within a given bunch crossing, called *in-time pile-up*. Large n_b reduces the bunch spacing which can be shorter than the detector latency, causing interactions from different bunch crossings to overlap and affect the measurement; this is known as *out-of-time pile-up*. Reducing $A_{x,y}$ increases both types of pile-up. Examples of reconstructed vertices, for different levels of pile-up are given in Figure 5.2. The average number of pile-up in the 8 TeV dataset was found to be $\langle\mu\rangle \sim 21$ [107].

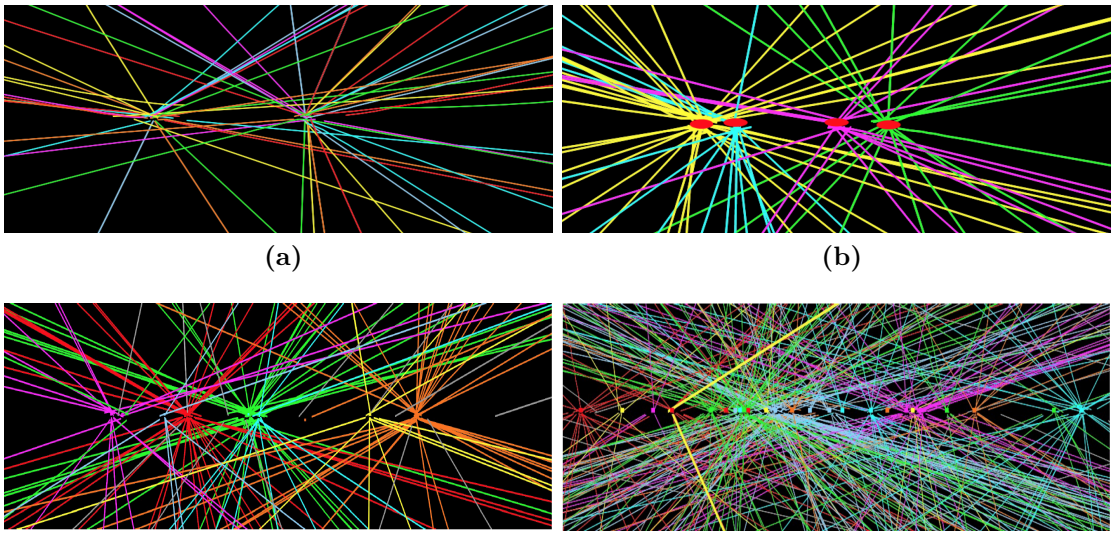

Figure 5.2 Vertex displays of collision events recorded in 2010-2012 by ATLAS with different pile-up conditions, of (a) $\langle\mu\rangle = 2$, (b) $\langle\mu\rangle = 4$, (c) $\langle\mu\rangle = 7$ and (d) $\langle\mu\rangle = 25$ [108].

The luminosity is constantly measured by ATLAS, see Section 5.7. A precise luminosity measurement is vital in calculating the cross section of an observed process. The luminosity $\mathcal{L}_b$ per bunch crossing [109] is monitored by measuring

the number of interactions per bunch crossing $\langle\mu\rangle$ as

$$\mathcal{L}_b = \frac{\langle\mu\rangle n_b f_{rev}}{\sigma_{inel}}. \tag{5.3}$$

Detector reconstruction inefficiencies mean that the observed values of $\langle\mu\rangle$ and σ_{inel} differ from the actual values. Chapter 7 describes a method to correct for such inefficiencies and determine the actual cross section of a measured process.

5.2 The ATLAS Detector

The description of the ATLAS detector refers to the Run 1 (2010 - 2012) configuration, with which the data for this thesis was collected. Upgrades to the detector post-2012 that have already been made, or planned for the future, are described in Section 6.2.

ATLAS is one of the two multi-purpose detectors at the LHC. It is designed to make both discoveries and perform precision studies of known processes. A primary goal of the experiment is to identify and characterise the Higgs boson. The detector is 44 m long, 25 m wide, about 7000 tonnes in weight and consists of multiple independent sub-detector systems in a cylindrically nested arrangement. Near full coverage over the solid angle around the interaction point at the centre of the detector is achieved by splitting the sub-detectors into *barrel* and *end-cap* components. An overview of the detector and its main components is given in Figure 5.3. ATLAS uses a right-handed coordinate system, as in Figure 5.4, with its origin at the nominal interaction point (IP) in the centre of the detector and the z-axis along the beam pipe. The x-axis points from the IP to the centre of the LHC ring, and the y-axis points upwards. Cylindrical coordinates (r, ϕ) are used in the transverse plane, ϕ being the azimuthal angle around the z-axis. The pseudorapidity is defined in terms of the longitudinal angle θ as $\eta = -\ln\tan(\theta/2)$. Thus η is a measure of the longitudinal angle against the beam line, where a large value of η, close to the beam line, is also called *forward*. The angular separation of two particles emerging form the IP is measured in units of $\Delta R \equiv \sqrt{(\Delta\eta)^2 + (\Delta\phi)^2}$.

ATLAS consists of an inner tracking detector surrounded by a thin superconducting solenoid, electromagnetic and hadronic calorimeters, and a muon spectrometer incorporating three large superconducting toroid magnets. The

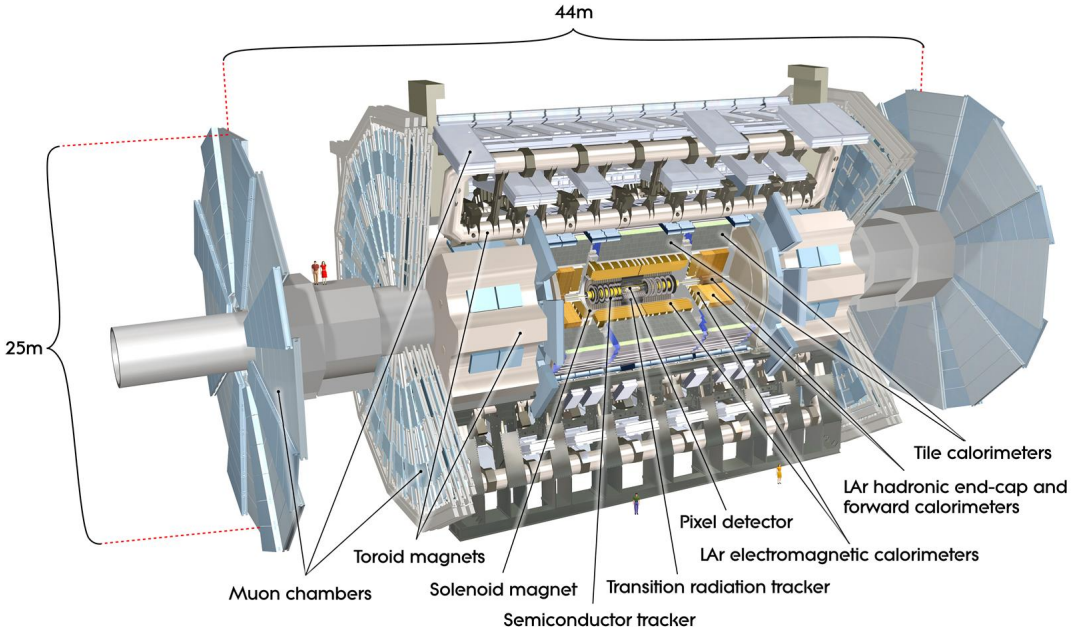

Figure 5.3 Cutaway drawing of the ATLAS detector [110].

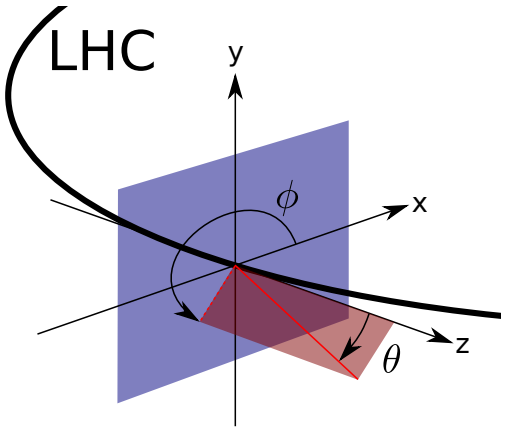

Figure 5.4 Coordinate system of ATLAS [111] The z-axis markes anti-clockwise direction of the beam line, with x pointing horizontally towards to radial centre of the LHC and y vertically upwards. The angle ϕ is in the plane transverse to z and measured with respect to x. The longitudinal angle θ is measured against z and is expressed as η, the pseudorapidity.

solenoid and toroid magnets generate fields in order to determine the momentum and charge of charged particles from their track curvature caused by the Lorentz force.

The innermost part of ATLAS is the beam pipe, separating the LHC beam from the detector. Running through the centre of the detector for 38 m, its central

part around the interaction point is integrated with the pixel detector. Here it has a diameter of 58 mm, a wall thickness of 0.8 mm and is made of beryllium. Beryllium allows for a beam pipe with low density, good mechanical stiffness and thermal stability.

5.3 Inner Detector

Closest to the interaction point, the silicon-pixel detector forms the three innermost layers of the inner detector. The silicon-microstrip tracker (SCT) surrounding it typically provides four additional two-dimensional measurement points per track. The silicon detectors are complemented by the transition-radiation tracker (TRT), which enables radially-extended track reconstruction up to $|\eta| = 2.0$ and provides electron identification information based on the fraction of hits above a higher-energy deposit threshold indicating the presence of transition radiation. The arrangement and radial distance of the Inner Detector barrel components are shown in Figure 5.5. The Inner detector (ID) is used for measuring particle tracks, which are reconstructed from individual hits from many layers of the different systems. The solenoid magnet encompasses the Inner detector and produces a near uniform 2 T magnetic field within it in the region of $|\eta| < 1.6$. The purpose of the solenoid magnet is to deflect charged particles and to measure the signed momentum.

Pixel Detector

The pixel detector [113] surrounds the beam pipe and is the sub-system closest to the interaction point. It therefore also has the highest granularity and is subject to the highest particle fluxes. It consists of three concentric cylindrical layers of silicon pixel modules in the central barrel region, with three additional circular disk layers in the end cap regions. The pixel detector has a total of about 80 million readout channels, where each pixel is of $50 \times 400\,\mu\text{m}^2$ in area and 250 μm thick. The intrinsic resolution in $r\phi$ of the barrel region is 10 μm and 115 μm in z and r.

The silicon pixels are reverse-biased p-n junctions in which a passing charged particle creates an electron-hole pair in the depletion region. The liberated charge carriers are attracted to the respective electrodes inducing an electrical signal.

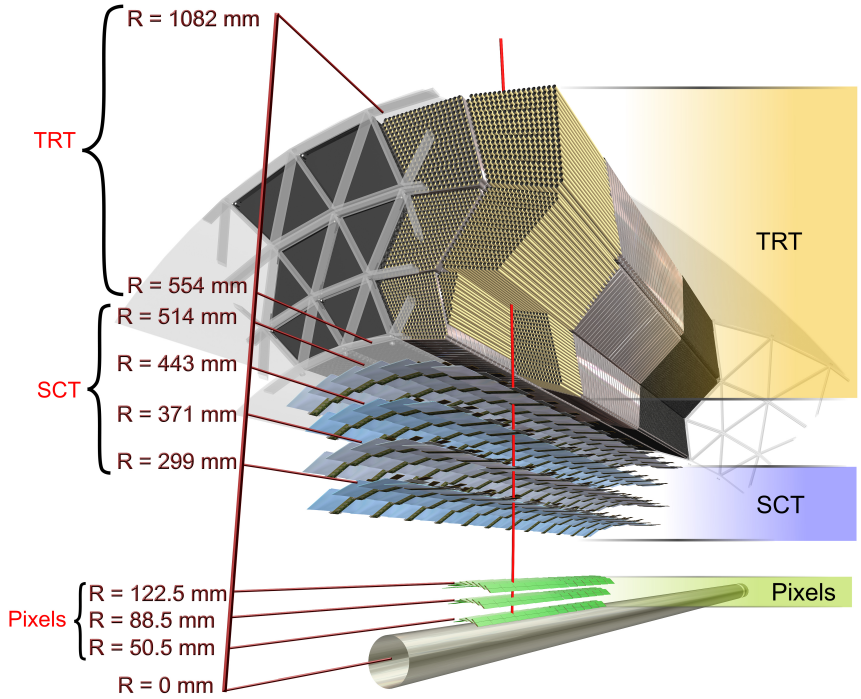

Figure 5.5 ATLAS Inner Detector Run 1 barrel configuration, showing the beam pipe, the Pixel Detector, the Silicon Strip Detectpr (SCT) and the Transition Radiation Tracker (TRT) [112].

SCT

The SCT [114] sits around the pixel detector and is also made of silicon semiconductor sensors. Instead of pixels, the SCT consists of 770 6 cm long strips, with a pitch of 80 μm. There are four double-layers of silicon strip modules in the barrel region which are aligned parallel to the beam axis. An angle of 40 mrad between the pair of each double-layer provides spatial information along the strip length in the z direction. The endcap region has nine double layers which are also twisted to provide radial information. The SCT has about 6.3 million readout channels with an intrinsic resolution of 17 μm in $r\phi$ and 580 μm in z and r.

TRT

The SCT is followed by the TRT [115] in radial direction. The TRT is made of 370 K straw tubes with a diameter of 4 mm which are aligned parallel to the beam line in the barrel region and aligned radially in the end caps. The straws are tubular drift chambers, made of thin aluminium, containing an anode wire. The straws are filled with Xeon-based gas mixture, which is ionised by traversing charged particles. The gas mixture additionally facilitates the drift of the liberated electrons. The conductive coating of the tubes and central anode wires collect the ionisation current and produce a signal. The drift time is used to determine the proximity of the interaction point to the anode within a tube. A typical track passes through about 30 straws and the combined information of these yield an intrinsic resolution of 130 μm in $r\phi$ [116]. The TRT provides no tracking information in the direction parallel to the straws.

The layers of straws are separated by polypropylene radiator foils which change the refractive index of the volume, causing the traversing charged particles to emit X-ray transition radiation (TR). The TR is then absorbed by the gas in the straws, inducing a distinct signal in addition to the charged track ionisation. The TR signal is proportional to the γ-factor of the charged particle, which provides mass information of a particle, given its energy. The TR measurement is primarily used for electron-pion discrimination, where the emission of TR is more likely for an electron than for a heavier pion of same momentum.

5.4 Calorimeter

Particle energies are measured in the calorimeter by inducing energy loss and measuring the absorbed energy. Sampling calorimeters are used, which are made of alternating layers of dense passive material and an active medium. The passive material induces particle showers in which one particle breaks down to multiple particles of lower momentum, which in turn induce a signal in the active medium via ionisation or scintillation, proportional to the total released energy. The calorimeter is segmented into cells, independent regions of the active material in which energy deposits are measured. Particles passing through the calorimeter lose their energy in multiple interactions, with deposits over many calorimeter cells. The interaction process of electrons and photons is characterised by the

radiation length X_0. High energy electrons and photons predominantly lose energy via bremsstrahlung and e^+e^--pair production respectively when passing through matter. In this case, X_0 is either the average distance over which the electron loses all but $1/e$ of its energy[1], or equivalently 7/9 of the mean free path of a photon. The mean free path of a hadron and thus the characteristic length of hadronic showers is given by the nuclear interaction length λ. Hadrons mainly lose energy by inelastic hadronic collisions in matter, which produce hadronic showers. The calorimeter must be sufficiently large to fully capture interactions of multiple lengths of X_0 and λ to sample energies precisely and avoid punch-through into the muon spectrometer. Muons, which are minimum ionising, pass through the calorimeters.

ATLAS makes use of two separate calorimeter systems, an inner electromagnetic and an outer hadronic calorimeter.

Electromagnetic Calorimeter (ECal)

The ECal [117] is made of alternating layers of lead absorber and liquid argon (LAr) active material. An accordion-like geometry ensures uniform coverage in ϕ, as shown in Figure 5.6. Passing through the lead, photons convert to e^+e^--pairs and electrons emit bremsstrahlung. A cascade of photon and e^+e^- conversions produces an electromagnetic shower which ionises the LAr. The liberated electrons produce an electrical signal collected by electrodes and processed by readout electronics. LAr is radiation-hard and has a linear ionisation response over a wide energy range, essential for a well calibrated ionisation-current to energy deposit proportionality. The LAr based calorimetry is performed in a thermally controlled environment of 87 K to maintain the liquid argon state [118]. The ECal is segmented into cells of $\Delta\eta \times \Delta\phi = 0.003 \times 0.025$ with three layers in depth. A fine segmentation is crucial to distinguish single photons from $\pi^0 \to \gamma\gamma$ decays. The ECal covers the range of $|\eta| < 3.2$ with a gap at $1.37 < |\eta| < 1.52$ where the barrel components stop and the end-cap starts. The total thickness of the ECal is equivalent to 22 X_0.

[1] here e refers to Euler's number and not the elementary electric charge

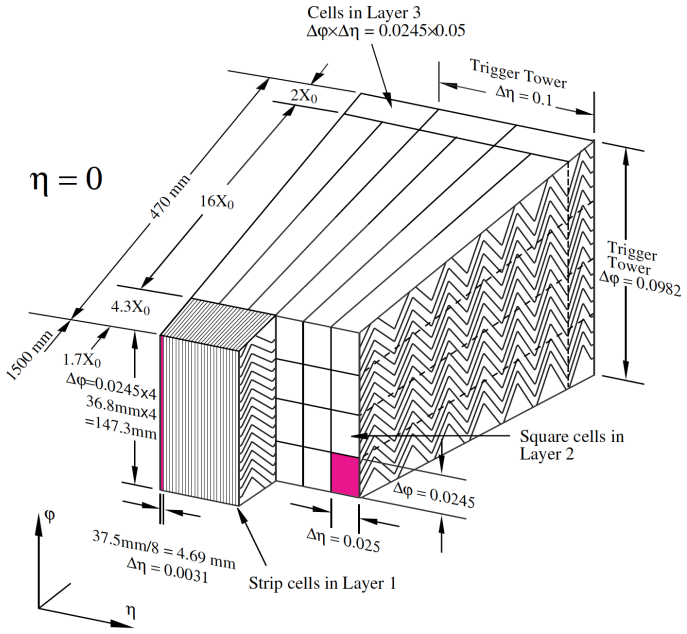

Figure 5.6 Sketch of the barrel module of the ATLAS electromagnetic calorimeter [95]. The segmentation in cells is shown, with three cells in depth. The accordion-like arrangement of the lead absorber can be seen.

Hadronic Calorimeter (HCal)

The HCal surrounds the ECal and consists of steel and scintillating tiles in the central region. The endcap calorimeters in the forward region use a combination of copper and tungsten as an absorber with a LAr active medium. The combination of all HCal systems cover a range of $|\eta| < 4.9$ with a typical segmentation of $\Delta\eta \times \Delta\phi = 0.1 \times 0.1$ across three layers in depth. In the tile calorimeter a steel absorber causes hadrons to shower to lower momentum hadrons, electrons and photons. These in turn excite atoms within the scintillator material which produce scintillation light. Scintillation light is then passed to photomultiplier tubes via wavelength-shifting fibres [119]. The total thickness of the ECal is equivalent to an interaction length of 10 λ.

5.5 Muon Spectrometer

The muon spectrometer (MS) [120] is the outermost detector system of ATLAS. The total MS system has approximately 1 million channels over an area of

12000 m^2. The MS extends over a large radius of about $4\,m < r < 11\,m$, making up most of the volume of the ATLAS detector. It allows for precise tracking of muons which are bent by a large air-core toroid magnet system with a field of up to 1 T. All other particle types that would generate a signal in the MS are absorbed by the preceding calorimeter. Covering the barrel and end-cap regions, the MS consists of three layers made of four different detector technologies detailed below, that either provide good spatial or timing resolution. Therefore the MS can be used for muon tracking as well as triggering. In either case, muon detection is performed with gaseous detectors sensitive to ionisation by muons.

Precise Tracking

Monitored drift tube (MDT) chambers and cathode strip chambers (CSCs) have a high spatial resolution of $\sim 40\,\mu$m, providing precise momentum measurements within $|\eta| < 2.7$, with precise position measurements from three layers of monitored drift tubes (MDTs), and cathode-strip chambers in the forward region. MDT chambers make up most of the MS detector and are made of three layers of 30 cm long aluminium drift tubes. CSCs are made up of multiwire proportional chambers with orthogonal planar cathodes. CSCs can resolve a higher occupancy and have a higher radiation tolerance than MDTs and are therefore placed in the forward region which experiences a higher particle flux.

Precise Timing

Dedicated muon trigger chambers cover the range $|\eta| < 2.4$. Resistive plate chambers (RPCs) are used in the barrel region and thin gap chambers (TGCs) are used in the endcap regions. These systems provide complementary tracking information with a comparatively lower spatial resolution, while their faster charge collection and readout speeds allow for triggering. RPCs are parallel plate gaseous detectors run in avalanche mode, ensuring good time resolution of 1.2 ns [121] and high rate performance. TGCs are thin multiwire proportional chambers operated in saturation mode [122] with a time resolution of about 2.3 ns [123].

5.6 Trigger

The trigger system [124] performs the run-time event selection, determining which events are recorded and which are discarded in light of the limited data bandwidth and storage capabilities. The selection intends to have a high acceptance rate for Higgs boson and other physics processes of interest while rejecting events without any characteristic kinematic signatures. A three-level hierarchy trigger system reduces the event rate, where each level has increased processing time and information available. The Level-1 trigger (L1) is implemented in dedicated hardware within the detector systems and uses a subset of detector information to reduce the event rate from the design LHC collision rate of 40 MHz[2] to a maximum of 75 kHz. The L1 selects events with high momentum tracks, large calorimeter deposits or large missing transverse energy. A processing time of 2.5 μs allows only for a coarse reconstruction of these features in the individual detector sub-systems, which feed all information to a central trigger processor. The trigger processor is programmed with a *trigger menu* defining what features are of interest. Identified regions of interest (RoI) in θ and ϕ containing selected features are passed on to the higher level triggers.

The two subsequent trigger levels, collectively referred to as the high-level trigger (HLT), are implemented in software on computer hardware external to the detector. The second level trigger (L2) inspects the individual RoIs selected by the L1 but with full detector granularity and thus higher precision. The RoIs are used to construct physics objects corresponding to particle candidates. It has 40 ms processing time and is designed to reduce the event rate to 3.5 kHz. The third level, also called *event-filter* reduces the event rate to about 400 Hz [125]. With a processing time of about 4 s, the event filter makes a selection decision based on the full event information over all physics objects. Events passing this selection are transmitted to the CERN data storage, and from there onwards to multiple computing facilities world-wide. All in all, the trigger reduces the initial data rate from about 64 TB/s to 1 GB/s [95].

[2]The design LHC collision rate of 40 MHz was not achieved in Run 1. A reduced bunch spacing of 50 ns lead to a collision rate of 20 MHz.

5.7 Luminosity Measurement

The beam luminosity is an essential measurement, needed to determine cross sections of observed processes. The luminosity ATLAS receives is determined from the combination of measurements from three independent systems, BCM (Beam Conditions Monitor), LUCID (Luminosity measurement using Cherenkov Integrating Detector) and ALFA (Absolute Luminosity For ATLAS) [126]. These systems all sit in the very forward region and measure inelastic proton-proton scattering at small angles. The number of particles that are detected by these systems is assumed to be proportional to the total number of interactions in a bunch crossing and from a well understood cross section of inelastic proton-proton scatter the beam luminosity can be calculated.

The BCM consists of four modules on each side of the interaction point, at a distance of 1.84 m corresponding to $|\eta| = 4.2$ [127]. The modules are equipped with radiation-hard diamond sensors and high-speed readout electronics. As well as performing luminosity measurements, the BCM monitors the stability of the LHC beam. LUCID is likewise positioned on either side of the interaction point at a distance of 17 m, corresponding to $|\eta| = 5.8$. Both stations are made of 16 aluminium tubes filled with C_4F_{10} gas, pointing towards the interaction point. Cherenkov radiation mainly produced by pions and electrons in the C_4F_{10} medium is measured by attached photo multiplier tubes, from which the luminosity is determined.

While BCM and LUCID measure the luminosity per bunch crossing, ALFA measures the total elastic cross section in special runs with low beam divergence. The ALFA detector is the furthest from the interaction point at 240 m. Composed of scintillating fibre trackers, it detects elastic scattering at very small angles of 3 μrad at which the scattering amplitude relates to the total cross section by the optical theorem [128]. Additional cross checks on the luminosity measurement are provided by the calorimeters and Medipix2 sensors [129], measuring the overall radiation levels at different points within ATLAS. BCM and LUCID are calibrated in special *van der Meer* scans [130], during which $A_{x,y}$ from Equation 5.2 can be determined.

5.8 Detector Performance

The detector performance as measured in Run 1 is shown in Table 5.1. The momentum resolution of the inner tracker $\Delta p_T/p_T$ is given by the quadratic sum of the intrinsic spatial resolution which is proportional to p_T and a constant term corresponding to scattering effects. The energy resolution of the calorimeters is dominated by the statistical fluctuations of the particle shower at low energies, while at high energies the systematic term due to non-uniform response is more important.

sub-system	resolution	$\lvert\eta\rvert$ coverage	
		measurements	L1 trigger
Inner tracker	$\Delta p_{\mathrm{T}}/p_{\mathrm{T}} = 0.03\% \times p_{\mathrm{T}} \oplus 1.5\%$	< 2.5	-
EM calorimeter	$\Delta E/E = 10\%/\sqrt{E} \oplus 1\%$	< 3.2	< 2.5
Hadronic calorimeter	$\Delta E/E = 50\%/\sqrt{E} \oplus 3\%$	< 4.9	< 4.9
Muon spectrometer	$\Delta p_{\mathrm{T}}/p_{\mathrm{T}} = 4\%$ for $p_{\mathrm{T}} = 100$ GeV	< 2.7	< 2.4

Table 5.1 Measured from Run 1 data [131–134]. Performance of measurement within $|\eta|$ coverage are shown, where momenta and energies are in GeV. The Muon performance is considered independently of the inner tracker. A pile-up dependent noise term proportional to $1/E$ is omitted. The L1 trigger $|\eta|$ coverage for the sub-systems is also given.

5.9 Definition of Physics Objects

The detector measures individual particle hits in the tracking layers or energy deposits in cells of the calorimeter. These measurements are used to reconstruct particle objects. The algorithms developed for this task are outlined below.

5.9.1 Tracks

A track is a sequence of hits in the inner detector, indicative of a charged particle trajectory. Track trajectories are helical, due to the pervading solenoidal magnetic field. However, multiple scattering and energy loss can induce deviations from this path. Track reconstruction is possible within the inner detector coverage of $|\eta| < 2.5$. Reconstruction is performed on the coordinates of hits in the pixel, SCT and TRT subsystems. The *inside-out* algorithm [135, 136] uses a Kalman filter to seed

tracks from hits in the three pixel layers and the first SCT layer. The seeds are then extended into the SCT and the TRT and fitted, whilst resolving ambiguities and applying quality criteria, for example requiring a track to originate from the primary vertex. Finally, the *outside-in* algorithm [135] considers unused track segments in the TRT, and extrapolates them into the SCT and pixel detector. This improves the tracking of secondary particles with a displaced vertex.

5.9.2 Vertices

A vertex is the location of an interaction which is identified by tracing tracks back to a common origin. Vertex reconstruction requires at least two matching tracks to originate from a vertex. Vertices along the beamline associated with the interactions of incoming protons are called *primary vertices*. Vertices displaced from the beamline, caused by particle decays, are called secondary vertices.

Vertex reconstruction associates tracks with vertices (vertex finding) and reconstructs the vertex position itself (vertex fitting). ATLAS employs an iterative *finding through fitting* algorithm to simultaneously perform both steps [137]. Firstly, tracks originating from the interaction region are identified and used to reconstruct the primary vertex. Tracks considered outliers are then used to construct secondary vertices and a second fit over all vertices is performed. The algorithm iterates, increasing the number of vertices, until the result stabilises. The decay process of a secondary vertex is determined from the kinematic properties of the decay products [138].

5.9.3 Electrons

Electrons will pass through the ID before being absorbed by the electromagnetic calorimeter (ECal). Electron candidates are built from clusters of energy depositions in the ECal [132] with an associated well-reconstructed track. They are required to have $E_{\mathrm{T}} > 10$ GeV, where the transverse energy E_{T} is defined as $E\sin(\theta)$. Electrons reconstructed with $|\eta| < 2.47$ are used, excluding $1.37 < |\eta| < 1.52$, which corresponds to the transition region between the barrel and the endcap calorimeters.

Electron objects can be misidentified hadrons, whilst many others are from photon conversions or electrons from heavy flavour decay. Energy depositions

in the hadronic calorimeter are used to veto hadronic decays. Additional identification criteria are applied to reject background, using the calorimeter shower shape, the quality of the match between the track and the cluster, and the amount of transition radiation emitted in the ID [139–141].

5.9.4 Muons

Muons are the only particles to pass through the dense calorimeters and to be measured in the muon spectrometer, resulting in a high reconstruction purity. Muons are identified as objects that have an inner detector track as well as a muon spectrometer track, the latter being a unique feature of a muon. Muon tracks are required to be reconstructed in all three muon spectrometer layers. Requiring a muon to have a reconstructed track in the inner detector and muon spectrometer can be used to associate a muon to a primary vertex and reject muons from secondary decays.

5.9.5 Jets

Energy deposits in the calorimeter cells need to be above a signal-to-noise ratio of 2 to be considered for jet clustering, while each cluster is built around a *seed* cell with a signal-to-noise ratio of at least 4. Energy measurements are corrected for non-linearity, non-compensation and energy losses of the calorimeter [142]. Jets are reconstructed objects describing the sum of all particles originating from particle showers. Hadronic jets originate from parton showers while photons or electrons are also identified as showers in the electromagnetic calorimeter. All jets including the photon and electron objects are reconstructed using the anti-k_{T} algorithm [143] using calorimeter and tracking information [144]. The calorimeter and tracker jet finding processes are performed independently. A *track-jet* is a pile-up robust jet definition in which the calorimeter and tracker information can be matched to a single jet object. This is a sequential clustering algorithm which iterates over all tracks with associated calorimeter energy deposits in an event and groups these into combined objects originating from multiple initial particles. A jet thus represents an initial particle that showered into multiple particles in the tracker and calorimeter. The transverse momenta p_{T} of all calorimeter deposits in question are sequentially combined if they fall within a chosen separation $\mathrm{R_{max}}$. The quantity $\mathrm{d_{ij}}$ is a measure of distance between two calorimeter cluster i and j

$$\mathrm{d}_{ij} = \min\left(p_{\mathrm{T}i}^2, p_{\mathrm{T}j}^2\right) \cdot \frac{\mathrm{R}_{ij}^2}{\mathrm{R}_{\mathrm{max}}^2} \tag{5.4}$$

which is compared to the distance between track i and the beam-line

$$\mathrm{d}_{i\mathrm{B}} = p_{\mathrm{T}i}^2 \tag{5.5}$$

measured in units of energy squared. If $\mathrm{d}_{ij} < d_{i\mathrm{B}}$, the two objects i and j are merged to a single object, otherwise they are considered to be two separate jets and removed from the collection of particles under consideration. This procedure is repeated until all objects are assigned to jet candidates.

The anti-k_{T} algorithm produces conical jets and unlike other sequential algorithms, such as k_{T} [145] and *Cambridge-Aachen* [146] it yields stable results. Stability of a jet definition is considered in terms of its insensitivity of collinear splitting (collinear safety) and soft gluon emission (infrared safety).

Jet energies are corrected for the effects of calorimeter non-compensation, signal losses due to noise threshold effects, energy lost in non-instrumented regions, contributions from in-time and out-of-time pile-up, and the position of the primary interaction vertex [147, 148]. The calibration to the hadronic energy scale follows Refs. [147, 149].

Additionally, association of jets to the primary vertex is used to suppress pile-up jets. The jet vertex fraction (JVF) relates the jets in an event to the primary vertex by comparing the momentum-sum of the tracks originating from the primary vertex to the momentum-sum of all jet tracks in the event.

$$\mathrm{JVF} = \frac{\sum_{\mathrm{PV\,tracks}} |\mathrm{p}_{\mathrm{T}}^{\mathrm{track}}|}{\sum_{\mathrm{all\,tracks}} |\mathrm{p}_{\mathrm{T}}^{\mathrm{track}}|} \tag{5.6}$$

Jets that primarily constitute pile-up activity assume JVF values approaching 0, while actual hard scatter jets have a JVF close to 1.

Flavour Tagging

Determining the flavour of the quark which formed a given hadronic jet plays an important role in identifying decay signatures. Particularly, the identification of heavy flavour jets is crucial for measuring processes like $\mathrm{H} \to b\bar{b}$ or vetoing b-

jets from top-quark background events for the H → WW channel. Identification algorithms make use of the impact parameter and the position of the decay vertex to separate b-jets, c-jets, light-quark jets[3] and gluon jets. Misidentification of jet flavour is common and a compromise between the efficiency of identifying a jet flavour and the purity of the flavour sample must be found. The strongest distinction can be achieved between b-jets and the other flavoured jets, due to the comparatively long life time of b-hadron of ~ 1.5 ps, resulting in a decay vertex displacement of a few mm.

B-jet identification is only possible in the $|\eta| < 2.5$ range covered by the inner detector and jets must have a minimum of $\mathrm{p_T} > 20$ GeV to be tagged. ATLAS uses different algorithms to identify b-jets [150]. The most common is the ATLAS MV1 tagger [151] which forms a discriminate for b-jets from the kinematic properties in a neural network, using MC simulation that is calibrated to data.

5.9.6 Overlap Removal

Misidentification of objects can result in one particle being reconstructed as more than one object. A set of rules is applied to remove this overlap based on the likelihood of a given misidentification for objects that are close to one another in ΔR.

- An electron candidate object is removed if its track extends to the muon spectrometer, as it is probably a misidentified muon. Similarly, any electron candidate separated by less than $\Delta R = 0.1$ from a muon candidate is removed, assuming that bremsstrahlung emitted by the muon converted to the electron candidate.

- Since high-p_{T} electrons always also get reconstructed as an electromagnetic jet, a reconstructed jet that overlaps with an electron $\Delta R < 0.3$ is always removed.

- Likewise, an overlapping jet and a muon is resolved by removing the muon, because it was most likely produced by heavy-flavour particle decays in jets.

- When two electron candidates are within $\Delta R < 0.1$ of each other, then one is probably the result of a converted photon, emitted by the other via

[3]light being up, down or strange quarks

bremsstrahlung as it passed through one of the innermost detector parts. In this case the electron candidate with the higher p_{T} is kept.

5.9.7 Missing Transverse Energy

Decays with final state neutrinos are identified by *missing* transverse energy $E_{\mathrm{T}}^{\mathrm{miss}}$ and momentum that go undetected. The near-complete coverage of the detector means the energy of the neutrinos can be inferred from measurements of other visible particles in an event. The initial state of the collision has zero transverse momentum which must be conserved in the p_{T}-sum of all final state particles. For events with final state neutrinos this sum does not equal zero, where the difference is equivalent to the $E_{\mathrm{T}}^{\mathrm{miss}}$ of the neutrinos. The longitudinal component of the neutrino momentum cannot be reconstructed. Measurements of $E_{\mathrm{T}}^{\mathrm{miss}}$ thus rely on precise identification of all other objects in the event, resulting in comparably poor experimental resolution. Measurement of $E_{\mathrm{T}}^{\mathrm{miss}}$ is the magnitude of the missing transverse momentum vector $\mathbf{E}_{\mathrm{T}}^{\mathrm{miss}}$ calculated from the p_{T} sum of all identified objects as

$$\mathbf{E}_{\mathrm{T}}^{\mathrm{miss}} = -\Big(\sum_{\text{identified}} \mathrm{p_T} + \sum_{\text{soft}} \mathrm{p_T} \Big) \tag{5.7}$$

where *soft* takes low p_{T} particles into account that are not identified as an object. The soft contributions are either quantified by calorimeter deposits or track measurements assigned to the primary vertex, leading to two different definitions of $E_{\mathrm{T}}^{\mathrm{miss}}$. A mixture of both approaches is used in the analyses presented, while the track-based definition is more robust to pile-up effects as an association to the primary vertex is made.

Corrections to the $E_{\mathrm{T}}^{\mathrm{miss}}$ must be made to account for other sources of missing energy. These include limited detector acceptance, dead or noisy read-out channels and noise sources in the form of pile-up jets or cosmic ray muons. The $E_{\mathrm{T}}^{\mathrm{miss}}$ calibration is performed by comparing measured and simulated $\mathrm{Z} \to \mathrm{ee}/\mu\mu$ samples, which lack genuine $E_{\mathrm{T}}^{\mathrm{miss}}$ [152].

Chapter 6

ATLAS and LHC Upgrades

In the near future the LHC will undergo a series of upgrades aimed at increasing the instantaneous luminosity. The aim is to acquire the largest possible dataset to preform precision measurements and make new discoveries that are not possible with the current LHC configuration. After delivering 300 fb^{-1} by 2022, the LHC will be upgraded to the High Luminosity LHC (HL-LHC) [153]. The HL-LHC will deliver up to 3000 fb^{-1} by about 2035, thus vastly extending the physics reach of the LHC programme. In particular this encompasses the measurement of low cross section processes, such as rare Higgs boson couplings including Higgs self-coupling and coupling to Dark Matter. Further, Beyond the Standard Model theories will also be probed, including Supersymmetry, new gauge bosons and additional heavy Higgs bosons. A spectrum of sensitivity studies have been conducted by the ATLAS collaboration assessing the feasibility and potential of future measurement that will be performed in future LHC and HL-LHC runs [154–162]. A study on the prospects of measuring the Higgs boson decay to bottom quarks in the associated VH channel is presented in Chaper 9. The error on the signal strength for SM H$\rightarrow b\bar{b}$ is estimated to be 12% at the end of the HL-LHC runnning, compared to 40% obtained in Run 1 [49]. The results of this analysis fed into a combined prospects study on the future measurements of Higgs boson couplings in all decay modes. Figure 6.1 shows the projected precision with which Higgs boson coupling will be measured in future LHC runs. The gain in precision of Figure 6.1a should be compared with current measurements in Figure 3.1. The coupling to vector bosons and fermions, κ_{V} and κ_{F} are expected to be measured with a precision of at least 3.3% and 5.1% respectively, by the end of the HL-LHC programme, shown in Figure 6.1b.

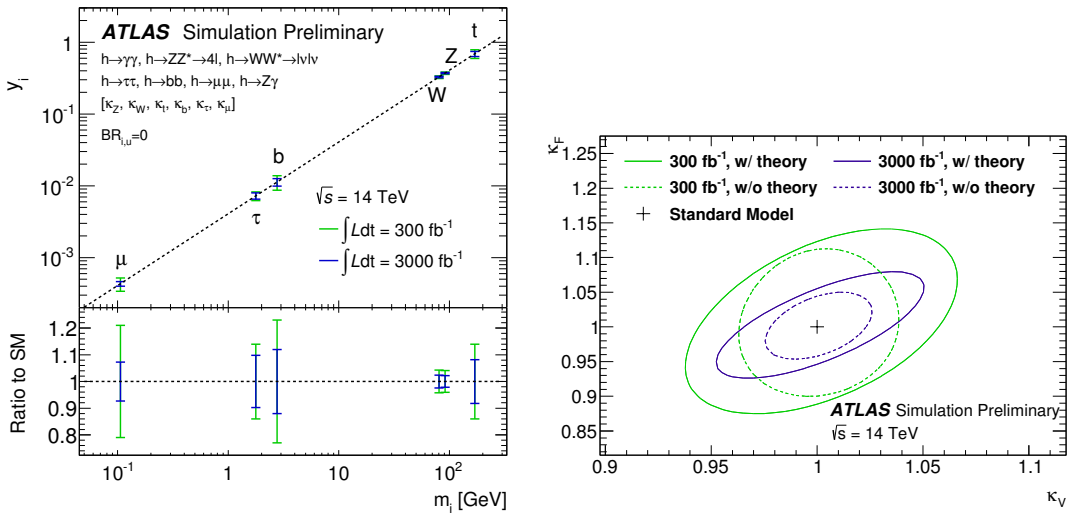

(a) **(b)**

Figure 6.1 Projections of the measurements of 125 GeV SM Higgs boson couplings to other SM particles with 300 and 3000 fb^{-1} of data [156]. (a) Fit results over all decay modes of the coupling scale factors $y_i = \sqrt{\kappa_V}\, m_{V,i}/v$ and $y_i = \kappa_F\, m_{F,i}/v$ for vector bosons and fermions respectively. The assumption is made that κ_V is constant for all vector bosons and κ_F is constant for all fermions. The b-quark results are derived in Chapter 9. (b) Corresponding 68% confidence level likelihood contours for κ_V and κ_F computed from all Higgs decay channels. Results are shown with and without considering current estimates of theoretical uncertainties.

The foreseen increase in luminosity poses a great challenge for ATLAS. An increase of pile-up events as well as radiation damage to the sensors dictate an upgrade of the detector, detailed below.

6.1 Upgraded LHC

The timeline of the LHC and its upgrade to the HL-LHC [153] is shown in Figure 6.2. Three long shutdowns (LS) are scheduled for maintenance and upgrade work to the accelerator and the detectors. This will allow for a continuous increase in instantaneous luminosity and the collection of large datasets. The periods of data taking between the shutdowns are called *Runs*. During Run 1, from 2010 to 2012, 4.5 fb^{-1} of data was collected of 7 TeV collisions and 20.3 fb^{-1} of 8 TeV collisions. Run 2 started in 2015, with the LHC producing 13 TeV collisions and reduced bunch spacing of 25 ns, compared to 50 ns in Run 1. By the end of Run 2 in 2018, it is hoped to run the LHC at its design energy

of 14 TeV [163]. During Run 2 and Run 3, which will end in 2022, the LHC will deliver a total of 300 fb^{-1}. During the Phase 1 upgrade between Run 2 and Run 3 the intensity of the injection pre-accelerating stages to the LHC will be increased by installing new RF cavities [164].

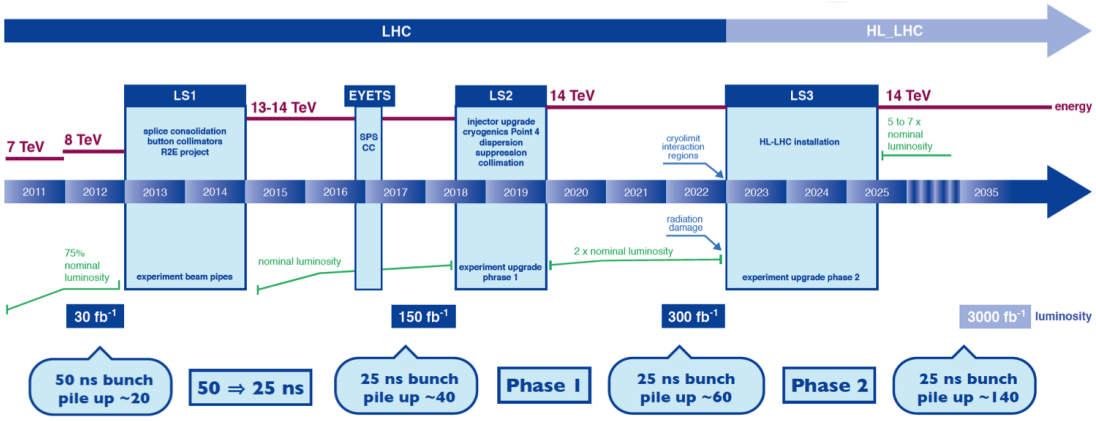

Figure 6.2 Timeline of the LHC with planned shutdowns, projected instantaneous and integrated luminosity levels, and expected pile-up conditions [165].

The long Phase 3 shutdown of 30 months beginning in 2023 is needed to upgrade and replace parts of the LHC, upgrading it to the HL-LHC. New 11 T superconducting Nb_3Sn dipole magnets, collimators and a new cryogenic system will be installed. As well as increasing the number of bunches to raise luminosity levels, crab cavities will be installed. Crab cavities [166] allow to increase the luminosity without the penalty of higher event pile-up, by tilting the proton bunches off-axis which allows for a larger geometrical overlap with lower density of vertices, shown in Figure 6.3.

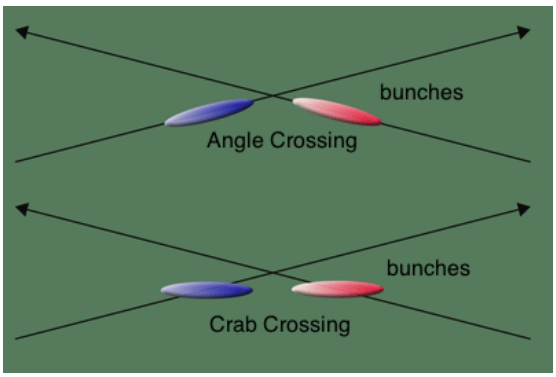

Figure 6.3 At the LHC the proton beams do not collide head-on but at a small angle (top). At the HL-LHC crab crossing will be used to enhance the luminosity.

6.2 Upgraded ATLAS Detector

The harsher radiation environment and higher detector occupancies at the HL-LHC call for significant changes to most ATLAS sub-systems. In order to maintain and improve upon the current detector performance, upgrades and additions will be made, in particular to components at low radii and large pseudorapidity, which experience the highest particle flux, namely the inner detector, forward calorimeter and forward muon wheels.

Radiation damage of the silicon sensors [167] is a major concern for future LHC runs. The current ATLAS pixel detector was designed to withstand $10^{15}\,\mathrm{n_{eq}/cm^2}$ 1 MeV neutron equivalent, which is estimated to be reached with 400 $\mathrm{fb^{-1}}$ equivalent of data, while the SCT was built to withstand $10^{14}\,\mathrm{n_{eq}/cm^2}$ [168]. Both these limits are expected to be exceeded by an orders of magnitude during the HL-LHC lifetime, see Figure 6.4. Measurements of the radiation damage to the SCT carried out by the author at the end of Run 1 are presented in Appendix C.

New radiation-hard inner detector tracking sensors with higher granularity and bandwidth will be installed, along with correspondingly suitable front-end readout electronics. An overhaul of trigger and data acquisition systems will address the increase in event sizes and rates. The barrel calorimeters and muon chambers are expected to cope with the high luminosity conditions. The ATLAS upgrade will take place in three phases, falling into the technical shutdowns of the LHC.

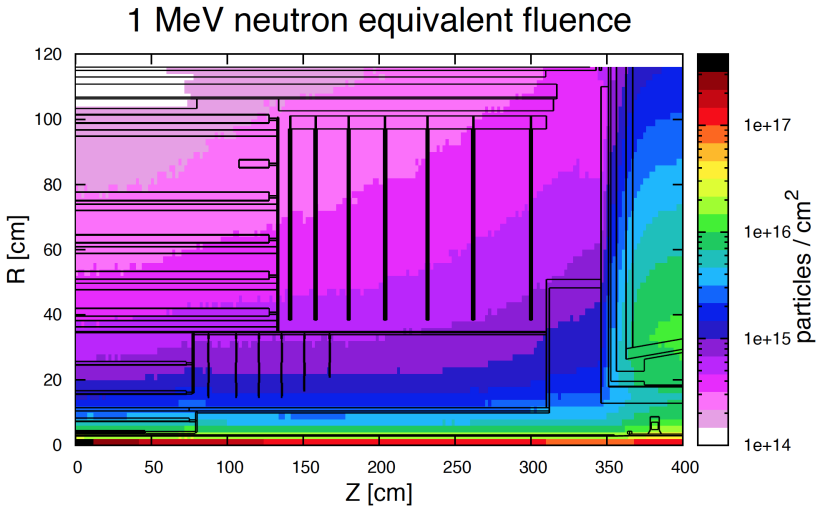

Figure 6.4 Projections of 1 MeV neutron equivalent fluence of the inner tracker regions ($r - z$ plane), normalised to 3000 fb^{-1} of 14 TeV minimum bias events, generated with PYTHIA8 [168].

6.2.1 Phase 0

Work carried out on the LHC during the 2013-2014 intervention has allowed ATLAS to run at a collision energy of $\sqrt{s} = 13$ TeV and with the design luminosity of $1 \times 10^{34}\,\mathrm{cm}^{-2}\mathrm{s}^{-1}$.

Insertable B-Layer

The main upgrade during Phase 0 was the installation of the Insertable B-Layer (IBL) [169]. The IBL is an additional 4th layer of pixel sensors inserted between the beam pipe and the innermost pixel layer of the inner detector. The additional tracking measurements the IBL provides at low radius has a positive impact on the vertex resolution, secondary vertex finding and b-jet tagging capabilities, hence improving physics analyses [170]. The IBL will ensure tracking performance at luminosities beyond $1 \times 10^{34}\,\mathrm{cm}^{-2}\mathrm{s}^{-1}$. It consists of 14 staves mounted directly on a new beampipe, populated with planar and 3D silicon sensors[1]. The sensors are attached to new front-end readout chip, the FE-I4, developed to function at high data transfer rates of 160 Mbs. The FE-I4 accommodates the smaller pixel sizes of the IBL sensors of $50 \times 250\,\mu\mathrm{m}$.

[1]While traditional planar sensors have electrodes on the surface, 3D sensors have electrodes embedded in the sensor bulk. In this way smaller drift distances and lower depletion voltages can be achieved, which in turn reduces the susceptibility to radiation-induced defects [171].

6.2.2 Phase I

The 2018 shutdown will see the upgrade of the LHC injectors and collimators. Improvements to the LINAC2 and the Proton Synchrotron Booster will increase their output energy and luminosity. Data-taking will resume in 2019 with twice the luminosity, $2 \times 10^{34}\,\mathrm{cm}^{-2}\mathrm{s}^{-1}$. ATLAS will install the new Muon Small Wheel and a new trigger scheme to handle the increase in luminosity.

New Muon Small Wheel

A replacement of the inner end cap of the Muon Spectrometer, the Muon Small Wheel (MSW) is proposed [172]. Consisting of Monitored Drift Tubes and Cathode Strip Chambers, the current MSW will not cope with luminosities greater $1 \times 10^{34}\,\mathrm{cm}^{-2}\mathrm{s}^{-1}$, due to the higher number of pile-up events per bunch-crossing and higher levels of cavern background radiation. These concerns of radiation damage and insufficient data bandwidth call for a replacement of the MSW. The new Muon Small Wheels must ensure efficient tracking at high particle rate up to $5 \times 10^{34}\,\mathrm{cm}^{-2}\mathrm{s}^{-1}$ for large $|\eta|$, with position resolution 100 μm, or better, and be suitable for Level-1 trigger information, requiring fast data processing. Combinations of different detector technologies are currently under investigation to meet these requirements.

Fast Track Trigger

The Fast Tracker (FTK) [173] is a hardware implemented pattern recognition approach to perform fast tracking despite high track multiplicity. With current methods, track reconstruction time increases non-linearly with pile-up, a combinatorial problem which scales with the number of hits in the inner detector. The FTK solves this combinatorial challenge inherent to tracking by exploiting massive parallelism of Associative Memories that can compare Inner Detector hits to millions of pre-calculated patterns simultaneously [174]. It will perform full track reconstruction at the Level-1 trigger output rate, at near-offline quality for processing by the HLT [175].

6.2.3 Phase II

A shutdown in 2022 and 2023 will allow the LHC to be fitted with crab cavities and new inner triplets, bringing the luminosity to $5 \times 10^{34}\,\mathrm{cm}^{-2}\mathrm{s}^{-1}$. Running in these conditions, the goal is to accumulate 3000 fb^{-1} of data by ~ 2035. For the Phase 2 upgrade ATLAS is preparing to completely overhaul the Inner Detector and perform trigger and calorimeter upgrades [176].

New Inner Tracker

Running at LHC design luminosity of $1 \times 10^{34}\,\mathrm{cm}^{-2}\mathrm{s}^{-1}$, an average pile-up of 28 is expected. For the 5-10 times higher luminosity at the HL-LHC pile-up level would be on the order of 140 or 200. This degree of detector occupancy is beyond the TRT design parameters, and by 2022 the Pixel and the SCT subsystems would seriously degrade their performance due to the radiation damage of their sensors and front-end electronics. Hence, ATLAS has decided to replace the entire Inner Detector with a new, all-silicon Inner Tracker (ITk) [176]. The ITk must satisfy the following criteria: higher granularity, low density, increased radiation resistivity of the readout components. At the moment, the ITk project is in an R&D phase. Different geometrical layouts are simulated and their performance is studied in search for the optimal tracker architecture. A major constraint on the design is the available space, defined by the volume taken by the inner detector in ATLAS. This implies a maximum radius of 1 m and limiting existing gaps for services. The current baseline design of the ITk consists of 4 pixel and 5 silicon-strip layers in the barrel part [177, 178]. The two endcap regions are each composed of 6 pixel and 5 Si-strip double-sided disks, built of rings of modules. The pixel modules are with identical pixels of $50 \times 250\,\mu$m in size, whereas the Si-strip modules come in two types, with short (24 mm) and long (96 mm) strips. As in the current SCT, the Si-strip modules are designed to be of 2 pairs of silicon microstrip sensors, glued back-to-back to provide 2D space-points. Intensive R&D studies are also in process to select the most suitable pixel sensor technology out of Si-planar, 3D and HV-CMOS [179], and to find the optimal layout of the silicon-strip modules.

The Edinburgh ATLAS group is testing the FE-I4 front-end readout chips for the New Inner Tracker upgrade. Initial chip characterisation results are presented in Appendix D.

Calorimeter and Trigger Upgrades

The harsh radiation conditions of the HL-LHC will degrade the performance of the calorimeter system. The active material of all calorimeter systems, as well as the on-detector readout electronics, will suffer radiation damage and will need replacing [180]. In particular the TileCal and the Forward Calorimeter will receive major upgrades including new radiation tolerant electronics [181]. The planned trigger upgrades for Phase-II, include an implementation of a Track Trigger and access of the full granularity of calorimeter at the Level-1 trigger, as well as extending the muon trigger η-coverage.

The performance of an upgraded ATLAS detector as described in this section is considered in the HL-LHC H$\rightarrow$ bb sensitivity in Chaper 9.

Chapter 7

Unfolding

The measured kinematic properties of experimental signatures are distorted by detector effects and selection efficiencies. Consequently, measured quantities differ from their true values. This difference can be corrected for, but requires a good understanding of the detector response.

In principle, it is possible to account for most understood reconstruction inefficiencies individually, such as those in object identification and momentum calibration as laid out in Section 5.9. This approach becomes impractical when there are many small effects to account for. Additionally, unexpected effects might be omitted and correlations unaccounted. Stochastic effects like the jet-energy resolution could however not be accounted for this manner.

Unfolding is an alternative procedure applied to reconstructed data to fully correct it to the particle-level [182]. The particle-level description is free from measurement effects, related to stable particles interacting with the detector. The underlying idea is that it is easier to calculate the detector response for a given particle-level signature than doing the reverse. Comparing particle-level distributions produced by MC generators before and after the detector simulation and reconstruction is applied (as described in Section 4.7) allows for a reverse mapping of the reconstructed to the particle-level measurement.

Unfolding is applied to the measured $\mathrm{H} \to \mathrm{WW}$ differential cross sections in Chapter 8. By eliminating detector specific effects the results can be compared to theoretical predictions and results from other experiments. Below, general considerations of unfolding are presented, followed by the description of specific

unfolding algorithms: The most commonly used bin-by-bin unfolding and Bayesian iterative unfolding which is applied to the H $\rightarrow$ WW measurement.

7.1 From Signal to Fiducial Volume

The signal and fiducial volumes are regions of phase space corresponding to the description of reconstructed and particle-level events respectively. Both regions are defined by selection cuts on the kinematic properties of the particles that are described within these phase spaces.

The signal volume is defined by the selection cuts imposed by the data selection to separate signal from background and by the acceptance limitations of the detector.

The fiducial volume is a sub-space of the full phase space. Ideally, one would use unfolding to extrapolate the signal volume to the inclusive volume. The typically large discrepancy between signal and inclusive volume however means that the unfolded results would suffer from large extrapolation uncertainties. Instead a fiducial volume is defined as a compromise between the limited signal and the inclusive volume. The selection cuts that define the fiducial volume are chosen to be sufficiently similar to the signal region to avoid large extrapolation uncertainties, while at the same time providing a sufficiently generic phase space to make comparisons to other measurements or calculations.

A crucial point is that unfolding corrects distributions, not individual events. In this sense events must be binned as part of a distribution or histogram.

In the following, each bin of the particle-level distribution is referred to by the index i, while each bin of the reconstructed distribution is referred to by the index j. The response matrix M_{ij} accounts for the detector response and is defined as the probability to observe an event in bin i when its particle-level value is located in bin j. The response matrix is built by relating the variables of a data sample S at reconstruction and particle-level in simulated events. The measured data events in bin j can be expressed by:

$$S_j = \sum_i \Big(M_{ij} \cdot S_i \Big) \tag{7.1}$$

The response matrix M_{ij} is constructed from simulated data; particle-level and reconstructed Monte Carlo samples of the signal process that is to be unfolded. Both samples follow the respective event selection of the fiducial and signal region, and are used to build a separate response matrix for each kinematic variable under study.

Missing and fake events

As both the signal and fiducial volume are restricted in phase space and do not completely overlap, an acceptance correction must be made. Events that lie within the fiducial volume are not necessarily reconstructed. These go *missing* due to reconstruction inefficiencies or resolution effects. Reconstruction inefficiencies lead to events not being reconstructed at all, while detector resolution causes a spread in reconstructed kinematics, sometimes moving an event outside of the signal volume. Likewise, *fake* events in the signal volume may result from detector resolution smearing and not correspond to an event in the fiducial volume. For example, a measurement of the $E_{\mathrm{T}}^{\mathrm{miss}}$ in an event could be lower than some selection threshold in the fiducial region, but the broad detector response leads to a reconstructed value that is above the threshold. As the response matrix only migrates events between bins, additional correction factors are needed to account for the normalisation of the fiducial and signal regions.

The selection efficiency, ε_i, is defined as the efficiency of particle-level events in the fiducial volume being reconstructed in the signal region and accounts for missing events in the signal region. The overall efficiency is determined by a combination of reconstruction, identification, isolation, trigger and selection efficiencies. The selection efficiency ε_i is thus defined as the fraction of events in bin i of the particle-level distribution that are reconstructed in any bin of the signal volume.

Events outside the fiducial volume may be selected in the signal volume as the result of bin-to-bin migrations. In general the signal volume would be a subspace of the fiducial volume, but large migrations due to detector resolution can for example occur if both volumes have a common kinematic cut. These fake events are corrected for by the fiducial correction factor, $f_j^{\text{reco-only}}$, defined as the ratio of reconstructed events in bin j that also exist in any bin of the fiducial region.

Subsequently, Equation 7.1 must be rewritten as

$$S_j = \frac{1}{f_j^{\text{reco-only}}} \sum_i \Big(M_{ij} \cdot \varepsilon_i \cdot S_i \Big) \tag{7.2}$$

7.2 Extracting Fiducial Cross Sections

The cross section of a process is calculated by measuring a signal, S_j, which in practice is obtained by subtracting estimated reconstructed background B_j from the measured data N_j. The substitution of $S_j = N_j - B_j$ is thus made in the following. The response matrix M_{ij}, as in Equation 7.2, represents the causal order of the reconstructed Monte Carlo data being constructed from the particle-level simulation. However, the inverse must be applied in order to obtain fiducial results from measured data. The signal distribution in the fiducial volume is thus given by

$$S_i = \frac{1}{\varepsilon_i} \cdot \sum_j \Big(\left(M^{-1}\right)_{ij} \cdot f_j^{\text{reco-only}} \cdot (N_j - B_j) \Big) \tag{7.3}$$

Figure 7.1 illustrates the mapping of a measured distribution to the fiducial volume.

Following Equation 4.6, the yield of the particle-level distribution can also be expressed in terms of $\mathcal{L}^{\text{int}}$, the integrated luminosity of the data sample, and σ the production cross section of the process. For a differential cross section, $d\sigma$ over bins of an observable X, S_i is given by

$$S_i = \frac{d\sigma}{dX_i} \Delta X_i \cdot \mathcal{L}^{\text{int}} \tag{7.4}$$

where ΔX_i is the width of the bins in the distribution of X.

Thus the problem that needs to be solved to measure differential cross sections is formulated in the following way:

$$\frac{d\sigma_i}{dX_i} = \frac{1}{\Delta X_i} \cdot \frac{1}{\varepsilon_i \cdot \mathcal{L}^{\text{int}}} \sum_j \Big(\left(M^{-1}\right)_{ij} \cdot f_j^{\text{reco-only}} \cdot (N_j - B_j) \Big) \tag{7.5}$$

Equation 7.5 suggests three sequential steps to determine the differential cross sections. First, the background contributions are subtracted from the measured data distribution and the fiducial correction factor $f_j^{\text{reco-only}}$ is applied to the

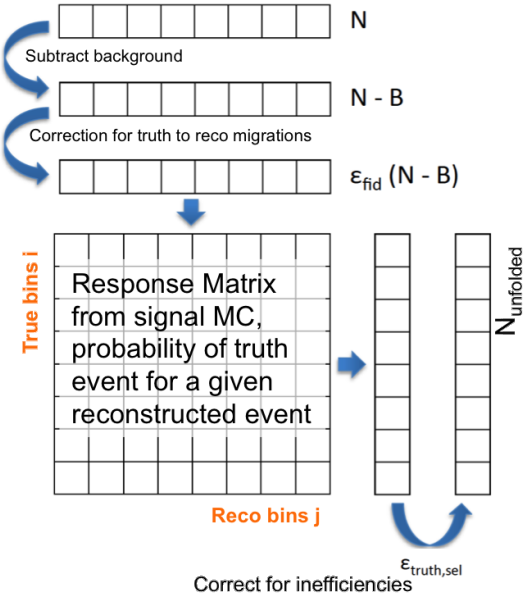

Figure 7.1 Unfolding of binned distribution, each box represents a bin of a distribution. The signal region is represented by rows of boxes and fiducial space by columns of boxes. The migration matrix is multiplied with the measured distribution to get the fiducial results. Correction factors are applied to account for differences in the definition of the signal and fiducial space.

resulting value. Then, the distribution is unfolded using the reverse of the response matrix, the migration matrix M_{ij}^{-1}. Finally, the unfolded distribution is divided by the acceptance efficiency, the luminosity, the branching ratio, and the bin width.

A naive approach to determine the migration matrix M_{ij}^{-1} would consider the inversion of the response matrix M_{ij} in order to recover the particle-level distribution. However it is not given that the response matrix is invertible with a unique solution. Such problems are described as *ill-posed* [183], since the outcome is susceptible to small changes of the input or yields un-physical results with negative probability densities.

Instead, a dedicated unfolding method is needed as an alternative to matrix inversion. Several methods are used in ATLAS to unfold a reconstructed distribution. In the analysis presented here an iterative Bayesian approach [184] is used. The results obtained with the iterative Bayesian approach are cross-checked by using a simple bin-by-bin unfolding method. The program RooUnfold [185] is used to implement all unfolding methods presented in this thesis.

7.3 Bin-by-Bin Unfolding

Bin-by-bin unfolding is possibly the simplest solution of an approximate unfolding. Here each bin of the distribution is treated independently. For each bin, the measured distribution is scaled by the ratio of the particle-level to reconstructed MC,

$$C_i^{\text{data}} = R_j^{\text{data}} \frac{T_i^{\text{MC}}}{R_j^{\text{MC}}} \delta_{ij} \tag{7.6}$$

with C_i^{data}, R_i^{data}, T_i^{MC}, R_i^{MC} the number of events in bin i of the unfolded data, measured data, particle-level MC and reconstructed MC distributions. Here the δ_{ij} function equals 1 if $i = j$ and 0 otherwise.

This method however yields model dependent results, i.e. strongly biased by the choice of Monte Carlo model used as input. Another major problem with bin-by-bin unfolding is that it does not account for migrations of signal events between bins. The impact of bin migrations depends on how large the difference between data and MC is. Both of these shortfallings are addressed by the Bayesian iterative unfolding method.

7.4 Bayesian Iterative Unfolding

An unfolding method based on Bayes' theorem was developed by G. D'Agostini and is fully described in Ref. [184]. The method is based on picturing the problem with an "effect" E and a "cause" C, for which Bayes' theorem states

$$\mathrm{P(C|E)} = \frac{\mathrm{P(E|C)\,P(C)}}{\mathrm{P(E)}} \tag{7.7}$$

where the posterior probability P(C|E) of C given E is proportional to a likelihood and the prior probability distribution function of P(E).

The cause and effect can be identified as the particle and detector level values of an observable. The effect is measured by the detector and the cause is the particle-level process. In this sense Bayes' theorem can be expressed in terms of the particle-level or *truth* Monte Carlo distribution T_i^{MC} and reconstructed Monte

Carlo distribution R_j^{MC}:

$$\mathrm{P}(T_i^{\mathrm{MC}}|R_j^{\mathrm{MC}}) = \frac{\mathrm{P}(R_j^{\mathrm{MC}}|T_i^{\mathrm{MC}})\,\mathrm{P}(T_i^{\mathrm{MC}})}{\mathrm{P}(R_j^{\mathrm{MC}})} \tag{7.8}$$

The above definition of the response matrix M_{ij} in Equation 7.1 corresponds to $\mathrm{P}(R_j^{\mathrm{MC}}|T_i^{\mathrm{MC}})$ and the sought-after migration matrix $(M^{-1})_{ij}$ corresponds to $\mathrm{P}(T_i^{\mathrm{MC}}|R_j^{\mathrm{MC}})$ which can be expressed in known terms without the need of matrix inversion. Thus the measured distribution R_j^{data} can be extrapolated to a particle-level description T_i^{data} as

$$n(T_i^{\mathrm{data}}) = \sum_j \mathrm{P}(T_i^{\mathrm{MC}}|R_j^{\mathrm{MC}})\,n(R_j^{\mathrm{data}}) = \sum_j \frac{\mathrm{P}(R_j^{\mathrm{MC}}|T_i^{\mathrm{MC}})\,\mathrm{P}(T_i^{\mathrm{MC}})}{\mathrm{P}(R_j^{\mathrm{MC}})}\,n(R_j^{\mathrm{data}}) \tag{7.9}$$

where n indicates the number of entries of a given bin of either distribution. The correction of detector effects can thus be performed but still relies on the choice of the prior $\mathrm{P}(T_i^{\mathrm{MC}})$. The choice of generator, for example, can bias the unfolded result. This model-dependence can, however, be reduced or even eliminated by correcting the prior using the measured data. This is achieved by an iterative process in which the unfolding is performed multiple times and the corrected distribution is used as a new prior in the following iteration. The data-corrected prior $\mathrm{P}(T_i^{\mathrm{MC/data}})$ is taken as

$$\mathrm{P}(T_i^{\mathrm{MC/data}}) = \frac{n(T_i^{\mathrm{data}})}{\sum n(T_i^{\mathrm{data}})}, \tag{7.10}$$

Final values for $n(T_i^{\mathrm{data}})$ and $\mathrm{P}(T_i^{\mathrm{MC/data}})$ are derived in an iterative way starting from the initial distribution $\mathrm{P}(\mathrm{T_i^{MC}})$, following Equation 7.9. The result from the previous and the current iteration are compared by constructing a χ^2 fit between the unfolded distribution and the particle-level expectation. The iterations are stopped once the value of χ^2 per degree of freedom is approximately 1.

Bayesian iterative unfolding is used in Chapter 8 to measure fiducial differential cross sections in the H→WW channel. The H→WW analysis shows a strong degree of bin correlations which requires this comparably complex unfolding technique. Reconstruction efficiencies, fiducial correction factors and migration

matrices specific to the analysis are presented in Section 8.9 in reference to this chapter. Tests of the unfolding procedure are also discussed included establishing the optimal number of iterations.

Chapter 8

Differential Cross Section Measurements in H→WW

Measuring the properties of the Higgs boson is one of the main goals of the LHC programme and the ATLAS experiment. Efforts in this direction include measuring the Higgs boson couplings and its properties: mass, spin, decay width, charge conjugation and parity. In addition to this, differential cross section measurements are performed to probe the kinematic properties of the Higgs boson and its production mechanisms. In a nearly model independent way, differential cross sections directly probe the production mechanism by studying the kinematics of the decay products. Making such measurements at the LHC allows to test the predictions of QCD at the highest possible energies. Differential cross section measurements of the Higgs boson have recently been made by both ATLAS and CMS collaborations in the $H \to ZZ \to 4\ell$ [186, 187] and $H \to \gamma\gamma$ [188, 189] final states. The results by the ATLAS collaboration have been combined in Ref. [190]. The $H \to WW$ final state has the largest Higgs boson yield of all the established Higgs boson decay modes and can provide complementary measurements.

This chapter presents measurements of fiducial and differential cross sections for Higgs boson production in the $H \to WW^* \to e\nu\mu\nu$ final state, which are published in Ref [1]. These measurements use 20.3 fb^{-1} of proton-proton collision data at a centre-of-mass energy of $\sqrt{s} = 8$ TeV recorded by ATLAS. A complementary study by CMS was also presented [191]. The measurements focus on the gluon-fusion production mode (ggF), which is the dominant signal contribution to the

$H \to WW^* \to e\nu\mu\nu$ event sample. The results are compared to QCD predictions of this production mechanism.

The H→WW channel is introduced in Section 8.1, including a summary of the initial observation. Section 8.2 motivates the choice of observables for which differential cross section measurements are made in H→WW. The analysis in presented in Section 8.3.

8.1 H→WW analysis

In the $H \to WW^* \to \ell\nu\ell\nu$ channel Higgs bosons are either produced by gluon-gluon fusion or vector boson fusion, where gluon-gluon fusion is the dominant process. Due to the large branching ratio for $H \to WW$ decays of 22%, this channel benefits from a Run 1 data set rich in Higgs boson candidates, resulting in low statistical uncertainties and a signal to background ratio of about 10%. The two dominant uncertainties on the expected signal yield are given by uncertainties on the QCD renormalisation and factorisation scale, and on the Parton Distribution Function (PDF); both introduce an uncertainty of 8% on the inclusive normalisation [192].

The experimental signature and its distinction against background processes with equal final states is presented for the discovered 125 GeV Higgs boson. The first observation of $H \to WW$ decays, published in Ref. [18], serves as the baseline for the measurements presented in this chapter. The $m_H = 125$ GeV Higgs boson decays into off-shell W bosons and only subsequent leptonic decays are considered. The experimental signature described in Section 8.1.1 is thus given by electrons, muons, jets and missing transverse energy, which are reconstructed as in Section 5.9.

The $H \to WW$ process is established from the final state particles; two charged leptons, two neutrinos, which are reconstructed as missing transverse energy, and jets, which are present in the vector boson fusion (VBF) production mode and/or from initial-state radiation. Reconstructing the neutrino momenta via the missing transverse energy $\boldsymbol{E}_{\mathrm{T}}^{\mathrm{miss}}$ presents several challenges. The reconstruction of the H→WW final state is based on the vector sum of the $\boldsymbol{E}_{\mathrm{T}}^{\mathrm{miss}}$ and the lepton momenta, and therefore relies on the relatively poorly resolved components of the

missing transverse energy. The H → WW process suffers from large and diverse background. Extracting a significant signal is in part achieved by splitting the analysis in categories of jet multiplicity, N_{jet}.

8.1.1 H→WW signature

The production by the ggF and the VBF mechanisms have distinctly different signatures, chiefly the two additional jets in VBF compared to ggF. Both channels have different background compositions and are studied independently. The VH production has a small cross section and is not studied individually in this analysis but only as contaminations to the ggF or VBF selection.

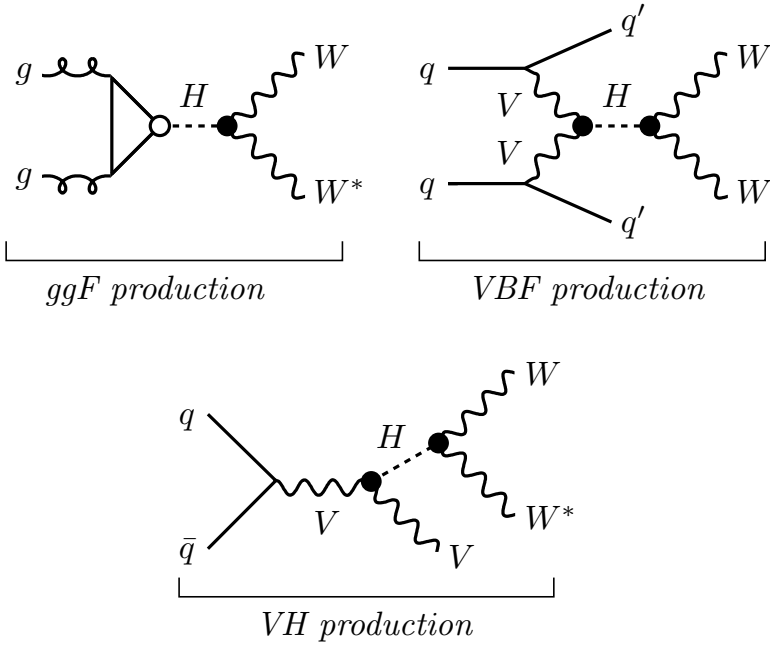

Figure 8.1 Feynman diagrams for the leading production modes (ggF, VBF, and VH), where the VVH and qqH coupling vertices are marked by • and ∘, respectively. The V represents a W or Z vector boson [18].

The H→WW decay is followed by subsequent decays of each W boson to either leptons or hadrons. The branching ratios are BR(W→ $\ell\nu$)=≈ 10.8% for each lepton flavour and BR(W→ hadrons)=67.6%. For two simultaneous W boson decays one can thus have a leptonic, hadronic or mixed final state. Despite the lower branching ratio, the leptonic mode is the most sensitive, with lower backgrounds. In the following only the leptonic mode is considered, where a lepton ℓ refers to either an electron or muon. Tau-leptons undergo predominantly

hadronic decays and are thus mostly excluded. Decays of $\tau \to e\nu_e\nu_\tau$ and $\tau \to \mu\nu_\mu\nu_\tau$ have a branching ratio of 17.85% and 17.36% respectively, and thus contribute to the lepton selection. The signature is thus given by two oppositely charged leptons and significant missing transverse momentum, carried away by the neutrinos. Given $m_{\mathrm{H}} < 2\,m_{\mathrm{W}}$, at least one W boson must be off-shell in H→WW decays. This results in final state leptons with low momentum, which have a low identification purity due to substantial misidentified hadronic backgrounds.

As the Higgs boson is spin-0 and the weak interaction displays a V−A symmetry, the opening angle θ between the two charged leptons is small, a result of spin conservation and effectively zero neutrino mass, illustrated in Figure 8.2. Thus the dilepton mass $m_{\ell\ell}$ is also small, given by $m^2_{\ell\ell} \approx 2E_{\ell_1}E_{\ell_2}(1-\cos\theta)$. Signal events are therefore selected by imposing $\Delta\phi(\ell,\ell) < 1.8$ and $m_{\ell\ell} < 55$ GeV. The choice of this selection can is given by the comparison of signal and background yields, shown in Figures A.3 and A.4.

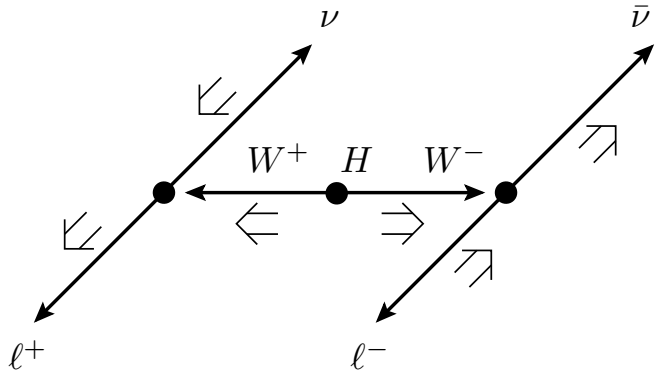

Figure 8.2 Illustration of the H→ WW decay. The small arrows indicate the particles' directions of motion and the large double arrows indicate their spin projections. The spin-0 Higgs boson decays to W bosons with opposite spins, and the spin-1 W bosons decay into leptons with aligned spins. The H and W decays are shown in the decaying particle's rest frame. Because of the V−A decay of the W bosons, the charged leptons have a small opening angle $\Delta\phi_{\ell\ell}$ in the laboratory frame and thus a low invariant mass $m_{\ell\ell}$ distributed below $m_{\mathrm{H}}/2$. This feature is also present when one W boson is off mass shell [18].

The mass of decay products, $\ell\ell + \nu\nu$ corresponds to m_{H}, within the experimental resolution. However, the neutrinos cannot be fully reconstructed and only their transverse momentum component can be inferred from the missing transverse momentum. Therefore, instead of setting cuts on the invariant mass, the

transverse mass m_{T} is used to select events mediated by a Higgs boson. Signal events are peaked in the dilepton transverse mass m_{T}, defined as

$$m_{\mathrm{T}} = \sqrt{(E_{\mathrm{T}}^{\ell\ell} + E_{\mathrm{T}}^{\mathrm{miss}})^2 - |\boldsymbol{p}_{\mathrm{T}}^{\boldsymbol{\ell\ell}} + \boldsymbol{p}_{\mathrm{T}}^{\mathrm{miss}}|^2}, \tag{8.1}$$

where

$$E_{\mathrm{T}}^{\ell\ell} = \sqrt{|\boldsymbol{p}_{\mathrm{T}}^{\boldsymbol{\ell\ell}}|^2 + m_{\ell\ell}^2}. \tag{8.2}$$

Signal events are selected by setting an upper bound on m_{T} of m_{H}. In practice, the limited detector resolution, particularly on measurements of $E_{\mathrm{T}}^{\mathrm{miss}}$, means that the reconstructed m_{T} distribution does not have a sharp cut-off at $m_{\mathrm{H}} = 125$ GeV.

8.1.2 Jet Categories

Three non-overlapping signal regions are defined, distinguished by the number of reconstructed jets: $N_{\mathrm{jet}} = 0$, $N_{\mathrm{jet}} = 1$, or $N_{\mathrm{jet}} \geq 2$. These separate the data into *signal regions* with different background composition. Performing the analysis in signal regions improves the sensitivity. The dominant background process is WW production for the $N_{\mathrm{jet}} = 0$ category, top-quark production for $N_{\mathrm{jet}} \geq 2$, and a mixture of the two for $N_{\mathrm{jet}} = 1$. For jet multiplicities above two, the number of events decreases with increasing number of jets but the background composition remains constant, so these events are all collected in the $N_{\mathrm{jet}} \geq 2$ signal region.

The multiplicity of jets drops off rapidly and most ggF signal is in the $N_{\mathrm{jet}} = 0$ category, with a sizeable yield in the $N_{\mathrm{jet}} = 1$ category. The $N_{\mathrm{jet}} \geq 2$ region shows a small ggF yield and is dominated by VBF production.

8.1.3 Backgrounds

Various background processes produce similar final states to H→WW signal. Sources of background include misidentification of photons as electrons, mistagging of jets as b-jets and detector inefficiencies. Feynman diagrams of the most important backgrounds are shown in Figure 8.3 and listed below.

WW Irreducible background with almost identical final state to the Higgs boson signal, but with a larger $\Delta\phi_{\ell\ell}$ and $m_{\ell\ell}$.

$\mathbf{t\bar{t}}$, tW A large source of background, characterised by high momentum jets and

to $\ell\ell + \nu\nu$, which can be reduced by binning in N_{jet}. In the $N_{\text{jet}} = 0$ and $N_{\text{jet}} = 1$ categories $t\bar{t}$ events are rejected by vetoing jets, this fails however if the jet p_{T} falls below the veto threshold. In the $N_{\text{jet}} = 1$ and $N_{\text{jet}} \geq 2$ categories b-jets are vetoed, but inefficiencies in b-tagging result in sizeable residual background.

tb, tbq Arises from an imperfect b-jet veto and hadronic initial states that produce an object which is identified as a lepton, due to misidentification or decay of the heavy flavour particle.

$\mathbf{Z}/\gamma* \to \ell\ell$ This mimics the signal when other sources of $E_{\text{T}}^{\text{miss}}$ are misidentified as neutrinos. This is the dominant source of events with two leptons, but can be rejected by requiring differently flavoured leptons.

$\mathbf{Z}/\gamma* \to \tau\tau$ For leptonic τ decays this process features a final state with the same particle content as the Higgs boson signal with two additional neutrinos. The additional neutrinos lower the missing transverse energy only moderately. A strong rejection is achieved by reconstructing $m_{\tau\tau}$ and requiring it to be incompatible with m_{Z}.

W+jets Produces one real lepton and neutrino together with a fake lepton from misidentification or decay of the heavy flavour particle forming the jet and misidentified neutrinos from other sources of $E_{\text{T}}^{\text{miss}}$.

The non-WW disoson background is collectively referred to as "other VV" or "VV", including Wγ^*, Wγ, WZ, and ZZ events.

Wγ Identical to the signal when the photon converts to an electron.

WZ, Wγ^*, ZZ Is generally rejected on the basis of multiplicity of charged leptons, but contribute to the background in cases where a lepton is not reconstructed correctly.

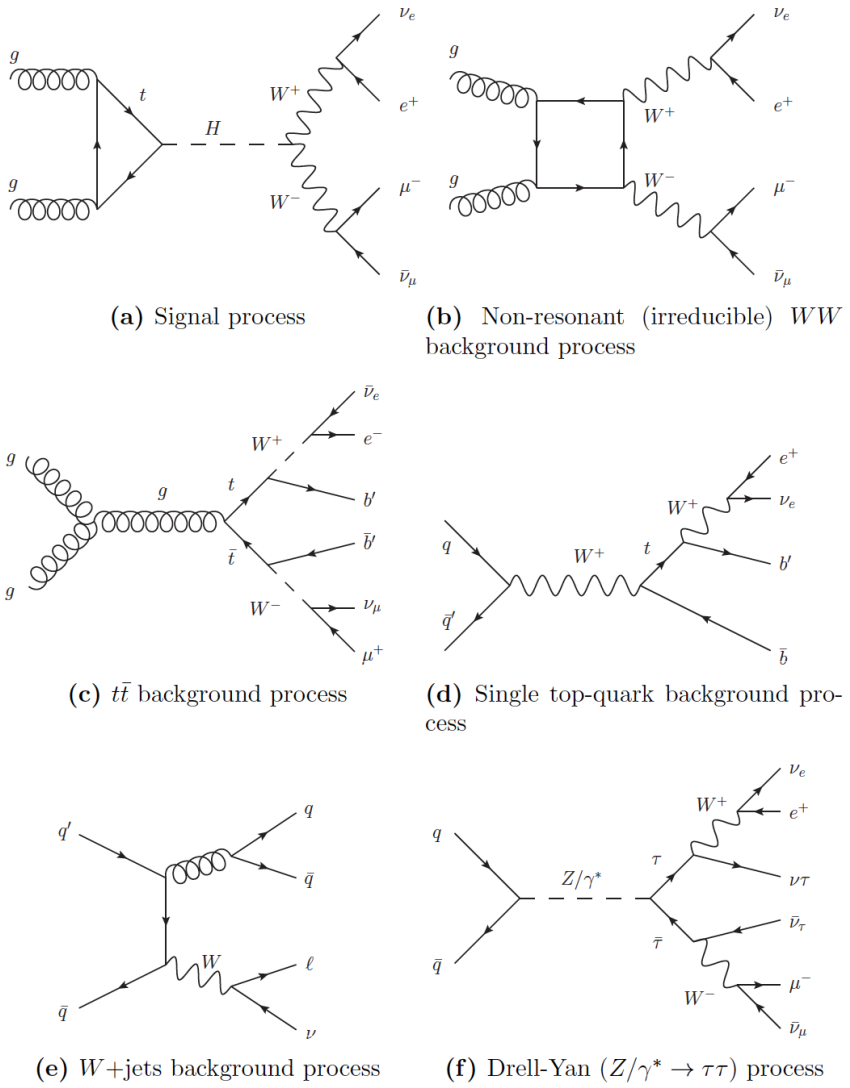

(a) Signal process

(b) Non-resonant (irreducible) WW background process

(c) $t\bar{t}$ background process

(d) Single top-quark background process

(e) W+jets background process

(f) Drell-Yan ($Z/\gamma^* \to \tau\tau$) process

Figure 8.3 Feynman diagrams of the ggF signal process and the most important backgrounds processes. Examples for leptonic final states are shown.

8.1.4 Observation of H→WW

The observation of the Higgs boson to WW decays is reported in Ref. [18]. Using 25 fb^{-1} of data at 7 and 8 TeV, an excess of 6.1 σ (standard deviations) was measured and evidence for VBF production was found with a significance of 3.2 σ. The m_{T} distributions from this analysis are shown in Figure 8.4. At $\sqrt{s} = 8$ TeV the total production cross sections times branching ratio were measured to be

$$\sigma \times \mathrm{BR}(\mathrm{H_{ggF}} \to \mathrm{WW}) = 4.6 \pm 0.9(\mathrm{stat}) \pm 0.8(\mathrm{sys})\ \mathrm{pb}$$
$$\sigma \times \mathrm{BR}(\mathrm{H_{VBF}} \to \mathrm{WW}) = 0.51 \pm 0.17(\mathrm{stat}) \pm 0.13(\mathrm{sys})\ \mathrm{pb}$$

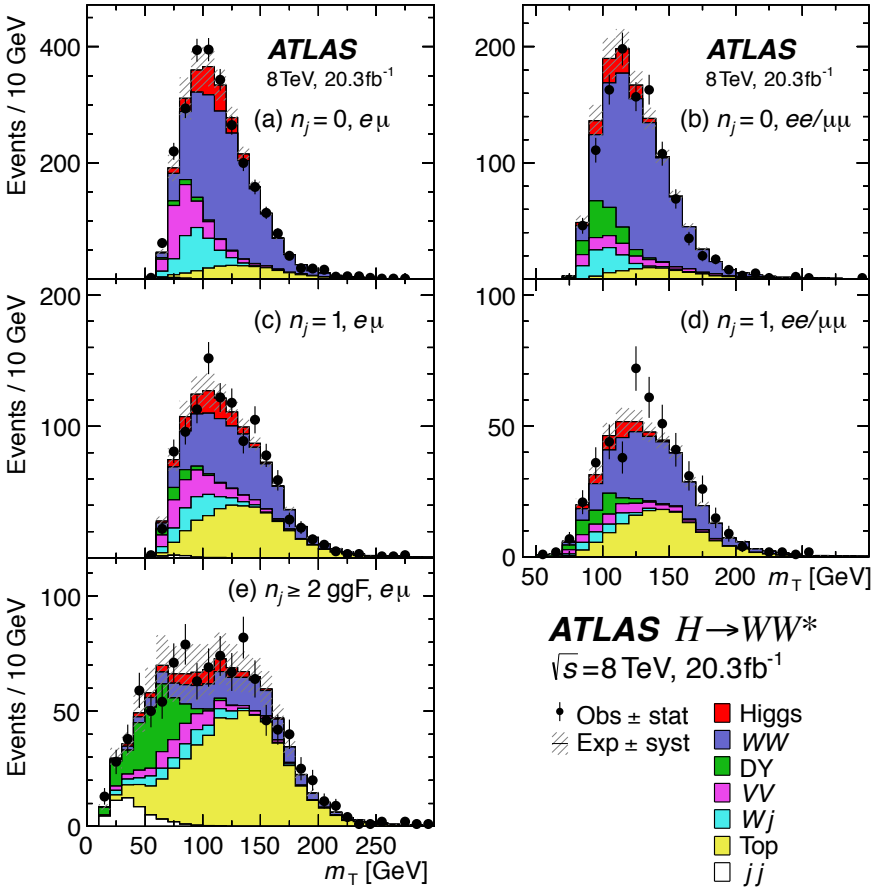

Figure 8.4 Distributions of the transverse mass m_{T} for the $N_{\mathrm{jet}} \leq 1$ and $N_{\mathrm{jet}} \geq 2$ ggF-enriched categories in the 8 TeV data analysis [18]. A cut is performed in m_{T} and a multivariate fit it applied to obtain the signal significance. The data is in agreement with the SM expectation.

Here (stat) and (sys) correspond to the total of all statistical and systematic uncertainties.

Total fiducial cross section were measured for the ggF production process in the $N_{\mathrm{jet}} = 0$ and $N_{\mathrm{jet}} = 1$ individually. The fiducial volume was defined in individual N_{jet} categories and includes all signal region cuts, primarily the lower lepton p_{T} thresholds. The fiducial cross section was found to be

$$\sigma^{\mathrm{ggF}}_{fid,0j} = 27.6 \pm 5.4(\mathrm{stat}) \pm 4.1(\mathrm{sys})\ \mathrm{fb}$$
$$\sigma^{\mathrm{ggF}}_{fid,1j} = 8.3 \pm 3.1(\mathrm{stat}) \pm 3.1(\mathrm{sys})\ \mathrm{fb}$$

for $m_{\mathrm{H}} = 125.36$ GeV and all W decay modes.

8.2 Differential Measurements in H→WW

Differential cross sections are chosen to probe QCD and PDF effects of the ggF Higgs boson production. The following observables are considered:

- $\boldsymbol{N_{\text{jet}}}$ Number of associated jets with the Higgs boson decay.
- $\boldsymbol{p_{\text{T}}^{\text{H}}}$ Transverse momentum of the Higgs boson.
- $\boldsymbol{p_{\text{T}}(j_1)}$ Transverse momentum of the highest-p_{T} or *leading* jet in the event.
- $\boldsymbol{\varepsilon_0}$ Jet-veto efficiency, the efficiency of selection H+0jets events for a given $p_{\text{T}}(j_1)$ threshold.
- $\boldsymbol{|y_{\ell\ell}|}$ The longitudinal angle of the di-lepton system from the $\text{H} \to \text{WW} \to \ell\nu\ell\nu$ decay.

In principle, new physical contributions could appear in any of these distributions, while leaving the integrated cross section consistent with the SM.

QCD

Higher order perturbative QCD contributions to ggF production are probed by measuring N_{jet} and $p_{\text{T}}(j_1)$. N_{jet} is proportional to the additional number of vertices present in higher order QCD terms, while $p_{\text{T}}(j_1)$ probes the distribution of these emissions in the high p_{T} region in which the perturbative approximation holds.

The QCD scale uncertainty arises from the limitations in perturbative QCD calculations. This generates an additional uncertainty on the shape of the N_{jet} distribution. N_{jet} represents a measure of the QCD radiative process in the initial state and is correlated to the Higgs boson p_{T} spectrum. The hard QCD process, reflected by N_{jet}, is modelled comparably well by perturbative calculations at fixed order in α_s, but lacks precise prediction for the high N_{jet} and high p_{T}^{H} regime as ever higher order calculations become computationally prohibitive. The poorly understood soft QCD process is only measured by the p_{T}^{H}, not N_{jet}. Resummation techniques have greatly improved the reliability of soft QCD calculations for the p_{T}^{H} spectrum modelling, but still give poor predictions at low p_{T}^{H} [193], resulting from the dominant soft gluon contribution in this phase space. Non-zero p_{T}^{H}

results from the Higgs boson recoiling against one or more soft partons. The low p_{T} region of the $p_{\mathrm{T}}(j_1)$ is also sensitive to soft emission. Experimental constraints from measurements of the Higgs boson cross section as a function of $p_{\mathrm{T}}^{\mathrm{H}}$ and N_{jet} are therefore needed. In addition, improved understanding of p_{T}^{H} and thus N_{jet} would greatly benefit analyses such as $\mathrm{H} \to \mathrm{WW}^* \to \ell\nu\ell\nu$ which are binned in N_{jet} and suffer from event migration between different bins.

In many Higgs boson decay channels, including WW, it is common to split the analysis according to the number of associated jets in the event. This facilitates background rejection. The $N_{\mathrm{jet}} = 0$ selection in $\mathrm{H} \to \mathrm{WW}$, for example, dramatically reduces the dominant top-quark background, where jets are vetoed with a transverse momentum above threshold $p_{\mathrm{T}} > p_{\mathrm{T}}^{\mathrm{veto}}$. However, for ggF Higgs production, jets can be created by additional QCD radiation off the incoming gluons. Requiring $N_{\mathrm{jet}} = 0$ thus not only rejects the top background but also cuts out a fraction of the ggF Higgs boson signal. In order to perform precision studies it is necessary to accurately determine the fraction of signal events that pass the $N_{\mathrm{jet}} = 0$ requirement, the *jet-veto efficiency* ε_0. The ATLAS H→WW analysis, for example, relies on a theoretical prediction of the jet-veto efficiency for jet momentum thresholds $p_{\mathrm{T}}^{\mathrm{veto}}$ in the 25 - 40 GeV range, which is a significant source of uncertainty. Due to the relatively soft momentum threshold, the calculation is governed by logarithmic enhancement of $\ln(p_{\mathrm{T}}^{\mathrm{veto}}/m_{\mathrm{H}})$ that requires resummation of the coupling constant α_s to all orders. Though the calculation are performed up to NNNLO ($\mathrm{N^3LO}$) and matched to NNLL terms, the theoretical uncertainties are still of 5-10% [194, 195].

PDF

The gluon PDF is probed by measuring the absolute value of the rapidity of the reconstructed dilepton system, $|y_{\ell\ell}|$.

Rapidity is defined as $y = 0.5 \times \ln[(E + p_z)/(E - p_z)] = 0.5 \times \ln[x_1/x_2]$, where E denotes the energy and p_z is the component of the momentum along the beam direction. x_1 and x_2 are the PDF momentum fractions of the gluons in the production of the Higgs boson. Since it is not possible to reconstruct y_{H} experimentally in the $\mathrm{H} \to \mathrm{WW}^* \to \mathrm{e}\nu\mu\nu$ final state, the differential cross section is measured as a function of $|y_{\ell\ell}|$, which is highly correlated to y_{H} as shown in Figure 8.5.

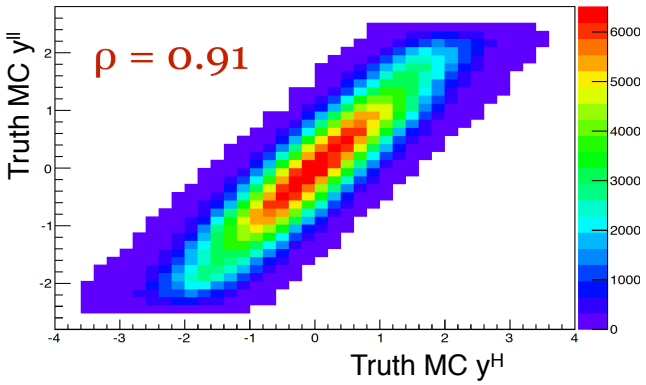

Figure 8.5 Longitudinal angle of the Higgs boson $|y^H|$ is highly correlated to $|y_{\ell\ell}|$. The plots shows particle-level Monte Carlo predictions, without event selection or detector effects.

The rapidity distribution of the Higgs boson is sensitive to QCD radiative corrections and PDFs of the colliding partons. By selecting Higgs events with different angular configurations, one can probe different ranges of the parton momentum fraction x and hard scattering scales Q^2. Theoretical predictions on the PDFs have substantial uncertainties, particularly for the gluon contributions at small x, large x or large Q^2. A detailed comparison between Higgs differential cross section data and simulation models has only recently become possible and will reduce the uncertainties and improve predictions on the Higgs production rates.

8.3 Analysis Overview

The measurement of fiducial differential cross sections in this thesis is an extension of the ggF+VBF coupling measurement reported in Ref. [18] and summarised in Section 8.1.4. It uses the same object definitions, background-estimation techniques, and strategies to evaluate the systematic uncertainties. However, simplifications were made, limiting the scope to the dominating ggF production mode and final states containing different flavoured leptons, i.e. one electron and one muon. Contributions from the VBF and vector-boson associated production (VH) modes are subtracted as background contributions, assuming their yields are given by the SM expectation. The modelling of the signal and all background processes is given in Section 8.4. Signal, background and data events are selected according to Section 8.5.

Dominant backgrounds are normalised from control regions in data, see Section 8.6. The signal is obtained by subtracting the background estimate from the data yield in distributions of N_{jet}, p_{T}^{H}, $|y_{\ell\ell}|$ and $p_{\text{T}}(j_1)$, shown in Section 8.7. The distributions are unfolded to a fiducial volume defined in Section 8.8. Details of the unfolding procedure are given in Section 8.9.

Statistical and systematic uncertainties are discussed in Section 8.10. Finally, fiducial cross section measurements are presented in Section 8.12. A total fiducial cross section of the ggF Higgs boson production is also calculated by summing over the N_{jet} distribution.

To minimise the model dependency of the correction for the detector acceptance and to allow direct comparison with theoretical prediction, all cross sections presented in this chapter are fiducial cross sections corrected for detector effects. This correction is performed by Bayesian iterative unfolding, introduced in Chapter 7. Thus, the cross sections are given in a fiducial phase space region which is defined to closely match the event selection performed on the reconstructed objects.

8.4 Signal and Background Models

This section describes which generators and parameters were used to simulate the signal and background samples, following the concepts presented in Chapter 4 and in close reference to Ref. [1].

The ggF and VBF production modes for $\text{H} \to \text{WW}^*$ are modelled at next-to-leading order (NLO) in the strong coupling α_{S} with the Powheg-box MC generator [78, 83, 84], interfaced with Pythia8 [77, 78] for the parton shower, hadronisation, and underlying event. The CT10 [196] PDF set is used and the parameters of the Pythia8 generator controlling the modelling of the parton shower and the underlying event are set to the values of the ATLAS Underlying Event Tune 2 [197]. The Higgs boson mass is set to 125 GeV in the simulation. To improve the modelling of the Higgs-boson p_{T} distribution, a reweighting scheme is applied to reproduce the prediction of the next-to-next-to-leading order (NNLO) and next-to-next-to-leading logarithm (NNLL) dynamic-scale calculation given by the HRes 2.1 program [90]. Events with ≥ 2 jets are further reweighted to reproduce the p_{T} spectrum predicted by the NLO Powheg-box simulation

of Higgs-boson production in association with two jets [198]. Interference with continuum WW production [199, 200] has a negligible impact on this analysis due to the transverse-mass selection criteria described in Section 8.5.2 and is not included in the signal model.

The cross sections at $\sqrt{s} = 8$ TeV for a Higgs boson mass of 125.0 GeV, calculated at NNLO+NNLL in QCD and NLO in the electroweak couplings, are 19.3 pb and 1.58 pb for ggF and VBF respectively [50]. The uncertainty on the ggF cross section is 10%, with approximately equal contributions from QCD scale variations (7.5%) and PDFs (7.2%). For the VBF cross section the uncertainty is 2.7%, mainly from PDF variations. The WH and ZH processes are modeled with Pythia8 and normalised to cross sections of 0.70 pb and 0.42 pb calculated at NNLO in QCD and NLO in the electroweak couplings [50]. The uncertainty is 2.5% on the WH cross section and 4.0% on the ZH cross section. For all $H \to WW$ production modes, the decay of one or both W bosons to $\tau\nu$ with the subsequent decay of the τ lepton to an electron or muon and neutrinos is included in the signal sample.

For all of the background processes, with the exception of $W+$jets and multijet events, MC simulation is used to model event kinematics and as an input to the background normalisation. The $W+$jets and multijet background model is derived from data and described in more detail in Section 8.6. For the dominant WW and top-quark backgrounds, the MC generator is Powheg-box+Pythia6 [201], also with CT10 for the input PDFs. The tune used for Pythia6 is the Perugia 2011 tune [202]. For the WW background with $N_{\text{jet}} \geq 2$, to better model the additional partons, the Sherpa [72] program with the CT10 PDF set is used. The Drell-Yan background, including $Z/\gamma^* \to \tau\tau$, is simulated with the Alpgen [203] program. It is interfaced with Herwig [71] set to values of the ATLAS Underlying Event Tune 2 [204] and uses the CTEQ6L1 [205] PDF set. The same configuration is applied for $W\gamma$ events. Events in the Z/γ^* sample are reweighted to the MRSTmcal PDF set [206]. For the $W\gamma^*$ background, the Sherpa program is used, with the same version number and PDF set as the WW background with $\geq$ 2 jets. Additional diboson backgrounds, from WZ and ZZ, are modelled using Powheg-box+Pythia8.

For all MC samples, the ATLAS detector response is simulated [207] using either Geant4 or a parametrised Geant4-based calorimeter simulation [208]. Pile-up contributions are modelled by overlaying minimum-bias interactions generated using Pythia8.

8.5 Event Selection

This section describes the analysis specific reconstruction criteria on physics objects and the reconstruction-level definition of the signal region. The signal region is defined by event selection criteria which are made to select signal events and suppress events from background processes. In Section 8.8 a fiducial region is defined which is largely based on the definition of the signal region detailed here.

All objects are defined with respect to a primary interaction vertex, which is required to have at least three associated tracks with $p_{\mathrm{T}} \geq 400$ MeV. With an average pile-up of 20 in the 8 TeV dataset, a typical event has multiple vertices fulfilling this requirement and the primary vertex is selected as the one with the largest value of $\sum(p_{\mathrm{T}}^2)$.

8.5.1 Object Selection

Objects are reconstructed following the definitions detailed in Section 5.9, with additional requirements specific to this analysis.

The electron selection is performed on the basis of isolation requirements which are stricter for low E_{T} electrons. For electrons with 15 GeV $< E_{\mathrm{T}} <$ 25 GeV, a likelihood-based electron selection at the "very tight" operating point is used, which sacrifices efficiency for improved background rejection. For $E_{\mathrm{T}} > 25$ GeV, a more efficient "medium" selection is used because background is less of a concern. The efficiency of these requirements varies strongly as a function of E_{T}, starting from 65–70% for $E_{\mathrm{T}} < 25$ GeV, jumping to $\approx 80\%$ with the change in identification criteria at $E_{\mathrm{T}} = 25$ GeV, and then steadily increasing as a function of E_{T} [140].

In this analysis, muons are required to have $|\eta| < 2.5$ and $p_{\mathrm{T}} > 10$ GeV. The reconstruction efficiency is between 96% and 98%, and stable as a function of p_{T} [209].

Additional criteria are applied to electrons and muons to reduce backgrounds with lepton-like signatures from hadronic activity or the decay of τ-particles.

Lepton[1] isolation is defined using track-based and calorimeter-based quantities. Object isolation requirements are optimised as a function of lepton p_{T}, with stricter criteria at lower p_{T} to reject background and looser criteria at higher p_{T} to enhance signal efficiency. The transverse and longitudinal impact-parameters describe the closest approach of a track to the primary vertex and can be used to ensure correct track to primary vertex association. The requirements on the impact parameter are optimised by the same considerations as the object isolation. The efficiency of the isolation and impact-parameter requirements for electrons passing all of the identification criteria requirements ranges from 68% for $10 < E_{\mathrm{T}} < 15$ GeV to greater than 90% for electrons with $E_{\mathrm{T}} > 25$ GeV. For muons, the equivalent efficiencies are 60%–96% [18]. Jets are reconstructed from topological clusters of calorimeter cells [147, 210, 211] using the anti-k_{T} algorithm with a radius parameter of $R = 0.4$ [212].

To reduce the chance of using a jet produced by a pileup event, jets within the inner-detector acceptance are required to have a sufficiently high jet vertex fraction, i.e. more than 50% of the sum of the scalar p_{T} of their associated tracks due to tracks associated with the primary vertex. Jets used for categorisation of the signal region are required to have $p_{\mathrm{T}} > 25$ GeV for $|\eta| < 2.4$ and $p_{\mathrm{T}} > 30$ GeV if $2.4 < |\eta| < 4.5$, where the higher threshold is needed to suppress the more prominent pile-up jets in the forward region.

Jets containing b-hadrons are identified using a multivariate b-tagging algorithm [151, 213] which combines impact-parameter information of tracks and the reconstruction of charm- and bottom-hadron decays, see Section 5.9.5. The working point with an efficiency of 85% for b-jets and a mis-tag rate for light-flavour jets of 10.3% is used, in order to reject top-quark background events.

Missing transverse momentum ($p_{\mathrm{T}}^{\mathrm{miss}}$) is produced in signal events by the two neutrinos from the W boson decays. It is reconstructed as the negative vector sum of the transverse momenta of muons, electrons, photons, jets, and tracks associated with the primary vertex but not associated with any of the previous objects.

[1]Following the bad choice of nomenclature which is common to high-energy physics, *Lepton* here refers only to electrons and muons.

8.5.2 Signal Region Selection

Events are selected from those with exactly one electron and one muon with opposite charge, a dilepton invariant mass $m_{\ell\ell}$ greater than 10 GeV, and $p_{\mathrm{T}}^{\mathrm{miss}} > 20$ GeV. At least one of the two leptons is required to have $p_{\mathrm{T}} > 22$ GeV and the lepton with higher p_{T} is referred to as the leading lepton. The other lepton is required to have $p_{\mathrm{T}} > 15$ GeV, referred to as subleading lepton.

The High Level Trigger (HLT) selects events with an electron or muon above a 24 GeV threshold that also meet isolation requirements. To improve the selection efficiency, a supporting trigger with no isolation requirement but higher p_{T} thresholds, 60 GeV for electrons and 36 GeV for muons, is used. An additional dilepton trigger requires an electron and a muon above a threshold of 10 GeV and 6 GeV, respectively, at Level-1, and 12 GeV and 8 GeV in the HLT. The reconstructed leptons are required to match those firing the trigger.

The selection is summarised in Table 8.1 and motivated by a comparison of signal and background distributions in Appendix A.1. The b-jet veto uses jets with $p_{\mathrm{T}} > 20$ GeV and $|\eta^{\mathrm{jet}}| < 2.4$, and rejects top-quark background in the $N_{\mathrm{jet}} = 1$ and $N_{\mathrm{jet}} \geq 2$ categories. Background from $\mathrm{Z}/\gamma^* \to \tau\tau$ and multijet events is reduced in the $N_{\mathrm{jet}} = 0$ category with a requirement on the transverse momentum of the dilepton system, $p_{\mathrm{T}}^{\ell\ell} > 30$ GeV. In the $N_{\mathrm{jet}} = 1$ category, this is accomplished in part by requirements on the single-lepton transverse mass m_{T}^{ℓ}, defined for each lepton as $m_{\mathrm{T}}^{\ell} = \sqrt{2(p_{\mathrm{T}}^{\mathrm{miss}} p_{\mathrm{T}}^{\ell} - \boldsymbol{p}_{\mathrm{T}}^{\ell} \cdot \boldsymbol{p}_{\mathrm{T}}^{\mathrm{miss}})}$. The lepton with the larger m_{T}^{ℓ} is required to fulfil $m_{\mathrm{T}}^{\ell} > 50$ GeV. The p_{T} of the $\tau\tau$ system from the $\mathrm{Z}/\gamma^* \to \tau\tau$ process is larger in the $N_{\mathrm{jet}} = 1$ and $N_{\mathrm{jet}} \geq 2$ categories than in $N_{\mathrm{jet}} = 0$ and the $\tau\tau$ invariant mass $m_{\tau\tau}$ can be calculated by the *collinear approximation* [214]. Most background from $\mathrm{Z}/\gamma^* \to \tau\tau$ is suppressed by requiring $m_{\tau\tau} < m_Z - 25$ GeV. This also rejects the kinematically similar events from the $\mathrm{H} \to \tau\tau$ process.

Requiring the di-jet invariant mass $m_{jj} < 600$ GeV or the difference in rapidity $\Delta y_{jj} < 3.6$ is an effective VBF veto, which rejects about 40% of VBF events but only 5% of ggF events, see Firgure A.3.

The selection cuts are

Figure 8.6 shows the m_{T} distribution after application of all other selection criteria in each of the signal regions. Selecting events with 85 GeV $< m_{\mathrm{T}} <$ 125 GeV increases the signal region purity and minimises the total uncertainty on this

Category	$N_{\text{jet}} = 0$	$N_{\text{jet}} = 1$	$N_{\text{jet}} \geq 2$
Preselection	Two isolated leptons ($\ell = e, \mu$) with opposite charge $p_{\text{T}}^{\text{lead}} > 22$ GeV, $p_{\text{T}}^{\text{sublead}} > 15$ GeV $m_{\ell\ell} > 10$ GeV $p_{\text{T}}^{\text{miss}} > 20$ GeV		
Background rejection	- $\Delta\phi(\ell\ell, p_{\text{T}}^{\text{miss}}) > 1.57$ $p_{\text{T}}^{\ell\ell} > 30$ GeV	$N_{b\text{-jet}} = 0$ $\max(m_{\text{T}}^{\ell}) > 50$ GeV $m_{\tau\tau} < m_Z - 25$ GeV	$N_{b\text{-jet}} = 0$ - $m_{\tau\tau} < m_Z - 25$ GeV
VBF veto	-	-	$m_{jj} < 600$ GeV .OR. $\Delta y_{jj} < 3.6$
$\text{H} \to \text{WW}^* \to \ell\nu\ell\nu$ topology	$m_{\ell\ell} < 55$ GeV $\Delta\phi_{\ell\ell} < 1.8$ 85 GeV $< m_{\text{T}} <$ 125 GeV		

Table 8.1 Event selection criteria used to define the signal regions in the $\text{H} \to \text{WW}^* \to \text{e}\nu\mu\nu$ differential analysis. The preselection and signal-topology selection criteria are identical across all signal regions. The background rejection and VBF-veto selection depend on N_{jet}, and a dash ('-') indicates no selection applied. Definitions including the p_{T} thresholds for jet counting are given in the text.

measurement of the ggF cross section. Removing events with $m_{\text{T}} \geq m_H$ also reduces the effect of interference with the continuum WW process to negligible levels compared to the observed event yield [199].

8.5.3 Binning of Distributions

The p_{T} of the Higgs boson is reconstructed as the magnitude of the vector sum of the missing transverse momentum and the $\boldsymbol{p}_{\text{T}}$ of the two leptons. The reconstructed and unfolded distributions are binned using the boundaries defined in Table 8.2.

p_{T}^{H} [GeV]:	[0–20], [20–60], [60–300]
$\lvert y_{\ell\ell} \rvert$:	[0.0–0.6], [0.6–1.2], [1.2–2.5]
$p_{\text{T}}(j_1)$ [GeV]:	[0–30], [30–60], [60–300]

Table 8.2 Bin edges for the reconstructed and unfolded distributions.

The bin edges are determined by balancing the expected statistical and systematic uncertainty in each bin. Small bins result in large statistical uncertainties, while large bins increase the systematic uncertainties, especially for distributions with a large gradient. The impact of bin-migration under unfolding due to the binning choice was also considered, described in Section 8.9. The resolution of the

variables is smaller than the bin size and does not affect the binning choice. The resolution in $p_{\mathrm{T}}^{\mathrm{H}}$, $p_{\mathrm{T}}(j_1)$ and $|y_{\ell\ell}|$ were found to be 10.3 GeV, 6.3 GeV and 0.01 respectively, by comparing the average difference between particle-level and reconstructed MC information. These represent mean values over the kinematic range of interest, in practice the resolutions vary as a function of the variable. The upper edges of the last bin in $p_{\mathrm{T}}^{\mathrm{H}}$ and $p_{\mathrm{T}}(j_1)$ is chosen so that less than 1% of the expected event yield in the fiducial region is excluded. The upper edge for $|y_{\ell\ell}|$ is given by the limit of the detector acceptance. N_{jet} is trivially binned in the number of jets.

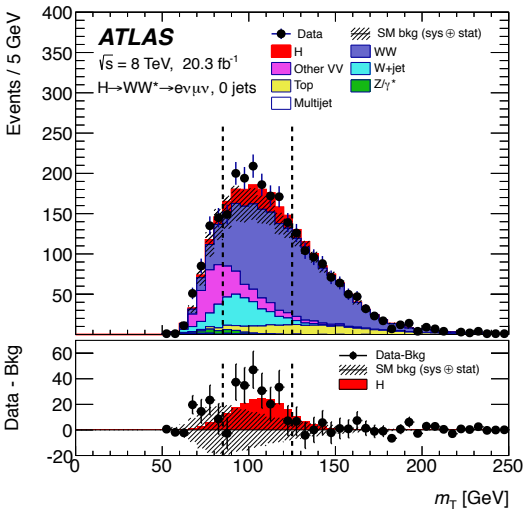

(a) $N_{\text{jet}} = 0$

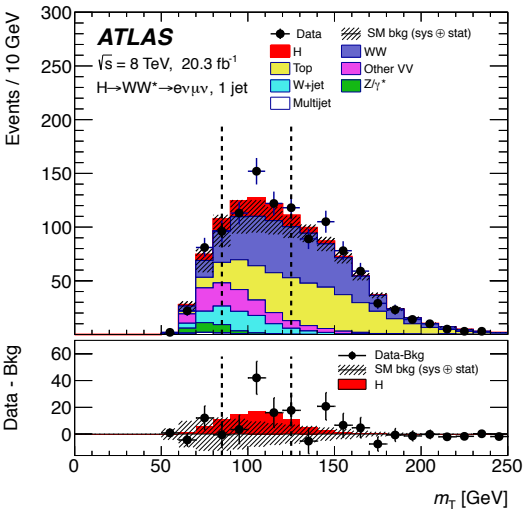

(b) $N_{\text{jet}} = 1$

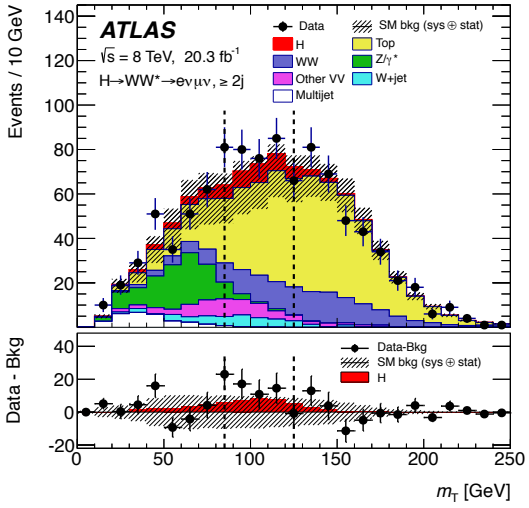

(c) $N_{\text{jet}} \geq 2$

Figure 8.6 Distribution of m_{T} after all other selection criteria have been applied for the $N_{\text{jet}} = 0$ (top left), $N_{\text{jet}} = 1$ (top right) and $N_{\text{jet}} \geq 2$ (bottom) signal regions. The background processes are normalised as described in Section 8.6. The hatched band shows the sum in quadrature of statistical and systematic uncertainties on the sum of the backgrounds. The data is in agreement with the SM expectation. The vertical dashed lines indicate the lower and upper selection boundaries on m_{T} at 85 and 125 GeV.

8.6 Background Estimation

The background samples are produced by MC generators and normalised to theoretical cross sections and the matching integrated luminosity in data, as described in Section 8.4. Additional corrections are applied to the background samples to reduce the model dependence and improve the estimate. Background normalisation and distribution shapes are either scaled to data or alternative MC generators. The normalisation strategy of the background processes is summarised in Table 8.3 and explained below. The shape scales of the kinematic distributions, apart from N_{jet}, are derived from MC stimulation, except for the W+jets background for which a comparison to data is used. As the scaling is performed in N_{jet} categories, a shape scale in N_{jet} amounts to a normalisation. Theoretical and experimental uncertainties are evaluated on all MC-simulation-derived shapes and included in the analysis, as described in Section 8.10.

Channel	WW	Top	$Z/\gamma^* \to \tau\tau$	$Z/\gamma^* \to ee/\mu\mu$	W+jets/multijet	VV	Non-ggF H
$N_{\text{jet}} = 0$	CR	CR	CR	MC	Data	CR	MC
$N_{\text{jet}} = 1$	CR	CR	CR	MC	Data	CR	MC
$N_{\text{jet}} \geq 2$	MC	CR	CR	MC	Data	MC	MC

Table 8.3 Summary of background-estimation procedures for the three signal regions. Each background is categorised according to whether it is normalised using a control region (CR), a fully data-derived estimate (Data), or the theoretical cross section and acceptance from MC simulation (MC).

The main background estimates in the signal region (SR) are normalised by considering control regions (CR). A CR is chosen so that it is identical to the signal region except for one or few inverted selection criteria. For a given background process a CR is constructed, in which the background is compared to data. The background is then scaled to match the data and the scale factor is used as the normalisation for that background in the signal region. A CR is enriched in the target background and orthogonal to the signal region. The CR definitions are summarised in Table 8.4.

Each control region supplies a normalisation factor (NF), defined as $(N - B')/B$, where N is the number of data events observed in the control region, B is the background yield in the CR for the target process based on the predicted cross section and acceptance from MC simulation, and B' is the predicted yield from other processes in the control region. The CRs have a small contribution from

the signal process. The effect of this choice is negligible. The normalisation of each background associated with a CR is scaled by the corresponding NF. The set of all such NFs is given in Table 8.5, along with their statistical uncertainties. These are included in the statistical uncertainty of the final results. Examples of CR plots are given below, all other control regions are shown in Appendix I.

CR	$N_{\text{jet}} = 0$	$N_{\text{jet}} = 1$	$N_{\text{jet}} \geq 2$
WW	$55 < m_{\ell\ell} < 110$ GeV $\Delta\phi_{\ell\ell} < 2.6$ $p_{\text{T}}^{\text{sublead}} > 15$ GeV	$m_{\ell\ell} > 80$ GeV $\lvert m_{\tau\tau} - m_Z \rvert > 25$ GeV $p_{\text{T}}^{\text{sublead}} > 15$ GeV b-jet veto $\max(m_{\text{T}}^{\ell}) > 50$ GeV	-
Top quark	No N_{jet} requirement $\Delta\phi_{\ell\ell} < 2.8$	$\geq$ 1 b-jet required	$m_{\ell\ell} > 80$ GeV b-jet veto
VV	Same-sign leptons All SR cuts	Same-sign leptons All SR cuts	-
$\text{Z}/\gamma^* \to \tau\tau$	$m_{\ell\ell} < 80$ GeV $\Delta\phi_{\ell\ell} > 2.8$	$m_{\ell\ell} < 80$ GeV $m_{\tau\tau} > m_Z - 25$ GeV b-jet veto	$m_{\ell\ell} < 70$ GeV $\Delta\phi_{\ell\ell} > 2.8$ b-jet veto

Table 8.4 Event selection criteria used to define the control regions (CR). Every control region starts from the same basic charged lepton and $p_{\text{T}}^{\text{miss}}$ and selection as the signal regions (SR) except that the subleading lepton p_{T} threshold is lowered to 10 GeV unless otherwise stated. Jet-multiplicity requirements also match the corresponding signal region, except where noted for some top-quark control regions. Dashes indicates that a particular control region is not defined; The definitions of $m_{\tau\tau}$, m_{T}^{ℓ}, and the jet counting p_{T} thresholds are as for the signal regions.

WW

The WW background is normalised using control regions in the $N_{\text{jet}} = 0$ and $N_{\text{jet}} = 1$ categories, in which it forms the dominant background. The primary distinction between the WW CR and the SR is the inverted selection in $m_{\ell\ell}$, designed to select the H→WW signal. In the $N_{\text{jet}} \geq 2$ category WW is modelled using the Sherpa generator and the normalisation is set to the NLO cross section calculated with MCFM [215].

The $|y_{\ell\ell}|$ distribution in the $N_{\text{jet}} = 0$ WW CR and the p_{T}^{H} distribution in the

$N_{\text{jet}} = 1$ WW CR are shown in Fig. 8.7. The relatively large $N_{\text{jet}} = 0$ WW normalisation factor of 1.22 has been studied in detail [18]; its deviation from unity is due to the modelling of the jet veto and higher-order corrections on the prediction of the WW cross section. A newer calculation of the inclusive WW cross section, with NNLO precision in α_S [216] brings the value closer to unity, compared to the calculation used here [217].

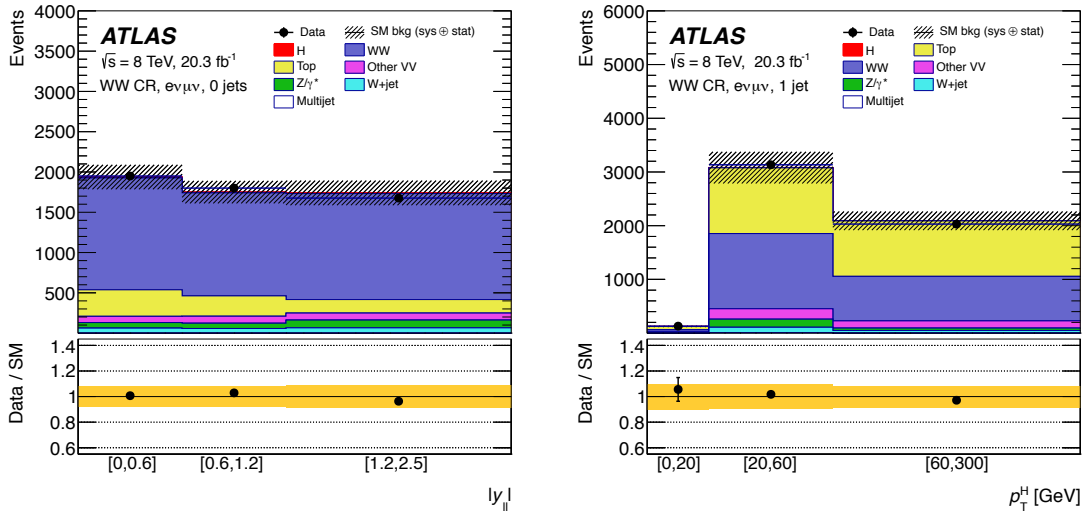

(a) $|y_{\ell\ell}|$, $N_{\text{jet}} = 0$ **(b)** p_{T}^{H}, $N_{\text{jet}} = 1$

Figure 8.7 Distributions of (a) $|y_{\ell\ell}|$ in the $N_{\text{jet}} = 0$ WW CR and (b) p_{T}^{H} in the $N_{\text{jet}} = 1$ WW CR. The hatched band in the upper plot and the shaded band in the lower plot shows the sum in quadrature of statistical and systematic uncertainties on the prediction. Relevant background normalisation factors have been applied.

Top

The top-quark background normalisation is estimated using control regions for all N_{jet} categories. The sum of $t\bar{t}$ and single-top backgrounds are treated together. For the $N_{\text{jet}} = 0$ CR, a pure sample of top events is selected by imposing all of the lepton and $p_{\text{T}}^{\text{miss}}$ preselection criteria with no requirements on the number of jets. The efficiency of the $N_{\text{jet}} = 0$ signal region selection is modelled using MC simulation, and the efficiency of the jet veto is corrected using the fraction of b-tagged events which have no jets in addition to the b-tagged one. Distinction from the SR for the $N_{\text{jet}} = 1$ category is achieved by requiring that the jet is b-tagged. To reduce the effect of b-tagging systematics, the extrapolation factor from the CR to the SR is corrected using an effective b-jet tagging scale factor

derived from a control region with two jets, where at least one is b-tagged. In the $N_{\text{jet}} \geq 2$ category, the number of top-quark events is sufficiently large that a CR with a b-jet veto can be defined at $m_{\ell\ell} > 80$ GeV. The $p_{\text{T}}(j_1)$ distribution in the $N_{\text{jet}} = 1$ top-quark CR and the p_{T}^{H} distribution in the $N_{\text{jet}} \geq 2$ top-quark CR are shown in Fig. 8.8.

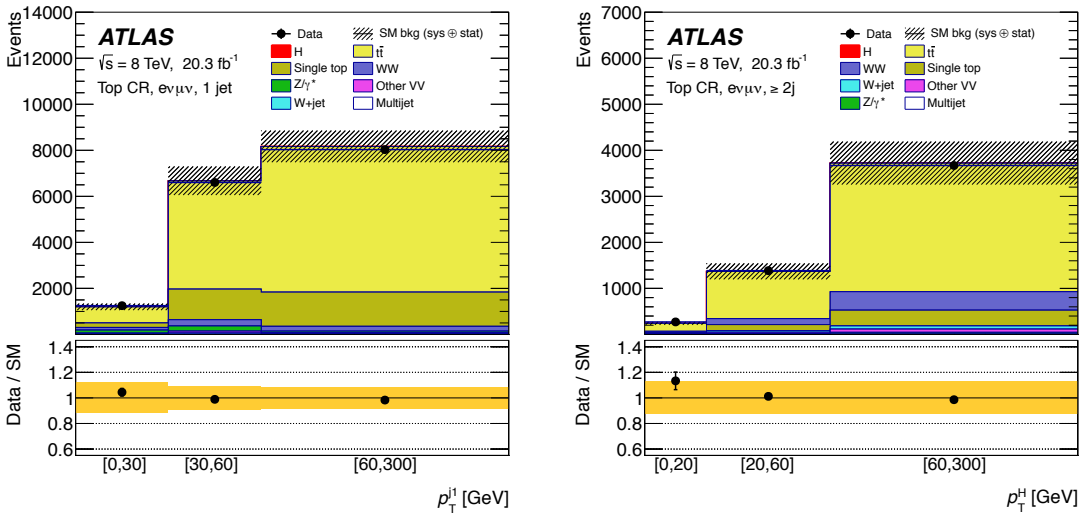

(a) $p_{\text{T}}(j_1)$, $N_{\text{jet}} = 1$ **(b)** p_{T}^{H}, $N_{\text{jet}} \geq 2$

Figure 8.8 Distributions of (a) $p_{\text{T}}(j_1)$ in the $N_{\text{jet}} = 1$ top-quark CR and (b) p_{T}^{H} in the $N_{\text{jet}} \geq 2$ top-quark CR. The hatched band in the upper plot and the shaded band in the lower plot shows the sum in quadrature of statistical and systematic uncertainties on the prediction. Relevant background normalisation factors have been applied.

VV

The background from diboson processes other than WW, which is primarily from Wγ^*, Wγ, and WZ events, is normalised in the $N_{\text{jet}} = 0$ and $N_{\text{jet}} = 1$ categories using a control region identical to the signal region except that the leptons are required to have the identical electrical charge (*same sign*). The VV same-sign yield in the $N_{\text{jet}} \geq 2$ category is too small to be used as a control region, and the background is estimated from the predicted inclusive cross sections and MC acceptance alone. Figure 8.9a shows the distribution of $|y_{\ell\ell}|$ in the $N_{\text{jet}} = 0$ same-sign control region.

$Z/\gamma^* \to \tau\tau$

The $Z/\gamma^* \to \tau\tau$ background normalisation is derived from control regions, while the small contributions from $Z/\gamma^* \to ee$ and $Z/\gamma^* \to \mu\mu$, including $Z\gamma$, are estimated from MC simulation and the predicted cross sections, as described in Section 8.4. Separation from the SR is achieved by inverting the requirements on $\Delta\phi_{\ell\ell}$ and $m_{\tau\tau}$ as detailed in Table 8.4. Figure 8.9b shows the distribution of $p_{\mathrm{T}}^{\mathrm{H}}$ in the $Z/\gamma^* \to \tau\tau$ control region with $N_{\mathrm{jet}} \geq 2$.

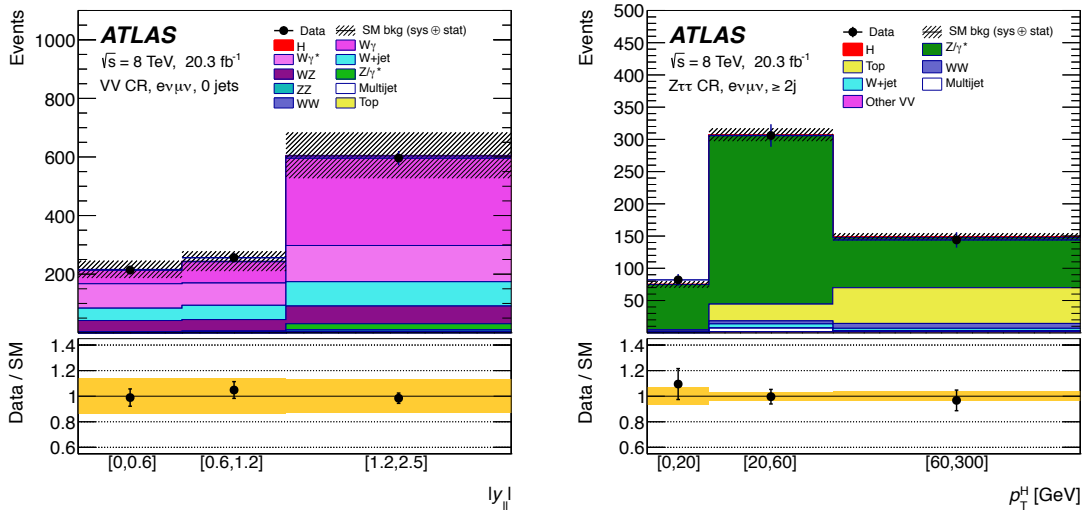

(a) $|y_{\ell\ell}|$, $N_{\mathrm{jet}} = 0$ VV CR **(b)** $p_{\mathrm{T}}^{\mathrm{H}}$, $N_{\mathrm{jet}} \geq 2$ $Z/\gamma^* \to \tau\tau$ CR

Figure 8.9 Distributions of (a) $|y_{\ell\ell}|$ in the $N_{\mathrm{jet}} = 0$ same-sign (VV) CR and (b) $p_{\mathrm{T}}^{\mathrm{H}}$ in the $N_{\mathrm{jet}} \geq 2$ $Z/\gamma^* \to \tau\tau$ CR. The hatched band in the upper plot and the shaded band in the lower plot shows the sum in quadrature of statistical and systematic uncertainties on the prediction. Relevant background normalisation factors have been applied.

Control Regions	WW	Top	$Z/\gamma^* \to \tau\tau$	VV
$N_{\mathrm{jet}} = 0$	1.22 ± 0.03	1.08 ± 0.02	0.99 ± 0.02	0.92 ± 0.07
$N_{\mathrm{jet}} = 1$	1.05 ± 0.05	1.06 ± 0.02	1.06 ± 0.04	0.96 ± 0.12
$N_{\mathrm{jet}} \geq 2$	-	1.05 ± 0.03	1.00 ± 0.09	-

Table 8.5 Background normalisation factors obtained from the control regions, for different background contributions and N_{jet} categories. The uncertainty quoted is the statistical uncertainty.

W + jets

The W + jets background contribution arises from leptonic decays of heavy flavour hadrons and hadronic showers mimicking the leptonic signal final state. The rate of reconstructing fake signal is low but difficult to model in MC. Thus the W + jets background is estimated from data in a control sample, which is selected by changing the lepton isolation requirement of the SR. Of the two lepton candidates, one must satisfy the identification and isolation criteria used to define the signal sample and is denoted as "fully identified". The other ("anti-identified") lepton must fail the nominal selection criteria but satisfy a less restrictive one, thus creating a similar yet orthogonal control sample to the SR, in which about 85% of the events contain a jet that was reconstructed as a lepton [18]. Events in the control sample are required to satisfy all other SR selection criteria.

The W + jets yield in the SR results from the control sample which is scaled by two factors, the *fake-factor* and the *flavour-factor*. The fake-factor is measured in Z + jets data, as the ratio of the number of events with fully-identified leptons to the number with one anti-identified lepton. The Z + jets is similar to W + jets and is more easily identified by reconstructing the di-lepton invariant mass. The fake-factor is measured in bins of anti-identified lepton p_{T} and η. To account for differences in the flavour composition of jets associated with W- and Z-boson production, the flavour-factor is measured from MC simulation, as the ratio of the total W + jets and Z + jets events.

The background due to multijet events is determined similarly to the W + jets background.

Non-ggF Higgs

The yields of the VBF and VH Higgs-boson production modes, and all contributions from H$\rightarrow \tau\tau$, are treated as a background assuming the Standard Model cross section, branching ratio, and acceptance for $m_{\mathrm{H}} = 125$ GeV. The contribution of H$\rightarrow \tau\tau$ events from ggF is negligible. The largest contribution from non-ggF Higgs boson processes is in the $N_{\mathrm{jet}} \geq 2$ category, in which events from VBF and VH amount to half the ggF yield, and constitute about 3% of the total background. All non-ggF Higgs backgrounds are normalised to the SM expectation.

8.7 Reconstructed Yields and Distributions

Following the event selection from Section 8.5 data, signal expectation and background yields are obtained, as the numbers of events passing all of the signal region selection criteria, shown in Table 8.6. The numbers of expected signal and background events contributing to the total are also shown, and all data-driven corrections and normalisation factors are applied. In each category, the background-subtracted number of events is larger than the expected signal by about one standard deviation, defined in terms of the total statistical and systematic uncertainty. The derivation of these uncertainties is discussed in Section 8.10.

	$N_{\text{jet}} = 0$	$N_{\text{jet}} = 1$	$N_{\text{jet}} \geq 2$
ggF H	$125.9 \pm 0.4 \pm 5.7$	$43.4 \pm 0.2 \pm 1.7$	$17.6 \pm 0.2 \pm 1.4$
VBF+VH	$2.2 \pm 0.2 \pm 0.2$	$7.1 \pm 0.3 \pm 0.5$	$8.2 \pm 0.3 \pm 0.4$
WW	$686 \pm 19 \pm 43$	$153 \pm 7 \pm 13$	$44 \pm 1 \pm 11$
WZ/ZZ/Wγ	$88 \pm 3 \pm 12$	$44 \pm 3 \pm 11$	$21.6 \pm 1.6 \pm 3.3$
Top	$60.2 \pm 1.5 \pm 3.8$	$111.2 \pm 2.7 \pm 8.2$	$164 \pm 2 \pm 16$
Z+jets	$8.7 \pm 2.3 \pm 2.3$	$6.2 \pm 1.3 \pm 2.2$	$7.3 \pm 1.5 \pm 2.2$
W+jets	$90 \pm 2 \pm 21$	$33.5 \pm 2.0 \pm 7.6$	$16.9 \pm 1.2 \pm 3.9$
Multijet	$1.3 \pm 0.5 \pm 0.5$	$0.7 \pm 0.2 \pm 0.3$	$0.9 \pm 0.1 \pm 0.4$
Total background	$936 \pm 21 \pm 41$	$355 \pm 9 \pm 12$	$263 \pm 6 \pm 9$
Observed	1107	414	301
Observed − background	$171 \pm 39 \pm 41$	$59 \pm 22 \pm 12$	$38 \pm 18 \pm 9$

Table 8.6 Predicted and observed event yields in the three signal regions. Predicted numbers are given with their statistical (first) and systematic (second) uncertainties evaluated as described in Section 8.10. The "VBF+VH" row also includes the small contribution from $H \to \tau\tau$. The total background in the third-from-last row is the sum of these and all other backgrounds.

The four distributions under study: N_{jet}, p_{T}^{H} (reconstructed as $p_{\text{T}}(\ell\ell p_{\text{T}}^{\text{miss}})$), $|y_{\ell\ell}|$, and $p_{\text{T}}(j_1)$ are shown in Fig. 8.10. The composition of the background is shown, to illustrate how it varies as a function of the quantities being measured. The WW background decreases as a function of the number of jets, and the top-quark background increases, as can also be seen in Table 8.6. In case of p_{T}^{H} and $p_{\text{T}}(j_1)$, the WW background decreases with p_{T} while the top-quark background increases. The background composition does not vary substantially as a function of $|y_{\ell\ell}|$.

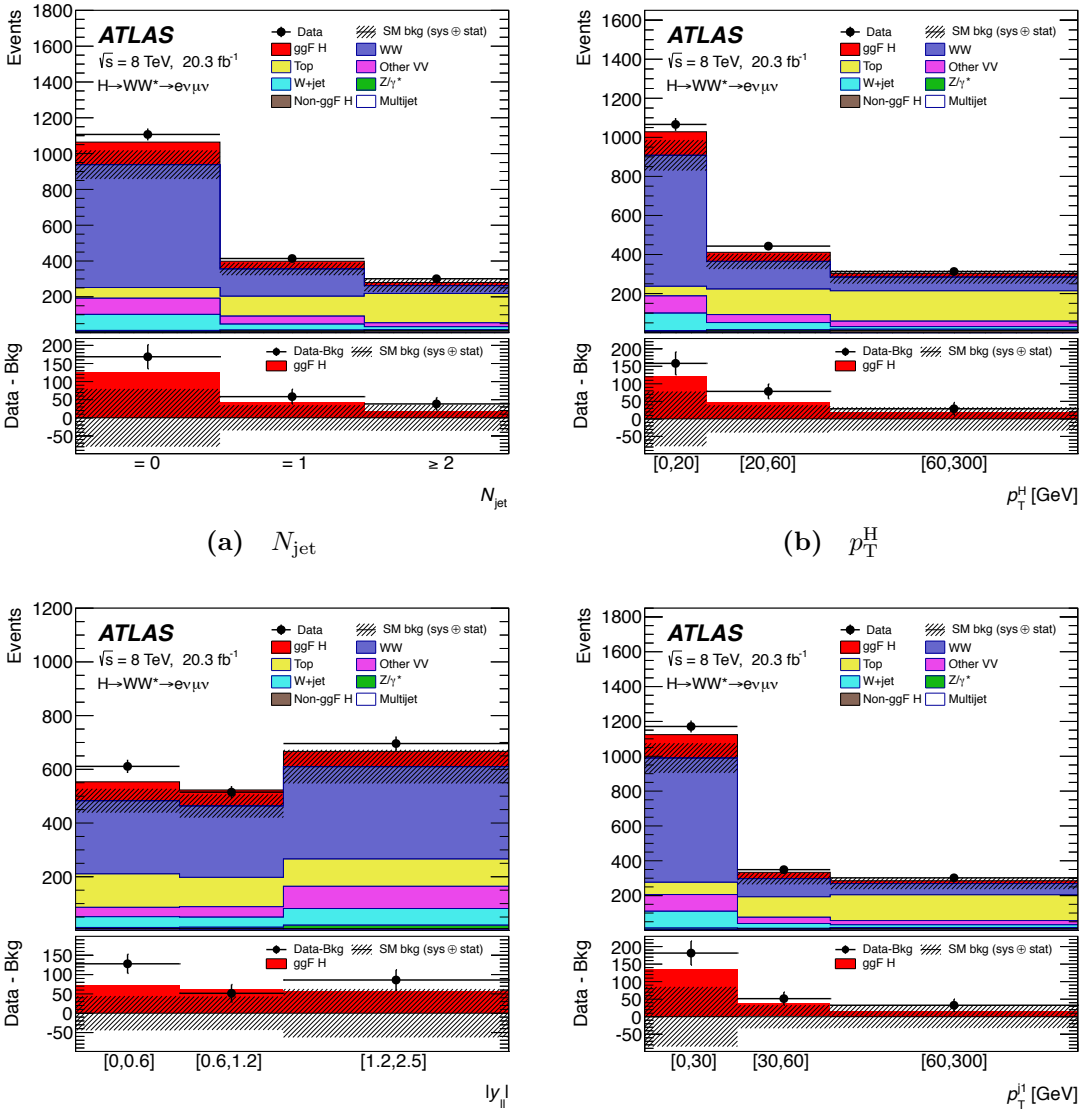

(a) N_{jet} **(b)** p_{T}^{H}

(c) $|y_{\ell\ell}|$ **(d)** $p_{\text{T}}(j_1)$

Figure 8.10 Observed distributions of (a) N_{jet}, (b) p_{T}^{H}, (c) $|y_{\ell\ell}|$, and (d) $p_{\text{T}}(j_1)$ with signal and background expectation, combined over the $N_{\text{jet}} = 0$, $= 1$, and ≥ 2 signal-region categories. The background processes are normalised as described in Section 8.6. The hatched band shows the sum in quadrature of statistical and systematic uncertainties on the sum of the backgrounds.

8.8 Fiducial Region

The reconstructed distributions presented in the previous section are unfolded according to Chapter 7 to correct for detector efficiencies and resolution. The unfolding procedure maps the reconstructed distributions that are measured in the signal region to distributions in a fiducial region, form which the differential cross section results are obtained. The following section defines the fiducial region to which the measurements are extrapolated, while the details of the unfolding are discussed in Section 8.9.

The fiducial selection is designed to replicate the analysis selection described in Section 8.5 as closely as possible at particle-level before the simulation of detector effects. The fiducial selection is performed on the particle-level ggF Higgs boson sample which is then used to construct the response matrix. A selected event has exactly two different-flavour leptons with opposite charge.

In this analysis measurements are performed in three signal-region categories differentiated by the number of jets in the event. In order to present results with events from all categories, the fiducial selection only applies the selection common to all categories and using the leptons and $p_{\mathrm{T}}^{\mathrm{miss}}$ in the final state. The criteria are summarised in Table 8.7.

The fiducial selection is applied to particle-level leptons defined as final-state electrons or muons. Here, electrons or muons from hadron decays and τ decays are rejected. The lepton momenta are corrected by adding the momenta of final-state radiation photons within a cone of $\Delta R < 0.1$ around each lepton. Leptons are required to pass the same kinematic requirements as in the signal region. Also, electrons are removed if they overlap with a selected muon within a cone of $\Delta R(e, \mu) < 0.1$.

The missing transverse momentum $p_{\mathrm{T}}^{\mathrm{miss}}$ is defined as the magnitude of the vector sum of all final-state neutrinos where neutrinos from hadron decays are rejected.

Particle-level jets are reconstructed using the anti-k_{T} algorithm, with a radius parameter of $R = 0.4$. For the clustering, all stable particles with a mean lifetime greater than 30 ps are used, except for electrons, photons, muons, and neutrinos not originating from hadron decays. Selected jets are required to have $p_{\mathrm{T}} > 25$ GeV if $|\eta| < 2.5$ or else $p_{\mathrm{T}} > 30$ GeV if $2.5 \leq |\eta| < 4.5$. Jets are removed if they overlap with a selected electron within $\Delta R(j, e) < 0.3$.

Selected events have passed all preselection introduced in Section 8.5 and the $H \to WW^* \to e\nu\mu\nu$ topology selection on $\Delta\phi_{\ell\ell}$ and $m_{\ell\ell}$. The m_T thresholds are not used to define the fiducial region. The difference in shape of the particle-level and reconstructed m_T shown in Figure 8.11 differ significantly. The distinct 125 GeV cut-off at particle-level is smeared to a smooth tail by reconstruction effects. Requiring a selection cut-off on m_T in the fiducial volume would lead to large migrations from unfolding reconstructed events outside the fiducial region. It would additionally introduce a m_T resolution systematic. Removing the m_T requirement in the fiducial region also increases the selection efficiency ε_i from Equation 7.2.

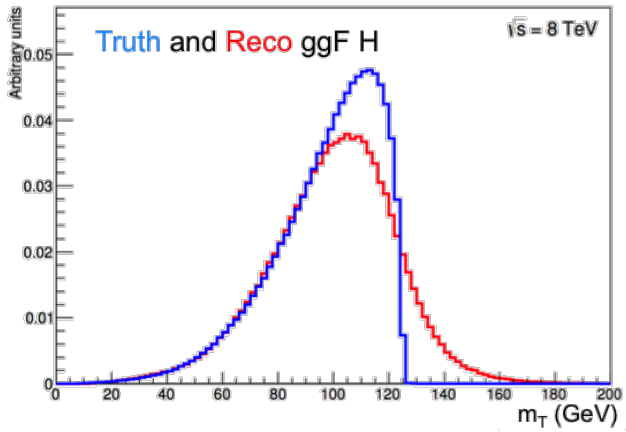

Figure 8.11 Shape comparison of reconstructed (red) and particle-level (blue) m_T for ggF signal MC events passing the reconstruction selection before applying the m_T boundaries.

All selection requirements applied are summarised in Table 8.7. For a SM Higgs boson the acceptance of the fiducial region with respect to the full phase space of $H \to WW^* \to e\nu\mu\nu$ is 11.3%.

Object selection	
Electrons	$p_{\mathrm{T}} > 15$ GeV, $\lvert\eta\rvert < 1.37$ or $1.52 < \lvert\eta\rvert < 2.47$
Muons	$p_{\mathrm{T}} > 15$ GeV, $\lvert\eta\rvert < 2.5$
Jets	$p_{\mathrm{T}} > 25$ GeV if $\lvert\eta\rvert < 2.5$, $p_{\mathrm{T}} > 30$ GeV if $2.5 \leq \lvert\eta\rvert < 4.5$
Event selection	
Preselection	$p_{\mathrm{T}}^{\mathrm{lead}}(\ell) > 22$ GeV
	$m_{\ell\ell} > 10$ GeV
	$p_{\mathrm{T}}^{\mathrm{miss}} > 20$ GeV
Topology	$\Delta\phi_{\ell\ell} < 1.8$
	$m_{\ell\ell} < 55$ GeV

Table 8.7 Summary of selection defining the fiducial region for the cross-section measurements.

8.9 Correction for Detector Effects

The measured distributions shown in Fig. 8.10 are corrected for detector effects and extrapolated to the fiducial region by the Bayesian iterative unfolding described in Chapter 7. A comparison to the bin-by-bin algorithm showed both methods to produce compatible results, see Appendix A.2. The corrections are applied to the individual jet-binned signal-region categories. A two dimensional unfolding is thus performed on $p_{\mathrm{T}}^{\mathrm{H}}$, $|y(\ell\ell)|$ and $p_{\mathrm{T}}(j_1)$ as a function of N_{jet}. This way the bin migration within and between the very differently defined signal regions is treated correctly as well as the correlation of each variable with N_{jet}. Final results corrected for detector effects are presented integrated over all values of N_{jet} in Section 8.12.

As before, each bin of the reconstructed distribution is referred to by the index j, while each bin of the particle-level distribution is referred to by the index i. The migration matrix $(\mathrm{M}^{-1})_{ij}$, selection efficiency ε_i and the fiducial correction factor $f_j^{\text{reco-only}}$ were derived from particle-level and reconstructed MC simulation of the ggF Higgs production process.

First, the relation between the reconstructed distributions in the signal region and the particle-level distribution in the fiducial region, the starting point and endpoint of the unfolding, is investigated for the gluon-fusion Higgs boson production. These distributions are shown in Figure 8.12 as well as in Figure 8.13 for the 2D distributions integrated over N_{jet}. It can be seen that the detector reconstruction shifts the shape of the N_{jet} distribution to lower multiplicities.

For the $p_{\mathrm{T}}(j_1)$ distribution in the $N_{\mathrm{jet}} = 0$ category all events are in the first bin $p_{\mathrm{T}}(j_1) < 30$ GeV by the definition of the jet-p_{T} threshold.

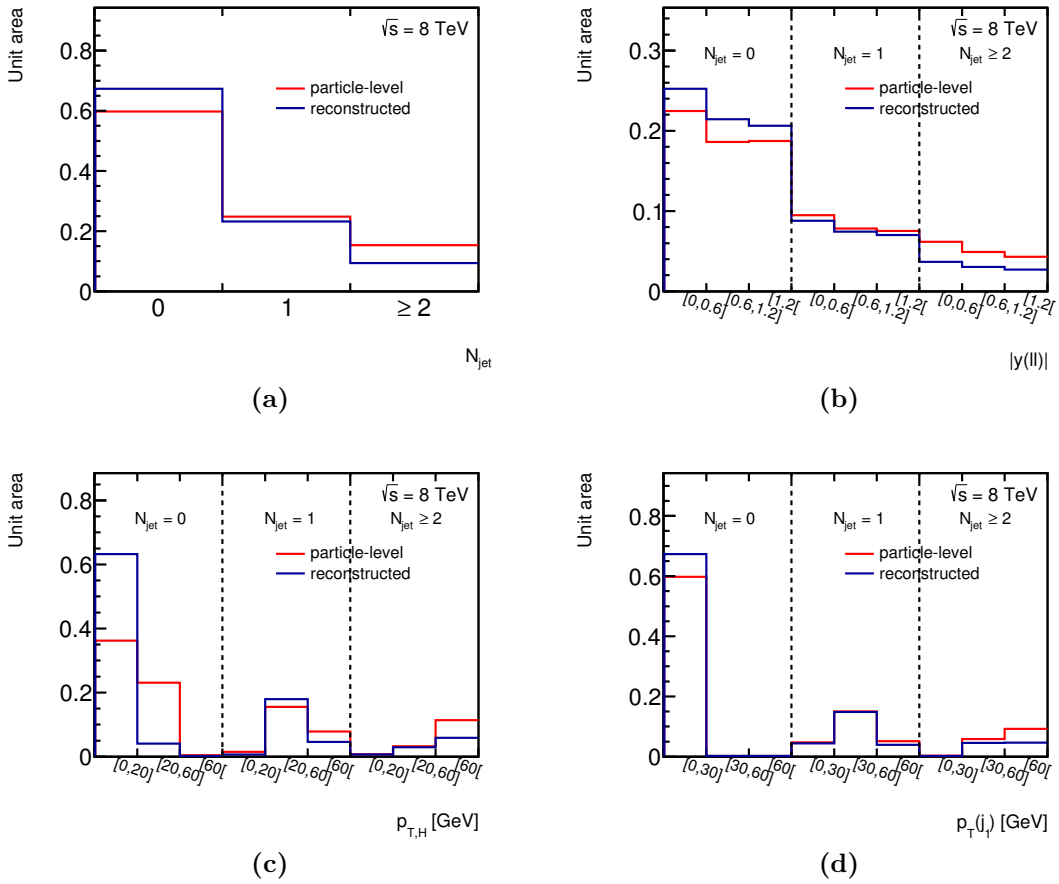

Figure 8.12 Shape comparison of the particle-level distribution in the fiducial volume and the reconstructed distribution in the signal region for the (a) N_{jet}, (b) $|y_{\ell\ell}|$ as a function of N_{jet}, (c) $p_{\mathrm{T}}^{\mathrm{H}}$ as a function of N_{jet}, and (d) $p_{\mathrm{T}}(j_1)$ as a function of N_{jet} distributions as predicted by the gluon-fusion signal MC.

8.9.1 Response Matrix

The migration matrix $(\mathrm{M}^{-1})_{ij}$ is built by relating the variables at reconstruction and particle-level in simulated ggF signal events that pass both the signal-region and fiducial-region selection criteria. To properly account for the migration of events between the different signal-region categories, the migration matrix accounts for the migration within one variable as well as migration between different values of N_{jet}. By using Bayesian iterative unfolding, the significant amount of migration can be accounted for. However, reliable unfolding results

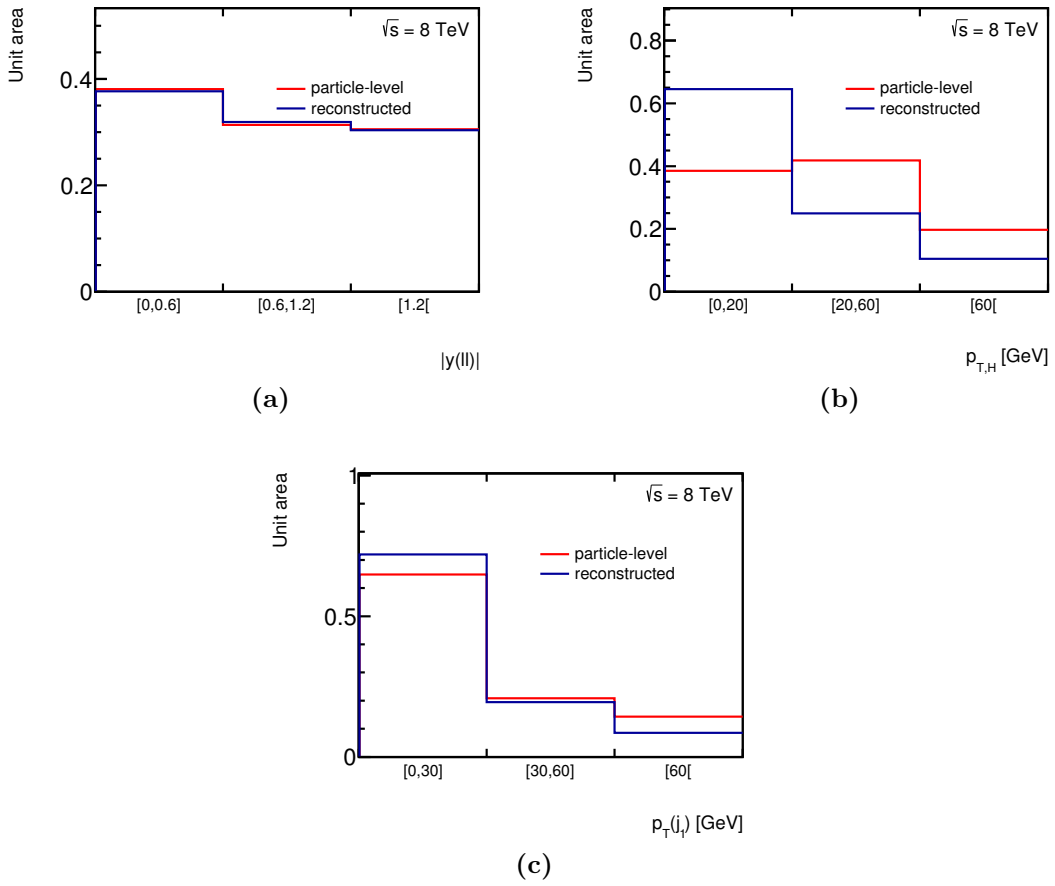

Figure 8.13 Shape comparison of the particle-level distribution in the fiducial volume and the reconstructed distribution in the signal region for the (a) $|y_{\ell\ell}|$, (b) $p_{\mathrm{T}}^{\mathrm{H}}$, and (c) $p_{\mathrm{T}}(j_1)$ distributions integrated over all bins of N_{jet} as predicted by the gluon-fusion signal MC.

depend on a sufficiently low degree of bin-migration. Migration is limited by choosing larger bins in the distribution. Bins were chosen to keep migration below 40%. Figure 8.14 shows the migration matrices for the distributions, constructed from Higgs boson signal Monte Carlo with $m_H = 125$ GeV. The off-diagonal elements that represent bin-to-bin migration are of 30-40%. Thus, a significant amount of migration is present in the observables. Some diagonal bins have an even larger migration, but these bins have a very low expectation of less than 2.5 events.

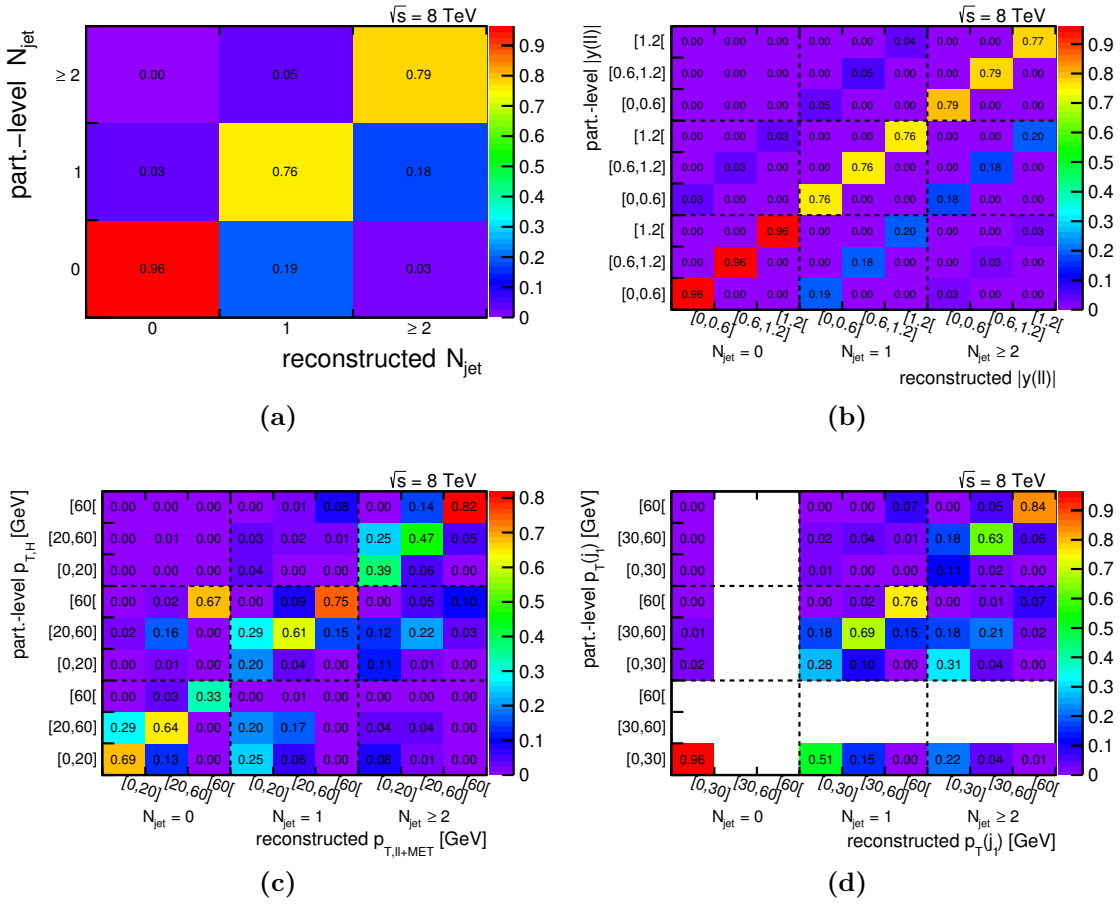

Figure 8.14 Migration matrices relating the particle-level shown on the y axis and the reconstruction level shown on the x axis for the (a) N_{jet}, (b) $|y_{\ell\ell}|$ as a function of N_{jet}, (c) p_{T}^{H} as a function of N_{jet}, and (d) $p_{\text{T}}(j_1)$ as a function of N_{jet} distributions in selected events. The $p_{\text{T}}(j_1)$ for $N_{\text{jet}} = 0$ events is by definition zero and thus only populates the first bin of [0, 30] GeV.

8.9.2 Correction Factors

Events in the fiducial region that are not selected in the signal region and vice-versa are taken into account by the reconstruction efficiency ε_i and the correction factor $f_j^{\text{reco-only}}$ derived from MC simulation.

The reconstruction efficiency ε_i in each bin i of each particle-level variable is defined as the ratio of the event yield where the event is selected by both the fiducial selection at particle-level and the event selection at reconstruction level, over the event yield where the event passes the fiducial event selection. The reconstruction efficiencies are typically in the range of 0.14 to 0.43 and a significant amount of migration is present in the observables. Distributions of ε_i

for each variable are given in Figure 8.15.

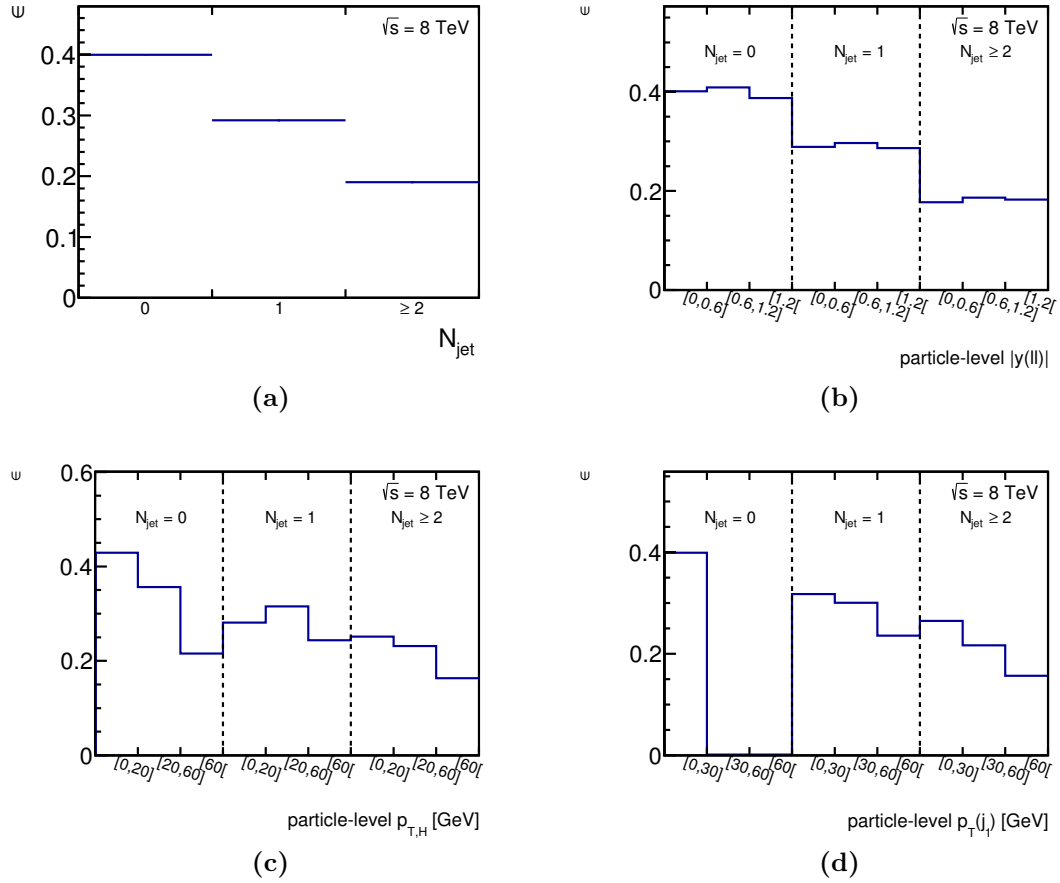

Figure 8.15 Reconstruction efficiencies in each bin of the (a) N_{jet}, (b) $|y_{\ell\ell}|$ as a function of N_{jet}, (c) p_{T}^{H} as a function of N_{jet}, and (d) $p_{\text{T}}(j_1)$ as a function of N_{jet} distribution. The reconstruction efficiency ε_i in each bin i of each variable is defined as the ratio of the particle-level event yield passing the fiducial and the reconstructed event selection over the particle-level event yield passing the fiducial event selection and is evaluated in simulated signal events.

The fiducial correction factor $f_j^{\text{reco-only}}$, in bin j, of the reconstructed distributions is defined as the ratio of events passing both the fiducial and the reconstructed selection, over all reconstructed events. The fiducial correction factors are typically in the range of 0.84 to 0.92. Distributions of $f_j^{\text{reco-only}}$ for each variable are given in Figure 8.16.

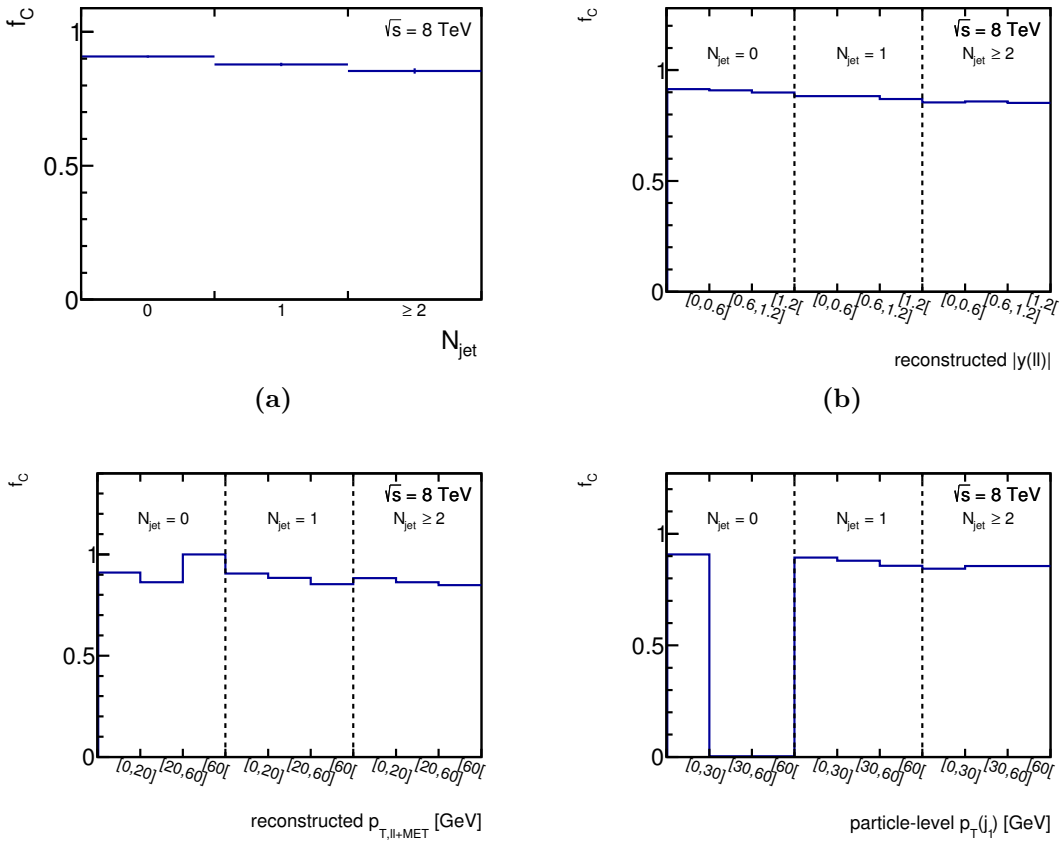

Figure 8.16 Fiducial correction factor in each bin of the (a) N_{jet}, (b) $|y_{\ell\ell}|$ as a function of N_{jet}, (c) p_{T}^{H} as a function of N_{jet}, and (d) $p_{\text{T}}(j_1)$ as a function of N_{jet} distribution. The fiducial correction factor $f_j^{\text{reco-only}}$ in each bin j of each variable is defined as the ratio of the reconstructed signal events in the fiducial region and all reconstructed signal events. It is evaluated in simulated signal events.

8.9.3 Test of the Unfolding Method and its Uncertainties

The performance of the method was tested by unfolding a simulated reconstructed distribution and comparing the outcome to the corresponding particle-level distribution. The following tests were performed to cross check the output of the complex unfolding tools and to calculate the uncertainty in the results obtained.

Closure Test

A closure test establishes the correct working of the unfolding method, by checking if the unfolding recovers the prior used to construct the response matrix. This is constructed from the nominal particle-level and reconstructed MC distributions. The same nominal reconstructed MC distribution is then unfolded and should be identical to the nominal particle-level distribution by definition. A failure of the closure test is indicative of major flaws in the unfolding procedure. The closure test was performed on the unfolding in this analysis. The difference between unfolded reconstructed and particle-level distribution was found to be zero, passing the test.

Model dependent Unfolding Uncertainty

To test the dependence of the results on the similarity of the reconstructed data to the response matrix model, the nominal response matrix is used to unfold toy data that is created by reweighting the reconstructed MC. Each event was reweighted by a first order polynomial in N_{jet}. This reweighted simulated signal is unfolded and compared to the particle-level signal that is modified by the same reweighting. The reweighting can be chosen arbitrarily, but was constructed so that the reweighted reconstructed MC matched the measured data. The reweighting in this case represents a typical difference between our model and the measured data that the unfolding must recover. The difference between unfolded reweighted data and reweighted particle-level data is taken as the uncertainty associated with the unfolding procedure. The resulting uncertainty is smaller than 5% in each measurement bin.

Number of Iterations

Iterative unfolding was performed in order to reduce the model dependence. The number of iterations is governed by the trade-off between reduction in model dependence versus the increase in statistical uncertainty as a function of unfolding iterations. Each iteration sees a correction by data of the unfolding prior, here the prior is particle-level MC in the response matrix. At the same time, each iteration compounds effects of the statistical error on the response matrix. The optimal number of iterations was determined by unfolding toy experiments and

comparing these to the expected particle-level distribution. Toy experiments are constructed from Possion distributions, with a mean given by the MC expectation. It was found that two iterations provided a good trade-off between recovering the expected distribution and increasing statistical errors, see Figure 8.17. The χ^2 per degree of freedom (DoF) for two iterations was found to be $\chi^2/DoF \sim 1$, indicated an appropriate match between the unfolded and expected data [218].

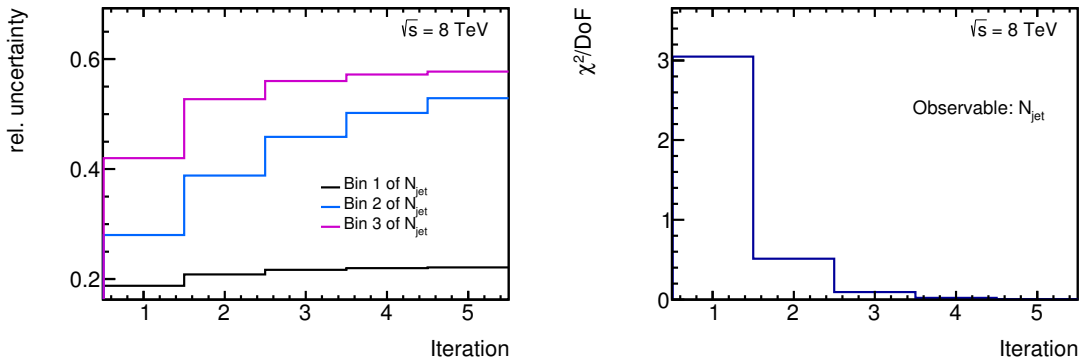

(a) **(b)**

Figure 8.17 (a) The relative uncertainty due to the limited data and MC statistics in each bin of the N_{jet} distribution as a function of the number of unfolding iterations. (b) The χ^2 per degree of freedom as a function of the number of unfolding iterations for the N_{jet} distribution.

8.10 Uncertainty Treatment

Sources of uncertainty on the differential cross sections can be grouped into five categories: statistical uncertainties, experimental systematic uncertainties, theoretical systematic uncertainties on the signal model, theoretical systematic uncertainties on the background model and uncertainties arising from the unfolding procedure.

The effect of each systematic uncertainty is estimated by repeating the full analysis, including the unfolding, for the variation in the signal or individual background. For experimental uncertainties, the migration matrix, reconstruction efficiency, unfolding uncertainties and the background estimation are varied simultaneously. For uncertainties that only apply to the background processes, the nominal migration matrix, reconstruction efficiency, and correction factor are varied.

The total uncertainty on the result from any individual source of uncertainty is taken as the difference between the shifted and the nominal corrected result. The total uncertainty of each measurement bin is defined as the sum in quadrature of all uncertainty components.

8.10.1 Statistical Uncertainties

Statistical uncertainties arise due to the limited size of the data and Monte Carlo samples. The statistical uncertainties on the differential cross sections are estimated using pseudoexperiments.

For the data statistical uncertainty, the content of each bin in the measured distribution is fluctuated according to a Poisson distribution, where the mean is set to the bin content. Values for the data statistical uncertainty are evaluated using 80,000 pseudoexperiments. In each pseudoexperiment the background is subtracted and the correction for detector effects is performed via unfolding. The root-mean square of the spread of the result in each bin is taken as the measure of the statistical uncertainty.

MC samples are generated with a fixed number of events and then normalised to the integrated luminosity of the corresponding data. The size of the generated sample is typically limited by available computing resources and the statistical power of the MC data must be taken into account.

The uncertainty due to the statistics of the background MC samples is evaluated using 50,000 pseudoexperiments. The bin content of the background distributions are fluctuated using a Gaussian distribution with a width corresponding to the statistical uncertainty on that bin. The nominal data is then subtracted by the fluctuated background estimate and unfolded. Again the root-mean square of the spread of the result in each bin is taken as the measure of the statistical uncertainty. This is evaluated for each background sample individually and given in Table 8.8 for the N_{jet} distribution.

The signal MC sample was similarly varied, which affects the bins of the migration matrix, the reconstruction efficiency, and the correction factor in a correlated way. In each pseudoexperiment the correction for detector effects is performed using the respective fluctuated template. The root-mean square of the spread of results of 50,000 pseudoexperiments is taken as the estimator of the uncertainty.

N_{jet}	0[%]	1[%]	≥ 2[%]
WW	3.12	3.92	4.44
VV	2.40	4.81	8.96
$t\bar{t}$	0.61	2.49	8.24
single top	0.39	1.45	2.28
Z+jets	1.04	2.28	5.93
W+jets	1.87	3.51	7.00
Multijet	0.36	0.49	0.64

Table 8.8 Background MC statistical uncertainty on the data−background sum for the N_{jet} distribution.

In the case of results integrated over all values of N_{jet}, each pseudoexperiment is likewise integrated and the uncertainty is re-evaluated for the integrated bin to take into account all correlations arising due to bin migration.

For the normalised results, each pseudoexperiment is also normalised and the uncertainty is re-evaluated for the normalised bin to take into account all correlations arising due to bin migration.

The statistical uncertainty on the background normalisations from the data yields in the control regions is calculated from the square root of the number of events observed. The resulting uncertainties on individual background yields are propagated through to the final results as a single variation rather than by pseudoexperiments.

8.10.2 Experimental Systematic Uncertainties

Experimental systematic uncertainties arise primarily from object calibrations, such as the jet energy scale, and affect the subtracted background normalisation and shape as well as the migration matrix, the reconstruction efficiency, and the correction factor. The values used for the experimental uncertainties are identical to those of Ref. [18] and are summarised here.

The dominant experimental uncertainties are those associated with the jet energy scale and resolution, the lepton identification efficiencies, and the uncertainty on the extrapolation factor used in estimation of the W + jets background. For each uncertainty, the upwards and downward variations are performed separately. Each variation is applied simultaneously to the migration matrix, the reconstruction efficiency, the correction factor, and the background subtraction so

that correlations are correctly preserved. The background-subtracted yields are allowed to assume negative values under the systematic variations. The impact of a given experimental systematic on the measurements is presented together with the results in Section 8.12.

Jet Energy Scale (JES) The JES is a correction for the calorimeter response. It is derived from simulated and measured data and provides an uncertainty on the jet energy. Further contributions arise from modelling and statistical uncertainties on extrapolating the jet calibration to the high-p_T regime, as well as uncertainties in modelling additional energy deposits due to pile-up. The JES uncertainty is in the range of 1-7% as a function of $|\eta|$ and p_T.

Jet Energy Resolution (JER) The jet energy resolution is 5-20%, changing as a function of $|\eta|$ and p_T.

b-tagging The tagging of b-jets is used to veto backgrounds. The b-jet identification efficiency has an uncertainty of 1-8% as a function of p_{T}, while the light-quark jet misidentification is 9-19% and charm-quark jet misidentification is 6-14%. The tagging efficiencies are evaluated using a simulated and measured sample of $t\bar{t}$ pairs, which produces a pure sample of b-jets. A likelihood fit to the samples establishes a correlation between the jet-flavour and jet momentum [219], from which the b-tagging efficiency can be determined. Differences between simulation and data account for further uncertainty contributions.

Pile-up The impact of pile-up on the calorimeter isolation is estimated on an event-by-event basis. Likewise, a correction to jet energies and $\sum E_{\mathrm{T}}$ as a function of primary vertices is made to account for additional energy due to pile-up. The associated uncertainty with this correction arises from the uncertainty in the pile-up model and is calculated by varying the pile-up scale within MC samples.

Leptons Uncertainties in reconstruction, identification, isolation and trigger efficiency of electron and muon objects as well as their momentum scale and resolutions are estimated from Z$\rightarrow ee, \mu\mu$, $J/\phi \rightarrow ee, \mu\mu$ and W$\rightarrow e\nu, \mu\nu$ decays. Efficiencies are determined by *Tag-and-Probe* methods [220, 221]. The electron identification efficiency uncertainty is 0.2-2.7% depending on $|\eta|$ and p_T, the corresponding uncertainty for muons is negligible. The uncertainty on electron and muon isolation is 1.6% and 2.7% respectively. The lepton trigger efficiency uncertainty is less than 1%.

Missing transverse momentum The previous systematic uncertainties all propagate to the calculation of $E_{\mathrm{T}}^{\mathrm{miss}}$. Additional sources of uncertainty arise from the uncertainty in modelling low energy particles which are measured in the calorimeter but have no matching track and are thus not considered a jet. The $E_{\mathrm{T}}^{\mathrm{miss}}$ can be determined with a resolution of 1.5-3.3 GeV and a scale variation of 0.3-1.4 GeV.

Luminosity The cross section is calculated from the number of events and the integrated luminosity by Equation 7.5. The luminosity is measured by ATLAS, see Section 5.7 with an uncertainty of 2.8% for the 8 TeV data (calculated by the method described in Ref. [222]), which directly propagates to the normalisation of cross section measurements.

No particular experimental systematic is dominant in this measurement. The impact on all distributions is given in Section 8.12.

8.10.3 Systematic Uncertainties on the Signal Model

Theoretical uncertainties on the ggF signal can affect the migration matrix, the reconstruction efficiency, and the correction factor. Sources of theoretical uncertainty on the signal model are the choice of QCD renormalisation and factorisation scale, PDF, parton shower/underlying event (PS/UE) model, and matrix element generator. It was shown in Ref. [18], that the theoretical uncertainty on the signal is dominated by the PS/UE model. This uncertainty is evaluated by constructing the migration matrix and performing the unfolding with Powheg-box+Herwig and Powheg-box+Pythia8 and comparing the corrected result. The resulting uncertainty is of the order of a few percent, presented for all distributions in Figure 8.18.

In addition to the difference between signal generators, a complementary uncertainty on the theoretical prediction of the exclusive ggF H + n-jet cross sections is assigned to account for jet modelling. The uncertainty on the exclusive cross sections is evaluated using the jet-veto-efficiency (JVE) description [223, 224] implemented as in Ref. [18]. Here, uncertainties due to renormalisation, factorisation, and resummation scale choices in the analytical calculations are taken into account. The correlation of the uncertainties on the different H + n-jet cross sections is determined using a covariance matrix as described in Ref. [92]. To evaluate the effect of this uncertainty on the migration matrix, the reconstruction

efficiency, and the correction factor, the particle-level N_{jet} distribution in the signal ggF MC sample is reweighted to reproduce the uncertainties on the exclusive cross sections. Then, the reconstructed distribution of the reweighted ggF signal MC sample is unfolded for each variable to evaluate the change arising from the uncertainty on the exclusive ggF H + n-jet cross sections. The contribution of this uncertainty to the differential distributions is of the order of a few percent for variables strongly correlated to N_{jet} such as p_{T}^{H} and negligible for the other variables like $|y_{\ell\ell}|$.

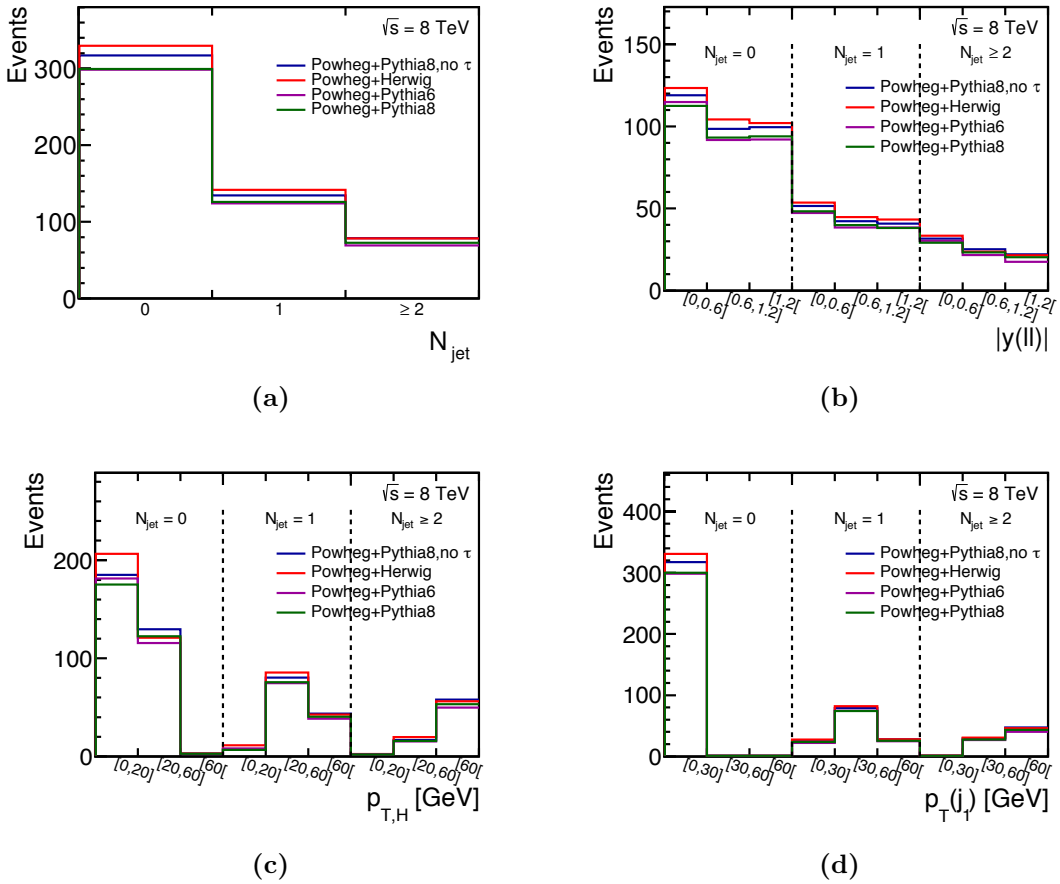

Figure 8.18 Comparison of the particle-level ggF Higgs boson distribution in the fiducial phase space after unfolding for different parton shower models. The POWHEG-BOX+HERWIG line is compared to "POWHEG-BOX+PYTHIA8, no τ", while POWHEG-BOX+PYTHIA6 is compared to "POWHEG-BOX+PYTHIA8". (a) N_{jet}, (b) $|y_{\ell\ell}|$ as a function of N_{jet}, (c) p_{T}^{H} as a function of N_{jet}, and (d) $p_{\text{T}}(j_1)$ as a function of N_{jet} distributions.

8.10.4 Systematic Uncertainties on the Background Model

Systematic uncertainties on the background model arise from choices made in the generation of simulated data. In particular, the modelling of QCD processes, as presented in Chapter 4, relies on a choice of the renormalisation and factorisation scale. Independently, the difference in predictions between generators must be considered. A normalisation uncertainty is established from the variation in estimates from different MC generators. Evaluated in similar fashion, shape uncertainties for the dominant WW and top-quark backgrounds were evaluated in each measured distribution. For backgrounds where the normalisation has been determined using control regions, see Section 8.6, the normalisation uncertainty is applied to both the signal and control regions, and thus partially cancels. The shape uncertainties are applied only on the signal region, after the control region NFs are applied.

The nominal MC sample used to model the WW background yield for the $N_{\text{jet}} = 0$ and $= 1$ categories is Powheg-box+Pythia6. The assessment of theoretical normalisation and shape uncertainties due to scale choices are detailed below. The treatment for $t\bar{t}$ and WW in other N_{jet} categories follows a similar description.

- The QCD renormalisation and factorisation scale, μ_R and μ_F are varied independently in aMC@NLO calculations [87], by a factor of two away from the nominal value $\mu_R = \mu_F = m_{\text{WW}}$. A constraint of $1/2 < \mu_R/\mu_F < 2$ is imposed.
- The choice of the matrix-element generator is evaluated by comparing the nominal Powheg-box to aMC@NLO yields, where both are interfaced with Herwig.
- The choice of the parton-shower and underlying-event models (PS/UE) are compared between the Powheg-box prediction interfaced with either Pythia6 or Herwig. The shape and normalisation are varied simultaneously for the PS/UE and matrix-element-generator uncertainties.
- The PDF uncertainties are derived from the difference between the CT10 and MSTW [225] or NNPDF [226] predictions.

The WW and top normalisation uncertainties are summarised in Table 8.9 and Table 8.10 respectively. It should be noted that the $N_{\text{jet}} = 0$ and $N_{\text{jet}} = 1$ WW uncertainties are directly correlated.

	$N_{\text{jet}} = 0$	$N_{\text{jet}} = 1$	$N_{\text{jet}} \geq 2$
Generator	5.2	1.5	2.7
PS/UE	−1.3	−4.5	-
Scale	−1.1	−1.7	22
PDF	0.6	0.6	9.7

Table 8.9 Theoretical uncertainties (in %) on the WW background normalisation estimate in each signal region. The relative sign between entries in a row indicates correlation or anti-correlation among the $N_{\text{jet}} = 0$ and $N_{\text{jet}} = 1$ signal regions, as a single variation is applied simultaneously to both of them. The $N_{\text{jet}} \geq 2$ uncertainties are treated as uncorrelated.

	$N_{\text{jet}} = 0$	$N_{\text{jet}} = 1$	$N_{\text{jet}} \geq 2$
Generator	−4.1	−3.5	−1.1
PS/UE	−0.6	2.7	4.5
Scale	−1.2	−0.6	−0.8
PDF	0.4	2.2	1.0

Table 8.10 Theoretical uncertainties (in %) on the top-quark background estimate in each signal region. The relative sign between entries in a row indicates correlation or anti-correlation among the signal regions.

Typically WW shape uncertainties were found to be 1–10% for p_{T}^{H} and $p_{\text{T}}(j_1)$, and less than a percent for $|y_{\ell\ell}|$, while the PDF shape uncertainty was negligible. The largest variations observed are from the PS/UE variation on p_{T}^{H} in sparsely-populated bins: 50% for zero-jet events with $p_{\text{T}}^{\text{H}} > 60$ GeV and 30% for one-jet events with $p_{\text{T}}^{\text{H}} < 20$ GeV.

The top shape uncertainties are of 5% or smaller, with the exception of the PS/UE uncertainty on $N_{\text{jet}} = 0$ events with $p_{\text{T}}^{\text{H}} > 60$ GeV, which is about 12%, and the PDF variation between CT10 and NNPDF on the $|y_{\ell\ell}|$ shape of up to 8%.

Very few data or MC-simulated events from the $\text{Z}/\gamma^* \to \tau\tau$ background pass the full event selections, so the theoretical uncertainties are calculated with modified and reduced SR and CR selection, in order for the relevant comparisons to be made with sufficient statistical precision. No shape uncertainty is assessed for the same reason, and the effect of any such uncertainty would be negligible due to the small contribution from this background.

For the VBF $\text{H} \to \text{WW}$ contribution to the signal region, the cross-section

uncertainties from the QCD scale (+2.6% −2.8%) and PDF (±0.2%) are included [50]. These have a negligible effect on the analysis, so additional uncertainties on the VBF acceptance in the ggF phase space are not considered.

The systematic uncertainties on WZ, Wγ, Wγ^*, and other small sources of background are unmodified from Ref. [18], each process has a cross-section uncertainty of 6–8%.

8.11 Theory Predictions

The results of the fiducial cross-section measurements are compared to analytical predictions calculated at parton level and predictions by MC event generators at particle-level. An overview of the ggF predictions used is given in Table 8.11. All predictions are for $m_{\mathrm{H}} = 125.0$ GeV and $\sqrt{s} = 8$ TeV, and all use the CT10 PDF set unless stated otherwise. The used generators are described in Section 4.8.

Total cross-section predictions	
LHC-XS [227]	NNLO+NNLL
Differential cross-section predictions	
JetVHeto [94, 228, 229]	NNLO+NNLL
ST [91]	NNLO
BLPTW [92]	NNLO+NNLL
STWZ [93]	NNLO+NNLL'
N3LO+NNLL+LL_R [230]	N3LO+NNLL+LL_R
Monte Carlo event generators	
Powheg-box NNLOPS [85, 86]	NNLO$_{\geq 0j}$, NLO$_{\geq 1j}$
Sherpa 2.1.1 [72–76]	H+0, 1, 2 jets @NLO
MG5_aMC@NLO [87–89]	H+0, 1, 2 jets @NLO

Table 8.11 Summary of the ggF predictions used in comparison with the measured fiducial cross sections. LHC-XS refers to the LHC Higgs cross section working group, which provides global averages on Higgs cross section predictions.

The default prediction for the inclusive cross section of ggF Higgs-boson production follows the recommendation of the LHC cross-section working group (LHC-XS) [227], which serves as a comparison to the measured total fiducial cross section.

Particle-level predictions for the measured differential cross sections are provided

by MC event generators. The most precise prediction for inclusive ggF production is given by POWHEG-BOX NNLOPS, that is accurate to NNLO for the inclusive production and to NLO for the inclusive H+1-jet production, including an NNLO calculation of the Higgs-boson rapidity. The sample is generated using the CT10nnlo PDF set [231] and is interfaced to PYTHIA8 for parton showering. The calculation of the uncertainties is given in Ref. [85].

Another ggF MC prediction is generated from the combination of Refs. [72–76, 232] interfaced with SHERPA, resulting in H+1-jet and H+2-jets inclusive production cross-sections at NLO accuracy, the H+3-jets cross section is generated at LO accuracy.

A similar NLO-merged H+0, 1, 2 jets sample is generated with MG5_aMC@NLO [87–89]. MG5_aMC@NLO is interfaced to PYTHIA8 for parton showering. QCD scale, merging scale and variations of the CT10 PDF set are assigned as uncertainties.

An additional parton-level prediction for the N_{jet} distribution is given by the BLPTW method [92], combining the NNLO+NNLL accurate H+0-jet and the NLO+NLL accurate H+1-jet cross sections.

For the efficiency, ε_0, of the jet veto, derived from the N_{jet} and $p_{\text{T}}(j_1)$ distributions and presented in Section 8.12, a parton-level prediction is calculated at NNLO+NNLL accuracy by JetVHeto [94, 228, 229]. The uncertainty is taken as the maximum effect of the scale variations on the calculation, or the maximum deviation of the other calculations from this one. An improved prediction for ε_0 is given by the STWZ calculation [93]. The calculation has NNLO accuracy and is matched to a resummation at NNLL that accounts in addition for the correct boundary conditions for the NNLL resummation. This calculation also predicts the spectrum of $p_{\text{T}}(j_1)$. Another parton-level prediction of ε_0 follows the Stewart-Tackmann (ST) prescription [91] utilising the total inclusive ggF cross section at NNLO accuracy in QCD and the inclusive H+1-jet cross section at NLO accuracy, calculated with HNNLO [90, 233, 234]. Recently, a prediction for the jet-veto efficiency ε_0 has become available at N3LO+NNLL accuracy [230].

All parton-level predictions are corrected to the particle-level to allow comparison to data using the acceptance of the fiducial region and non-perturbative correction factors to account for the impact of hadronisation and underlying event activity. These factors are determined using POWHEG-BOX NNLOPS+PYTHIA8 [85, 86] with the associated uncertainties from the renormalisation and factorisation scales as well as the PDFs. An uncertainty is assigned to the non-perturbative correction

by comparing PYTHIA8 with HERWIG. All factors are given in Appendix A.

8.12 Results and Comparison

The fiducial cross section measurements in the channel $gg \to \mathrm{H} \to \mathrm{WW}^* \to \mathrm{e}\nu\mu\nu$ are presented and compared to theory predictions. Differential cross sections were determined as a function of N_{jet}, $p_{\mathrm{T}}^{\mathrm{H}}$, $|y_{\ell\ell}|$ and $p_{\mathrm{T}}(j_1)$, which are also presented as normalised distributions. The jet-veto efficiency was calculated from the normalised N_{jet} and $p_{\mathrm{T}}(j_1)$ distributions.

All cross sections measured in the fiducial region are of ggF produced Higgs bosons and implicitly include the branching ratio $\mathrm{H} \to \mathrm{WW}^* \to \mathrm{e}\nu\mu\nu$ from the definition of the fiducial selection.

The total fiducial cross section of ggF Higgs-boson production was measured to be:

$$\begin{aligned}\sigma_{\mathrm{ggF}}^{\mathrm{fid}} &= 36.0 \pm 7.2(\mathrm{stat}) \pm 6.4(\mathrm{sys}) \pm 1.0(\mathrm{lumi})\ \mathrm{fb} \\ &= 36.0 \pm 9.7\ \mathrm{fb}\end{aligned}$$

where (stat) includes all statistical uncertainties from the signal and control regions, and (sys) refers to the sum in quadrature of the experimental and theoretical systematic uncertainties. The mass of the Higgs boson is assumed to be $m_H = 125.0$ GeV. The fiducial cross section is calculated from the number of events after the event selection and detector corrections, using an integrated luminosity of 20.3 fb^{-1} with an associated uncertainty of 2.8%. The uncertainty on the integrated luminosity is derived following the same methodology as in Ref. [235]. More details on the sources of systematic uncertainty are given in Table 8.12.

The uncertainty categories used in this and all tables in this section are as follows. Statistical uncertainties are quoted separately for the signal region data, the control region data, and the MC simulated events. Experimental uncertainties ("Exp.") are grouped according to the reconstructed object they effect. The "Exp. other" category includes uncertainties in the modelling of pile-up events, electrons from conversions, and the modelling of the p_{T} of Z bosons with $N_{\mathrm{jet}} = 0$. Theory uncertainties are grouped by process, with the subdominant background uncertainties collected in the "Theory other Bkg" line.

The "Detector corrections" line gives the effect of the use of the ggF signal MC sample to construct the migration matrix, as described in Section 8.9.

Source	$\Delta\sigma^{\text{fid}}_{\text{ggF}}/\sigma^{\text{fid}}_{\text{ggF}}$ [%]
Data statistical	17
MC statistical	3.0
CR data statistical	9.9
Exp. JER	4.9
Exp. JES	2.1
Exp. b-tag	3.3
Exp. leptons	5.5
Exp. $p_{\text{T}}^{\text{miss}}$	2.2
Exp. other	4.2
Theory WW	14
Theory top	7.1
Theory other BG	5.6
Theory signal	2.5
Detector corrections	0.4
Total	27

Table 8.12 Relative uncertainties (in %) on the measured total fiducial cross section.

The prediction of the fiducial cross section is given by the LHC-XS calculation as

$$\text{LHC-XS: } \sigma^{\text{fid}}_{\text{ggF}} = 25.1^{+1.8}_{-2.0}(\text{scale})^{+1.9}_{-1.7}(\text{PDF})\ \text{fb} = 25.1 \pm 2.6\ \text{fb}.$$

The dependence of the cross-section measurement on m_{H} is mainly due to acceptance effects and is approximated by a linear function, which is sufficient within the experimental uncertainties on the Higgs boson mass. The function is determined using dedicated signal samples with different values of m_{H} and has a slope of -0.20 fb/GeV.

8.12.1 Differential Fiducial Cross Sections

Differential fiducial cross sections are measured as a function of the N_{jet}, p_{T}^{H}, $|y_{\ell\ell}|$ and $p_{\text{T}}(j_1)$ distributions. For the p_{T}^{H}, $|y_{\ell\ell}|$ and $p_{\text{T}}(j_1)$ distributions, the cross sections are measured in separate bins of N_{jet} to fully take correlations into account between the different N_{jet} categories and the variable itself. After

applying the detector corrections the distributions are integrated over N_{jet}, and the uncertainties are combined accounting for correlations. The measured differential fiducial cross sections as a function of N_{jet}, p_{T}^{H}, $|y_{\ell\ell}|$, and $p_{\text{T}}(j_1)$ are given in Tables 8.13–8.16, together with a summary of the associated uncertainties.

Figure 8.19 shows the differential cross sections as a function of N_{jet}, p_{T}^{H}, $|y_{\ell\ell}|$, and $p_{\text{T}}(j_1)$. The results are compared to particle-level predictions of ggF Higgs-boson production by Powheg-box NNLOPS, Sherpa, and MG5_aMC@NLO that are generated as described in Section 8.11 and normalised to the cross section prediction calculated by LHC-XS. In addition, the results for the N_{jet} distribution are compared to the parton-level BLPTW calculation, and the results for the $p_{\text{T}}(j_1)$ distribution are compared to the parton-level STWZ calculation. The ratios of the results to the predictions are given in the sub-panel of each figure. The measured distributions agree with the predictions within the uncertainties, except for some tension in $|y_{\ell\ell}|$, where the data prefer lower $|y_{\ell\ell}|$ than the predictions. The statistical and systematic uncertainties are comparable for most bins, and the dominant systematic uncertainties are from the background model, in particularly on the top quark and WW production, although uncertainties on the experimental inputs are non-negligible.

8.12.2 Normalised Differential Fiducial Cross Sections

To reduce the impact of systematic uncertainties, normalised differential cross sections $1/\sigma \cdot (d\sigma/dX_i)$ are calculated by dividing the differential cross section by the total fiducial cross section evaluated by integrating over all bins of variable X. Normalising brings partial cancellation in the experimental and theoretical uncertainty terms. Normalisation uncertainties are reduced, but shape uncertainties are unchanged. The relative statistical uncertainties are also reduced, as these are correlated across bins due to the unfolding.

The normalised differential cross sections as a function of N_{jet}, p_{T}^{H}, $|y_{\ell\ell}|$, and $p_{\text{T}}(j_1)$ are given in Tables 8.17–8.20, along with details of the associated uncertainties. The same distributions are shown in Figure 8.20 compared to particle-level predictions of ggF Higgs-boson production by Powheg-box NNLOPS, Sherpa, and MG5_aMC@NLO, that are generated as described in Section 8.11. In each figure, the ratio of the result to the predictions is shown below the distribution.

N_{jet}	0	1	≥ 2
$d\sigma/dN_{\text{jet}}$ [fb]	19.0	8.2	8.8
Statistical uncertainty [fb]	4.5	3.5	5.0
Total uncertainty [fb]	6.8	4.0	5.9
in [%]:			
Data statistical	20	38	54
MC statistical	4	7	9
CR data statistical	12	18	14
Exp. JER	5	4	7
Exp. JES	1	10	6
Exp. b-tag	1	4	8
Exp. leptons	6	6	6
Exp. $p_{\text{T}}^{\text{miss}}$	2	4	4
Exp. other	5	4	3
Theory WW	24	15	5
Theory top	2	4	24
Theory other BG	5	6	21
Theory signal	4	6	3
Detector corrections	0	4	5
Total	36	48	67

Table 8.13 Differential fiducial cross section in femtobarn as a function of N_{jet} with the uncertainties for each bin given in absolute values and in percent.

$p_{\mathrm{T}}^{\mathrm{H}}$ [GeV]	$[0, 20]$	$[20, 60]$	$[60, 300]$
$d\sigma/dp_{\mathrm{T}}^{\mathrm{H}}$ [fb/GeV]	0.61	0.39	0.034
Statistical uncertainty [fb/GeV]	0.16	0.09	0.021
Total uncertainty [fb/GeV]	0.29	0.15	0.027
in [%]:			
Data statistical	22	22	60
MC statistical	4	4	10
CR data statistical	13	5	18
Exp. JER	7	4	16
Exp. JES	6	10	17
Exp. b-tag	2	4	8
Exp. leptons	7	6	7
Exp. $p_{\mathrm{T}}^{\mathrm{miss}}$	9	8	7
Exp. other	7	4	4
Theory WW	31	17	13
Theory top	4	7	25
Theory other BG	6	8	14
Theory signal	14	1	6
Detector corrections	0	3	3
Total	47	37	77

Table 8.14 Differential fiducial cross section in femtobarn as a function of $p_{\mathrm{T}}^{\mathrm{H}}$ with the uncertainties for each bin given in absolute values and in percent.

$\lvert y_{\ell\ell}\rvert$	$[0.0, 0.6]$	$[0.6, 1.2]$	$[1.2, 2.5]$
$d\sigma/d\lvert y_{\ell\ell}\rvert$ [fb]	31	9.5	9.5
Statistical uncertainty [fb]	7.3	5.0	3.5
Total uncertainty [fb]	10	6.5	5.2
in [%]:			
Data statistical	22	52	33
MC statistical	3	9	6
CR data statistical	9	1	16
Exp. JER	4	10	4
Exp. JES	5	9	6
Exp. b-tag	3	4	5
Exp. leptons	4	10	9
Exp. $p_{\mathrm{T}}^{\mathrm{miss}}$	3	8	4
Exp. other	4	8	6
Theory WW	15	31	20
Theory top	12	14	8
Theory other BG	3	7	17
Theory signal	4	6	3
Detector corrections	0	0	1
Total	33	69	53

Table 8.15 Differential fiducial cross section in femtobarn as a function of $|y_{\ell\ell}|$ with the uncertainties for each bin given in absolute values and in percent.

$p_{\mathrm{T}}(j_1)$ [GeV]	$[0, 30]$	$[30, 60]$	$[60, 300]$
$d\sigma/dp_{\mathrm{T}}(j_1)$ [fb/GeV]	0.69	0.26	0.034
Statistical uncertainty [fb/GeV]	0.16	0.10	0.021
Total uncertainty [fb/GeV]	0.24	0.13	0.025
in [%]:			
Data statistical	19	40	61
MC statistical	3	7	10
CR data statistical	12	2	18
Exp. JER	4	6	10
Exp. JES	2	14	15
Exp. b-tag	1	8	10
Exp. leptons	6	6	8
Exp. $p_{\mathrm{T}}^{\mathrm{miss}}$	2	6	4
Exp. other	5	5	4
Theory WW	23	12	14
Theory top	2	13	23
Theory other BG	5	13	13
Theory signal	5	4	3
Detector corrections	0	0	0
Total	34	51	75

Table 8.16 Differential fiducial cross section in femtobarn as a function of $p_{\mathrm{T}}(j_1)$ with the uncertainties for each bin given in absolute values and in percent.

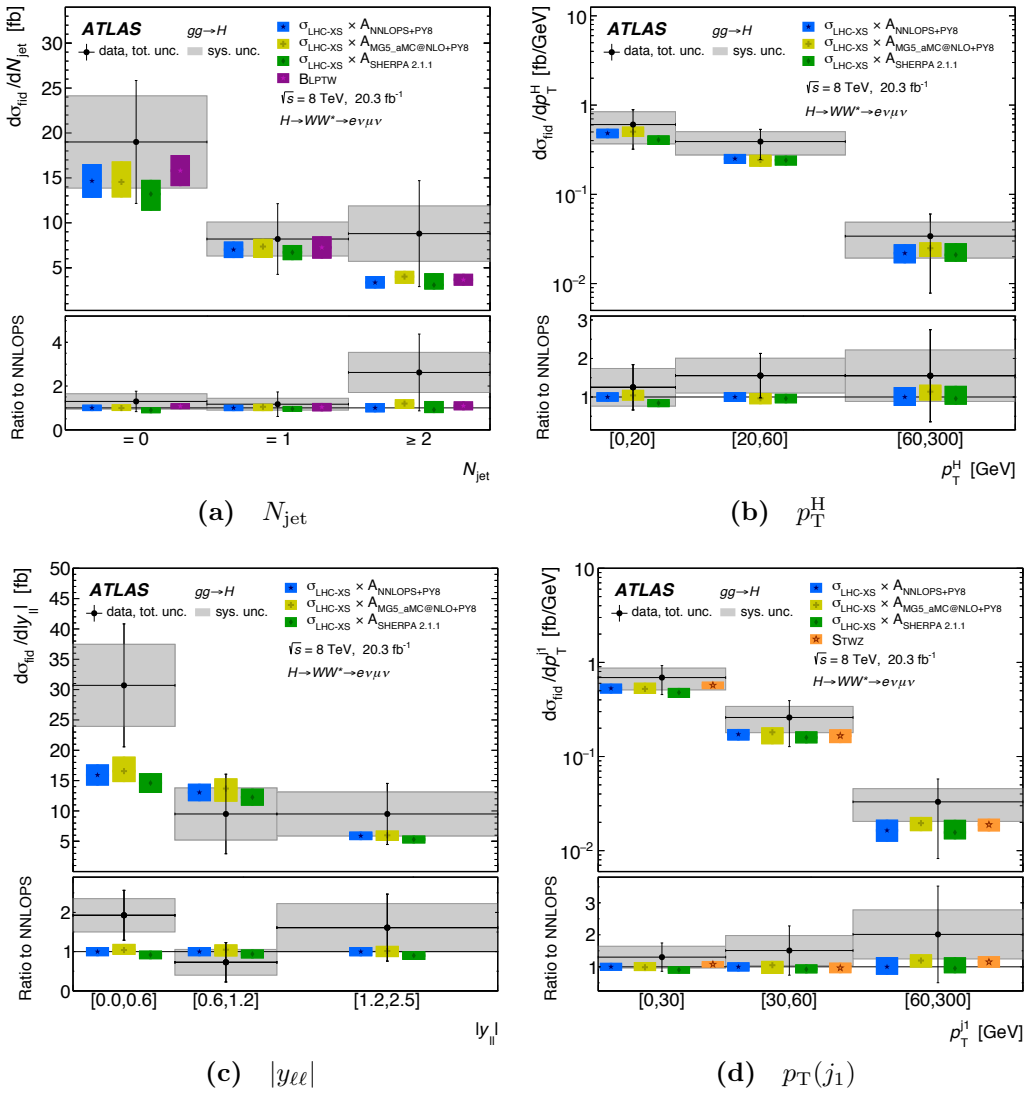

(a) N_{jet} **(b)** p_{T}^{H}

(c) $|y_{\ell\ell}|$ **(d)** $p_{\text{T}}(j_1)$

Figure 8.19 Observed fiducial differential cross section as a function of (a) N_{jet}, (b) p_{T}^{H}, (c) $|y_{\ell\ell}|$, and (d) $p_{\text{T}}(j_1)$, overlaid with the signal predictions. The $[0, 30]$ GeV bin of the $p_{\text{T}}(j_1)$ distribution corresponds to events without jets above 30 GeV. The systematic uncertainty on each point is shown by a grey band labeled "syst. unc." and includes the experimental and theoretical uncertainties. The uncertainty bar, labeled "data, tot. unc." is the total uncertainty and includes all systematic and statistical uncertainties. The measured results are compared to various theoretical predictions.

N_{jet}	0	1	≥ 2
$1/\sigma \; d\sigma/dN_{\text{jet}}$	0.53	0.23	0.24
Statistical uncertainty	0.11	0.09	0.12
Total uncertainty	0.14	0.10	0.14
in [%]:			
Data statistical	19	34	42
MC statistical	4	8	17
CR data statistical	9	16	14
Exp. JER	0	1	2
Exp. JES	3	7	4
Exp. b-tag	3	3	5
Exp. leptons	2	2	4
Exp. $p_{\text{T}}^{\text{miss}}$	1	4	4
Exp. other	2	2	3
Theory WW	12	15	17
Theory top	7	5	18
Theory other BG	6	5	16
Theory signal	1	3	5
Detector corrections	0	4	4
Total	26	43	57

Table 8.17 Normalised differential fiducial cross section as a function of N_{jet} with the uncertainties for each bin given in absolute values and in percent.

$p_{\mathrm{T}}^{\mathrm{H}}$ [GeV]	$[0, 20]$	$[20, 60]$	$[60, 300]$
$1/\sigma \; d\sigma/dp_{\mathrm{T}}^{\mathrm{H}}$ [10^{-3}GeV^{-1}]	17.0	11.0	0.96
Statistical uncertainty [10^{-3}GeV^{-1}]	3.5	2.0	0.50
Total uncertainty [10^{-3}GeV^{-1}]	6.0	3.4	0.63
in [%]:			
Data statistical	20	18	48
MC statistical	4	3	8
CR data statistical	8	7	18
Exp. JER	2	4	11
Exp. JES	8	9	16
Exp. b-tag	4	4	6
Exp. leptons	3	2	5
Exp. $p_{\mathrm{T}}^{\mathrm{miss}}$	10	8	7
Exp. other	4	2	4
Theory WW	19	15	21
Theory top	9	8	17
Theory other BG	7	8	12
Theory signal	10	2	10
Detector corrections	0	3	3
Total	37	31	65

Table 8.18 Normalised differential fiducial cross section as a function of $p_{\mathrm{T}}^{\mathrm{H}}$ with the uncertainties for each bin given in absolute values and in percent.

$\lvert y(\ell\ell)\rvert$	$[0.0, 0.6]$	$[0.6, 1.2]$	$[1.2, 2.5]$
$1/\sigma\ d\sigma/d\lvert y(\ell\ell)\rvert$	0.83	0.27	0.26
Statistical uncertainty	0.17	0.13	0.08
Total uncertainty	0.22	0.15	0.11
in [%]:			
Data statistical	18	48	26
MC statistical	3	8	5
CR data statistical	7	6	14
Exp. JER	2	5	2
Exp. JES	4	9	7
Exp. b-tag	3	5	5
Exp. leptons	3	5	5
Exp. $p_{\mathrm{T}}^{\mathrm{miss}}$	3	7	4
Exp. other	3	6	5
Theory WW	11	21	18
Theory top	10	15	9
Theory other BG	5	8	17
Theory signal	0	2	1
Detector corrections	0	0	0
Total	27	60	43

Table 8.19 Normalised differential fiducial cross section as a function of $|y_{\ell\ell}|$ with the uncertainties for each bin given in absolute values and in percent.

$p_{\mathrm{T}}(j_1)$ [GeV]	$[0, 30]$	$[30, 60]$	$[60, 300]$
$1/\sigma\ d\sigma/dp_{\mathrm{T}}(j_1)$ [$10^{-3}\mathrm{GeV}^{-1}$]	19.0	7.0	0.91
Statistical uncertainty [$10^{-3}\mathrm{GeV}^{-1}$]	3.7	2.7	0.51
Total uncertainty [$10^{-3}\mathrm{GeV}^{-1}$]	4.7	3.3	0.58
in [%]:			
Data statistical	17	36	49
MC statistical	3	6	9
CR data statistical	7	8	18
Exp. JER	2	3	5
Exp. JES	3	13	14
Exp. b-tag	3	7	9
Exp. leptons	2	3	5
Exp. $p_{\mathrm{T}}^{\mathrm{miss}}$	1	6	4
Exp. other	2	3	5
Theory WW	11	17	17
Theory top	7	9	18
Theory other BG	5	11	11
Theory signal	2	2	5
Detector corrections	0	0	0
Total	24	47	63

Table 8.20 Normalised differential cross section as a function of $p_{\mathrm{T}}(j_1)$ with the uncertainties for each bin given in absolute values and in percent.

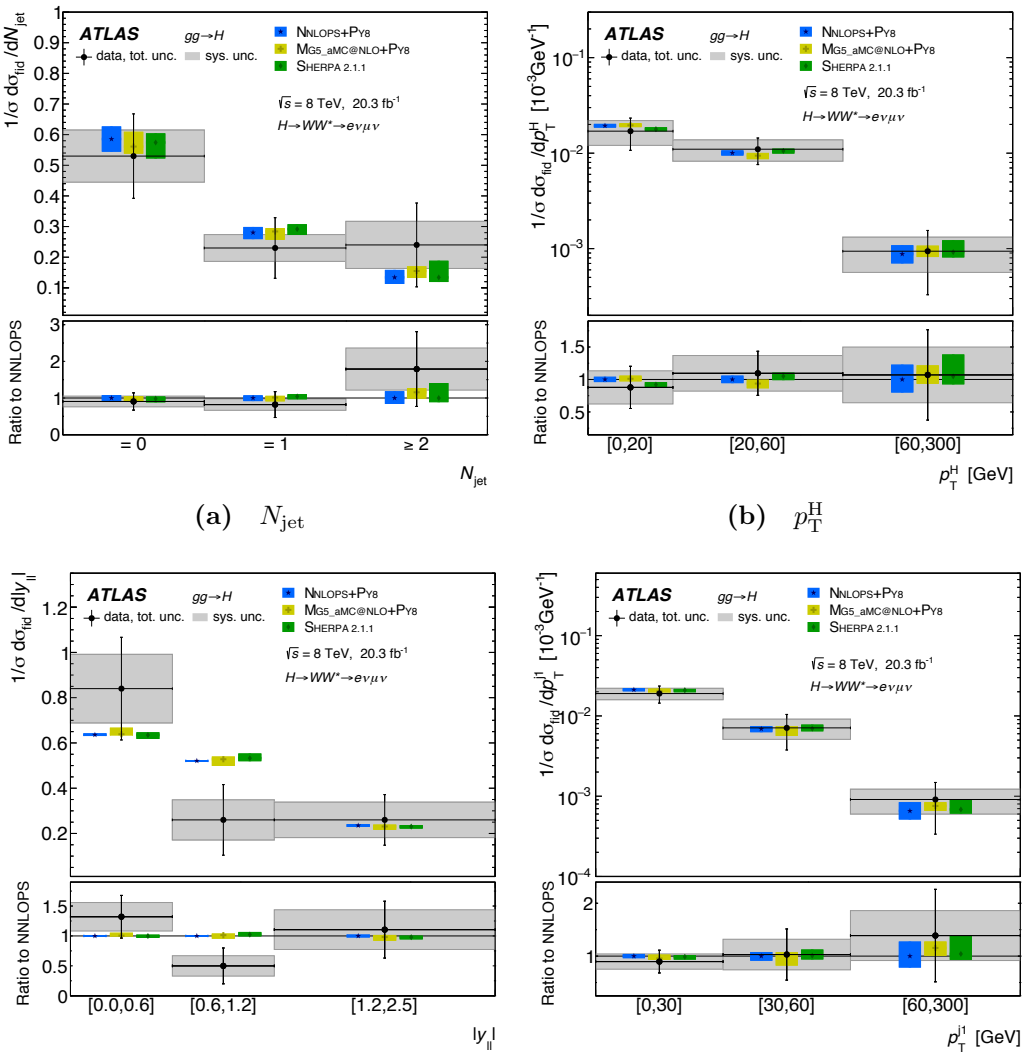

(a) N_{jet} **(b)** p_{T}^{H}

(c) $|y_{\ell\ell}|$ **(d)** $p_{\text{T}}(j_1)$

Figure 8.20 Normalised fiducial differential cross section as a function of (a) N_{jet}, (b) p_{T}^{H}, (c) $|y_{\ell\ell}|$, and (d) $p_{\text{T}}(j_1)$, overlaid with the signal predictions. The $[0, 30]$ GeV bin of the $p_{\text{T}}(j_1)$ distribution corresponds to events without jets above 30 GeV. The systematic uncertainty on each point is shown by a grey band labelled "syst. unc." and includes the experimental and theoretical uncertainties. The uncertainty bar, labelled "data, tot. unc." is the total uncertainty and includes all systematic and statistical uncertainties. The measured results are compared to various theoretical predictions.

8.12.3 Jet Veto Efficiency

The jet veto efficiency ε_0 for the H+0-jet events is defined at particle-level as the fraction of events in the fiducial phase space with the leading particle-level jet below a given threshold. This is measured, in practice, using the leading-jet p_{T} distribution, since the lowest-p_{T} bin will be exactly the fraction of events with the leading jet below the threshold defining the upper bin edge. The jet veto efficiency for the jet selection used in the analysis, 25 GeV for central jets ($|\eta| < 2.5$) and 30 GeV for forward jets ($2.5 < |\eta| < 4.5$), corresponds to the $N_{\mathrm{jet}} = 0$ fraction from the normalised differential cross section measured as a function of N_{jet} (see Table 8.17). Results for the analysis jet selection, and thresholds of 30 GeV and 40 GeV, are given in Table 8.21 and compared to predictions in Figure 8.21. The predictions are calculated with JetVHeto, ST, STWZ, N3LO+NNLL+LL_R, and POWHEG-BOX NNLOPS as described in Section 8.11. The results are in excellent agreement with the predictions within uncertainties. The precision of measurement is limited by statistical uncertainties.

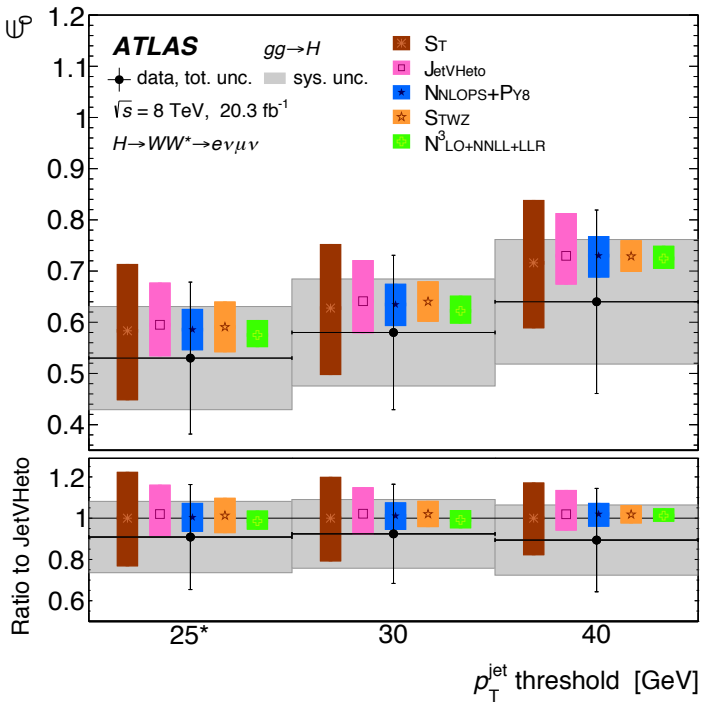

Figure 8.21 Measured jet veto efficiency as a function of the jet p_{T} threshold, compared to predictions. The asterisk on the 25 GeV bin label indicates that the results are for a mixed p_{T} threshold, which is raised from 25 GeV to 30 GeV for jets with $2.5 < |\eta| < 4.5$, corresponding to the selection used to define the signal regions for the analysis. The total uncertainty includes all statistical, experimental, and theoretical uncertainties.

jet p_{T} threshold	25 GeV*	30 GeV	40 GeV
ε_0	0.53	0.57	0.64
Statistical uncertainty	0.11	0.11	0.12
Total uncertainty	0.14	0.14	0.17
in [%]:			
Data statistical	19	17	17
MC statistical	4	3	3
CR data statistical	9	7	8
Exp. JER	0	2	3
Exp. JES	3	3	5
Exp. b-tag	3	3	4
Exp. leptons	2	2	2
Exp. $p_{\mathrm{T}}^{\mathrm{miss}}$	1	1	1
Exp. other	2	2	5
Theory WW	12	11	12
Theory top	7	7	9
Theory other BG	6	5	8
Theory signal	1	2	2
Detector corrections	0	0	0
Total	26	24	27

Table 8.21 Measured jet veto efficiency ϵ_0 for different jet p_{T} thresholds given with absolute and relative uncertainties. The asterisk for the 25 GeV column header indicates that the results are for a mixed p_{T} threshold, which is raised from 25 GeV to 30 GeV for jets with $2.5 < |\eta| < 4.5$, corresponding to the selection used to define the signal regions for the analysis.

Bin-to-bin correlations of all distributions are given in Appendix I.

8.13 Discussion

All fiducial differential cross section measurements shown in the previous section are in agreement with the SM predictions. The large relative errors of the results however provide little containing power on QCD or PDF models. Normalising the results allows for a shape-only comparison with reduced uncertainties. The reduced uncertainties result in a more stringent comparison of the measured and predicted distributions. The agreement is still qualitatively good although the data prefers lower values of $|y_{\ell\ell}|$ than the MC simulation.

SHERPA seems to consistently give lower cross sections in N_{jet}, although not significantly. This is also seen in the corresponding results from the combined $\gamma\gamma$ and ZZ channels [190].

The dominant uncertainties are given by the WW and top background model and the limited data statistics. Increased data statistics will be gathered in future LHC runs and advances in modelling the WW and top background will be a crucial factor in obtaining higher precision measurements. Despite a relatively small fractional uncertainty on the WW background yield, the size of the WW background to the most sensitive $N_{\text{jet}} = 0$ channel means this uncertainty has a high impact on the measurement. A modelling uncertainty of $m_{\ell\ell}$ in the $N_{\text{jet}} \geq 2$ top CR extrapolates to the signal yield. The uncertainty in the top background enters the $N_{\text{jet}} = 0$ and $N_{\text{jet}} = 1$ channels through the experimental modelling of the explicit N_{jet} requirements including the b-jet veto.

Comparison to WW Observation Analysis

The ratio of observed to predicted values is larger yet still compatible with the global value of $\hat{\mu} = 1.02^{+0.29}_{-0.26}$ reported in Section 8.1.4, but those results include the 7 TeV data, the $ee + \mu\mu$ signal regions, and a fit to the m_{T} shape in the signal regions rather than a selection on m_{T}, which in combination account for the differences. Ref. [18] also reports ggF fiducial cross sections but these use different fiducial volumes and a different procedure to correct for detector effects that did not use events reconstructed with a different N_{jet} than the one at particle level.

Comparison to CMS Results

Differential, fiducial results of $p_{\mathrm{T}}^{\mathrm{H}}$ in the $\mathrm{H} \to \mathrm{WW}^* \to \mathrm{e}\nu\mu\nu$ channel have been reported by the CMS collaboration [191]. A direct comparison to these can not be made, due to differing analysis choices. Firstly, the definition of fiducial volume differs, most significantly by a selection in m_{T}. Further, correlations between N_{jet} and $p_{\mathrm{T}}^{\mathrm{H}}$ are not accounted for, it is unclear to which extent this introduces a bias. Lastly, the CMS analysis considers all $pp \to$H not just gluon fusion, which introduces a non-negligible source of uncertainty from the assumption made on the ggF/VBF cross section ratio. Nevertheless, a similar total fiducial cross section of $\sigma_{fid} = 39 \pm 8(\mathrm{stat}) \pm 9(\mathrm{sys})$ fb is reported, with a comparable total uncertainty of 31% with respect to 27% presented here. Both measurements agree with the SM prediction.

Outlook on 14 TeV Results

These measurements will be repeated for the 14 TeV dataset collected in Run 2 and beyond. A comparison of the increase in cross sections between the signal and main backgrounds suggests the sensitivity of the 2-jet channel will suffer significantly due to the strong rise in $t\bar{t}$ production compared to $\sqrt{s} = 8$ TeV. At the same time the shape of N_{jet} will be different for 13 and 14 TeV collisions and will change the relative sensitivity of the individual jet binned channels. A naive scaling of the Run 1 yield by the increase of production cross sections for the increased collision energy and the expected integrated luminosity of Run 2 leads to the conclusion that the signal to background ratio of the $N_{\mathrm{jet}} = 0$ channel will improve over the Run 1 dataset, while the 1-jet channel will maintain current sensitivity and the 2-jet channel will be substantially degraded due to the increase in $t\bar{t}$ background events. This assumes that current MET and b-tagging efficiencies can be maintained despite increase in pile-up. In each case, the dominant uncertainty from data statistics will be greatly improved on with the larger dataset in Run 2, resulting in differential cross section measurements with improved constraining power over theoretical predictions. The impact of pile-up is currently small, but will be an increasing concern, especially as other uncertainties are expected to improve. Degradation of detector performance due to pile-up will primarily impact the jet and $E_{\mathrm{T}}^{\mathrm{miss}}$ reconstruction.

The selection could be futher improved. For example the same flavour lepton final

state could be included as well as a full treatment of the other Higgs production modes besides ggF.

Most ATLAS analyses extract the cross section from likelihood fits. Unfolding such results obtained from a fit is technically challenging, but holds potential improvements in terms of signal to background ratio.

Chapter 9

A Study of VH→Vb$\bar{b}$ for High Luminosity LHC Running

The coupling of the Higgs boson to fermions is the most important outstanding measurement in verifying the Standard Model description of the Higgs boson. The high branching ratio of 57% of H→ $b\bar{b}$ makes the bottom quark channel, alongside the observed H→ $\tau\tau$ decay, the most promising mode to study Higgs fermion coupling. One infers such coupling by measuring the rate of H→ $b\bar{b}$ decays, which are identified from the invariant mass of the Higgs decay products. In this case, the b quarks themselves only have a lifetime of 1.5 ps before they hadronise to b-jets, which are measured in the ATLAS detector. The high rate of background processes with similar experimental signatures makes observing the H→ $b\bar{b}$ decay challenging. An algorithm for b-jet tagging with a high background rejection of other hadronic jets is applied that also greatly reduces the signal selection efficiency. In order to improve the signal to background ratio, the H→ $b\bar{b}$ decay is studied in events where the Higgs boson is produced in association with a vector boson, a W or Z boson. The subsequent leptonic decay of the vector bosons allows for enhanced signal identification. The cross section for this process where the Higgs boson is radiated off the vector boson and the vector boson decays leptonically is about a factor of 111 lower than direct production through gluon-gluon fusion at $\sqrt{s} = 8$ TeV. But by selecting the leptonic decay products of the vector bosons the background from directly produced $b\bar{b}$ pairs can be rejected, which has a production cross section 7 orders magnitude higher than the Higgs boson, making the associated production the preferred experimental signature to study H→ $b\bar{b}$ [222].

The Run 1 ATLAS H$\rightarrow b\bar{b}$ analysis only measures a 1.4 σ signal significance for $m_{\mathrm{H}} = 125$ GeV, whereas a signal significance of 2.6 σ [236] is expected. A larger dataset than gathered in Run 1 is needed to make a 5 σ observation claim.

The detector design for the high luminosity phase, see Chapter 6, is not yet completely defined and it will take years to adapt and optimise the event reconstruction software to the high-pile-up conditions. The goal is that the performance of the new detector in the harsh conditions of the high luminosity phase will not be worse than the performance of the Run 1 detector with an average pile-up of $\langle\mu\rangle \sim 20$.

Generating high pile-up, fully reconstructed Monte Carlo data for the different future scenarios was considered too resource consuming, instead this study follows the strategy of modifying the particle-level MC by applying efficiency and resolution functions to smear the physical objects and so mimic the detector response. The MC samples used are presented in Section 9.2. The smearing functions are discussed in Section 9.3. In the following the particle-level plus smearing analysis will be referred to as *smeared analysis*. Electron and jets-related functions were derived from samples using the Run-1 ATLAS detector with various values of $\langle\mu\rangle$, up to a maximum average of $\langle\mu\rangle = 60$ [237]. $b-$tagging, missing transverse energy and muon related functions were derived using full simulation of the Phase-I detector with $\langle\mu\rangle$ values up to 80, and the Phase-II detector with $\langle\mu\rangle$ values of 80, 140 and 200 [238].

This study investigates the sensitivity of Higgs boson production in association with a W or Z boson, where the Higgs boson decays as H$\rightarrow b\bar{b}$, the Z decays as Z$\rightarrow \ell^+\ell^-$ (2-lepton channel) and W decays as W$\rightarrow \ell\nu$ (1-lepton channel) for integrated luminosities of 300 fb^{-1} and 3000 fb^{-1}, collision energy of $\sqrt{s} = 14$ TeV and pileup of $\langle\mu\rangle = 60$ and $\langle\mu\rangle = 140$, respectively. As before, ℓ represents either an electron or a muon.

The results for the Z$\rightarrow \ell^+\ell^-$ channel were produced by the author and combined with the W$\rightarrow \ell\nu$ produced by collaborators.

The analysis strategy is based on the Run 1 8 TeV analysis [20] from 2013, but optimises the p_T cuts of the jets to be safer against the high pileup scenarios, see Sections 9.4 and 9.5. The software and method were validated against the 8 TeV analysis, by running the smearing functions over the truth objects of the MC samples used in the analysis, and comparing to the simulation results using the fully simulated and reconstructed objects. The resulting distributions of the

invariant mass of the two b-tagged jets are then used as input to a simplified version of the likelihood fit with a reduced set of systematic uncertainties, which allows a direct comparison to the published result of the expected significance and error in the signal strength, assuming a SM 125 GeV Higgs boson. The validation results are given in Section 9.6.

The same simplified fit model and systematics input is then used to evaluate the significance and expected error on $\hat{\mu}$ of the H$\to b\bar{b}$ signal in the high pileup HL-LHC scenario. The expected significance and error in $\hat{\mu}$ is also quoted for different scenarios with simplified yet robust estimation of the systematic uncertainties. The estimated yields for future LHC runs are given in Section 9.7, the systematic uncertainties are discussed in Section 9.8 and the fit model is presented in Section 9.9. Lastly, the results are given in Section 9.10.

9.1 VH→Vbb̄ Analysis

The search for H $\to b\bar{b}$ decays at ATLAS is performed in the associated production mode, where the Higgs boson is produced together with a Z or W boson. The final states in which the Z or W bosons decays leptonically are considered, as shown in Figure 9.1.

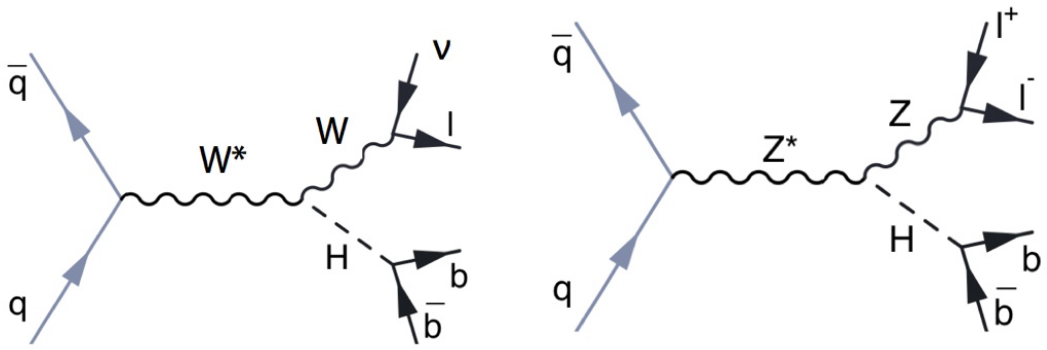

Figure 9.1 Feynman diagrams of a Higgs boson produced in association with a W or Z boson. The Higgs boson decays to a bottom and an anti-bottom. A selection of leptonic W and Z boson decays are made. Besides the shown decay of the Z boson decaying to two charged leptons, it can also decay to two neutrinos.

The analysis is split into orthogonal channels on the basis of the lepton final states. The zero, one and two lepton channels correspond to the Z $\to \nu\bar{\nu}$, W $\to \ell\nu$ and

$Z \to \ell\ell$ decays respectively. Each channel is again split into bins of the vector boson transverse momentum p_T^V, number of jets and number of b-tagged jets in the event. Bins of increasing p_T^V have fewer events but a larger signal to background ratio and separate consideration of all bins allows for optimisation of the sensitivity. Likewise, the separation by jet multiplicity and number of b-tagged jets allows for better background rejection. The signal significance is established from distributions of the b-jet pair invariant mass $m_{b\bar{b}}$.

The Run 1 results are summarised in Section 9.1.1 and the rest of this chapter presents a sensitivity study of the $H \to b\bar{b}$ for future 14 TeV LHC runs. Projections are made for the 1 and 2 lepton channels individually and their combination.

As shown in Figure 9.2, the primary sources of background are vector boson production in association with a heavy flavour jet and $t\bar{t}$. Smaller contributions to the background arise from diboson, single top quarks and multijet production.

V+jets A vector boson which is produced along with two heavy flavour jets is virtually irreducible from the signal. The associated production with c and light jets contributes to the background due to misidentification and is greatly reduced by a well performing b-tagging algorithm. The production occurs via quark scattering, $q\bar{q}' \to V + b\bar{b}$ or gluon induced bottom quark fusion, $gg \to Z + b\bar{b}$ can lead to final states with different combinations of jet flavours.

$t\bar{t}$ Due to their large production cross section, t-quark pairs represent a sizeable background. Each top quark of the $t\bar{t}$ pair decays to $W + b$. Leptonic W decays result in a final state with two b-jets, two charged leptons and significant E_T^{miss}, which can mimic the WH signal process. For high p_T^W the highly collimated b-jets originating from the WH decay can be exploited to reduce the $t\bar{t}$ background. Requiring $p_T^{miss} < 60$ GeV in the ZH channel greatly reduces the $t\bar{t}$ bar contribution.

Diboson Decays of VZ pairs produce the same final state as VH. The VZ background has about 5 times larger cross section than the signal and can be rejected by selecting events by the dijet mass of the resulting $b\bar{b}$ pair. For $Z \to b\bar{b}$ the invariant mass $m_{b\bar{b}}$ is lower than for $H \to b\bar{b}$. The separation of diboson background and signal thus depends on sufficient resolution in the reconstructed dijet mass.

Single top Single top-quark processes result in tb or tW states via weak interaction of W$\rightarrow tb$,$b \rightarrow t$W or bW $\rightarrow t\bar{b}q$. Subsequent decays of the W and t lead to a final state with at least one b-jet. As for the $t\bar{t}$ background, angular requirements on the b-jets allow for suppression of this background.

Multijet QCD multijet background arises from misidentification of jets as leptons or incorrect calculation of the $E_{\mathrm{T}}^{\mathrm{miss}}$. These *fake* jets have a sizeable impact due to the very large cross section of QCD multijets.

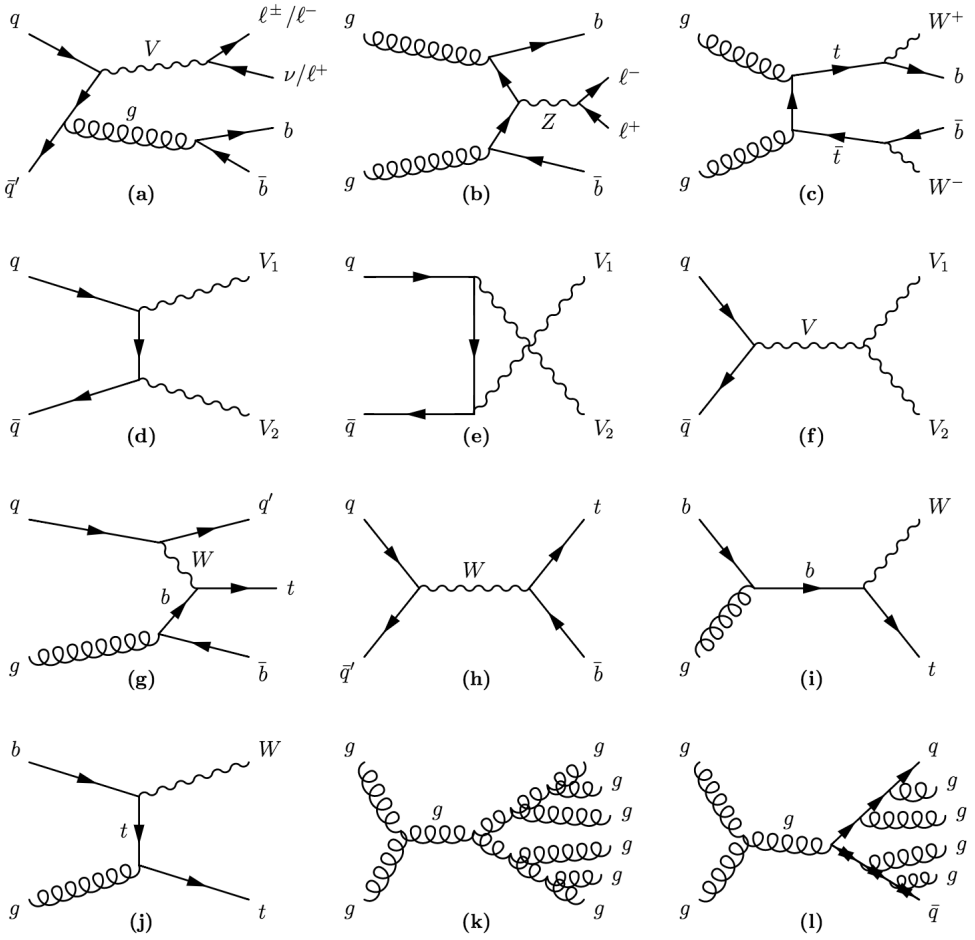

Figure 9.2 Feynman diagrams of the main background processes to the VH$\rightarrow b\bar{b}$ analysis [239]. (a,b) V+jets, (c) $t\bar{t}$, (d-f) diboson, (g-h) single top, (i,j) Wt and (k,l) examples of multijet.

In the one lepton channel the main backgrounds are W+2 b-jets and $t\bar{t}$, with contributions from multiple QCD jets and single top-quark processes. With increasing $p_{\mathrm{T}}^{\mathrm{V}}$, the $t\bar{t}$ contribution again decreases but Wbb increases. For the two lepton channel the main background is Z+2 b-jets with a smaller $t\bar{t}$ contribution, particularly in the low $p_{\mathrm{T}}^{\mathrm{V}}$ bins.

9.1.1 Run 1 Results

The 8 TeV analysis from the 2013 ATLAS publication [20] serves as a reference analysis. The analysis was performed on 4.7 fb^{-1} of 7 TeV and 20.3 fb^{-1} of 8 TeV data recorded during Run 1 of the LHC. No significant excess of the Higgs boson signal was observed. Assuming $m_{\mathrm{H}} = 125$ GeV a upper limit on the cross section times branching ratio of the $\mathrm{VH}, \mathrm{H} \to b\bar{b}$ channel was set at 1.4 times the SM expectation with a 95% confidence level. The ratio of the measured signal strength to the SM expectation is $\mu = 0.2 \pm 0.5(\mathrm{stat}) \pm 0.4(\mathrm{sys})$ in the combination of all analysis categories. Here $\mu = 1$ would represent the measurement of a signal that corresponds to the SM expectation. An overview of the obtained signal strength parameters is given in Figure 9.3. The results are obtained from a likelihood fit to all analysis bins.

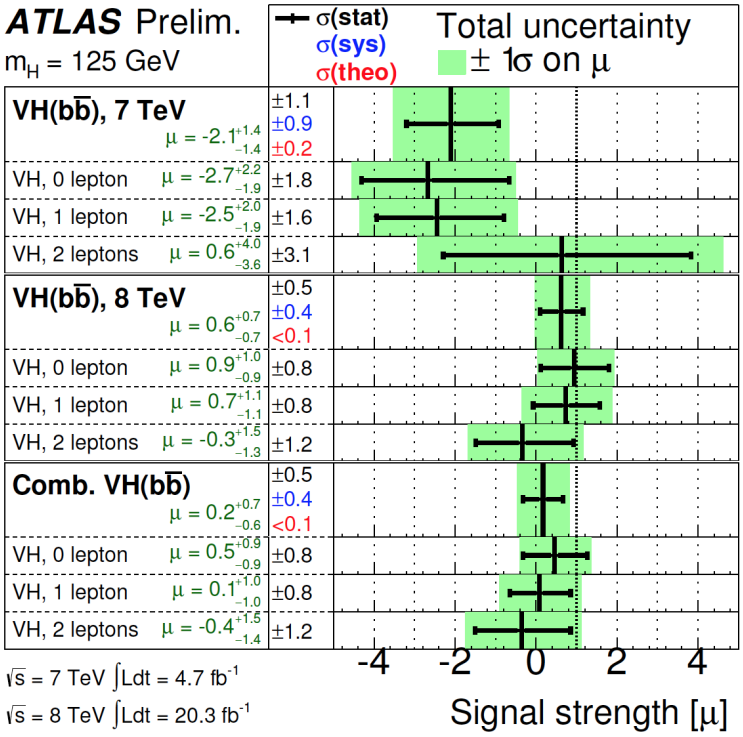

Figure 9.3 Comparison of measured signal strength to the $m_{\mathrm{H}} = 125$ GeV SM expectation, given by the vertical line at $\mu = 1$ [20].

9.2 Signal and Background Samples

Assuming the Standard Model expectation, VH production is dominated by quark-initiated processes. ZH production also has significant contributions from gluon-initiated processes [240, 241]. Monte Carlo events for the $qq \rightarrow$WH and $qq \rightarrow$ZH signal are generated using the Pythia8 generator [242] with the CTEQ6L1 [205] PDFs and the AU2 tune for parton showering and hadronisation [243]. $gg \rightarrow$ZH events were generated using POWHEG [244, 245], the parton showering was performed by Pythia8 with the CT10 [196] PDFs and the AU2 tune. The total production cross sections and associated uncertainties computed at next-to-next-to-leading order (NNLO) in QCD and with next-to-leading order (NLO) electroweak corrections are taken from Refs [241, 246–249]. Additional NLO corrections are applied to qq initiated processes as a function of the transverse momentum of the vector boson [20, 250]. Samples were generated using a Higgs mass of 125 GeV, decaying into two b-quarks. W bosons decay as W$\rightarrow e\nu_e$, W$\rightarrow \mu\nu_\mu$, W$\rightarrow \tau\nu_\tau$ and Z bosons decay as Z$\rightarrow e^+e^-$, Z$\rightarrow \mu^+\mu^-$ and Z$\rightarrow \tau^+\tau^-$.

The main background processes are $t\bar{t}$ and diboson production for both WH and ZH, single-top quark production and W+jets for WH and Z+jets for ZH. The Monte Carlo generators and central values of the cross section for the signal and background processes are listed in Table 9.1. The production cross section of all processes increases as a function of proton-proton centre of mass energy. The ratio of production cross sections for 8 to 14 TeV collisions of all major processes are also shown.

The V+jets background is categorised according to the flavour of the two leading jets selected to reconstruct the di-b-jet mass.

Background due to QCD multijet production is estimated from the known multijet background in $\sqrt{s} = 8$ TeV data [20]. The large multijet background is effectively rejected by the selection cuts and a prohibitively large MC dataset would need to be generated to obtain a statistically significant sample. The estimate from data is taken from a control region selection with a high purity of multijet events. It is scaled by the increase in gluon-gluon parton luminosity between 8 and 14 TeV, which corresponds to a factor of ~ 2.3. In the two-lepton channel, the multijet background is considered negligible.

Process	Generator	$\sigma_{14\,\mathrm{TeV}}$ [pb]	$\sigma_{14\,\mathrm{TeV}}/\sigma_{8\,\mathrm{TeV}}$
$pp \to \mathrm{WH} \to l\nu b\bar{b}$	Pythia8 [242]	0.87 [205]	2.3
$pp \to \mathrm{ZH} \to l^+l^-b\bar{b}$	Pythia8	0.056 [205]	2.2
$gg \to \mathrm{ZH} \to l^+l^-b\bar{b}$	POWHEG	0.0076 [205]	3.7
$pp \to$ W+jets ($p_{\mathrm{T}}^W > 70$ GeV)	Sherpa [72]	2315 [251]	1.8
$pp \to$ Z+jets	Sherpa	6850 [251]	1.9
$pp \to t\bar{t}$	POWHEG [244]	977 [252]	3.8
single top (t-channel)	AcerMC [253]	248 [254]	2.8
single top (s-channel)	POWHEG	11.9 [254]	2.1
single top (Wt-channel)	POWHEG	83.6 [254]	3.7
$pp \to$ WW	HERWIG [71]	118 [251]	2.1
$pp \to$ WZ	HERWIG	49 [251]	2.2
$pp \to$ ZZ	HERWIG	16 [251]	2.2

Table 9.1 Summary of the Monte Carlo samples used in the study presented in this note. The central values of the cross sections at $\sqrt{s} = 14$ TeV used in the fit are given. In this Table, l refers to any charged lepton: e, μ, or τ. Samples were generated at LO and normalised to NLO precision cross sections, by the calculations referenced. V+jets and the $\mathrm{t\bar{t}}$ sample are generated at NLO and normalised to NNLO precision.

9.3 Parametrisation of Future ATLAS Detector Performance

The simulation of LHC data is described in Chapter 4 including the detector reconstruction in Section 4.7. A special feature of this analysis is that the standard detector reconstruction is not performed. Instead of fully simulating each particle as it passes through the ATLAS detector, parametrisation functions are used. These functions are derived from fully reconstructed data samples and represent the average detector response for different particle types and kinematic properties. In particular, these response functions are constructed for different pile-up scenarios. Thus different pile-up dependent detector performances can be applied to the same data samples in a time efficient manner.

Identification and reconstruction efficiencies as well as response functions, referred to as *smearing functions*, of physics objects for the expected detector and object performance for benchmark high luminosity scenarios are applied to Monte Carlo generator quantities. The efficiencies and smearing functions used in this analysis are summarised below and are taken from studies presented in Refs [237]

and [238]. An increase in the number of reconstructed jets in an event is a direct consequence of higher pile-up as shown in Figure 9.4 for different jet p_T thresholds. It can be seen that pile-up jets can be effectively suppressed by imposing stricter requirements on the jet p_T.

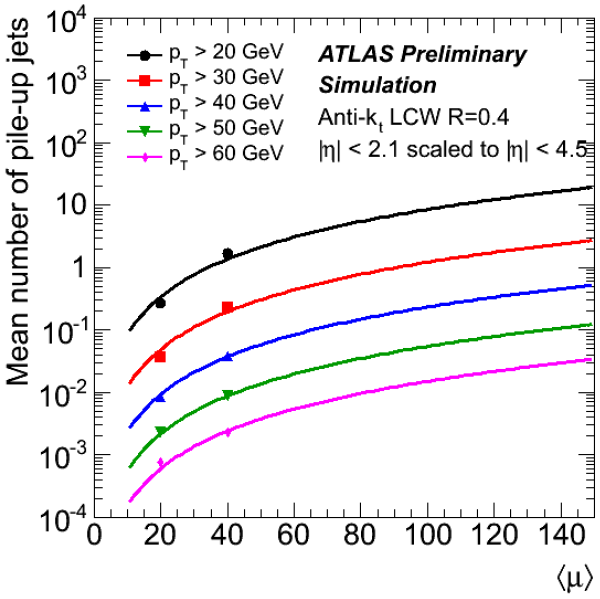

Figure 9.4 Mean pile-up jet multiplicity extrapolation as a function of $\langle\mu\rangle$ for each p_T threshold [237]. The fit is a power law proportional to $\langle\mu\rangle^2$.

The very high pile-up environment introduces challenges to jet reconstruction and calibration including degradation of the jet energy resolution due to the additional jet activity. The energy of the particle jets is smeared using an η- and $\langle\mu\rangle$-dependent correction derived from fully simulated di-jet Monte Carlo samples [237]. For a central jet with $p_{\mathrm{T}} = 60$ GeV at $\langle\mu\rangle = 140$ the relative jet energy resolution contribution due to pile-up is $\sim 32\%$.

It is important for this analysis that the b-tagging efficiency, which depends on tracking and calorimeter performance, is not degraded. The simulated b-jet tagging efficiency versus the light-jet rejection efficiency is shown in Figure 9.5. Different pile-up scenarios are considered with either the Run 1 Inner Detector, including the IBL upgrade, or the proposed ITK upgrade. The near factor of 10 improvement of light-jet rejection for a given b-tagging efficiency and pile-up scenario make a strong case for the upgrade to the ITK design [176], which is used in this analysis.

The probability of a jet being misidentified as an electron is treated as a η-dependent efficiency of up to 11% for a jet to be misidentified as a loose electron

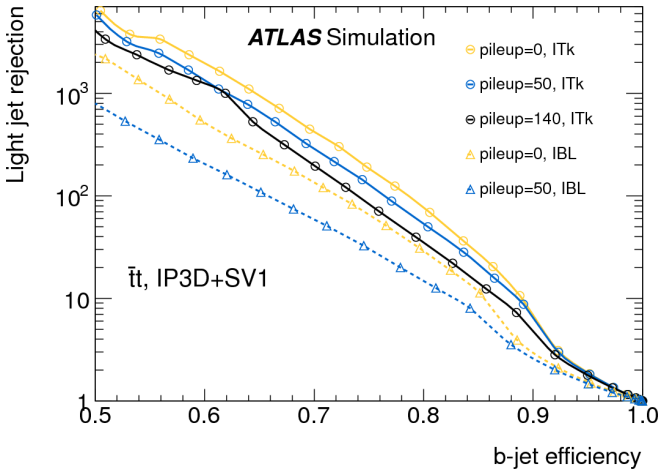

Figure 9.5 Comparison of the ATLAS b-tagging performance in full simulation for various pileup scenarios and detector configurations [162]. The IP3D+SV1 tagging algorithm uses a combination of 3-dimensional impact parameter likelihood and secondary vertexing to achieve high performance, especially when the Insertable B-Layer pixel detector (IBL) or proposed all-silicon Inner Tracker (ITK) are used.

and up to 0.48% for a jet to be misidentified as a tight electron [237, 238]. Leptons originating from b/c hadron decays are removed from the analysis.

Missing transverse momentum, $E_{\mathrm{T}}^{\mathrm{miss}}$, is calculated from the vector sum of particles in the detector acceptance region and is smeared by a parameterized resolution function, derived from samples of Z'$\rightarrow t\bar{t}$ production with a full detector simulation, as described in Ref. [238].

9.4 Object Selection and Reconstruction

The VH, H $\rightarrow b\bar{b}$ 14 TeV analysis follows the selection criteria used by the 8 TeV analysis [20], but with a harder requirement on the p_{T} of the jets.

To increase the sensitivity of the search the analysis is performed in bins; bins are defined using the momentum of the vector boson, p_{T}^{V}, the exclusive number of b-jet tags and the exclusive number of total jets as given in Table 9.2. The signal region, consisting of the bins with exactly two b-jets, has 18 bins: eight for the one-lepton channel and ten for the two-lepton channel.

Particle jets are reconstructed using the anti-k_{T} algorithm [143], using a distance parameter of $R = \sqrt{\phi^2 + \eta^2} = 0.4$. The flavour of the jets is classified using

p_{T}^{V} bins		Exclusive number of b-jets	Exclusive number of total jets
Bin 1	$p_{\mathrm{T}}^{V} < 90$ GeV		
Bin 2	90 GeV $< p_{\mathrm{T}}^{V} <$ 120 GeV	0	2
Bin 3	120 GeV $< p_{\mathrm{T}}^{V} <$ 160 GeV	1	3
Bin 4	160 GeV $< p_{\mathrm{T}}^{V} <$ 200 GeV	2	
Bin 5	$p_{\mathrm{T}}^{V} > 200$ GeV		

Table 9.2 Definition of the bins used in the analysis. The one-lepton analysis uses only p_{T}^{V} bins 2 - 5; bin 1 is not used to avoid the large multijet contamination.

hadrons in a $R = 0.4$ cone around the jet axis: if a b-hadron is found, the jet is labeled as a b-jet, if no b-hadron is found but a c-hadron the jet is labeled as a c-jet otherwise the jet is labeled as a light jet. The b-tag, c and light jet mis-tag efficiency parametrisation corresponds to the ATLAS MV1 tagger [237], with an average b-jet identification efficiency of 70%, as measured in a semi-leptonic $t\bar{t}$ sample.

Requiring a track-jet confirmation as described in Section 5.9.5 greatly reduces the impact of pile-up. The efficiency of this requirement is emulated in this analysis and is parameterized as 75% for jets with $p_{\mathrm{T}} < 25$ GeV, 85% for jets with 25 GeV $< p_{\mathrm{T}} <$ 35 GeV and 95% for jets with $p_{\mathrm{T}} > 35$ GeV [237].

Two categories of electrons and muons are defined, denoted in increasing order of purity as *loose* and *tight*. Loose electrons and muons are required to have transverse energy $E_{\mathrm{T}} > 10$ GeV and must fall within the acceptance of the appropriate detector: $|\eta| < 2.47$ for electrons and $|\eta| < 2.7$ for muons. Tight leptons are required to have $E_{\mathrm{T}} > 25$ GeV with $|\eta| < 2.47$ for electrons and $|\eta| < 2.5$ for muons. Additionally both loose and tight leptons must pass isolation requirements to reject jets. A track isolation requirement is defined using the sum of p_{T} of all charged particles in a cone of $\Delta R = 0.4$ around the lepton direction over the lepton-p_{T} and a calorimeter isolation requirement is defined using the sum of E_{T} of all particles in a cone of $\Delta R = 0.3$ around the lepton direction over the lepton-E_{T}. For loose leptons the track isolation must be $< 10\%$. For tight leptons the track isolation must be $< 4\%$ and the calorimeter isolation must be $< 7\%$.

Quantity	One-lepton	Two-lepton
Leptons	1 tight lepton+0 loose lepton	2 loose leptons
Jets	2 b-tags with $\|\eta\| < 2.5$ p_{T}(leading jet) > 60 GeV, p_{T}(sub-leading jet) > 40 GeV ≤ 1 extra jet ($p_{\mathrm{T}} > 30$ GeVand $\|\eta\| < 2.5$)	
Vector boson	–	83 GeV $< m_{\ell\ell} <$ 99 GeV

Table 9.3 Event selection criteria.

9.5 Event Selection

The event selection requirements are summarised in Tables 9.3 and 9.4.

Events are required to pass a parameterized trigger requirement of a single electron or muon trigger, as detailed in Ref. [237]. It is assumed that trigger thresholds for HL-LHC running will only need to be slightly raised compared to Run 1 operations. The single electron trigger requires one electron with $p_{\mathrm{T}} > 18$ GeV within $|\eta| < 2.5$ and has an efficiency of 88%. The single muon trigger requires one muon with $p_{\mathrm{T}} > 20$ GeV with an efficiency of 64% for muons with $|\eta| < 1.0$ and 86% for muons with $1.0 < |\eta| < 2.4$.

Events are required to have at least two jets with $|\eta| < 2.5$, with a minimum p_{T} requirement of 60 GeV on the highest-p_{T} jet and $p_{\mathrm{T}} > 40$ GeV on the sub-leading jet, plus requirements on the ΔR between the two jets, as detailed in Table 9.4. For the signal region selection both leading jets are required to be b-tagged. The four-momenta of the two leading jets is used to reconstruct the di-jet invariant mass. A maximum of one additional jet in the event with $p_{\mathrm{T}} > 30$ GeV and $|\eta| < 2.5$ is allowed.

Besides the jet conditions, the presence of the 2-lepton ZH signal is established by selecting Z$\to \ell\ell$ decays. Two loose leptons are required with an invariant mass consistent with a Z-boson. In addition, the missing transverse energy, $E_{\mathrm{T}}^{\mathrm{miss}}$, is required to be less than 60 GeV, see Figure 9.6.

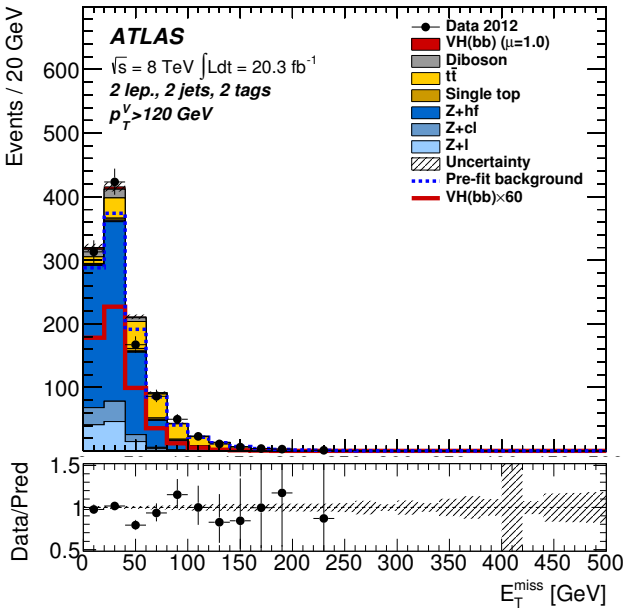

Figure 9.6 The $E_{\mathrm{T}}^{\mathrm{miss}}$ distribution for 8 TeV collisions, in the 2-lepton channel for the 2-jet 2-tag category, taken from Ref. [255]. The expected Higgs boson signal is shown in front of the summed background, scaled by a factor of 60 for visibility.

	p_{T}^{V}(GeV)	$0-90$	$90-120$	$120-160$	$160-200$	>200
All channels	$\Delta R(b,b)$	$0.7-3.4$	$0.7-3.0$	$0.7-2.3$	$0.7-1.8$	<1.4
One-lepton	$E_{\mathrm{T}}^{\mathrm{miss}}$	>25 GeV				>50 GeV
	m_{T}^{W}	$40-120$ GeV			<120 GeV	
Two-lepton	$E_{\mathrm{T}}^{\mathrm{miss}}$	<60 GeV				

Table 9.4 p_{T}^{V}-dependent event selection criteria.

9.6 Validation against $\sqrt{\mathrm{s}} = 8$ TeV Analysis

The analysis framework was validated against the $\sqrt{s} = 8$ TeV benchmark analysis. The detector parametrisations were applied to the $\sqrt{s} = 8$ TeV particle-level Monte Carlo samples. These samples are listed in Ref. [20] and have been extensively studied and validated against collision data. The aim of the validation was to understand the object definitions, event selection, the applied corrections, the fit model presented in Section 9.9 as well as any discrepancies between the approach applied in the smeared analysis and the full simulation analysis.

Cuts as in Tables 9.3 and 9.4 are applied, but with a lower p_{T} cut on the jets of 45 GeV on the leading jet and 20 GeV on the sub-leading jet, as done in the

benchmark analysis. In addition, the p_{T} cut of the extra jet veto is lowered to 20 GeV.

The smearing functions applied to the $\sqrt{s} = 14$ TeV samples [237, 238] have been derived assuming different pile-up conditions and an upgraded ATLAS detector, and therefore are not directly applicable to the benchmark analysis samples.

The following summarises the parameterisation of the smearing and efficiency functions applied to the $\sqrt{s} = 8$ TeV Monte Carlo samples. Where the functions depend on the pile-up, $\langle\mu\rangle = 20$ has been used.

- Single lepton trigger efficiencies were taken from $\sqrt{s} = 8$ TeV studies in Refs. [256] for electrons and [257] for muons. The values used for the reconstruction and identification efficiencies are as for $\sqrt{s} = 14$ TeV as these efficiencies were derived assuming the current 2012 performance.

- The same η- and $\langle\mu\rangle$-dependent jet energy resolution parameterisation as used for $\sqrt{s} = 14$ TeV samples are applied. For a central jet with $p_{\mathrm{T}} = 60$ GeV at $\langle\mu\rangle = 20$ the relative jet energy resolution contribution due to pile-up is $\sim 25\%$.

- A *track-jet confirmation* is applied to suppress background due to pile-up. It requires jets to match a track originating from the primary vertex. The efficiency of this selection is between 90% for tracks of $p_{\mathrm{T}} = 25$ GeV up to 95% for tracks with p_{T} of 50 GeV or above [237].

- $b-$tagging efficiency maps were derived from $\sqrt{s} = 8$ TeV data and applied.

- The missing transverse energy resolution parameterisation given in Ref. [237] is used, since it incorporates a parameterisation with continuous $\langle\mu\rangle$. The missing transverse energy resolution degrades with increasing $\langle\mu\rangle$.

Figure 9.7 show the resulting distribution of the invariant di-b-jet mass m_{bb} for the $\sqrt{s} = 8$ TeV Monte Carlo generator plus smearing quantities, compared to the results from full simulation of the same samples and the data taken from the benchmark analysis.

It was found that the number of selected muons agrees well, within uncertainties, between the smeared particle-level and the full simulation analysis. However, low-p_{T} electrons were ($\sim 20\%$) more likely to be selected in the particle-level

Sample		significance of $\hat{\mu} = 1$	error on $\hat{\mu}$
$\sqrt{s} = 8$ TeV validation	One-lepton	0.84	$+1.28 \ -1.19$
	Two-lepton	0.75	$+1.49 \ -1.32$
	One+Two-lepton	1.14	$+0.90 \ -0.83$

Table 9.5 Fit results on the expected signal sensitivity for the $\sqrt{s} = 8$ TeV samples, based on the analysis performed in this thesis.

analysis than in the full simulation analysis. Differences in the $E_{\mathrm{T}}^{\mathrm{miss}}$ distributions were also observed. The parametrisation of the $E_{\mathrm{T}}^{\mathrm{miss}}$ distribution has an equivalent resolution which was approximately 5% lower when compared to the full simulation. These differences in principle have an impact on the m_{T}^{V} and p_{T}^{V} distributions, but have little impact in the two-lepton channel. The presence of pile-up jets in the full simulation analysis is another source of discrepancy. Due to the additional pile-up jets, more events in the full simulation analysis are rejected compared to the smeared particle-level analysis when the events are categorised in the 2 and 3-jet bins, especially for the $t\bar{t}$ background.

The analysis method was also validated by performing the fit to the $\sqrt{s} = 8$ TeV samples, as described in Section 9.9, with the results given in Table 9.5. The differences in event yields and kinematics discussed above have a minor impact once the one-lepton and two-lepton channels are combined, and the expected significance and signal strength errors are compatible with the benchmark analysis to better than 5%.

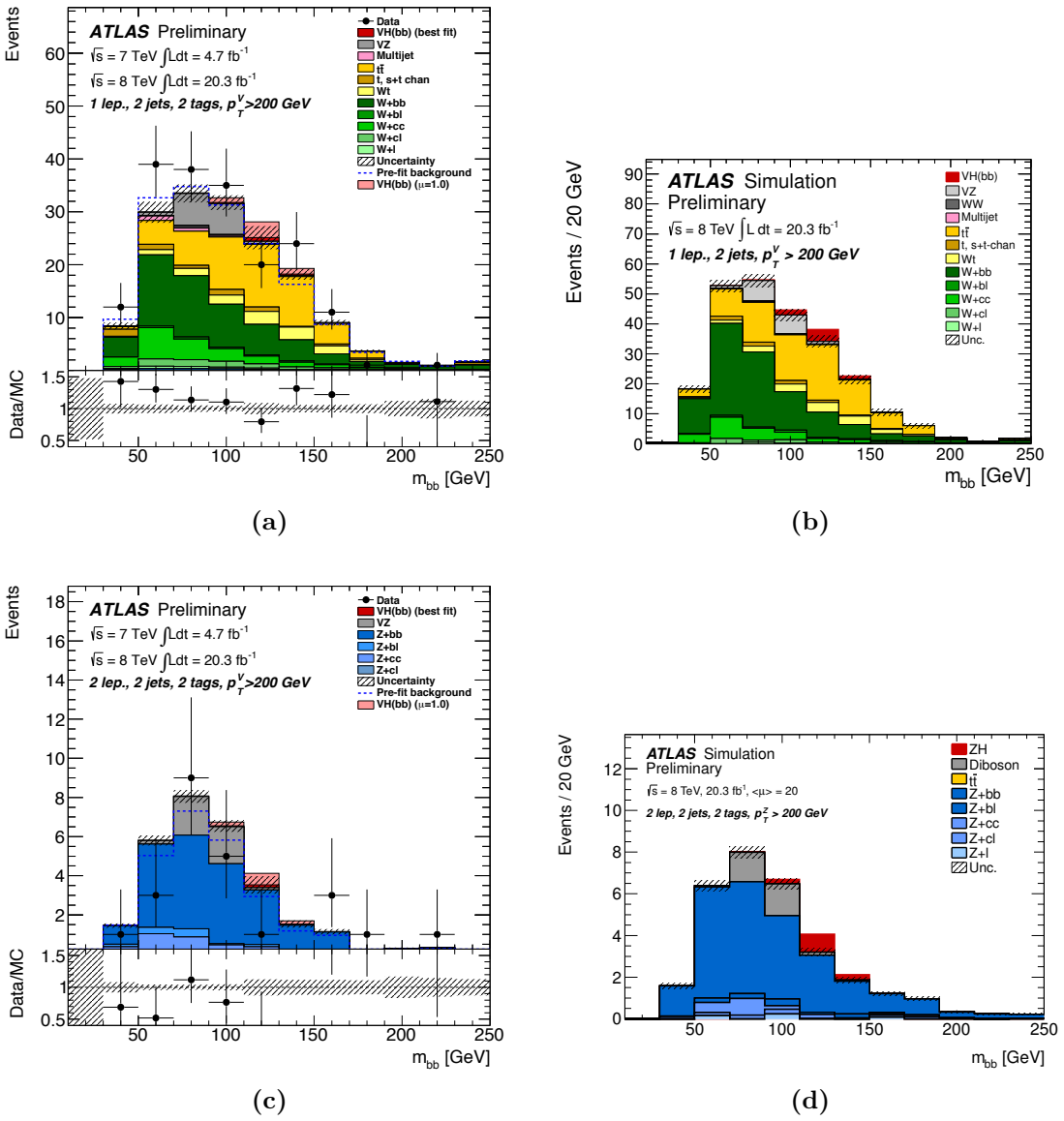

Figure 9.7 Validation of $\sqrt{s} = 8$ TeV analysis in the one-lepton (top) and two-lepton (bottom) channel. Invariant di-b-jet mass distribution in the analysis bin with the highest signal significance (exactly two jets, exactly two b-jets tags and $p_{\mathrm{T}}^{V} > 200$ GeV). Left: from the benchmark analysis (Ref. [20]) using fully simulated Monte Carlo samples and including data taken at $\sqrt{s} = 7$ TeV. The points on the ratio plots are off the scale for some of the low statistics bins. Right: Validation from this work using parameterised detector efficiencies and resolutions. The dashed band corresponds to the statistical uncertainties only.

9.7 Signal and Background Yields

Projected ZH signal and background yields and m_{bb} distributions are given for the 300 fb^{-1} and 3000 fb^{-1} benchmarks. Corresponding WH results are given in Appendix B.

Table 9.6 shows the ZH event yields for signal and background for an integrated luminosity of 300 fb^{-1}, assuming the appropriate smearing and efficiency functions for pile-up of $\langle\mu\rangle = 60$. Table 9.7 shows the ZH event yields for 3000 fb^{-1}, assuming the appropriate smearing and efficiency functions for pile-up of $\langle\mu\rangle = 140$.

Figures 9.8 and 9.9 show the di-b-jet mass distributions for all the ZH signal regions defined in Section 9.4 for $\sqrt{s} = 14$ TeV and an integrated luminosity of 300 fb^{-1} (with $\langle\mu\rangle = 60$) and 3000 fb^{-1} ($\langle\mu\rangle = 140$) after applying the selection criteria in Tables 9.3 and 9.4.

Two-lepton 2-jet signal region, 300 fb^{-1}

Process	$p_{\mathrm{T}}^{\mathrm{Z}}$[GeV]				
	0 – 90	90 – 120	120 – 160	160 – 200	>200
$qq \rightarrow$ZH	44.6 ± 1.4	23.5 ± 1.1	25.9 ± 1.1	19.5 ± 0.9	32 ± 1
$gg \rightarrow$ZH	3.1 ± 0.4	3.7 ± 0.4	7.8 ± 0.6	5.8 ± 0.5	4.6 ± 0.5
ZH total	47.7 ± 1.5	27.2 ± 1.1	33.7 ± 1.3	25.3 ± 1.1	36.6 ± 1.1
ZZ	123 ± 17	64 ± 13	86 ± 15	59 ± 12	106 ± 16
$t\bar{t}$	7580 ± 280	1090 ± 110	190 ± 50	0 ± 0	0 ± 0
Z+bb	9600 ± 190	2480 ± 90	1600 ± 70	510 ± 40	740 ± 50
Z+bl	480 ± 40	155 ± 22	97 ± 18	7 ± 5	38 ± 12
Z+cc	1880 ± 140	300 ± 60	220 ± 40	104 ± 18	173 ± 24
Z+cl	460 ± 70	71 ± 29	49 ± 16	49 ± 12	24 ± 9
Z+ll	40 ± 20	12 ± 12	2.3 ± 2.3	0 ± 0	12 ± 6
Total bkg	20200 ± 400	4160 ± 160	2200 ± 100	730 ± 50	1090 ± 60
S/B ($\times 10^{-3}$)	2.36 ± 0.09	6.54 ± 0.34	15.3 ± 0.9	34.7 ± 2.8	33.6 ± 2.1
$S/\sqrt{B}$	0.336 ± 0.011	0.422 ± 0.018	0.718 ± 0.031	0.94 ± 0.05	1.11 ± 0.05

Two-lepton, 3-jet signal region, 300 fb^{-1}

Process	$p_{\mathrm{T}}^{\mathrm{Z}}$[GeV]				
	0 – 90	90 – 120	120 – 160	160 – 200	>200
$qq \rightarrow$ZH	22.3 ± 1.1	9.2 ± 0.6	11.0 ± 0.7	8.2 ± 0.6	16.4 ± 0.9
$gg \rightarrow$ZH	4.3 ± 0.5	4.2 ± 0.5	6.7 ± 0.6	4.8 ± 0.5	6.5 ± 0.6
ZH total	26.6 ± 1.1	13.4 ± 0.8	17.7 ± 0.9	13.0 ± 0.8	22.9 ± 1.1
ZZ	99 ± 16	42 ± 10	30 ± 9	15 ± 6	47 ± 11
$t\bar{t}$	4890 ± 230	630 ± 80	53 ± 24	21 ± 15	0 ± 0
Z+bb	7360 ± 160	1950 ± 80	1040 ± 60	460 ± 40	980 ± 60
Z+bl	450 ± 40	112 ± 18	33 ± 11	22 ± 9	32 ± 11
Z+cc	1420 ± 119	410 ± 70	210 ± 40	70 ± 17	223 ± 29
Z+cl	390 ± 60	120 ± 40	18 ± 13	28 ± 9	9 ± 5
Z+ll	62 ± 28	35 ± 25	12 ± 12	6 ± 4	0 ± 0
Total bkg	14670 ± 320	3300 ± 140	1400 ± 80	620 ± 50	1290 ± 70
S/B ($\times 10^{-3}$)	1.81 ± 0.09	4.06 ± 0.29	12.6 ± 1.1	21.0 ± 2.1	17.8 ± 1.3
$S/\sqrt{B}$	0.220 ± 0.010	0.233 ± 0.014	0.473 ± 0.028	0.52 ± 0.04	0.638 ± 0.035

Table 9.6 Event yields for signal and background, for the two-lepton channel in p_{T}^{Z} bins. The yields are for $\sqrt{s} = 14$ TeV, $\langle\mu\rangle = 60$ and an integrated luminosity of 300 fb^{-1} and before the fit model has been applied. The uncertainties correspond to limited Monte Carlo statistics.

Two-lepton, 2-jet signal region, 3000 fb^{-1}

Process	p_{T}^{Z}[GeV]				
	0 – 90	90 – 120	120 – 160	160 – 200	>200
$qq \rightarrow$ZH	272 ± 11	135 ± 8	162 ± 8	118 ± 7	194 ± 9
$gg \rightarrow$ZH	12.7 ± 2.5	23.0 ± 3.4	46 ± 5	32 ± 4	29 ± 4
ZH total	285 ± 11	158 ± 9	208 ± 9	150 ± 8	223 ± 10
ZZ	890 ± 150	490 ± 110	590 ± 120	400 ± 100	590 ± 120
$t\bar{t}$	54000 ± 2400	7600 ± 900	960 ± 320	110 ± 110	0 ± 0
Z+bb	55800 ± 1400	14200 ± 700	9000 ± 500	3100 ± 300	4400 ± 400
Z+bl	3300 ± 350	1000 ± 170	450 ± 120	110 ± 60	170 ± 80
Z+cc	12100 ± 1100	2300 ± 500	1540 ± 330	780 ± 160	1100 ± 200
Z+cl	2500 ± 500	350 ± 200	600 ± 220	60 ± 40	230 ± 90
Z+ll	3400 ± 3300	350 ± 250	70 ± 40	0 ± 0	0 ± 0
Total bkg	132000 ± 5000	26000 ± 1300	13200 ± 800	4600 ± 400	6600 ± 500
S/B ($\times 10^{-3}$)	2.16 ± 0.12	6.1 ± 0.5	15.8 ± 1.2	32.6 ± 3.3	33.8 ± 3.0
$S/\sqrt{B}$	0.784 ± 0.034	0.98 ± 0.06	1.81 ± 0.10	2.21 ± 0.15	2.74 ± 0.16

Two-lepton 3-jet signal region, 3000 fb^{-1}

Process	p_{T}^{Z}[GeV]				
	0 – 90	90 – 120	120 – 160	160 – 200	>200
$qq \rightarrow$ZH	139 ± 8	55 ± 5	70 ± 6	52 ± 5	97 ± 7
$gg \rightarrow$ZH	24.4 ± 3.5	18.5 ± 3.0	41 ± 5	23.4 ± 3.4	41 ± 5
ZH total	163 ± 9	74 ± 6	111 ± 8	75 ± 6	138 ± 9
ZZ	590 ± 120	200 ± 70	200 ± 70	150 ± 60	350 ± 90
$t\bar{t}$	31600 ± 1800	5300 ± 800	320 ± 180	0 ± 0	0 ± 0
Z+bb	43500 ± 1300	11700 ± 600	5800 ± 400	3090 ± 340	5900 ± 500
Z+bl	2150 ± 280	620 ± 140	540 ± 130	110 ± 60	130 ± 70
Z+cc	7300 ± 900	1500 ± 400	1230 ± 320	460 ± 120	1490 ± 220
Z+cl	1900 ± 400	560 ± 240	0 ± 0	120 ± 60	520 ± 130
Z+ll	180 ± 180	0 ± 0	0 ± 0	0 ± 0	0 ± 0
Total bkg	87200 ± 2500	20000 ± 1000	8100 ± 600	3900 ± 400	8400 ± 600
S/B ($\times 10^{-3}$)	1.87 ± 0.11	3.68 ± 0.34	13.7 ± 1.4	19.3 ± 2.5	16.4 ± 1.6
$S/\sqrt{B}$	0.553 ± 0.031	0.52 ± 0.04	1.23 ± 0.10	1.21 ± 0.11	1.51 ± 0.11

Table 9.7 Event yields for signal and background, for the two-lepton channel in p_{T}^{Z} bins. The yields are for $\sqrt{s} = 14$ TeV, $\langle\mu\rangle = 140$ and an integrated luminosity of 3000 fb^{-1}, before the fit model has been applied. The uncertainties correspond to limited Monte Carlo statistics.

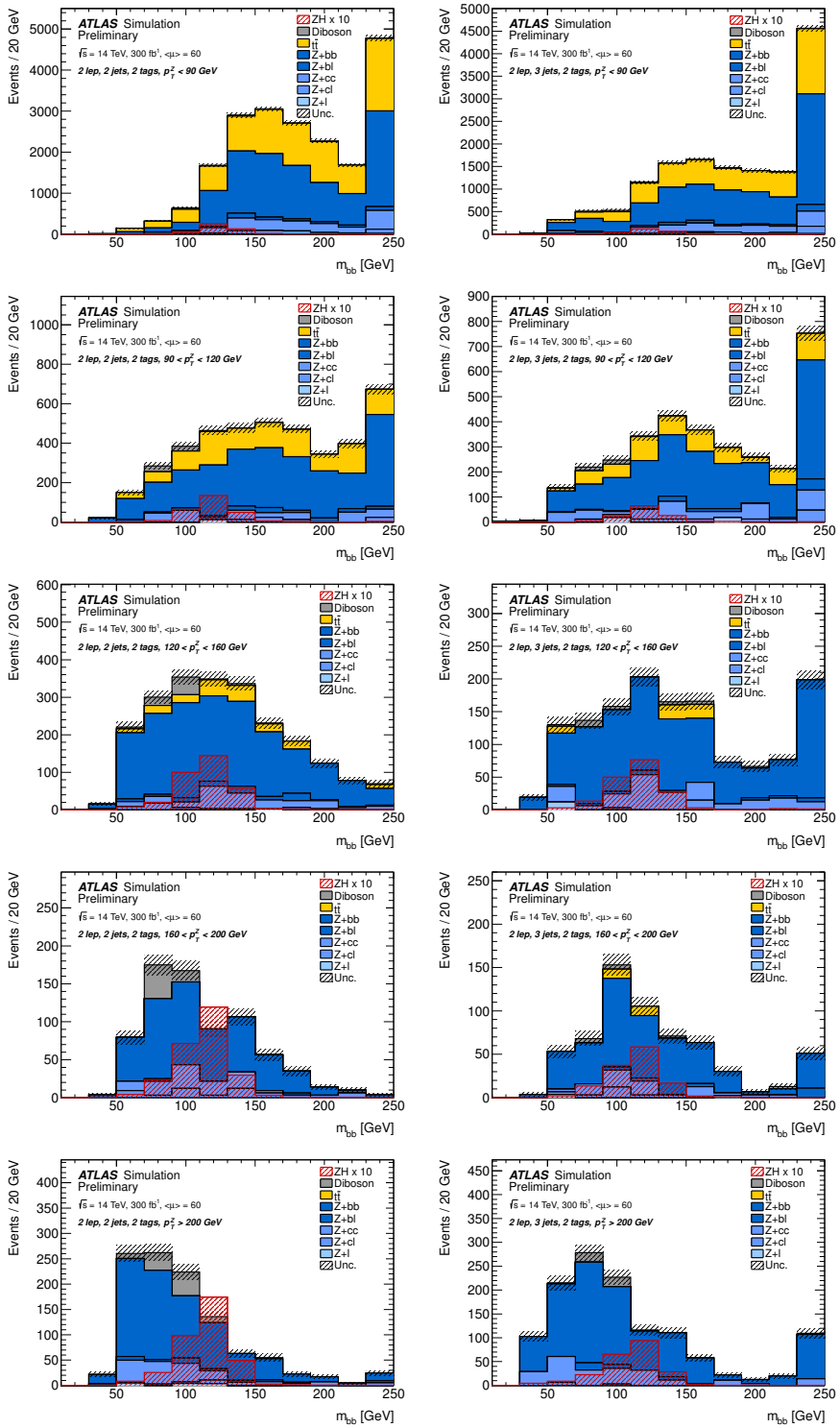

Figure 9.8 m_{bb} distribution for the 2-jet (left) and 3-jet (right) bins of the two-lepton channel for $\sqrt{s} = 14$ TeV, $\langle\mu\rangle = 60$ and an integrated luminosity of 300 fb^{-1}. The entries in overflow are included in the last bin. The Higgs boson signal cross section has been multiplied by a factor of 10. The dashed band corresponds to the statistical uncertainties only.

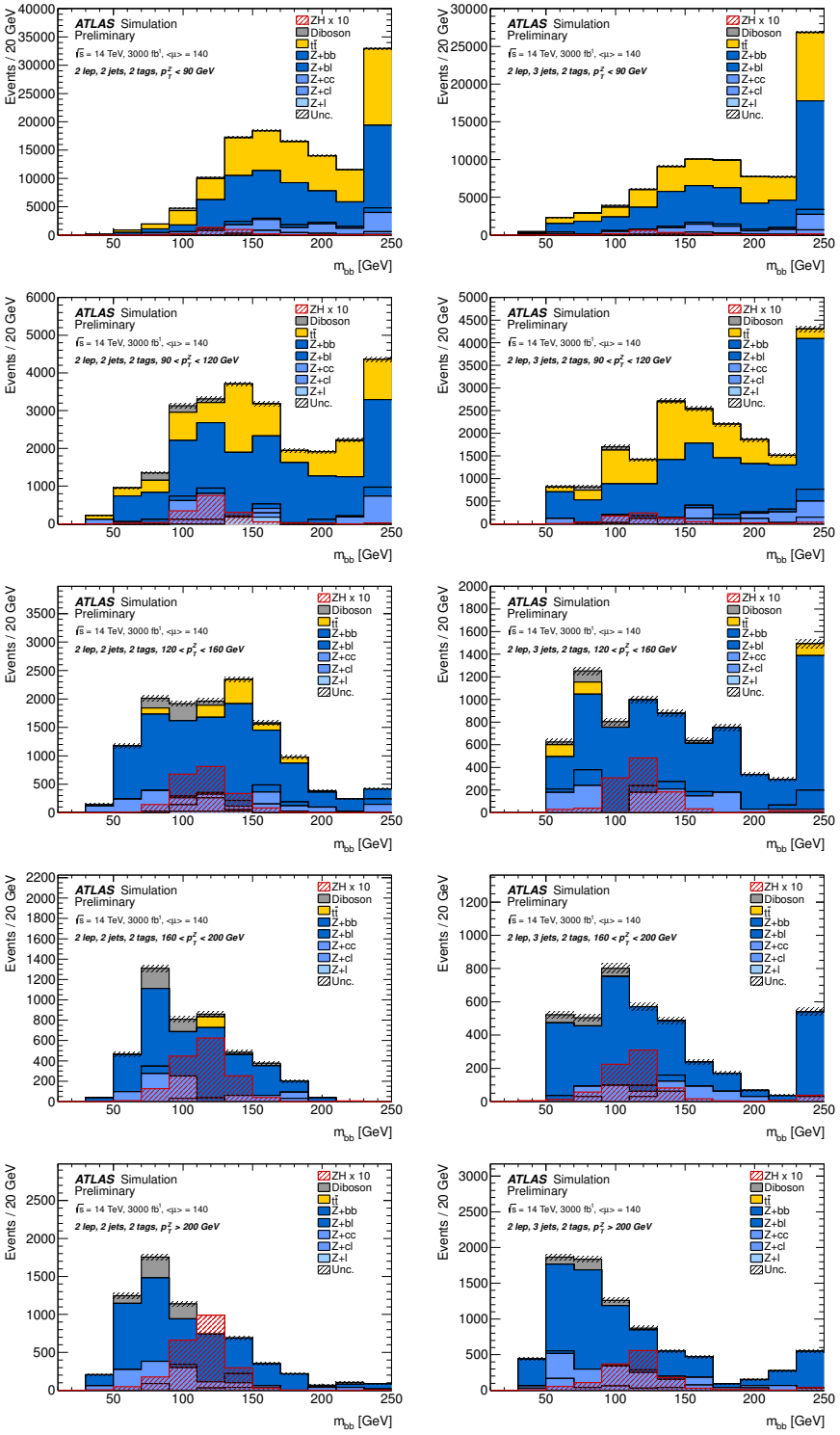

Figure 9.9 m_{bb} distribution for the 2-jet (left) and 3-jet (right) bins of the two-lepton channel for $\sqrt{s} = 14$ TeV, $\langle\mu\rangle = 140$ and an integrated luminosity of 3000 fb^{-1}. The entries in overflow are included in the last bin. The Higgs boson signal cross section has been multiplied by a factor of 10. The dashed band corresponds to the statistical uncertainties only.

9.8 Systematic Uncertainties

The study of systematic uncertainties follows closely the strategy used in the benchmark analysis. Only those systematic uncertainties with a non negligible impact in the benchmark analysis are used to build the simplified model of systematic uncertainties for this analysis. Systematic uncertainties affect the normalisation of the signal or background samples and/or the shapes of the di-b-jet mass distribution. Each systematic uncertainty is considered as a *nuisance parameter* in to the likelihood fit as discussed in Section 9.9.

9.8.1 Experimental Uncertainties

In this analysis only experimental systematic uncertainties on lepton identification, on the jet energy calibration or jet energy scale, on the resolution of the missing transverse energy and the b-tagging efficiencies are considered. Other experimental uncertainties such as on the integrated luminosity were found to have a negligible impact on the analysis.

An uncertainty of $\pm 1\%$ is assigned to the identification efficiencies of the electrons and muons.

The default uncertainties on the JES are taken from studies with $\sqrt{s} = 8$ TeV collision data. These uncertainties are scaled in their p_{T} range by a factor of 14 TeV/8 TeV= 1.75 for the HL-LHC running to approximate what can be expected at higher energy. The 8 TeV input uncertainties are p_{T}- and η-dependent and vary between $\sim 5\%$ for $p_{\mathrm{T}} = 20$ GeV jets in the central region of the detector to $\sim 2\%$ for jets with $p_{\mathrm{T}} = 1$ TeV. The largest component of the JES uncertainty is due to the uncertainty in the quark and gluon flavour composition of jets. The impact on the m_{bb} distribution is illustrated in Figure 9.10.

The large samples of identified b-jets which will be obtained in HL-LHC running can be used to vastly reduce the JES uncertainty. Therefore, the signal expectation has been calculated for a JES uncertainty scenario in which it is 0.1 times the Run 1 estimate. This is in line with scaling of systematic uncertainties by the square-root of the integrated luminosity, $\mathcal{L}^{-\frac{1}{2}}$, performed in other prospects studies [258].

A systematic uncertainty associated to the $E_{\mathrm{T}}^{\mathrm{miss}}$ parametrisation used in this

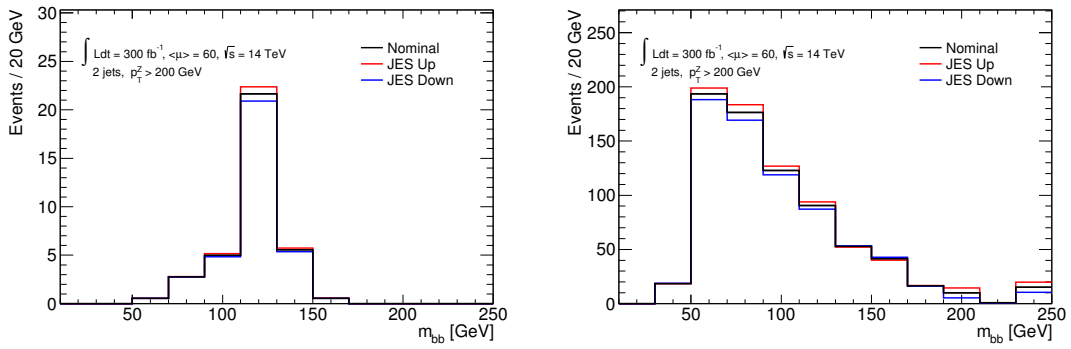

Figure 9.10 Distributions of m_{bb} in the (a) ZH signal and (b) in the dominant $Z + bb$ background samples 2-lepton channel, when applying the jet energy scale systematic uncertainty for $\sqrt{s} = 14$ TeV, $\langle\mu\rangle = 60$ and integrated luminosity of 300 fb^{-1}. The most performant $p_{\mathrm{T}}^{\mathrm{Z}}$ bin in the 2-jet signal region is show as an example

analysis is applied. Two sources of uncertainties are considered [238]: A $\pm 5\%$ variation in the predictions from different MC generators is assumed. Secondly, reconstruction of calorimeter energy clusters depends on the applied threshold to minimise pile-up noise. This threshold was optimised as a function of pile-up. A systematic variation on the threshold of ± 5 GeV was applied, representing the uncertainty in what the exact choice of the threshold during data-taking will be.

The b-tagging uncertainties correspond to those used in the benchmark analysis [20]: the efficiency for b-, c- and light-jets is measured from $\sqrt{s} = 8$ TeV data in dedicated samples. Seven (six) nuisance parameters are used to model the p_{T} dependence of the b-tagging (c-tagging) efficiency uncertainties for b-jets. The mis-tag uncertainty is modelled by a single nuisance parameter. In order to simplify the fit model used in this thesis, only the dominant systematic uncertainty components of the flavour-tagging uncertainties are considered.

In addition a luminosity uncertainty of $\pm 2.8\%$ is used, as obtained from analysis of special runs with beam-separation scans performed in November 2012 [259]. It is applied to all the backgrounds estimated from simulation.

9.8.2 Background Uncertainties

Systematics related to the background modelling are due to the overall normalisation of the cross sections, the relative normalisation of the backgrounds in

the analysis bins (of exclusive jet multiplicities and of p_{T}^{V}) and on the shape of the m_{bb} distributions. The systematic uncertainties affecting the normalisations were taken from the benchmark analysis [20]. These are considered to be a good estimate as the analysis presented in here follows that one closely. Besides the normalisation, only a few of the dominant overall uncertainties were kept, in order to simplify the fitting model. A summary of the variations of the backgrounds is given in Table 9.8.

Background processes are normalised to their repective theoretical cross sections. In most cases an uncertainty of 10% is assigned to this normalisation, as for the $t\bar{t}$, V+light-jets, diboson and multijet backgrounds, and 30% for V+cc and V+bb. Single top is normalised to an approximate NNLO cross section with an uncertainty of 4%, 4% and 7% for the $t-$, $s-$ and Wt channels respectively.

Uncertainties on the shape of m_{bb} reflect the difference in MC generator predictions.

9.8.3 Signal Uncertainties

The uncertainties on the signal cross sections consist of the renormalisation and factorisation scales, $0.5 - 1.5\%$ for qq and 50% for gg induced processes, and the PDFs, 3.8% for $q\bar{q}$ and 17% for gg induced processes [246]. The relative uncertainty on the Higgs boson branching ratio to $b\bar{b}$ is 3.3% for $m_H = 125$ GeV [260].

As described in Section 9.2, a NLO electroweak correction is applied to the qq generated signal as a function of p_{T}^{V}. The uncertainty on these corrections is 2% [20]. It is assumed to be correlated across $p_{\mathrm{T}}^{\mathrm{V}}$ intervals and channels. Uncertainties on the signal acceptance due to variations of scale and PDF of the order of 3-5% are also applied for different jet multiplicity bins. These uncertainties are treated as correlated for qq initial states and decorrelated for $gg \rightarrow$ZH [20].

Background		Normalisation			Shape
		Cross section	2-jet to 3-jet ratio	$p_{\mathrm{T}}^{\mathrm{V}}$	m_{bb}
Diboson	WZ, WW and ZZ	±10%	-	-	-
Multijet		±10%	-	-	-
Single-top	t-channel	±4%	±9%	-	Y
Single-top	s-channel	±4%	±9%	-	Y
Single-top	Wt-production	±7%	±15%	-	Y
V+jets	V+bb production	±30%	±20%	Y	Y
V+jets	V+cc production	±30%	±10%	Y	Y
V+jets	V+light production	±10%	±10%	Y	Y
$t\bar{t}$		±10%	±5%	Y	Y

Table 9.8 A summary of the systematic uncertainties considered on the background samples. The table shows the normalisation uncertainty on each of the backgrounds, between the analysis bins, and whether a shape uncertainty on m_{bb} is considered. For example, on the $t\bar{t}$ background, the central value of the cross section has an uncertainty of ±10%, in addition the ratio of the number of events in the 2-jet bin versus the 3-jet bin is allowed to vary up or down by 5% from the generator prediction, and similarly the numbers of events in successive p_{T}^{V} is allowed to vary. Finally the shape of the m_{bb} distribution used in the fit can vary within certain limits.

9.9 Fit Model

The statistical analysis uses a likelihood function, $\mathcal{L}(\mu, \theta)$, constructed as the product of Poisson probability terms. A signal strength parameter, $\mu = \sigma/\sigma_{\mathrm{SM}}$, multiplies the expected SM Higgs boson production cross section. The impact of systematic uncertainties (see Section 9.8) on the signal and background expectations is described by the set of nuisance parameters, $\boldsymbol{\theta}$, which are parametrised by Gaussian priors. The expected numbers of signal and background events, S_i and B_i, in each bin are functions of $\boldsymbol{\theta}$. N_i denotes the measured histogram bins, S_i and B_i are the signal expectation and background expectation distributions respectively, in bins of i.

The likelihood [261] for a value of μ given N_i, S_i and B_i follows a Poisson distribution and is evaluated over all bins i in the signal region (SR):

$$\mathcal{L}_{\mathrm{SR}}(\mu, \boldsymbol{\theta} | N_i, S_i, B_i) = \prod_i \frac{(\mu S_i + B_i)^{N_i}}{N_i!} \exp\big(- \mu S_i + B_i \big) \tag{9.1}$$

which varies as a function of $\boldsymbol{\theta}$. The likelihood thus depends on the distribution

of each nuisance parameter (NP) which typically follow Gaussian distributions. For each nuisance parameter θ in the set of $\boldsymbol{\theta}$ the distribution is defined by the nominal value of the nuisance parameter, $\bar{\theta}$ and the width of the uncertainty estimate σ_θ as [262]:

$$\mathcal{L}_{\mathrm{NP}}(\theta|\bar{\theta},\sigma_\theta) = \frac{1}{\sqrt{2\pi\sigma_\theta^2}} \exp\Big(\frac{-(\theta-\bar{\theta})^2}{2\sigma_\theta^2}\Big) \tag{9.2}$$

The total likelihood is given by

$$\mathcal{L}(\mu,\boldsymbol{\theta}) = \prod_{\text{histograms}} \mathcal{L}_{\mathrm{SR}}(\mu,\boldsymbol{\theta}|N_i,S_i,B_i) \prod_{\boldsymbol{\theta}} \mathcal{L}_{\mathrm{NP}}(\theta|\bar{\theta},\sigma_\theta) \tag{9.3}$$

Although the likelihood estimator depends on the signal strength and nuisance parameters, one is only interested in the maximum likelihood as function of μ. The nuisance parameters are thus expressed in terms of μ and the maximum likelihood is estimated without determining the best fit values of the nuisance parameters, known as a profile likelihood. The test statistic q_μ of the minimum log likelihood is then constructed according to the profile likelihood ratio:

$$q_\mu = -2\ln\left(\frac{\mathcal{L}(\mu,\hat{\hat{\boldsymbol{\theta}}}_\mu)}{\mathcal{L}(\hat{\mu},\hat{\boldsymbol{\theta}})}\right) \quad , \tag{9.4}$$

where $\hat{\mu}$ and $\hat{\boldsymbol{\theta}}$ are the parameters that maximise the likelihood (with the constraint $0 \leq \hat{\mu} \leq \mu$), and $\hat{\hat{\boldsymbol{\theta}}}_\mu$ are the nuisance parameter values that maximise the likelihood for a given μ. The factor of -2 follows numerical minimisation conventions.

The test is normally used to obtain the best fit value of μ to confirm or reject a signal hypothesis. Here the assumption is made that the signal hypothesis of a SM Higgs boson is true and is in complete agreement with the measurement. As this analysis is performed on simulated data corresponding to a fixed μ=1 and $N_i = S_i + B_i$, the test statistic is only used to obtain the median experimental sensitivity of the search using an *Asimov dataset* as defined in Ref. [261]. The smallest value of q_μ thus corresponds to the best choice of the uncertainty on μ given by the statistical and systematic constraints over all distributions and is a measure of how well a SM Higgs boson signal can be measured. The exclusion intervals are derived with the CLs method, defined in Ref. [263].

The inputs to the Asimov dataset are the m_{bb} distributions in the 18 two-b-tag signal bins (see Table 9.2): ten bins for the two-lepton analysis and eight bins for the one-lepton analysis. The normalisations of the different backgrounds are constrained within their uncertainties as described in Section 9.8.

9.10 Results

The results of the sensitivity study for the 2 lepton channel are presented alongside the 1 lepton channel conducted by collaborators and the combination of both channels. The profile likelihood fit is performed on the simulated datasets to extract the sensitivity over statistical and systematic uncertainties, assuming the SM Higgs boson hypothesis with $m_{\mathrm{H}} = 125$ GeV.

For the $\sqrt{s} = 14$ TeV samples with 300 fb^{-1} with $\langle\mu\rangle = 60$ and 3000 fb^{-1} with $\langle\mu\rangle = 140$, the expected signal sensitivity for $m_{\mathrm{H}} = 125$ GeV as well as the precision on the signal strength measurement for $\mathrm{VH}, \mathrm{H} \to b\bar{b}$ are shown in Tables 9.9 and 9.10. The main systematic uncertainties for the combined analysis for 300 fb^{-1} with $\langle\mu\rangle = 60$ correspond to the jet energy scale systematic and the modelling of the $t\bar{t}$ and W+bb backgrounds, while for 3000 fb^{-1} with $\langle\mu\rangle = 140$ they correspond to theory signal uncertainties (PDF and signal acceptance due to variations of scale) and $t\bar{t}$ modelling. A breakdown of the impact of each systematic uncertainty on the fit result in given in Appendix B.

		One-lepton	**Two-lepton**	**One+Two-lepton**
Stat-only	Significance	2.7	3.0	4.1
	$\hat{\mu}_{\mathrm{Stats}}$ error	$+0.37\ -0.37$	$+0.33\ -0.33$	$+0.25\ -0.25$
Theory-only	$\hat{\mu}_{\mathrm{Theory}}$ error	$+0.08\ -0.05$	$+0.08\ -0.05$	$+0.09\ -0.06$
	Significance	1.2	2.4	2.6
Stat+Theory+Sys	$\hat{\mu}_{\mathrm{w/Theory}}$ error	$+0.86\ -0.85$	$+0.44\ -0.43$	$+0.39\ -0.38$
	$\hat{\mu}_{\mathrm{wo/Theory}}$ error	$+0.85\ -0.85$	$+0.43\ -0.43$	$+0.38\ -0.38$

Table 9.9 Expected signal sensitivity as well as the precision on the signal strength measurement for $m_{\mathrm{H}} = 125$ GeV for the one-lepton, two-lepton and combined searches with 300 fb^{-1} and $\langle\mu\rangle = 60$.

		One-lepton	Two-lepton	One+Two-lepton
Stat-only	Significance	7.7	7.5	10.7
	$\hat{\mu}_{\text{Stats}}$ error	$+0.13\ -0.13$	$+0.14\ -0.13$	$+0.09\ -0.09$
Theory-only	$\hat{\mu}_{\text{Theory}}$ error	$+0.09\ -0.07$	$+0.07\ -0.08$	$+0.07\ -0.07$
	Significance	1.8	5.6	5.9
Stat+Theory+Sys	$\hat{\mu}_{\text{w/Theory}}$ error	$+0.56\ -0.54$	$+0.20\ -0.19$	$+0.19\ -0.19$
	$\hat{\mu}_{\text{wo/Theory}}$ error	$+0.54\ -0.54$	$+0.18\ -0.18$	$+0.18\ -0.17$

Table 9.10 Expected signal sensitivity as well as the precision on the signal strength measurement for $m_H = 125$ GeV for the one-lepton, two-lepton and combined searches with 3000 fb^{-1} with $\langle\mu\rangle = 140$.

Further improvements in the sensitivity can be achieved using multivariate analysis techniques to select events, a jet calibration with better resolution as would be the case for instance using the ATLAS Global Sequential calibration [264, 265], and new b-tagging approaches with improved efficiency such as splitting the events into several categories with different b-flavour purities. An approximate estimate of the impact of such improvements is taken into account, assuming uncertainty reduction factors based on preliminary studies carried out during Run-I analyses.

Tables 9.11 and 9.12 show the final sensitivity results including the perspective of a more performant updated b-tagging strategy and jet calibration and the introduction of a multivariate event selection in the analysis.

		One-lepton	Two-lepton	One+Two-lepton
Stat-only	Significance	5.5	4.6	7.1
	$\hat{\mu}_{\text{Stats}}$ error	$+0.18\ -0.18$	$+0.23\ -0.22$	$+0.14\ -0.14$
Theory-only	$\hat{\mu}_{\text{Theory}}$ error	$+0.08\ -0.05$	$+0.08\ -0.06$	$+0.09\ -0.06$
	Significance	1.8	3.5	3.9
Stat+Theory+Sys	$\hat{\mu}_{\text{w/Theory}}$ error	$+0.57\ -0.57$	$+0.30\ -0.29$	$+0.27\ -0.26$
	$\hat{\mu}_{\text{wo/Theory}}$ error	$+0.56\ -0.57$	$+0.29\ -0.29$	$+0.26\ -0.26$

Table 9.11 Expected signal sensitivity as well as the precision on the signal strength measurement for $m_{\text{H}} = 125$ GeV for the one-lepton, two-lepton and combined searches with 300 fb^{-1} and $\langle\mu\rangle = 60$ after including the perspective of a more performant analysis.

In this context, with an integrated luminosity of 300 fb^{-1}, evidence for VH($\text{H} \to bb$) production will be observed with an expected significance of 3.9 σ. The uncertainty on $\hat{\mu}$ is expected to be $^{+0.27}_{-0.26}$. With an integrated luminosity of 3000 fb^{-1} it can be observed with an expected significance of 8.8 σ and $\Delta\hat{\mu} = \pm 0.14$.

		One-lepton	Two-lepton	One+Two-lepton
Stat-only	Significance	15.4	11.3	19.1
	$\hat{\mu}_{\text{Stats}}$ error	$+0.07\ -0.06$	$+0.09\ -0.09$	$+0.05\ -0.05$
Theory-only	$\hat{\mu}_{\text{Theory}}$ error	$+0.09\ -0.07$	$+0.07\ -0.08$	$+0.07\ -007$
Stat+Theory+Sys	Significance	2.7	8.4	8.8
	$\hat{\mu}_{\text{w/Theory}}$ error	$+0.37\ -0.36$	$+0.15\ -0.15$	$+0.14\ -0.14$
	$\hat{\mu}_{\text{wo/Theory}}$ error	$+0.36\ -0.36$	$+0.14\ -0.12$	$+0.12\ -0.12$

Table 9.12 Expected signal sensitivity as well as the precision on the signal strength measurement for $m_H = 125$ GeVfor the one-lepton, two-lepton and combined searches with 3000 fb^{-1} with $\langle\mu\rangle = 140$ after including the perspective of a more performant analysis.

9.11 Summary

Following the discovery of a Higgs boson with $m_{\text{H}} \sim 125$ GeV by the ATLAS and CMS Collaborations, it is important to understand the prospects for measuring Standard Model Higgs boson processes with the High Luminosity (HL) LHC. For an estimate of the precision with which the SM Higgs boson couplings to other particles can be measured at the HL-LHC several Higgs boson decays have been considered in the past [155, 266]: H$\rightarrow$ ZZ $\rightarrow 4l$, H$\rightarrow \gamma\gamma$ (including VBF, VH and $t\bar{t}$H production), H$\rightarrow$ WW $\rightarrow \ell\nu\ell\nu$, H$\rightarrow \tau\tau$ and H$\rightarrow \mu\mu$, where the latter will only become accessible at the HL-LHC. The experimental uncertainties for the accessible coupling parameters reach 5% for the best cases.

Despite the success of the ATLAS Higgs programme in Run 1, the decay of Higgs boson to bottom quark pairs is not yet established. A vital test of the Standard Model, H $\rightarrow bb$ is the best suited decay channel to directly observe couplings of the Higgs bosons to the quark sector. The study I presented shows that a 5 σ significant measurement of the Higgs boson to bottom quark coupling will not be achievable with the expected 300 fb^{-1} collected at the LHC. An upgrade to the HL-LHC is needed to fully probe the Higgs boson and all its couplings. With a collected luminosity of 3000 fb^{-1} a significant measurement of H $\rightarrow bb$ will be achieved. In light of such large data statistics the measurement will be limited by theoretical and experimental systematic uncertainties. From Tables 9.9 - 9.12 it can be seen that the 2-lepton channel is significantly more performant than the 1-lepton channel, driving the sensitivity of the combined results. At least this is the case when considering the full treatment of the systematic uncertainties. The comparison of the two channels without any systematic uncertainties shows that the 1-lepton channel in particular would benefit from an improvement in the

experimental systematic uncertainties, which would recover much of its signal significance.

An additional improvement can be obtained by including the ZH$\rightarrow \nu\bar{\nu}b\bar{b}$ final state in the analysis, but a careful investigation of the high luminosity prospects in this channel is beyond the scope of this thesis.

Chapter 10

Conclusion

The Higgs boson discovery at the LHC in July 2012 marked the beginning of Higgs boson property measurements. A multitude of measurements have been performed, establishing that the discovered Higgs boson with a mass of 125 GeV is compatible with the Standard Model description. In this thesis I present two studies of Higgs boson properties at the ATLAS detector.

An observation of the $H \to WW$ decay with a significance of 6.1 σ, at the ATLAS detector, was published in December 2014. Following the observation, fiducial differential cross section measurements in the $H \to WW$ channel are presented in this thesis. The $H \to b\bar{b}$ decay has not yet been observed, and the second part of this thesis presents a sensitivity study investigating the prospects of making this observation at ATLAS in the coming LHC runs.

Measurements of fiducial and differential cross sections in the $H \to WW^* \to e\nu\mu\nu$ final state of gluon-fusion Higgs-boson production are presented. They are based on 20.3 fb^{-1} of proton–proton collision data produced at a centre-of-mass energy of $\sqrt{s} = 8$ TeV at the LHC, recorded by the ATLAS detector in 2012. The data is corrected for detector efficiencies and resolution using an iterative Bayesian method. Results are presented in a fiducial region requiring two oppositely charged leptons of different flavour and missing transverse momentum of at least 20 GeV. Additional selection requirements are applied on the dilepton system to select the Higgs boson candidate events. The fiducial cross section of ggF Higgs-boson production is measured to be:

$$\sigma_{\text{ggF}}^{\text{fid}} = 36.0 \pm 7.2(\text{stat}) \pm 6.4(\text{sys}) \pm 1.0(\text{lumi}) \text{ fb} \tag{10.1}$$

for a Higgs boson of mass 125.0 GeV produced in the fiducial region described in Table 8.7. The SM prediction is $\sigma_{\text{ggF}}^{\text{fid}} = 25.1 \pm 2.6\,\text{fb}$. In addition, differential and normalised differential cross sections are measured in the fiducial region as a function of the jet multiplicity, the Higgs boson transverse momentum, the rapidity of the dilepton system, and the transverse momentum of the leading jet, probing the Higgs-boson kinematics and the jet activity produced in association with the Higgs boson.

The first ever fiducial measurement of the jet-veto efficiencies of H+0-jet events are also reported for three different thresholds of the transverse momentum of the leading jet. The presented results agree with the predictions from fixed-order Standard Model calculations and Monte-Carlo generators.

A vital test of the Standard Model description of the Higgs sector is the measurement of the Higgs boson decay to bottom quarks. The ATLAS Run 1 analysis of the 8 TeV data set for this process did not find a significant signal.

A sensitivity study on simulated data for 14 TeV collisions is presented, showing that the observation of $H \to b\bar{b}$ will require a vastly larger data set than collected in Run 1 of the LHC. The study considers Higgs boson production in association with W and Z bosons that, in turn, decay leptonically, resulting in either $ZH \to \ell\ell b\bar{b}$ or $WH \to \ell\nu b\bar{b}$ final states, where ℓ is either an electron or muon. The future detector performance is simulated using parametrised functions to model the behaviour of the upgraded ATLAS detector and the Standard Model expectation of the Higgs boson to bottom quark coupling is assumed.

The expected sensitivity to measure Standard Model $H \to b\bar{b}$ decays, with the 300 fb^{-1} of data gathered at the LHC, is 3.9 σ. A corresponding error on the signal strength, $\hat{\mu}$, the ratio of measured to expected signal yield, was evaluated at $\pm 27\%$. An average pile-up of $\langle\mu\rangle = 60$ was assumed for this data set. The planned upgrade to the High Luminosity LHC (HL-LHC) will provide 3000 fb^{-1}, with which a sensitivity of 8.8 σ and signal strength error of $\pm 14\%$ will be achieved. A projection on the average pile-up of $\langle\mu\rangle = 140$ was assumed for the HL-LHC scenario, which since has been revised to $\langle\mu\rangle = 200$.

Run 2 of the LHC has begun, with higher center-of-mass energy and luminosity than Run 1. Combined with the following Run 3 and the planned HL-LHC program, a total 3000 fb^{-1} of data will be collected, dwarfing the Run 1 data set of 25 fb^{-1}. More measurements will become accessible, with large expected gains in precision and discovery potential. The search for new phenomena such

as supersymmetry or dark matter and the precision study of the Higgs boson will be of high priority for the ATLAS experiment over the next 20 years. Differential cross section measurements of the Higgs boson, as presented in this thesis, will take on increased significance in future runs. With increased statistics, such measurements will become more feasible and also more important, as analyses become limited by systematic and theory uncertainties. The results presented here lay the groundwork for future measurements that will constrain or improve theoretical models and may be used to discover new physics. The large data statistics required to test Higgs boson properties, such as the $H \to b\bar{b}$ coupling discussed in this thesis, strengthens the case for an upgrade of the LHC beyond its original design luminosity.

Bibliography

[1] ATLAS Collaboration, *Measurement of fiducial differential cross sections of gluon-fusion production of Higgs bosons decaying to $WW^* \to e\nu\mu\nu$ with the ATLAS detector at $\sqrt{s} = 8$ TeV*, tech. rep. CERN-EP-2016-019, CERN, 2016, URL: https://cds.cern.ch/record/2145362.

[2] ATLAS Collaboration, *Prospects for the study of the Higgs boson in the VH(bb) channel at HL-LHC*, tech. rep. ATL-PHYS-PUB-2014-011, CERN, 2014, URL: https://cds.cern.ch/record/1740962.

[3] ATLAS Collaboration, *Observation of a new particle in the search for the Standard Model Higgs boson with the ATLAS detector at the LHC*, Phys. Lett. B **716** (2012) 1, arXiv:1207.7214 [hep-ex].

[4] CMS Collaboration, *Observation of a new boson at a mass of 125 GeV with the CMS experiment at the LHC*, Phys. Lett. B **716** (2012) 30, arXiv:1207.7235 [hep-ex].

[5] S. L. Glashow, *Partial-symmetries of weak interactions*, Nucl. Phys. **22** (1961) 579, ISSN: 0029-5582, URL: http://www.sciencedirect.com/science/article/pii/0029558261904692.

[6] S. Weinberg, *A Model of Leptons*, Phys. Rev. Lett. **19** (1967) 1264, ISSN: 0031-9007, URL: http://journals.aps.org/prl/abstract/10.1103/PhysRevLett.19.1264.

[7] G. t. Hooft and M Veltman, *Regularization and renormalization of gauge fields*, Nucl. Phys. B **44** (1972) 189, ISSN: 0550-3213, URL: http://www.sciencedirect.com/science/article/pii/0550321372902799.

[8] F. Englert and R. Brout, *Broken Symmetry and the Mass of Gauge Vector Mesons*, Phys. Rev. Lett. **13** (9 1964) 321, URL: http://link.aps.org/doi/10.1103/PhysRevLett.13.321.

[9] P. W. Higgs, *Broken symmetries, massless particles and gauge fields*, Phys. Lett. **12** (1964) 132, ISSN: 00319163, URL: http://www.sciencedirect.com/science/article/pii/0031916364911369.

[10] P. W. Higgs, *Broken Symmetries and the Masses of Gauge Bosons*, Phys. Rev. Lett. **13** (16 1964) 508, URL: http://link.aps.org/doi/10.1103/PhysRevLett.13.508.

[11] G. S. Guralnik, C. R. Hagen and T. W. B. Kibble, *Global Conservation Laws and Massless Particles*, Phys. Rev. Lett. **13** (20 1964) 585, URL: http://link.aps.org/doi/10.1103/PhysRevLett.13.585.

[12] P. W. Higgs, *Spontaneous Symmetry Breakdown without Massless Bosons*, Phys. Rev. **145** (4 1966) 1156, URL: http://link.aps.org/doi/10.1103/PhysRev.145.1156.

[13] ATLAS Collaboration, *Measurements of the Higgs boson production and decay rates and coupling strengths using pp collision data at $\sqrt{s} = 7$ and 8 TeV in the ATLAS experiment*, Eur. Phys. J. C **76** (2016) 6, arXiv:1507.04548 [hep-ex].

[14] CMS Collaboration, *Precise determination of the mass of the Higgs boson and tests of compatibility of its couplings with the standard model predictions using proton collisions at 7 and 8 TeV*, Eur. Phys. J. C **75** (2015) 212, arXiv:1412.8662 [hep-ex].

[15] ATLAS and CMS Collaborations, *Combined Measurement of the Higgs Boson Mass in pp Collisions at $\sqrt{s} = 7$ and 8 TeV with the ATLAS and CMS Experiments*, Phys. Rev. Lett. **114** (2015) 191803, arXiv:1503.07589 [hep-ex].

[16] ATLAS Collaboration, *Study of the spin and parity of the Higgs boson in diboson decays with the ATLAS detector*, Eur. Phys. J. C **75** (2015) 476, arXiv:1506.05669 [hep-ex].

[17] CMS Collaboration, *Constraints on the spin-parity and anomalous HVV couplings of the Higgs boson in proton collisions at 7 and 8 TeV*, Phys. Rev. D **92** (2015) 012004, arXiv:1411.3441 [hep-ex].

[18] ATLAS Collaboration, *Observation and measurement of Higgs boson decays to WW^* with the ATLAS detector*, Phys. Rev. D **92** (2015) 012006, arXiv:1412.2641 [hep-ex].

[19] ATLAS Collaboration, *Evidence for Higgs-Boson Yukawa couplings in the $H \to \tau\tau$ decay mode with the ATLAS detector*, ATLAS-CONF-2014-061, 2014, URL: http://cdsweb.cern.ch/record/1954724.

[20] ATLAS Collaboration, *Search for the bb decay of the Standard Model Higgs boson in associated W/ZH production with the ATLAS detector*, ATLAS-CONF-2013-079 (), URL: https://cds.cern.ch/record/1563235.

[21] K. A. Olive et al., *Review of Particle Physics*, Chin. Phys. **C38** (2014).

[22] E. Noether, *Invariante Variationsprobleme*, ger, Nachrichten von der Gesellschaft der Wissenschaften zu Goettingen, Mathematisch-Physikalische Klasse **1918** (1918) 235, URL: http://eudml.org/doc/59024.

[23] S. L. Glashow, *Partial Symmetries of Weak Interactions*, Nucl. Phys. **22** (1961) 579.

[24] S. Weinberg, *A Model of Leptons*, Phys. Rev. Lett. **19** (21 1967) 1264, URL: http://link.aps.org/doi/10.1103/PhysRevLett.19.1264.

[25] A. Salam, *Weak and Electromagnetic Interactions*, Conf. Proc. **C680519** (1968) 367.

[26] M. Y. Han and Y. Nambu, *Three-Triplet Model with Double* SU(3) *Symmetry*, Phys. Rev. **139** (4B 1965) B1006, URL: http://link.aps.org/doi/10.1103/PhysRev.139.B1006.

[27] D. Griffiths, *Introduction to Elementary Particles*, John Wiley & Sons, 2008 399, ISBN: 3527618473.

[28] M. Gell-Mann, *A Schematic Model of Baryons and Mesons*, Phys. Lett. **8** (1964) 214.

[29] G. Rajasekaran, *Fermi and the Theory of Weak Interactions*, Resonance J. Sci. Educ. **19** (2014) 18, arXiv:1403.3309 [physics.hist-ph].

[30] T. Y. Cao, *Conceptual Developments of 20th Century Field Theories*, Cambridge University Press, 1998.

[31] C. S. Wu et al., *Experimental Test of Parity Conservation in Beta Decay*, Phys. Rev. **105** (4 1957) 1413, URL: http://link.aps.org/doi/10.1103/PhysRev.105.1413.

[32] E. C. G. Sudarshan and R. E. Marshak, *Chirality Invariance and the Universal Fermi Interaction*, Phys. Rev. **109** (5 1958) 1860, URL: http://link.aps.org/doi/10.1103/PhysRev.109.1860.2.

[33] W. de Boer, "The Discovery of the Higgs Boson with the CMS Detector and its Implications for Supersymmetry and Cosmology", *Time and Matter 2013 (TAM2013) Venice, Italy*, 2013, arXiv:1309.0721 [hep-ph], URL: https://inspirehep.net/record/1252561/files/arXiv:1309.0721.pdf.

[34] J. Goldstone, A. Salam and S. Weinberg, *Broken Symmetries*, Phys. Rev. **127** (3 1962) 965, URL: http://link.aps.org/doi/10.1103/PhysRev.127.965.

[35] Y. Nambu, *Quasi-Particles and Gauge Invariance in the Theory of Superconductivity*, Phys. Rev. **117** (3 1960) 648, URL: http://link.aps.org/doi/10.1103/PhysRev.117.648.

[36] P. W. Anderson, *Plasmons, Gauge Invariance, and Mass*, Phys. Rev. **130** (1 1963) 439, URL: http://link.aps.org/doi/10.1103/PhysRev.130.439.

[37] W. Meissner and R. Ochsenfeld, *Ein neuer Effekt bei Eintritt der Supraleitfähigkeit*, Naturwissenschaften **21** (Nov. 1933) 787.

[38] J. Bardeen, L. N. Cooper and J. R. Schrieffer, *Microscopic Theory of Superconductivity*, Phys. Rev. **106** (1 1957) 162, URL: http://link.aps.org/doi/10.1103/PhysRev.106.162.

[39] A. Doff and C. Siqueira, *Composite Higgs models, Technicolor and the muon anomalous magnetic moment*, Physics Letters B **754** (2016) 294 , ISSN: 0370-2693, URL: http://www.sciencedirect.com/science/article/pii/S0370269316000605.

[40] T. W. B. Kibble, *Symmetry Breaking in Non-Abelian Gauge Theories*, Phys. Rev. **155** (5 1967) 1554, URL: http://link.aps.org/doi/10.1103/PhysRev.155.1554.

[41] Q. R. Ahmad et al., *Direct evidence for neutrino flavor transformation from neutral current interactions in the Sudbury Neutrino Observatory*, Phys. Rev. Lett. **89** (2002) 011301, arXiv:nucl-ex/0204008 [nucl-ex].

[42] J. Ellis, M. K. Gaillard and D. V. Nanopoulos, *A Historical Profile of the Higgs Boson*, (2012), arXiv:1201.6045 [hep-ph].

[43] F. Englert and R. Brout, *Broken symmetry and the mass of gauge vector mesons*, Phys. Rev. Lett. **13** (1964) 321.

[44] P. W. Higgs, *Broken symmetries, massless particles and gauge fields*, Phys. Lett. **12** (1964) 132.

[45] P. W. Higgs, *Broken symmetries and the masses of gauge bosons*, Phys. Rev. Lett. **13** (1964) 508.

[46] G. Guralnik, C. Hagen and T. Kibble, *Global conservation laws and massless particles*, Phys. Rev. Lett. **13** (1964) 585.

[47] P. W. Higgs, *Spontaneous symmetry breakdown without massless bosons*, Phys. Rev. **145** (1966) 1156.

[48] T. Kibble, *Symmetry breaking in non-Abelian gauge theories*, Phys. Rev. **155** (1967) 1554.

[49] ATLAS Collaboration, *Measurements of the Higgs boson production and decay rates and coupling strengths using pp collision data at $\sqrt{s} = 7$ and 8 TeV in the ATLAS experiment*, ATLAS-CONF-2015-007, 2015, URL: http://cdsweb.cern.ch/record/2002212.

[50] J. R. Andersen et al., *Handbook of LHC Higgs Cross Sections: 3. Higgs Properties*, (2013), ed. by S Heinemeyer et al., arXiv:1307.1347 [hep-ph].

[51] CMS Collaboration, *Limits on the Higgs boson lifetime and width from its decay to four charged leptons*, Phys. Rev. D **92** (2015) 072010, ISSN: 1550-7998, arXiv:1507.06656, URL: http://arxiv.org/abs/1507.06656.

[52] CMS Collaboration, *Evidence for the 125 GeV Higgs boson decaying to a pair of τ leptons*, JHEP **05** (2014) 104, arXiv:1401.5041 [hep-ex].

[53] ATLAS Collaboration, *Evidence for the Higgs-boson Yukawa coupling to tau leptons with the ATLAS detector*, JHEP **04** (2015) 117, arXiv:1501.04943 [hep-ex].

[54] Particle Data Group, *Review of Particle Physics*, Chinese Physics C **38** (2014) 090001, URL: http://stacks.iop.org/1674-1137/38/i=9/a=090001.

[55] ATLAS Collaboration, *Observation and measurement of Higgs boson decays to WW^* with ATLAS at the LHC*, ATLAS-CONF-2014-060, 2014, URL: http://cdsweb.cern.ch/record/1954714.

[56] ATLAS Collaboration, *Search for the Standard Model Higgs boson produced in association with a vector boson and decaying to bottom quarks with the ATLAS detector*, ATLAS-CONF-2012-161, 2012, URL: http://cdsweb.cern.ch/record/1493625.

[57] K. G. Wilson, *Confinement of quarks*, Phys. Rev. D **10** (8 1974) 2445, URL: http://link.aps.org/doi/10.1103/PhysRevD.10.2445.

[58] D. J. Gross and F. Wilczek, *Ultraviolet Behavior of Non-Abelian Gauge Theories*, Phys. Rev. Lett. **30** (26 1973) 1343, URL: http://link.aps.org/doi/10.1103/PhysRevLett.30.1343.

[59] K. A. e. a. Olive, *Review of Particle Physics, 2014-2015. Review of Particle Properties*, Chin. Phys. C **38** (2014) 090001. 15 p, All tables, listings, and reviews (and errata) are also available on the Particle Data Group website: http://pdg.lbl.gov, URL: http://cds.cern.ch/record/1753419.

[60] I. Aitchison et al., *Gauge Theories in Particle Physics, Third Edition - 2 volume set*, Graduate Student Series in Physics v. 2, Taylor & Francis, 2004, ISBN: 9780750309820.

[61] R. Placakyte, "Parton Distribution Functions", *Proceedings, 31st International Conference on Physics in collisions (PIC 2011)*, 2011, arXiv:1111.5452 [hep-ph], URL: https://inspirehep.net/record/954990/files/arXiv:1111.5452.pdf.

[62] M. Wing, "Measurements of deep inelastic scattering at HERA", *Proceedings, 32nd International Symposium on Physics in Collision (PIC 2012)*, 2013 93, arXiv:1301.7572 [hep-ex], URL: https://inspirehep.net/record/1217122/files/arXiv:1301.7572.pdf.

[63] V. N. Gribov and L. N. Lipatov, *Deep inelastic e p scattering in perturbation theory*, Sov. J. Nucl. Phys. **15** (1972) 438, [Yad. Fiz.15,781(1972)].

[64] G. Altarelli and G. Parisi, *Asymptotic freedom in parton language*, Nuclear Physics B **126** (1977) 298 , ISSN: 0550-3213, URL: http://www.sciencedirect.com/science/article/pii/0550321377903844.

[65] A. D. Martin et al., *Parton distributions for the LHC*, Eur. Phys. J. **C63** (2009) 189, arXiv:0901.0002 [hep-ph].

[66] J. C. Collins, D. E. Soper and G. F. Sterman, *Factorization of Hard Processes in QCD*, Adv. Ser. Direct. High Energy Phys. **5** (1989) 1, arXiv:hep-ph/0409313 [hep-ph].

[67] Y. Nagashima, *Elementary Particle Physics: Foundations of the Standard Model, Volume 2*, (2013), URL: http://dx.doi.org/10.1002/9783527648887.

[68] M. M. Thomson, *Modern particle physics*, Cambridge University Press, ISBN: 9781107034266.

[69] B. R. Webber, *Fragmentation and hadronization*, Int. J. Mod. Phys. **A15S1** (2000) 577, [,577(1999)], arXiv:hep-ph/9912292 [hep-ph].

[70] J. e. a. Beringer, *Review of Particle Physics**, Phys. Rev. D **86** (1 2012) 010001, URL: http://link.aps.org/doi/10.1103/PhysRevD.86.010001.

[71] G. Corcella et al., *HERWIG 6: An event generator for hadron emission reactions with interfering gluons (including super-symmetric processes)*, JHEP **0101** (2001) 010.

[72] T. Gleisberg et al., *Event generation with SHERPA 1.1*, JHEP **02** (2009) 007, arXiv:0811.4622 [hep-ph].

[73] F. Krauss, R. Kuhn and G. Soff, *AMEGIC++ 1.0: A Matrix element generator in C++*, JHEP **0202** (2002) 044, arXiv:hep-ph/0109036 [hep-ph].

[74] S. Hoeche et al., *QCD matrix elements + parton showers: The NLO case*, JHEP **1304** (2013) 027, arXiv:1207.5030 [hep-ph].

[75] T. Gehrmann et al., *NLO QCD matrix elements + parton showers in $e^+e^- \to$ hadrons*, JHEP **1301** (2013) 144, arXiv:1207.5031 [hep-ph].

[76] S. Hoeche, F. Krauss and M. Schonherr, *Uncertainties in MEPS@NLO calculations of h+jets*, Phys. Rev. **D90** (2014) 014012, arXiv:1401.7971 [hep-ph].

[77] P. S. E. Bagnaschi G. Degrassi and A. Vicini, *Higgs production via gluon fusion in the POWHEG approach in the SM and in the MSSM*, JHEP **1202** (2012) 88, arXiv:1111.2854 [hep-ph].

[78] P. Nason and C. Oleari, *NLO Higgs boson production via vector-boson fusion matched with shower in POWHEG*, JHEP **1002** (2010) 037, arXiv:0911.5299 [hep-ph].

[79] D. Amati and G. Veneziano, *Preconfinement as a property of perturbative QCD*, Physics Letters B **83** (1979) 87 , ISSN: 0370-2693, URL: http://www.sciencedirect.com/science/article/pii/0370269379908967.

[80] B. R. Webber, "Hadronization", *Proceedings: Summer School on Hadronic Aspects of Collider Physics, Zuoz, Switzerland, Aug 23-31, 1994*, 1994, arXiv:hep-ph/9411384 [hep-ph], URL: http://alice.cern.ch/format/showfull?sysnb=0192251.

[81] *Geant4 - a simulation toolkit*, Nuclear Instruments and Methods in Physics Research Section A: Accelerators, Spectrometers, Detectors and Associated Equipment **506** (2003) 250 , ISSN: 0168-9002, URL: http://www.sciencedirect.com/science/article/pii/S0168900203013688.

[82] W. Lukas, *Fast Simulation for ATLAS: Atlfast-II and ISF*, Journal of Physics: Conference Series **396** (2012) 022031, URL: http://stacks.iop.org/1742-6596/396/i=2/a=022031.

[83] P. Nason, *A new method for combining NLO QCD with shower Monte Carlo algorithms*, JHEP **0411** (2004) 040, arXiv:hep-ph/0409146 [hep-ph].

[84] S. Alioli et al., *NLO Higgs boson production via gluon fusion matched with shower in POWHEG*, JHEP **04** (2009) 002, arXiv:0812.0578 [hep-ph].

[85] K. Hamilton et al., *NNLOPS simulation of Higgs boson production*, JHEP **1310** (2013) 222, arXiv:1309.0017 [hep-ph].

[86] K. Hamilton, P. Nason and G. Zanderighi, *Finite quark-mass effects in the NNLOPS POWHEG+MiNLO Higgs generator*, JHEP **05** (2015) 140, arXiv:1501.04637 [hep-ph].

[87] J. Alwall et al., *The automated computation of tree-level and next-to-leading order differential cross sections, and their matching to parton shower simulations*, J. High Energy Phys. **07** (2014) 079, arXiv:1405.0301 [hep-ph].

[88] P. Artoisenet et al., *A framework for Higgs characterisation*, JHEP **11** (2013) 043, arXiv:1306.6464 [hep-ph].

[89] R. Frederix and S. Frixione, *Merging meets matching in MC@NLO*, J. High Energy Phys. **12** (2012) 061, arXiv:1209.6215 [hep-ph].

[90] M. Grazzini and H. Sargsyan, *Heavy-quark mass effects in Higgs boson production at the LHC*, JHEP **09** (2013) 129, arXiv:1306.4581 [hep-ph].

[91] I. W. Stewart and F. J. Tackmann, *Theory Uncertainties for Higgs and Other Searches Using Jet Bins*, Phys. Rev. **D85** (2012) 034011, arXiv:1107.2117 [hep-ph].

[92] R. Boughezal et al., *Combining Resummed Higgs Predictions Across Jet Bins*, Phys. Rev. **D89** (2014) 074044, arXiv:1312.4535 [hep-ph].

[93] I. W. Stewart et al., *Jet p_T resummation in Higgs production at $NNLL' + NNLO$*, Phys. Rev. **D89** (2014) 054001, arXiv:1307.1808.

[94] A. Banfi et al., *Higgs and Z-boson production with a jet veto*, Phys. Rev. Lett. **109** (2012) 202001, arXiv:1206.4998 [hep-ph].

[95] ATLAS Collaboration, *The ATLAS Experiment at the CERN Large Hadron Collider*, JINST **3** (2008) S08003.

[96] CMS collaboration, *The CMS experiment at the CERN LHC*, Journal of Instrumentation **3** (2008) S08004, URL: http://stacks.iop.org/1748-0221/3/i=08/a=S08004.

[97] LHCb Collaboration, *The LHCb Detector at the LHC*, Journal of Instrumentation **3** (2008) S08005, URL: http://stacks.iop.org/1748-0221/3/i=08/a=S08005.

[98] ALICE Collaboration, *The ALICE experiment at the CERN LHC*, Journal of Instrumentation **3** (2008) S08002, URL: http://stacks.iop.org/1748-0221/3/i=08/a=S08002.

[99] LHCf Collaboration, *The LHCf detector at the CERN Large Hadron Collider*, Journal of Instrumentation **3** (2008) S08006, URL: http://stacks.iop.org/1748-0221/3/i=08/a=S08006.

[100] TOTEM Collaboration, *The TOTEM Experiment at the CERN Large Hadron Collider*, Journal of Instrumentation **3** (2008) S08007, URL: http://stacks.iop.org/1748-0221/3/i=08/a=S08007.

[101] MoEDAL Collaboration, *Technical Design Report of the MoEDAL Experiment*, tech. rep. CERN-LHCC-2009-006. MoEDAL-TDR-001, CERN, 2009, URL: https://cds.cern.ch/record/1181486.

[102] L. Evans and P. Bryant, *LHC Machine*, Journal of Instrumentation **3** (2008) S08001, URL: http://stacks.iop.org/1748-0221/3/i=08/a=S08001.

[103] S. Myers and E. Picasso, *The design, construction and commissioning of the CERN large Electron–Positron collider*, Contemporary Physics **31** (1990) 387, eprint: http://dx.doi.org/10.1080/00107519008213789, URL: http://dx.doi.org/10.1080/00107519008213789.

[104] F. Marcastel, *CERN's Accelerator Complex.*, (2013), URL: https://cds.cern.ch/record/1621583.

[105] O. S. Bruning et al., *LHC Design Report Vol.1: The LHC Main Ring*, (2004).

[106] R. Perin, *Status of LHC programme and magnet development*, IEEE Transactions on Applied Superconductivity **5** (1995) 189, ISSN: 1051-8223.

[107] ATLAS Collaboration, *Luminosity Results*, (2010-2012), URL: https://twiki.cern.ch/twiki/bin/view/AtlasPublic/LuminosityPublicResults.

[108] ATLAS Collaboration, *Event Displays*, (2010-2012), URL: https://twiki.cern.ch/twiki/bin/view/AtlasPublic/EventDisplayStandAlone.

[109] ATLAS Collaboration, *Improved luminosity determination in pp collisions at $\sqrt{s} = 7$ TeV using the ATLAS detector at the LHC.*, Eur. Phys. journal. C, Part. fields **73** (2013) 2518, ISSN: 1434-6044, eprint: 1302.4393, URL: http://arxiv.org/abs/1302.4393.

[110] ATLAS Collaboration, *ATLAS Photos*, (2016), URL: http://atlas.ch/photos/index.html.

[111] B. Wynne, "private communication", 2015.

[112] J. Pequenao, "Computer generated image of the ATLAS inner detector", 2008, URL: https://cds.cern.ch/record/1095926.

[113] A. Collaboration, *ATLAS pixel detector electronics and sensors*, J. Instrum. **3** (2008) P07007, URL: http://stacks.iop.org/1748-0221/3/i=07/a=P07007.

[114] A et al Ahmad, *The silicon microstrip sensors of the {ATLAS} semiconductor tracker*, Nucl. Instruments Methods Phys. Res. Sect. A Accel. Spectrometers, Detect. Assoc. Equip. **578** (2007) 98, ISSN: 0168-9002, URL: http://www.sciencedirect.com/science/article/pii/S0168900207007644.

[115] B. Mindur, {*ATLAS*} *Transition Radiation Tracker (TRT): Straw tubes for tracking and particle identification at the Large Hadron Collider*, Nuclear Instruments and Methods in Physics Research Section A: Accelerators, Spectrometers, Detectors and Associated Equipment (2016) –, ISSN: 0168-9002, URL: http://www.sciencedirect.com/science/article/pii/S0168900216301905.

[116] T. Petersen, *Public TRT Plots for Collision Data: Notes of explanation*, July 2014, URL: https://twiki.cern.ch/twiki/pub/AtlasPublic/TRTPublicResults/TRTetaPID.png.

[117] L. Hervas, "The ATLAS liquid argon electromagnetic calorimeter: construction., commissioning and elected test beam results", *Instrumentation and Measurement Technology Conference, 2004. IMTC 04. Proceedings of the 21st IEEE*, vol. 2, 2004 1257.

[118] H. Wilkens and the ATLAS LArg Collaboration, *The ATLAS Liquid Argon calorimeter: An overview*, Journal of Physics: Conference Series **160** (2009) 012043, URL: http://stacks.iop.org/1742-6596/160/i=1/a=012043.

[119] P. Adragna, *The ATLAS hadronic Tile Calorimeter: From construction toward physics*, IEEE Trans. Nucl. Sci. **53** (2006) 1275, ISSN: 00189499.

[120] *ATLAS muon spectrometer: Technical Design Report*, Technical Design Report ATLAS, Geneva: CERN, 1997, URL: https://cds.cern.ch/record/331068.

[121] G. Chiodini, N. Orlando and S. Spagnolo, "ATLAS RPC time-of-flight performance", CERN, Geneva: CERN, 2012, URL: http://cdsweb.cern.ch/record/1437020/files/ATL-MUON-PROC-2012-002.pdf.

[122] A Nisati, *An Integrated RPC and TGC Detector for the ATLAS Muon Trigger*, tech. rep. ATL-MUON-94-042. ATL-M-PN-42, CERN, 1994, URL: https://cds.cern.ch/record/685822.

[123] T. Suigmoto et al., "Cosmic ray test system for the ATLAS thin gap chamber modules at KOBE", *Nuclear Science Symposium Conference Record, 2003 IEEE*, vol. 5, 2003 3740.

[124] ATLAS Collaboration.

[125] ATLAS Collaboration, *Performance of the ATLAS Trigger System in 2010*, Eur. Phys. J. C **72** (2012) 1849, arXiv:1110.1530 [hep-ex].

[126] P. Jenni et al., *ATLAS Forward Detectors for Measurement of Elastic Scattering and Luminosity*, Technical Design Report ATLAS, Geneva: CERN, 2008, URL: https://cds.cern.ch/record/1095847.

[127] V Cindro et al., *The ATLAS Beam Conditions Monitor*, Journal of Instrumentation **3** (2008) P02004, URL: http://stacks.iop.org/1748-0221/3/i=02/a=P02004.

[128] R. G. Newton, *Optical theorem and beyond*, American Journal of Physics **44** (1976) 639, URL: http://scitation.aip.org/content/aapt/journal/ajp/44/7/10.1119/1.10324.

[129] A Sopczak, *Luminosity monitoring in ATLAS with MPX detectors*, en, J. Instrum. **9** (2014) C01027, ISSN: 1748-0221, URL: http://iopscience.iop.org/article/10.1088/1748-0221/9/01/C01027.

[130] V. Balagura, *Notes on van der Meer Scan for Absolute Luminosity Measurement*, Nucl. Instrum. Meth. **A654** (2011) 634, arXiv:1103.1129 [physics.ins-det].

[131] *Alignment of the ATLAS Inner Detector and its Performance in 2012*, tech. rep. ATLAS-CONF-2014-047, CERN, 2014, URL: https://cds.cern.ch/record/1741021.

[132] ATLAS Collaboration, *Electron and photon energy calibration with the ATLAS detector using LHC Run 1 data*, Eur. Phys. J. C **74** (2014) 3071, ISSN: 1434-6044, URL: http://arxiv.org/abs/1407.5063.

[133] S Sacerdoti, G Otero y Garzon and R Piegaia, *Jet momentum resolution with the ATLAS detector in proton-proton collisions at $\sqrt{s}$ = 8 TeV recorded in 2012.*, tech. rep. ATL-COM-PHYS-2014-010, CERN, 2014, URL: https://cds.cern.ch/record/1642375.

[134] ATLAS collaboration, *Measurement of the muon reconstruction performance of the ATLAS detector using 2011 and 2012 LHC proton-proton collision data.*, Eur. Phys. journal. C, Part. fields **74** (2014) 3130, ISSN: 1434-6044, URL: http://arxiv.org/abs/1407.3935.

[135] T Cornelissen et al., *The new ATLAS track reconstruction (NEWT)*, Journal of Physics: Conference Series **119** (2008) 032014, URL: http://stacks.iop.org/1742-6596/119/i=3/a=032014.

[136] ATLAS Collaboration, *Expected performance of the ATLAS experiment: detector, trigger and physics*, (2009), URL: https://cds.cern.ch/record/1125884.

[137] G Piacquadio, K Prokofiev and A Wildauer, *Primary vertex reconstruction in the ATLAS experiment at LHC*, Journal of Physics: Conference Series **119** (2008) 032033, URL: http://stacks.iop.org/1742-6596/119/i=3/a=032033.

[138] E. Bouhova-Thacker et al., *Expected Performance of Vertex Reconstruction in the ATLAS Experiment at the LHC*, Nuclear Science, IEEE Transactions on **57** (2010) 760.

[139] ATLAS Collaboration, *Electron reconstruction and identification efficiency measurements with the ATLAS detector using the 2011 LHC proton–proton collision data*, Eur. Phys. J. C **74** (2014) 2941, arXiv:1404.2240 [hep-ex].

[140] ATLAS Collaboration, *Electron efficiency measurements with the ATLAS detector using the 2012 LHC proton–proton collision data*, ATLAS-CONF-2014-032, 2014, URL: http://cdsweb.cern.ch/record/1706245.

[141] ATLAS Collaboration, *Electron and photon energy calibration with the ATLAS detector using LHC Run 1 data*, Eur. Phys. J. C **74** (2014) 3071, arXiv:1407.5063 [hep-ex].

[142] ATLAS Collaboration, *Topological cell clustering in the ATLAS calorimeters and its performance in LHC Run 1*, (2016), arXiv:1603.02934 [hep-ex].

[143] M. Cacciari, G. P. Salam and G. Soyez, *The Anti-k(t) jet clustering algorithm*, JHEP **04** (2008) 063, arXiv:0802.1189 [hep-ph].

[144] ATLAS Collaboration, *Jet energy measurement with the ATLAS detector in proton-proton collisions at $\sqrt{s} = 7$ TeV*, Eur. Phys. J. **C73** (2013) 2304, arXiv:1112.6426 [hep-ex].

[145] S. D. Ellis and D. E. Soper, *Successive combination jet algorithm for hadron collisions*, Phys. Rev. **D48** (1993) 3160, arXiv:hep-ph/9305266 [hep-ph].

[146] M. Wobisch and T. Wengler, "Hadronization corrections to jet cross-sections in deep inelastic scattering", *Monte Carlo generators for HERA physics. Proceedings, Workshop, Hamburg, Germany, 1998-1999*, 1998, arXiv:hep-ph/9907280 [hep-ph], URL: https://inspirehep.net/record/484872/files/arXiv:hep-ph_9907280.pdf.

[147] ATLAS Collaboration, *Jet energy measurement and its systematic uncertainty in proton–proton collisions at $\sqrt{s} = 7$ TeV with the ATLAS detector*, Eur. Phys. J. C **75** (2015) 17, arXiv:1406.0076 [hep-ex].

[148] ATLAS Collaboration, *Pile-up corrections for jets from proton–proton collisions at $\sqrt{s} = 7$ TeV in ATLAS in 2011*, ATLAS-CONF-2012-064, 2012, URL: http://cdsweb.cern.ch/record/1459529.

[149] ATLAS Collaboration, *Jet energy measurement with the ATLAS detector in proton–proton collisions at $\sqrt{s} = 7$ TeV*, Eur. Phys. J. C **73** (2013) 2304, arXiv:1112.6426 [hep-ex].

[150] ATLAS Collaboration, *Commissioning of the ATLAS high performance b-tagging algorithms in the 7 TeV collision data*, ATLAS-CONF-2011-102, 2011, URL: http://cdsweb.cern.ch/record/1369219.

[151] ATLAS Collaboration, *Calibration of b-tagging using dileptonic top pair events in a combinatorial likelihood approach with the ATLAS experiment*, ATLAS-CONF-2014-004, 2014, URL: http://cdsweb.cern.ch/record/1664335.

[152] ATLAS Collaboration, *Performance of Missing Transverse Momentum Reconstruction in Proton-Proton Collisions at 7 TeV with ATLAS*, Eur. Phys. J. **C72** (2012) 1844, arXiv:1108.5602 [hep-ex].

[153] HiLumi LHC Collaboration, *HL-LHC Preliminary Design Report: Deliverable: D1.5*, (2014), URL: https://cds.cern.ch/record/1972604.

[154] ATLAS Collaboration, *A study of Standard Model Higgs boson production in the decay mode $H \to b\bar{b}$ in association with a W or Z boson for High Luminosity LHC Running*, ATL-PHYS-PUB-2014-011, 2014, URL: https://atlas.web.cern.ch/Atlas/GROUPS/PHYSICS/PUBNOTES/ATL-PHYS-PUB-2014-011.

[155] ATLAS Collaboration, *Projections for measurements of Higgs boson cross sections, branching ratios and coupling parameters with the ATLAS detector at a HL-LHC*, ATL-PHYS-PUB-2013-014, 2013, URL: http://cdsweb.cern.ch/record/1611186.

[156] ATLAS Collaboration, *Projections for measurements of Higgs boson signal strengths and coupling parameters with the ATLAS detector at the HL-LHC*, ATL-PHYS-PUB-2014-016, 2014, URL: http://cdsweb.cern.ch/record/1956710.

[157] ATLAS Collaboration, *Prospects for New Physics in Higgs Couplings Studies with the ATLAS Detector at the HL-LHC*, ATL-PHYS-PUB-2014-017, 2014, URL: http://cdsweb.cern.ch/record/1956711.

[158] ATLAS Collaboration, *Prospects for measuring Higgs pair production in the channel $H(\rightarrow \gamma\gamma)H(\rightarrow b\bar{b})$ using the ATLAS detector at the HL-LHC*, ATL-PHYS-PUB-2014-019, 2014, URL: http://cdsweb.cern.ch/record/1956733.

[159] ATLAS Collaboration, *Prospects for benchmark Supersymmetry searches at the high luminosity LHC with the ATLAS Detector*, ATL-PHYS-PUB-2013-011, 2013, URL: http://cdsweb.cern.ch/record/1604505.

[160] ATLAS Collaboration, *Prospect for a search for direct pair production of a chargino and a neutralino decaying via a W boson and the lightest Higgs boson in final states with one lepton, two b-jets and missing transverse momentum at the high luminosity LHC with the ATLAS Detector.*, tech. rep. ATL-PHYS-PUB-2015-032, CERN, 2015, URL: http://cds.cern.ch/record/2038565.

[161] ATLAS Collaboration, *Dijet resonance searches with the ATLAS detector at 14 TeV LHC*, ATL-PHYS-PUB-2015-004, 2015, URL: http://cdsweb.cern.ch/record/2002136.

[162] ATLAS Collaboration, *Physics at a High-Luminosity LHC with ATLAS*, ATL-PHYS-PUB-2013-007, 2013, URL: http://cdsweb.cern.ch/record/1564937.

[163] C. O'Luanaigh, *Restarting the LHC: Why 13 Tev?*, (2014), URL: http://cds.cern.ch/record/1998739.

[164] H Damerau et al., *LHC Injectors Upgrade, Technical Design Report, Vol. I: Protons*, tech. rep. CERN-ACC-2014-0337, CERN, 2014, URL: https://cds.cern.ch/record/1976692.

[165] A. D. Rosso, *HL-LHC updates in Japan. Projet HL-LHC : une réunion fait le point au Japon*, (2014) 4, URL: https://cds.cern.ch/record/1975962.

[166] R. Calaga, *Crab Cavities for the LHC Upgrade*, 2012, URL: https://cds.cern.ch/record/1493034.

[167] Z Li, *Radiation damage effects in Si materials and detectors and rad-hard Si detectors for SLHC*, Journal of Instrumentation **4** (2009) P03011, URL: http://stacks.iop.org/1748-0221/4/i=03/a=P03011.

[168] ATLAS Collaboration, *Letter of Intent for the Phase-II Upgrade of the ATLAS Experiment*, tech. rep. CERN-LHCC-2012-022. LHCC-I-023, Draft version for comments: CERN, 2012, URL: https://cds.cern.ch/record/1502664.

[169] M Capeans et al., *ATLAS Insertable B-Layer Technical Design Report*, tech. rep. CERN-LHCC-2010-013. ATLAS-TDR-19, CERN, 2010, URL: https://cds.cern.ch/record/1291633.

[170] Y. Rodina, *ATLAS b-tagging performance during LHC Run 2 with the new Insertable B-layer*, tech. rep. ATL-PHYS-PROC-2015-179, CERN, 2015, URL: https://cds.cern.ch/record/2112120.

[171] J. Lange, *Recent Progress on 3D Silicon Detectors*, PoS **VERTEX2015** (2015) 026, arXiv:1511.02080 [physics.ins-det].

[172] T Kawamoto et al., *New Small Wheel Technical Design Report*, tech. rep. CERN-LHCC-2013-006. ATLAS-TDR-020, ATLAS New Small Wheel Technical Design Report: CERN, 2013, URL: https://cds.cern.ch/record/1552862.

[173] M Shochet et al., *Fast TracKer (FTK) Technical Design Report*, tech. rep. CERN-LHCC-2013-007. ATLAS-TDR-021, ATLAS Fast Tracker Technical Design Report: CERN, 2013, URL: https://cds.cern.ch/record/1552953.

[174] A. Annovi et al., *Development of FTK architecture: a fast hardware track trigger for the ATLAS detector*, (2009), arXiv:0910.1126 [physics.ins-det].

[175] T Iizawa, *The ATLAS FTK system: how to improve the physics potential with a tracking trigger*, tech. rep. ATL-DAQ-PROC-2014-034, CERN, 2014, URL: https://cds.cern.ch/record/1954071.

[176] ATLAS Collaboration, *ATLAS Phase-II Upgrade Scoping Document*, tech. rep. CERN-LHCC-2015-020. LHCC-G-166, CERN, 2015, URL: https://cds.cern.ch/record/2055248.

[177] R. Bates, *ATLAS pixel upgrade for the HL-LHC*, PoS **VERTEX2015** (2015) 006.

[178] C. Garcia-Argos, *The ATLAS ITk Strip Detector. Status of R&D*, tech. rep. ATL-UPGRADE-PROC-2016-001, CERN, 2016, URL: https://cds.cern.ch/record/2139342.

[179] I. Perić et al., *Overview of HVCMOS pixel sensors*, Journal of Instrumentation **10** (2015) C05021, URL: http://stacks.iop.org/1748-0221/10/i=05/a=C05021.

[180] A. S. Cerqueira, *Tile Calorimeter Upgrade Program for the Luminosity Increasing at the LHC*, (2015), arXiv:1509.08994 [physics.ins-det].

[181] A. Gomes, *The new front-end electronics for the ATLAS Tile Calorimeter Phase 2 Upgrade*, Journal of Instrumentation **11** (2016) C02015, URL: http://stacks.iop.org/1748-0221/11/i=02/a=C02015.

[182] V. Blobel, "An Unfolding method for high-energy physics experiments", *Advanced Statistical Techniques in Particle Physics. Proceedings, Conference, Durham, UK, March 18-22, 2002*, 2002 258, arXiv:hep-ex/0208022 [hep-ex], URL: http://www.ippp.dur.ac.uk/Workshops/02/statistics/proceedings//blobel2.pdf.

[183] I. Nedelkov, *Improper problems in computational physics*, Computer Physics Communications **4** (1972) 157 , ISSN: 0010-4655, URL: http://www.sciencedirect.com/science/article/pii/0010465572900021.

[184] G. D'Agostini, *A Multidimensional unfolding method based on Bayes' theorem*, Nucl. Instrum. Meth. **A362** (1995) 487.

[185] T. Adye, *Unfolding algorithms and tests using RooUnfold*, ArXiv (2011) 6, arXiv:1105.1160, URL: http://arxiv.org/abs/1105.1160.

[186] ATLAS Collaboration, *Fiducial and differential cross sections of Higgs boson production measured in the four-lepton decay channel in pp collisions at $\sqrt{s} = 8$ TeV with the ATLAS detector*, Phys. Lett. B **738** (2014) 234, arXiv:1408.3226 [hep-ex].

[187] CMS Collaboration, *Measurement of inclusive and differential fiducial cross sections for Higgs boson production in the H-to-4l decay channel in p-p collisions at 7 TeV and 8 TeV*, tech. rep. CMS-PAS-HIG-14-028, CERN, 2015, URL: https://cds.cern.ch/record/2040210.

[188] ATLAS Collaboration, *Measurements of fiducial and differential cross sections for Higgs boson production in the diphoton decay channel at $\sqrt{s} = 8$ TeV with ATLAS*, JHEP **1409** (2014) 112, arXiv:1407.4222 [hep-ex].

[189] CMS Collaboration, *Measurement of differential cross sections for Higgs boson production in the diphoton decay channel in pp collisions at $\sqrt{s} = 8$ TeV*, (2015), arXiv:1508.07819 [hep-ex].

[190] ATLAS Collaboration, *Measurements of the Total and Differential Higgs Boson Production Cross Sections Combining the $H \to \gamma\gamma$ and $H \to ZZ^* \to 4\ell$ Decay Channels at $\sqrt{s} = 8$ TeV with the ATLAS Detector*, Phys. Rev. Lett. **115** (2015) 091801, arXiv:1504.05833 [hep-ex].

[191] CMS Collaboration, *Measurement of the transverse momentum spectrum of the Higgs boson produced in pp collisions at $\sqrt{s} = 8$ TeV using the H→WW decays*, tech. rep. CMS-PAS-HIG-15-010, CERN, 2015, URL: https://cds.cern.ch/record/2116452.

[192] ATLAS Collaboration, *Measurements of Higgs boson production and couplings in diboson final states with the ATLAS detector at the LHC*, Physics Letters B **726** (2013) 88 , ISSN: 0370-2693, URL: http://www.sciencedirect.com/science/article/pii/S0370269313006369.

[193] D. de Florian et al., *Higgs boson production at the LHC: transverse momentum resummation effects in the H→2gamma, H→WW→lnu lnu and H→ZZ→4l decay modes*, JHEP **06** (2012) 132, arXiv:1203.6321 [hep-ph].

[194] A. Banfi et al., *Jet-vetoed Higgs cross section in gluon fusion at N^3LO+NNLL with small-R resummation*, JHEP **04** (2016) 049, arXiv:1511.02886 [hep-ph].

[195] A. Banfi et al., *Higgs and Z-boson production with a jet veto*, Phys. Rev. Lett. **109** (2012) 202001, arXiv:1206.4998 [hep-ph].

[196] H.-L. Lai et al., *New parton distributions for collider physics*, Phys. Rev. D **82** (2010) 074024, arXiv:1007.2241 [hep-ph].

[197] ATLAS Collaboration, *Summary of ATLAS Pythia 8 tunes*, ATL-PHYS-PUB-2012-003, 2012, URL: http://cds.cern.ch/record/1474107.

[198] K. Hamilton, P. Nason and G. Zanderighi, *MINLO: Multi-Scale Improved NLO*, JHEP **1210** (2012) 155, arXiv:1206.3572 [hep-ph].

[199] J. M. Campbell, R. K. Ellis and C. Williams, *Gluon-Gluon Contributions to W+ W- Production and Higgs Interference Effects*, JHEP **10** (2011) 005, arXiv:1107.5569 [hep-ph].

[200] J. M. Campbell, R. K. Ellis and C. Williams, *Bounding the Higgs width at the LHC: Complementary results from $H \to WW$*, Phys. Rev. **D89** (2014) 053011, arXiv:1312.1628 [hep-ph].

[201] T. Sjöstrand, S. Mrenna, and P. Z. Skands, *PYTHIA 6.4 physics and manual*, JHEP **0605** (2006) 026, arXiv:hep-ph/0603175.

[202] P. Z. Skands, *Tuning Monte Carlo Generators: The Perugia Tunes*, Phys. Rev. **D82** (2010) 074018, arXiv:1005.3457 [hep-ph].

[203] M. L. Mangano et al., *ALPGEN, a generator for hard multi-parton processes in hadronic collisions*, JHEP **0307** (2003) 001, arXiv:hep-ph/0206293.

[204] ATLAS Collaboration, *New ATLAS event generator tunes to 2010 data*, ATL-PHYS-PUB-2011-008, 2011, URL: http://cds.cern.ch/record/1345343.

[205] P. M. Nadolsky et al., *Implications of CTEQ global analysis for collider observables*, Phys. Rev. **D78** (2008) 013004, arXiv:0802.0007 [hep-ph].

[206] A. Sherstnev and R. S. Thorne, *Parton Distributions for LO Generators*, Eur. Phys. J. **C55** (2008) 553, arXiv:0711.2473 [hep-ph].

[207] ATLAS Collaboration, *The ATLAS Simulation Infrastructure*, Eur. Phys. J. C **70** (2010) 823, arXiv:1005.4568 [hep-ex].

[208] ATLAS Collaboration, *The simulation principle and performance of the ATLAS fast calorimeter simulation FastCaloSim*, ATL-PHYS-PUB-2010-013, 2010, URL: http://cds.cern.ch/record/1300517.

[209] ATLAS Collaboration, *Measurement of the muon reconstruction performance of the ATLAS detector using 2011 and 2012 LHC proton–proton collision data*, Eur. Phys. J. C **74** (2014) 3130, arXiv:1407.3935 [hep-ex].

[210] W Lampl et al., *Calorimeter Clustering Algorithms: Description and Performance*, ATL-LARG-PUB-2008-002, 2008, URL: http://cds.cern.ch/record/1099735.

[211] ATLAS Collaboration, *Tagging and suppression of pileup jets with the ATLAS detector*, ATLAS-CONF-2014-018, 2014, URL: http://cdsweb.cern.ch/record/1700870.

[212] M. Cacciari, G. P. Salam and G. Soyez, *The anti-k_t jet clustering algorithm*, JHEP **0804** (2008) 063, arXiv:0802.1189 [hep-ex].

[213] ATLAS Collaboration, *Calibration of the performance of b-tagging for c and light-flavour jets in the 2012 ATLAS data*, ATLAS-CONF-2014-046, 2014, URL: http://cdsweb.cern.ch/record/1741020.

[214] T. Plehn, D. L. Rainwater and D. Zeppenfeld, *A Method for identifying $H \to \tau^+\tau^- \to e^\pm\mu^\mp p_T$ at the CERN LHC*, Phys. Rev. **D61** (2000) 093005, arXiv:hep-ph/9911385 [hep-ph].

[215] J. M. Campbell, R. K. Ellis and G. Zanderighi, *Next-to-Leading order Higgs + 2 jet production via gluon fusion*, JHEP **0610** (2006) 028, arXiv:hep-ph/0608194 [hep-ph].

[216] T. Gehrmann et al., *W^+W^- Production at Hadron Colliders in Next to Next to Leading Order QCD*, Phys. Rev. Lett. **113** (2014) 212001, arXiv:1408.5243 [hep-ph].

[217] ATLAS Collaboration, *Measurement of total and differential W^+W^- production cross sections in proton-proton collisions at $\sqrt{s} = 8$ TeV with the ATLAS detector and limits on anomalous triple-gauge-boson couplings*, (2016), arXiv:1603.01702 [hep-ex].

[218] P. R. Bevington, *Data reduction and error analysis for the physical sciences*, 1969.

[219] ATLAS Collaboration, *Calibration of the performance of b-tagging for c and light-flavour jets in the 2012 ATLAS data*, tech. rep. ATLAS-CONF-2014-046, CERN, 2014, URL: https://cds.cern.ch/record/1741020.

[220] ATLAS Collaboration, *Electron reconstruction and identification efficiency measurements with the ATLAS detector using the 2011 LHC proton-proton collision data*, Eur. Phys. J. **C74** (2014) 2941, arXiv:1404.2240 [hep-ex].

[221] ATLAS Collaboration, *A measurement of the ATLAS muon reconstruction and trigger efficiency using J/ψ decays*, ATLAS-CONF-2011-021, 2011, URL: http://cdsweb.cern.ch/record/1336750.

[222] J. Stirling, *key plots*, Hepforge.org (2016), URL: http://http://mstwpdf.hepforge.org/plots/plots.html.

[223] LHC Higgs cross section working group, *Handbook of LHC Higgs Cross Sections: 2. Differential Distributions*, CERN-2012-002 (2012), arXiv:1201.3084 [hep-ph].

[224] J. R. Andersen et al., *Les Houches 2013: Physics at TeV Colliders: Standard Model Working Group Report*, (2014), arXiv:1405.1067 [hep-ph].

[225] A. D. Martin et al., *Parton distributions for the LHC*, Eur. Phys. J. **C63** (2009) 189, arXiv:0901.0002 [hep-ph].

[226] R. D. Ball et al., *Parton distributions with LHC data*, Nucl. Phys. **B867** (2013) 244, arXiv:1207.1303 [hep-ph].

[227] LHC Higgs cross section working group, *Handbook of LHC Higgs cross sections: 1. Inclusive observables*, CERN-2011-002 (2011), arXiv:1101.0593 [hep-ph].

[228] A. Banfi, G. P. Salam and G. Zanderighi, *NLL+NNLO predictions for jet-veto efficiencies in Higgs-boson and Drell-Yan production*, J. High Energy Phys. **06** (2012) 159, arXiv:1203.5773 [hep-ph].

[229] A. Banfi, P. F. Monni and G. Zanderighi, *Quark masses in Higgs production with a jet veto*, J. High Energy Phys. **01** (2014) 097, arXiv:1308.4634 [hep-ph].

[230] A. Banfi et al., *Jet-vetoed Higgs cross section in gluon fusion at N3LO+NNLL with small-R resummation*, (2015), arXiv:1511.02886 [hep-ph].

[231] J. Gao et al., *CT10 next-to-next-to-leading order global analysis of QCD*, Phys. Rev. **D89** (2014) 033009, arXiv:1302.6246 [hep-ph].

[232] S. Catani et al., *QCD matrix elements + parton showers*, JHEP **11** (2001) 063, arXiv:hep-ph/0109231 [hep-ph].

[233] S. Catani and M. Grazzini, *An NNLO subtraction formalism in hadron collisions and its application to Higgs boson production at the LHC*, Phys.Rev.Lett. **98** (2007) 222002, arXiv:hep-ph/0703012 [hep-ph].

[234] M. Grazzini, *NNLO predictions for the Higgs boson signal in the $H \to WW \to \ell\nu\ell\nu$ and $H \to ZZ \to 4\ell$ decay channels*, JHEP **0802** (2008) 043, arXiv:0801.3232 [hep-ph].

[235] ATLAS Collaboration, *Improved luminosity determination in pp collisions at sqrt(s) = 7 TeV using the ATLAS detector at the LHC*, Eur. Phys. J. **C73** (2013) 2518, arXiv:1302.4393 [hep-ex].

[236] ATLAS Collaboration, *Search for the $b\bar{b}$ decay of the Standard Model Higgs boson in associated $(W/Z)H$ production with the ATLAS detector*, JHEP **1501** (2015) 069, arXiv:1409.6212 [hep-ex].

[237] ATLAS Collaboration, *Performance assumptions for an upgraded ATLAS detector at a High-Luminosity LHC*, ATL-PHYS-PUB-2013-004, 2013, URL: http://cdsweb.cern.ch/record/1527529.

[238] ATLAS Collaboration, *Performance assumptions based on full simulation for an upgraded ATLAS detector at a High-Luminosity LHC*, ATL-PHYS-PUB-2013-009, 2013, URL: http://cdsweb.cern.ch/record/1604420.

[239] M. Proissl, "Dijet Invariant Mass Studies in the Higgs boson $H \to b\bar{b}$ resonance search in association with a W/Z boson using the ATLAS detector", Presented 2014, PhD thesis: Edinburgh U., 2014, URL: https://cds.cern.ch/record/1997808.

[240] C. Englert, M. McCullough and M. Spannowsky, *Gluon-initiated associated production boosts Higgs physics*, Phys. Rev. D **89** (2014) 013013, arXiv:1310.4828 [hep-ph].

[241] L. Altenkamp et al., *Gluon-induced Higgs-strahlung at next-to-leading order QCD*, JHEP **1302** (2013) 078, arXiv:1211.5015 [hep-ph].

[242] T. Sjostrand, S. Mrenna and P. Z. Skands, *PYTHIA 6.4 Physics and Manual*, JHEP **0605** (2006) 026, arXiv:hep-ph/0603175 [hep-ph].

[243] ATLAS Collaboration, *ATLAS tunes of* Pythia *6 and Pythia 8 for MC11*, ATL-PHYS-PUB-2011-009, 2011, URL: http://cds.cern.ch/record/1363300.

[244] S. Frixione, P. Nason and C. Oleari, *Matching NLO QCD computations with Parton Shower simulations: the POWHEG method*, JHEP **0711** (2007) 070, arXiv:0709.2092 [hep-ph].

[245] S. Alioli et al., *A general framework for implementing NLO calculations in shower Monte Carlo programs: the POWHEG BOX*, JHEP **1006** (2010) 043, arXiv:1002.2581 [hep-ph].

[246] S. Dittmaier et al., *Handbook of LHC Higgs Cross Sections: 1. Inclusive Observables*, CERN-2011-002 (2011), arXiv:1101.0593.

[247] H. Baer, B. Bailey and J. F. Owens, *$O(\alpha_s)$ Monte Carlo approach to W+Higgs associated production at hadron supercolliders*, PhysRevD **47** (1993) 2730.

[248] J. Ohnemus and W. J. Stirling, *Order α_s corrections to the differential cross-section for the WH intermediate mass Higgs signal*, Phys. Rev. **D47** (1993) 2722.

[249] S. Dittmaier, M. Kramer and M. Spira, *Higgs radiation off bottom quarks at the Tevatron and the CERN LHC*, Phys.Rev. **D70** (2004) 074010, arXiv:hep-ph/0309204.

[250] A. Denner et al., *EW corrections to Higgs strahlung at the Tevatron and the LHC with HAWK*, PoS **EPS-HEP2011** (2011) 235, arXiv:1112.5258 [hep-ph].

[251] ATLAS Collaboration, *Single Boson and Diboson Production Cross Sections in pp Collisions at 7 TeV*, ATL-COM-PHYS-2010-695 (2010), URL: https://cds.cern.ch/record/1287902.

[252] M. Aliev et al., *HATHOR: HAdronic Top and Heavy quarks crOss section calculatoR*, Comput. Phys. Commun. **182** (2011) 1034, arXiv:1007.1327 [hep-ph].

[253] B. P. Kersevan and E. Richter-Was, *The Monte Carlo event generator AcerMC versions 2.0 to 3.8 with interfaces to PYTHIA 6.4, HERWIG 6.5 and ARIADNE 4.1*, Comput. Phys. Commun. **184** (2013) 919, arXiv:hep-ph/0405247 [hep-ph].

[254] N. Kidonakis, *Differential and total cross sections for top pair and single top production*, (2012) 831, arXiv:1205.3453 [hep-ph].

[255] ATLAS Collaboration, *Search for the $b\bar{b}$ decay of the Standard Model Higgs boson in associated $(W/Z)H$ production with the ATLAS detector*, J. High Energy Phys. **01** (2014) 069. 69 p, URL: https://cds.cern.ch/record/1757231.

[256] *Performance of the Electron and Photon Trigger in $p-p$ Collisions at sqrt(s) = 7 TeV*, ATLAS-CONF-2011-114 (), URL: https://cds.cern.ch/record/1375551.

[257] ATLAS Collaboration, *Preliminary results on the muon reconstruction efficiency, momentum resolution, and momentum scale in ATLAS 2012 pp collision data*, tech. rep. ATLAS-CONF-2013-088, CERN, 2013.

[258] CMS Collaboration, "Projected Performance of an Upgraded CMS Detector at the LHC and HL-LHC: Contribution to the Snowmass Process", *Community Summer Study 2013: Snowmass on the Mississippi (CSS2013) Minneapolis, MN, USA, July 29-August 6, 2013*, 2013, arXiv:1307.7135, URL: https://inspirehep.net/record/1244669/files/arXiv:1307.7135.pdf.

[259] ATLAS Collaboration, *Improved luminosity determination in pp collisions at $\sqrt{s}$ = 7 TeV using the ATLAS detector at the LHC*, Eur. Phys. J. **C73** (2013) 2518, arXiv:1302.4393 [hep-ex].

[260] A. Djouadi, J. Kalinowski and M. Spira, *HDECAY: A Program for Higgs boson decays in the standard model and its supersymmetric extension*, Comput. Phys. Commun. **108** (1998) 56, arXiv:hep-ph/9704448 [hep-ph].

[261] G. Cowan et al., *Asymptotic formulae for likelihood-based tests of new physics*, Eur.Phys.J. **C71** (2011) 1554, arXiv:1007.1727 [physics.data-an].

[262] G. Cowan, *Statistical Data Analysis*, Oxford University Press, Oxford, 1998.

[263] A. L. Read, *Presentation of search results: The CL(s) technique*, J. Phys. **G28** (2002) 2693, [,11(2002)].

[264] ATLAS Collaboration, *Jet energy resolution in proton-proton collisions at $\sqrt{s} = 7$ TeV recorded in 2010 with the ATLAS detector*, Eur.Phys.J. **C73** (2013) 2306, arXiv:1210.6210 [hep-ex].

[265] ATLAS Collaboration, *Jet energy measurement and its systematic uncertainty in proton–proton collisions at $\sqrt{s} = 7$ TeV with the ATLAS detector*, (2014), arXiv:1406.0076 [hep-ex].

[266] ATLAS Collaboration, *Physics at a High-Luminosity LHC with ATLAS (Update)*, ATL-PHYS-PUB-2012-004, 2012, URL: http://cdsweb.cern.ch/record/1484890.

[267] A. Peisert, *Silicon microstrip detectors*, Adv. Ser. Direct. High Energy Phys. **9** (1992) 1.

[268] C. Kittel, *Introduction to Solid State Physics*, 8th Edition, Wiley, 2004 194.

[269] S. M. Gibson, *Monitoring radiation damage in the ATLAS Silicon Tracker*, (2011), URL: http://cds.cern.ch/record/1384156.

[270] C. Oropeza Barrera, *Study of the dynamics of soft interactions with two-particle angular correlations at ATLAS*, (2012), URL: https://cds.cern.ch/record/1602221.

[271] J. R. Hook and H. E. Hall, *Solid State Physics*, 2nd edition, Wiley, 1995.

[272] S. M. Gibson, *Radiation damage to currently running LHC silicon detectors*, (2012), URL: https://cds.cern.ch/record/1483028.

[273] T. Kondo, *Status of radiation effects of the ATLAS SCT detector*, 22nd RD50 Workshop on Radiation Hard Semiconductor Devices for Very High Luminosity Colliders, University of New Mexico, June 3 (2013).

[274] E Fretwurst et al., *Radiation Damage in Silicon Detectors Caused by Hadronic and Electromagnetic Irradiation*, December, 2002, ISBN: 4940899829.

[275] M Capeans et al., *ATLAS Insertable B-Layer Technical Design Report*, (2010), URL: http://cds.cern.ch/record/1291633/export/hx?ln=en.

[276] M Garcia-Sciveres and E. Al, *The FE-I4 pixel readout integrated circuit*, Nucl. Instruments Methods Phys. Res. Sect. A Accel. Spectrometers, Detect. Assoc. Equip. **636** (2011) S155.

[277] M. Barbero et al., *FE-I4 ATLAS pixel chip design*, Proceedings, 18th International Workshop on Vertex detectors and related techniques **VERTEX2009** (2009) 027.

[278] L. Caminada et al., *Atlas FE-I4 ASIC*, International 21st Workshop on Vertex detectors and related techniques **VERTEX2012 023** (2012) 1.

[279] M Backhaus et al., *Development of a versatile and modular test system for {ATLAS} hybrid pixel detectors*, Nucl. Instruments Methods Phys. Res. Sect. A Accel. Spectrometers, Detect. Assoc. Equip. **650** (2011) 37, ISSN: 0168-9002, URL: http://www.sciencedirect.com/science/article/pii/S0168900210028676.

[280] M. Kretz, *Performance Evaluation of the ATLAS IBL Calibration*, Journal of Physics: Conference Series **664** (2015) 082022, URL: http://stacks.iop.org/1742-6596/664/i=8/a=082022.

Appendix A: Differential Cross Section Measurements

A.1 H→WW selection cuts

The selection of the H→WW signal over the background processes is described in Table 8.1. The selection cuts are motivated by the comparison of signal and background in the following plots of kinematic variables in the different N_{jet} categories, taken from Ref. [18]. The selection cuts are indicated by vertical arrows.

The di-jet invariant mass m_{jj} or the difference in rapidity Δy_{jj} is used to select and veto the VBF production mode.

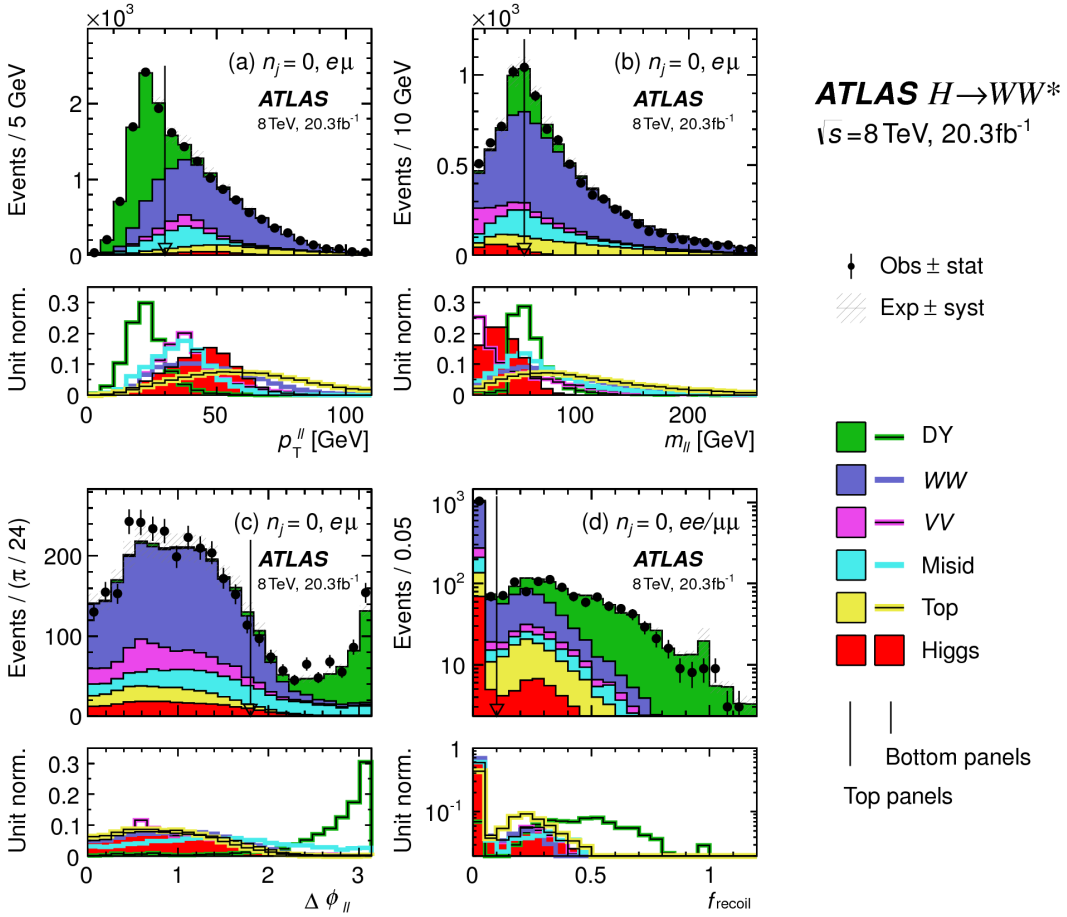

Figure A.1 $N_{\text{jet}} = 0$: For each variable, the top panel compares the observed and the cumulative expected distributions; the bottom panel shows the overlay of the distributions of the individual expected contributions, normalized to unit area, to emphasize shape differences.

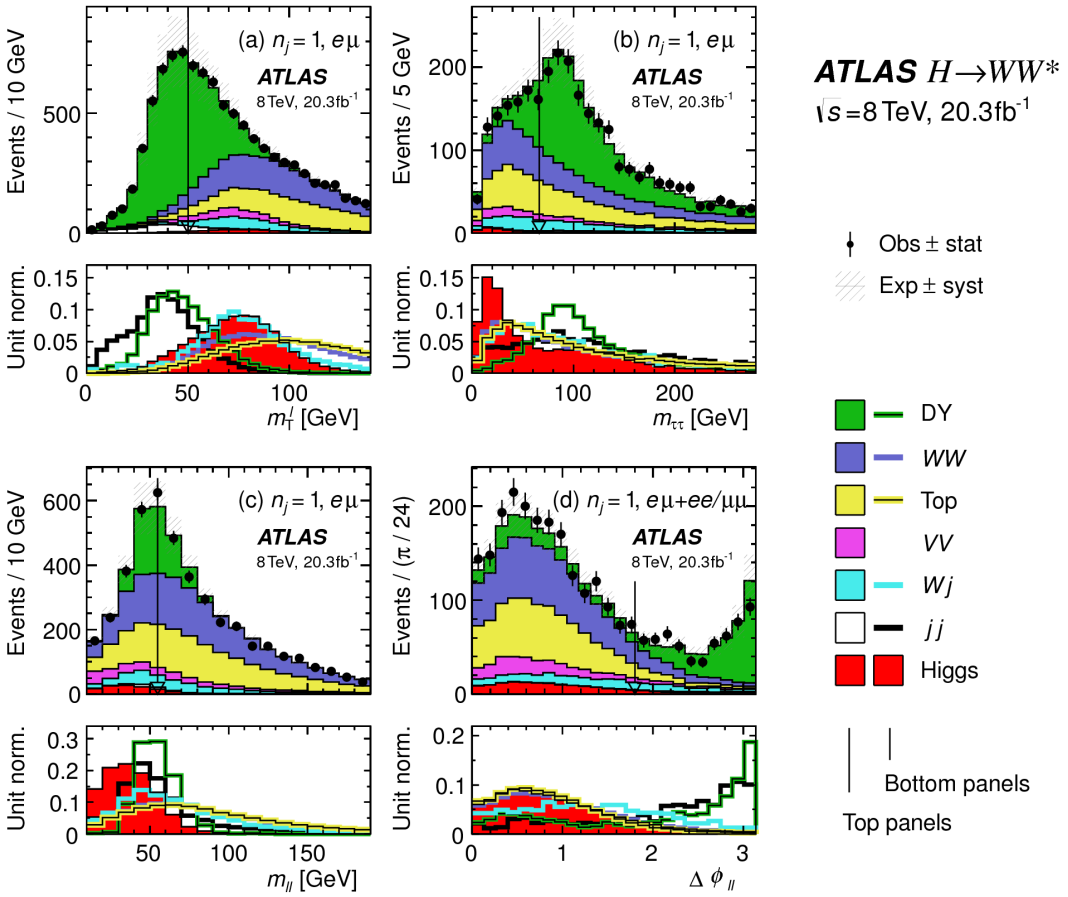

Figure A.2 $N_{\text{jet}} = 1$: For each variable, the top panel compares the observed and the cumulative expected distributions; the bottom panel shows the overlay of the distributions of the individual expected contributions, normalized to unit area, to emphasize shape differences.

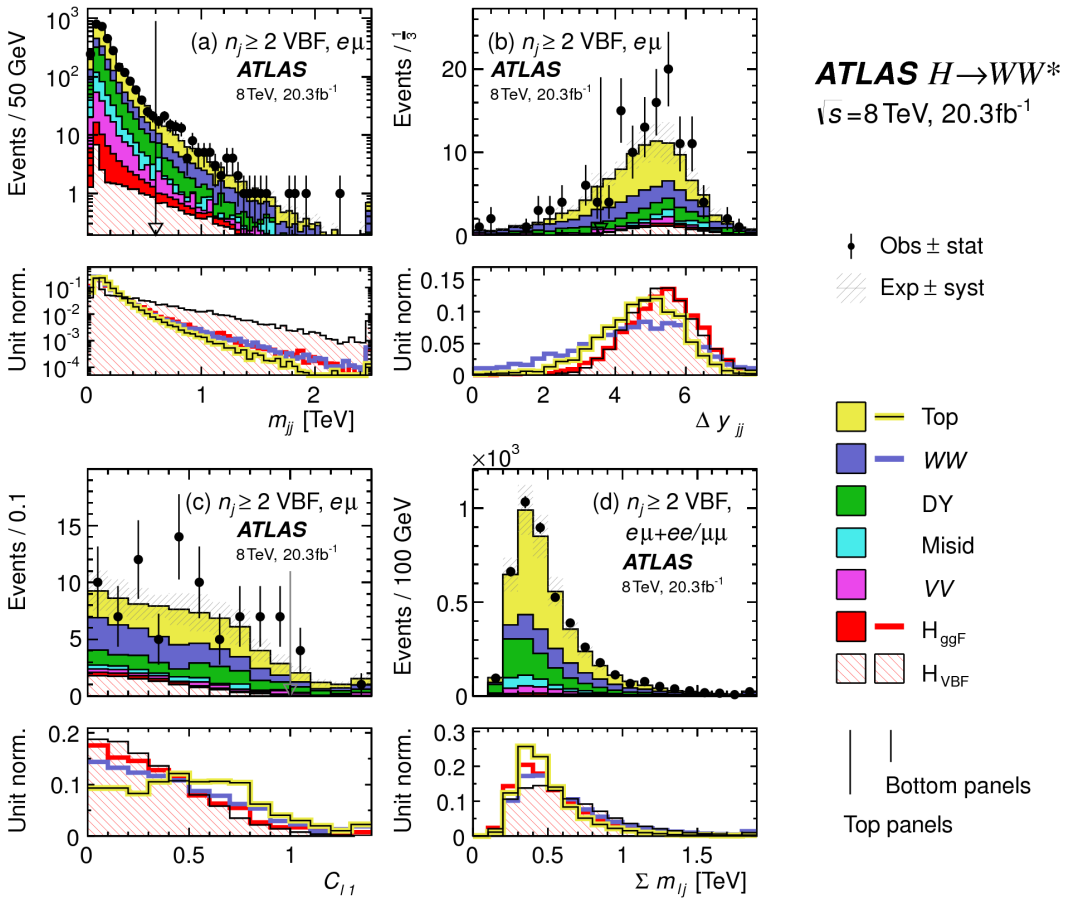

Figure A.3 $N_{\text{jet}} \geq 2$: For each variable, the top panel compares the observed and the cumulative expected distributions; the bottom panel shows the overlay of the distributions of the individual expected contributions, normalized to unit area, to emphasize shape differences.

A.2 Comparison of Bayesian Iterative and Bin-by-Bin Unfolding

The Bayesian iterative and bin-by-bin unfolding produce compatible results within the statistical and unfolding uncertainties, illustrated in Figure A.4. The overall higher yield of the Bayesian iterative unfolding is due to additional correction of off-diagonal entries of the migration matrix. The Bayesian iterative unfolding was used in this thesis, as discussed in Section 7.4.

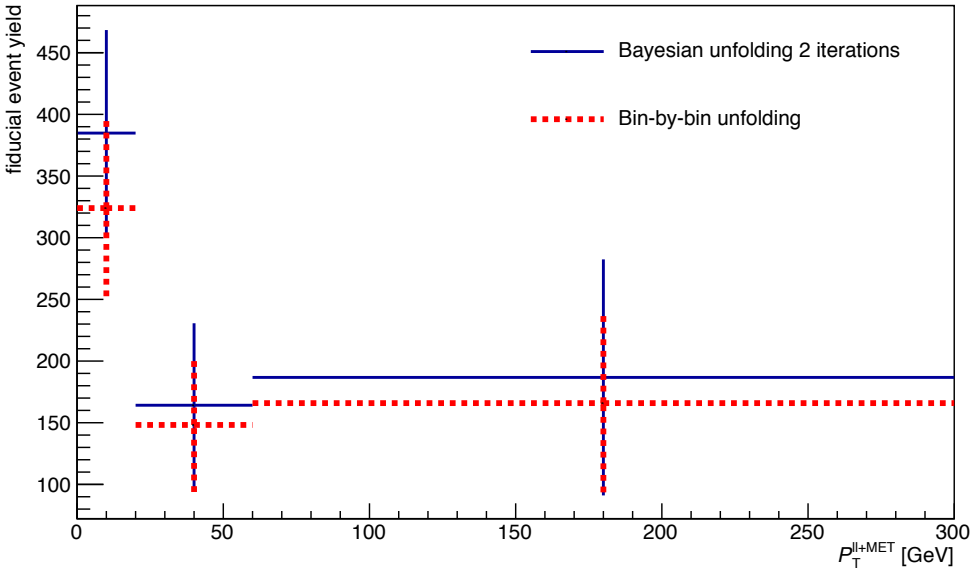

Figure A.4 Unfolded data-background yield of the $p_{\mathrm{T}}^{\mathrm{H}}$ distribution using the Bayesian iterative unfolding with two iterations and the bin-by-bin unfolding. The vertical errors bars represent the statistical and unfolding uncertainties only.

A.3 Inputs to Jet Veto Efficiency

For easier comparison, the values that make-up Figure 8.21 are shown below in Table A.1 before the cross section and bin-width normalisation is applied. Table A.1 thus gives the fiducial cross section results of H+0-jet events in fb for three different values of $p_{\mathrm{T}}^{\mathrm{thresh}}$.

jet p_{T} threshold	25 GeV*	30 GeV	40 GeV
σ [fb]	19.0	20.7	23.3
Statistical uncertainty	4.5	4.7	5.1
Total uncertainty	6.8	7.1	8.2
Data statistical	20%	19%	18%
MC statistical	4%	3%	3%
CR data statistical	12%	12%	12%
Exp. jets	5%	5%	8%
Exp. leptons	6%	6%	6%
Exp. $p_{\mathrm{T}}^{\mathrm{miss}}$	2%	2%	2%
Exp. other	5%	6%	7%
Theory WW	24%	23%	22%
Theory top	2%	2%	4%
Theory other BG	5%	5%	6%
Theory signal	4%	5%	5%
Detector corrections	0%	0%	0%
Total	36%	34%	35%

Table A.1 Fiducial cross section of H+0-jet events in femtobarn for different values of $p_{\mathrm{T}}^{\mathrm{thresh}}$ with the uncertainties for each bin given in absolute values and in percent. The asterisk for the 25 GeV column header indicates that the results are for a mixed p_{T} threshold, which is raised from 25 GeV to 30 GeV for jets with $2.5 < |\eta| < 4.5$, corresponding to the selection used to define the signal regions for the analysis.

A.4 Correlation Matrices

Fiducial differential cross section measurements are presented in Section 8.12 and compared to theoretical predictions. For completeness, in order to at a later stage perform a goodness-of-fit comparison between data and predictions, as in a χ^2 regression, the correlation matrices for Figures 8.19 & 8.20 are provided.

Bin-wise correlation matrices for the total uncertainty are given in Figure A.5 for the differential cross sections and in Figure A.6 for the normalised differential cross sections.

The correlation $cor_{k,l}$ between two bins k and l in the fiducial volume is calculated as

$$cor_{k,l} = \frac{cov_{k,l}}{\sqrt{|cov_{k,k}|}\sqrt{|cov_{l,l}|}}, \tag{A.1}$$

where $cov_{k,l}$ is the covariance between two bins k and l in the fiducial volume. The covariance is computed for each systematic variation and each pseudo experiment that was used for the statistical uncertainty calculation. The total covariance is

the combined sum. The covariance of all pseudo experiments is given by

$$cov_{k,l}^{\text{stat}} = \frac{1}{N_{\text{pseudo}}} \sum_{n}^{N_{\text{pseudo}}} \Big(\mu_k - x_k^n\Big)\Big(\mu_l - x_l^n\Big), \tag{A.2}$$

where N_{pseudo} is the number of pseudo experiments, μ_k is the mean yield of bin k of all pseudo experiments and x_k^n is the yield in bin k of the n-th pseudo experiment. $cov_{k,l}^{\text{stat}}$ was calculated separately for data and Monte Carlo statistical uncertainty.

The covariance of all systematic variations including the control region statistical errors is given by

$$cov_{k,l}^{\text{sys}} = \sum_{\text{s}}^{N_{\text{sys}}} \Big(y_k - x_k^s\Big)\Big(y_l - x_l^s\Big), \tag{A.3}$$

where y_k is the nominal yield of bin k and x_k^s is the bin yield modified by a systematic variation s.

Thus $cov_{k,l} = cov_{k,l}^{\text{stat}} + cov_{k,l}^{\text{sys}}$ and the correlation follows Equation A.1.

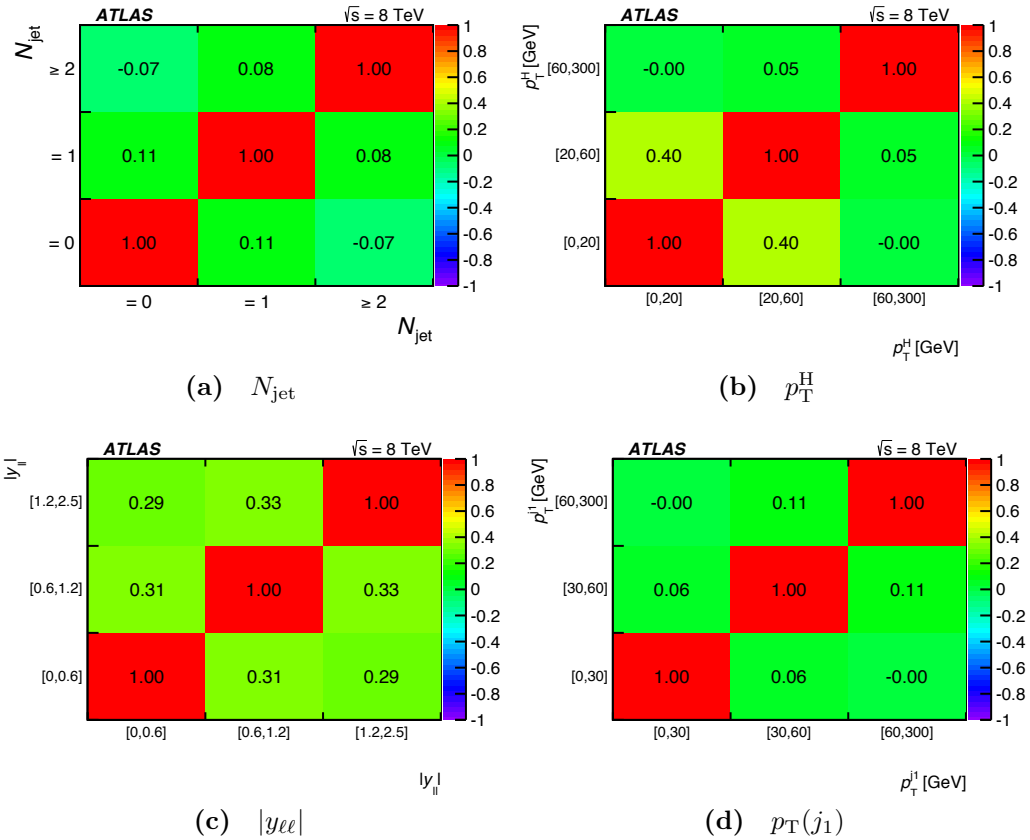

(a) N_{jet} **(b)** p_{T}^{H}

(c) $|y_{\ell\ell}|$ **(d)** $p_{\text{T}}(j_1)$

Figure A.5 Full correlation matrices for the differential cross sections as a function of (a) N_{jet}, (b) p_{T}^{H}, (c) $|y_{\ell\ell}|$, and (d) $p_{\text{T}}(j_1)$ taking into account statistical and systematic uncertainties.

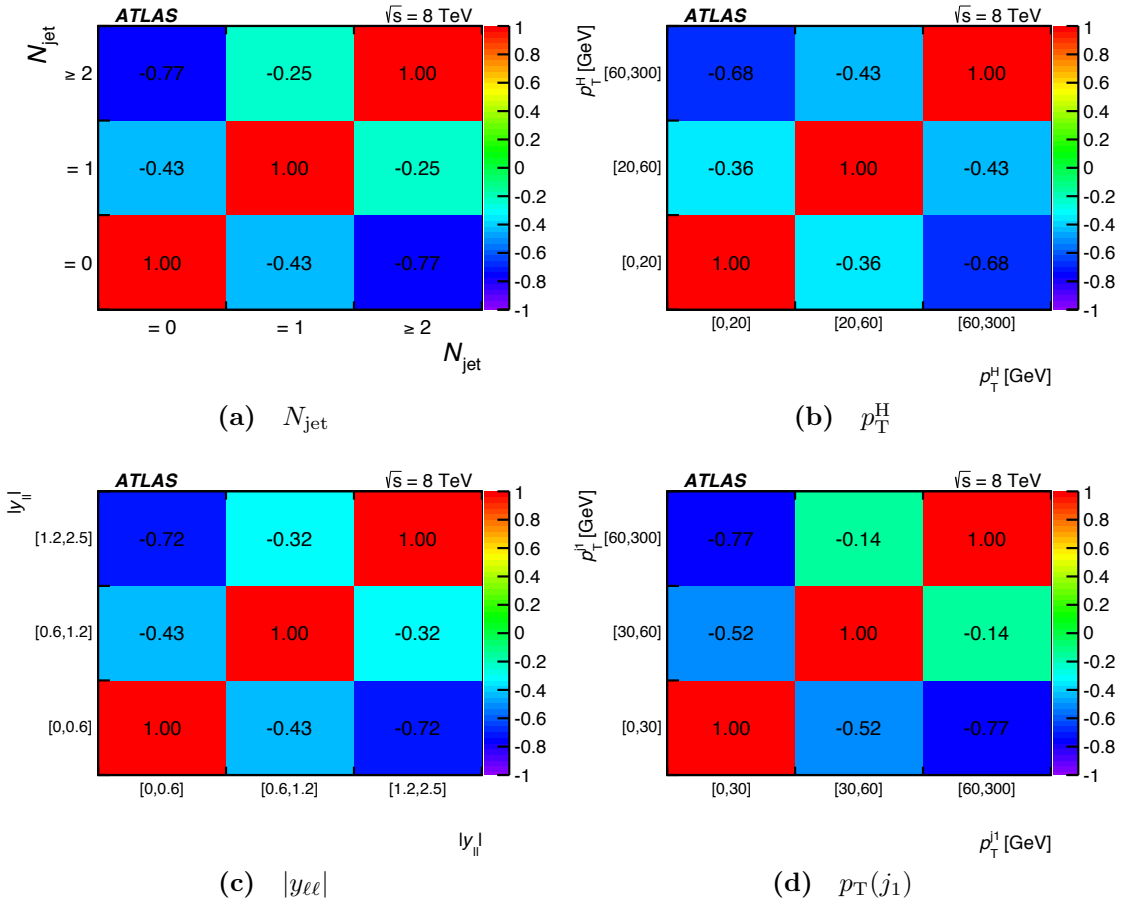

Figure A.6 Full correlation matrices for the normalised differential cross sections as a function of (a) N_{jet}, (b) p_{T}^{H}, (c) $|y_{\ell\ell}|$, and (d) $p_{\text{T}}(j_1)$ taking into account statistical and systematic uncertainties.

A.5 Correction Factors for Parton-level Predictions

All parton-level predictions in Chapter 8 are corrected by the acceptance of the fiducial region and non-perturbative factors to account for the impact of hadronisation and underlying event activity. These factors are determined using Powheg-box NNLOPS+Pythia8 with the associated uncertainties from the renormalisation and factorisation scales as well as the PDFs. An uncertainty is assigned to the non-perturbative correction by comparing Pythia8 with Herwig.

The parton-level predictions for the N_{jet} distribution from BLPTW and for the $p_{\text{T}}(j_1)$ distribution from STWZ are fully inclusive except for the requirement that jets have $p_{\text{T}} > 25$ GeV in case of BLPTW or $p_{\text{T}} > 30$ GeV in case of STWZ. The correction factors for the predictions in each bin are given by the ratio of the default Powheg-box NNLOPS+Pythia8 prediction in the fiducial volume over the fully inclusive Powheg-box NNLOPS+Pythia8 prediction with the

requirements on the jets applied and the hadronisation and the underlying event in PYTHIA8 turned off. The factors are given in Table A.2 for the N_{jet} prediction and in Table A.3 for the $p_{\text{T}}(j_1)$ prediction.

	$N_{\text{jet}} = 0$	$N_{\text{jet}} = 1$	$N_{\text{jet}} \geq 2$
Correction factor	$0.0567^{+3.1\%}_{-2.6\%}$	$0.0580^{+4.4\%}_{-4.5\%}$	$0.0628^{+6.3\%}_{-6.7\%}$

Table A.2 Applied to BLPTW calculation shown in Figure 8.19(a). Correction factors from inclusive parton-level to fiducial particle-level for bins of N_{jet} derived with POWHEG-BOX NNLOPS+PYTHIA8. Uncertainties due to the non-perturbative correction are dominant for the correction factors.

$p_{\text{T}}(j_1)$	$[0, 30]$ GeV	$[30, 60]$ GeV	$[60, 300]$ GeV
Correction factor	$0.0551^{+3.0\%}_{-2.7\%}$	$0.0569^{+5.5\%}_{-5.5\%}$	$0.0718^{+7.0\%}_{-7.0\%}$

Table A.3 Applied to STWZ calculation shown in Figure 8.19(d). Correction factors from inclusive parton-level to fiducial particle-level for bins of $p_{\text{T}}(j_1)$ derived with POWHEG-BOX NNLOPS+PYTHIA8. Uncertainties due to the non-perturbative correction are dominant for the correction factors.

The parton-level predictions for the jet veto efficiency ε_0 from the ST, JetVHeto, STWZ, and N3LO+NNLL+LL_R are again calculated in the inclusive phase space. For the predictions of the jet veto efficiency for the jet selection used in the analysis, 25 GeV for central jets ($|\eta| < 2.5$) and 30 GeV for forward jets ($2.5 < |\eta| < 4.5$) the inclusive parton-level predictions with $p_{\text{T}}(j_1) > 25$ GeV are used. All correction factors and their uncertainty are given in Table A.4.

jet p_{T} threshold	25 GeV*	30 GeV	40 GeV
Correction factor inclusive	$0.9798^{+1.2\%}_{-0.3\%}$	$0.9529^{+1.0\%}_{-0.5\%}$	$0.9534^{+1.0\%}_{-0.5\%}$

Table A.4 Applied to calculations shown in Figure 8.21. Correction factors from inclusive parton-level to fiducial particle-level for the jet veto efficiency with different jet p_{T} thresholds derived with POWHEG-BOX NNLOPS+PYTHIA8.

A.6 Control Region Distributions

Backgrounds are normalised from control regions as discussed in Section 8.6, in which a selection of the control region plots are presented. The rest is given here.

The predicted and observed distributions in the WW, top-quark, $Z/\gamma^* \to \tau\tau$, and same-sign (VV) control regions for the $p_{\mathrm{T}}^{\mathrm{H}}$, $p_{\mathrm{T}}(j_1)$, and $|y_{\ell\ell}|$ distributions, all of which are modelled using MC simulation for the backgrounds.

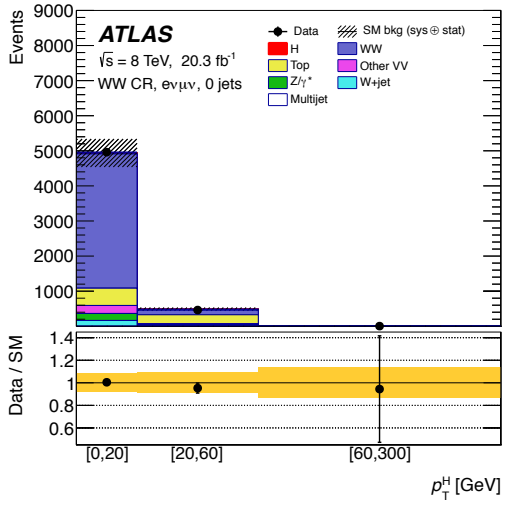

(a) $p_{\mathrm{T}}^{\mathrm{H}}$, $N_{\mathrm{jet}} = 0$

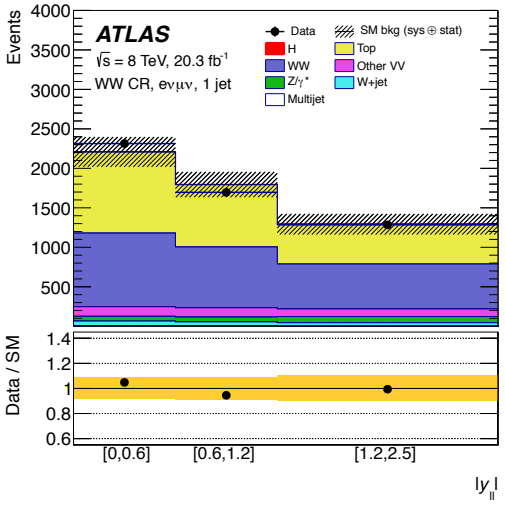

(b) $|y_{\ell\ell}|$, $N_{\mathrm{jet}} = 1$

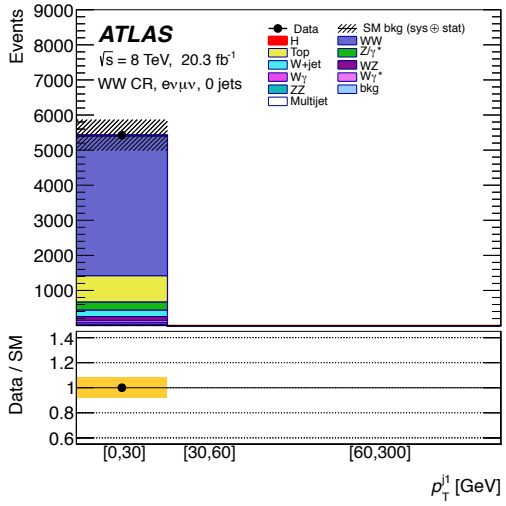

(c) $p_{\mathrm{T}}(j_1)$, $N_{\mathrm{jet}} = 0$

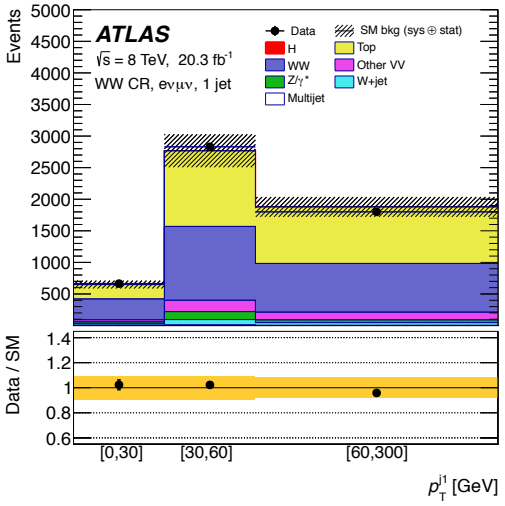

(d) $p_{\mathrm{T}}(j_1)$, $N_{\mathrm{jet}} = 1$

Figure A.7 Distributions of (a) $p_{\mathrm{T}}^{\mathrm{H}}$ in the $N_{\mathrm{jet}} = 0$, (b) $|y_{\ell\ell}|$ in the $N_{\mathrm{jet}} = 1$, and (c) $p_{\mathrm{T}}(j_1)$ in the $N_{\mathrm{jet}} = 1$ WW control regions. The hatched band in the upper plot and the shaded band in the lower plot shows the sum in quadrature of statistical and systematic uncertainties on the prediction, and relevant background normalisation factors have been applied.

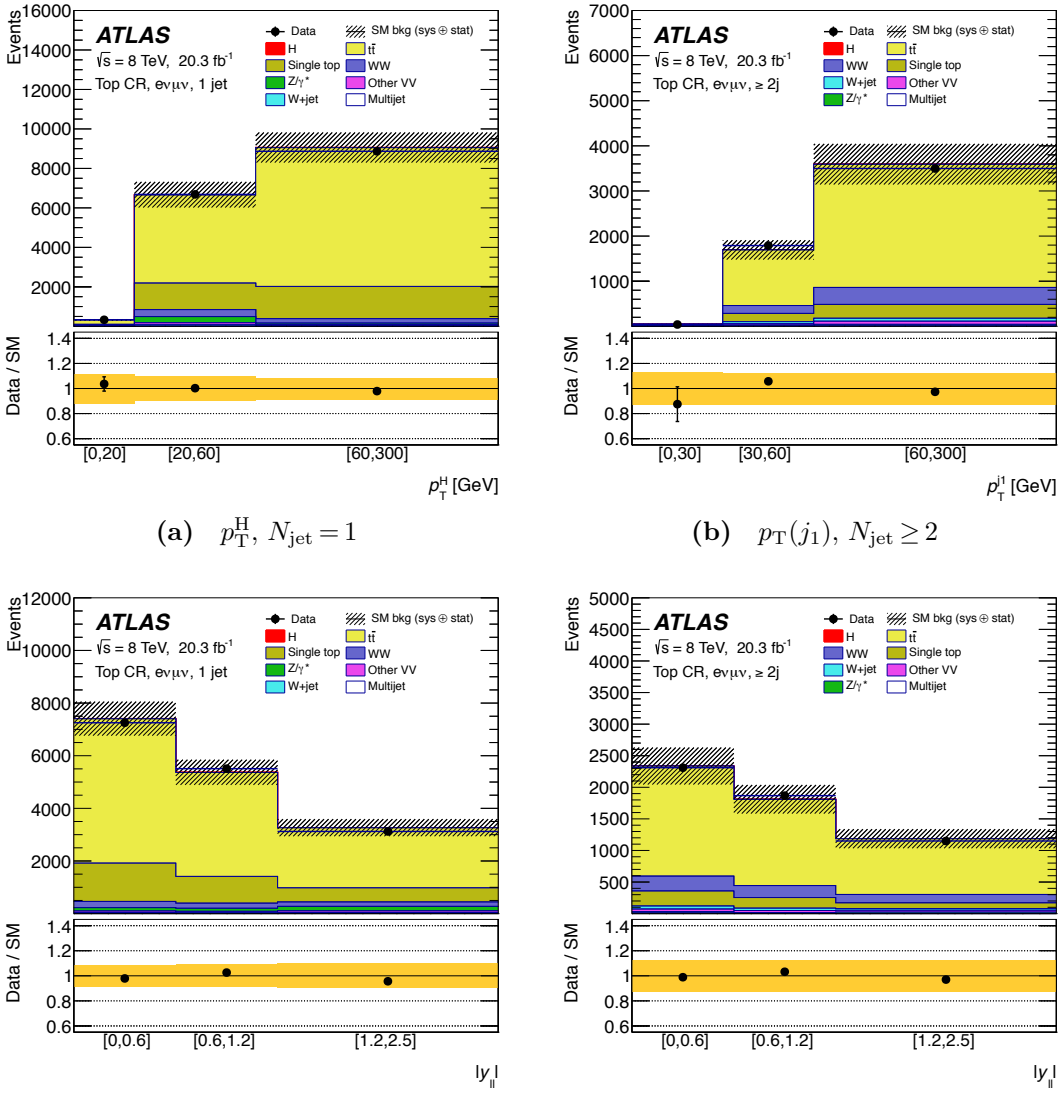

(a) $p_{\mathrm{T}}^{\mathrm{H}}$, $N_{\mathrm{jet}} = 1$ **(b)** $p_{\mathrm{T}}(j_1)$, $N_{\mathrm{jet}} \geq 2$

(c) $|y_{\ell\ell}|$, $N_{\mathrm{jet}} = 1$ **(d)** $|y_{\ell\ell}|$, $N_{\mathrm{jet}} \geq 2$

Figure A.8 Distributions of (a) $p_{\mathrm{T}}^{\mathrm{H}}$ in the $N_{\mathrm{jet}} = 1$, (b) $p_{\mathrm{T}}(j_1)$ in the $N_{\mathrm{jet}} \geq 2$, and (c, d) $|y_{\ell\ell}|$ in the (c) $N_{\mathrm{jet}} = 1$ and (d) $N_{\mathrm{jet}} \geq 2$ top-quark control regions. The hatched band in the upper plot and the shaded band in the lower plot shows the sum in quadrature of statistical and systematic uncertainties on the prediction, and relevant background normalisation factors have been applied.

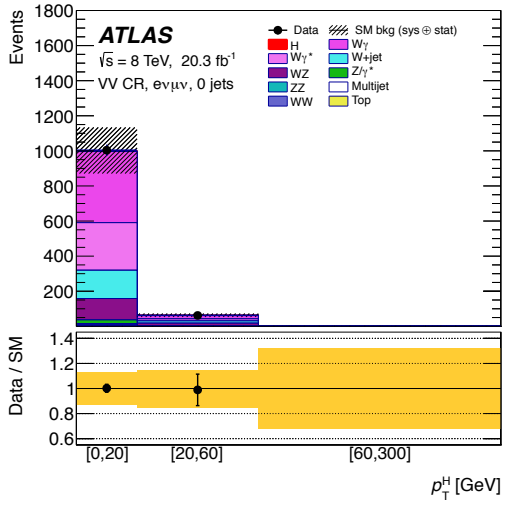

(a) $p_{\mathrm{T}}^{\mathrm{H}}$, $N_{\mathrm{jet}} = 0$

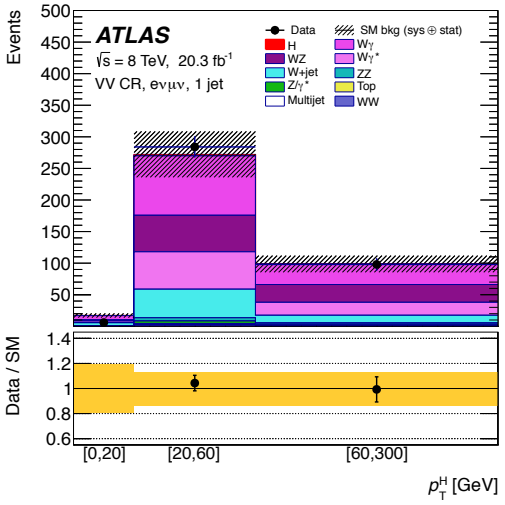

(b) $p_{\mathrm{T}}^{\mathrm{H}}$, $N_{\mathrm{jet}} = 1$

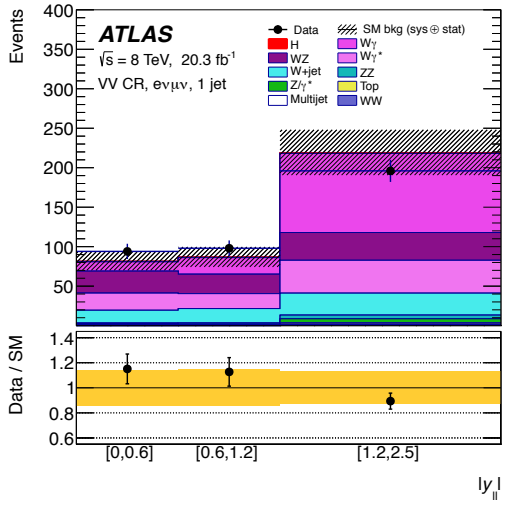

(c) $|y_{\ell\ell}|$, $N_{\mathrm{jet}} = 1$

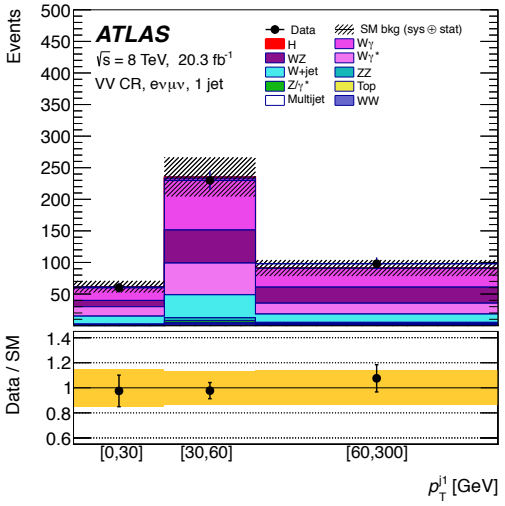

(d) $p_{\mathrm{T}}(j_1)$, $N_{\mathrm{jet}} = 1$

Figure A.9 Distributions of (a, b) $p_{\mathrm{T}}^{\mathrm{H}}$, (c) $|y_{\ell\ell}|$, and (d) $p_{\mathrm{T}}(j_1)$ in the (a) $N_{\mathrm{jet}} = 0$ and (b, c, d) $N_{\mathrm{jet}} = 1$ same-sign control regions. The hatched band in the upper plot and the shaded band in the lower plot shows the sum in quadrature of statistical and systematic uncertainties on the prediction, and relevant background normalisation factors have been applied.

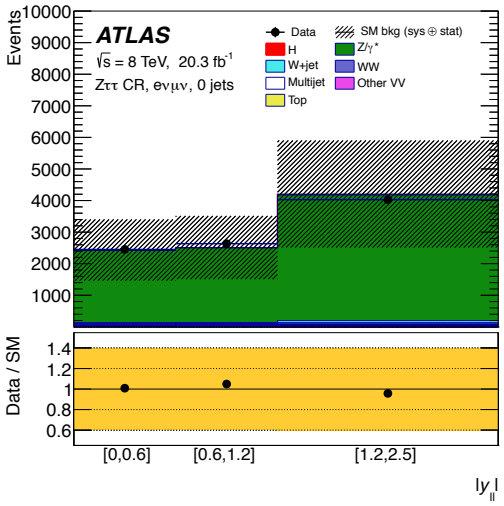

(a) $|y_{\ell\ell}|$, $N_{\text{jet}} = 0$

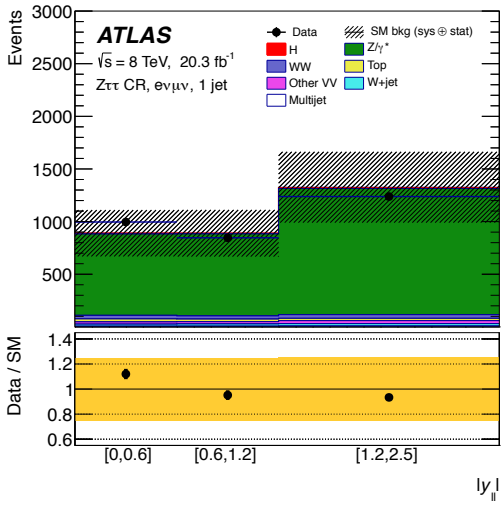

(b) $|y_{\ell\ell}|$, $N_{\text{jet}} = 1$

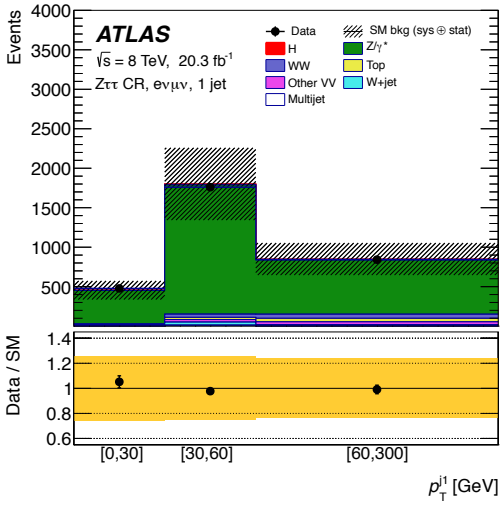

(c) $p_{\text{T}}(j_1)$, $N_{\text{jet}} = 1$

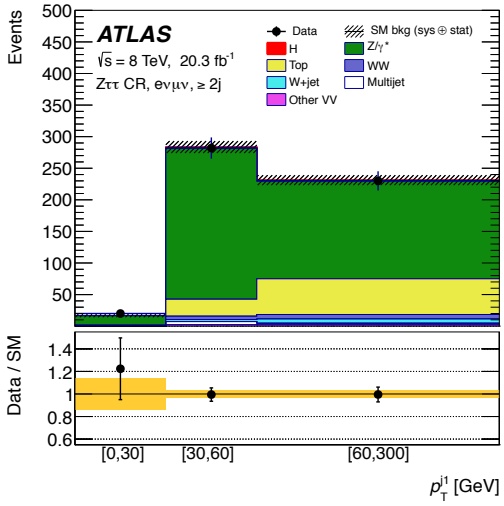

(d) $p_{\text{T}}(j_1)$, $N_{\text{jet}} \geq 2$

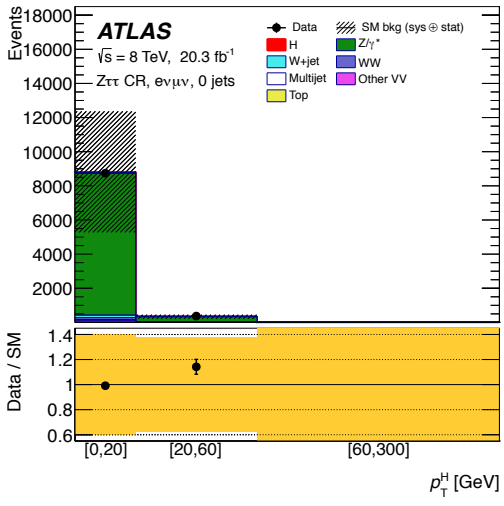

(e) p_{T}^{H}, $N_{\text{jet}} = 0$

Figure A.10 Distributions of (a, b) $|y_{\ell\ell}|$, (c, d) $p_{\text{T}}(j_1)$, and (e) p_{T}^{H} in the (c, e) $N_{\text{jet}} = 0$, (b,c) $N_{\text{jet}} = 1$, and (d) $N_{\text{jet}} \geq 2$ $Z/\gamma^* \to \tau\tau$ control regions. The hatched band in the upper plot and the shaded band in the lower plot shows the sum in quadrature of statistical and systematic uncertainties on the prediction, and relevant background normalisation factors have been applied.

A.7 Signal Region Distributions in Logarithmic Scale

Signal yield distributions from Section 8.7 are given here in logarithmic scale to visualise smaller background contributions. Figure A.11 shows the distributions to be unfolded in the signal region, prior to unfolding, summed over N_{jet}. These are identical to Fig. 8.10 but with the upper plot in logarithmic scale.

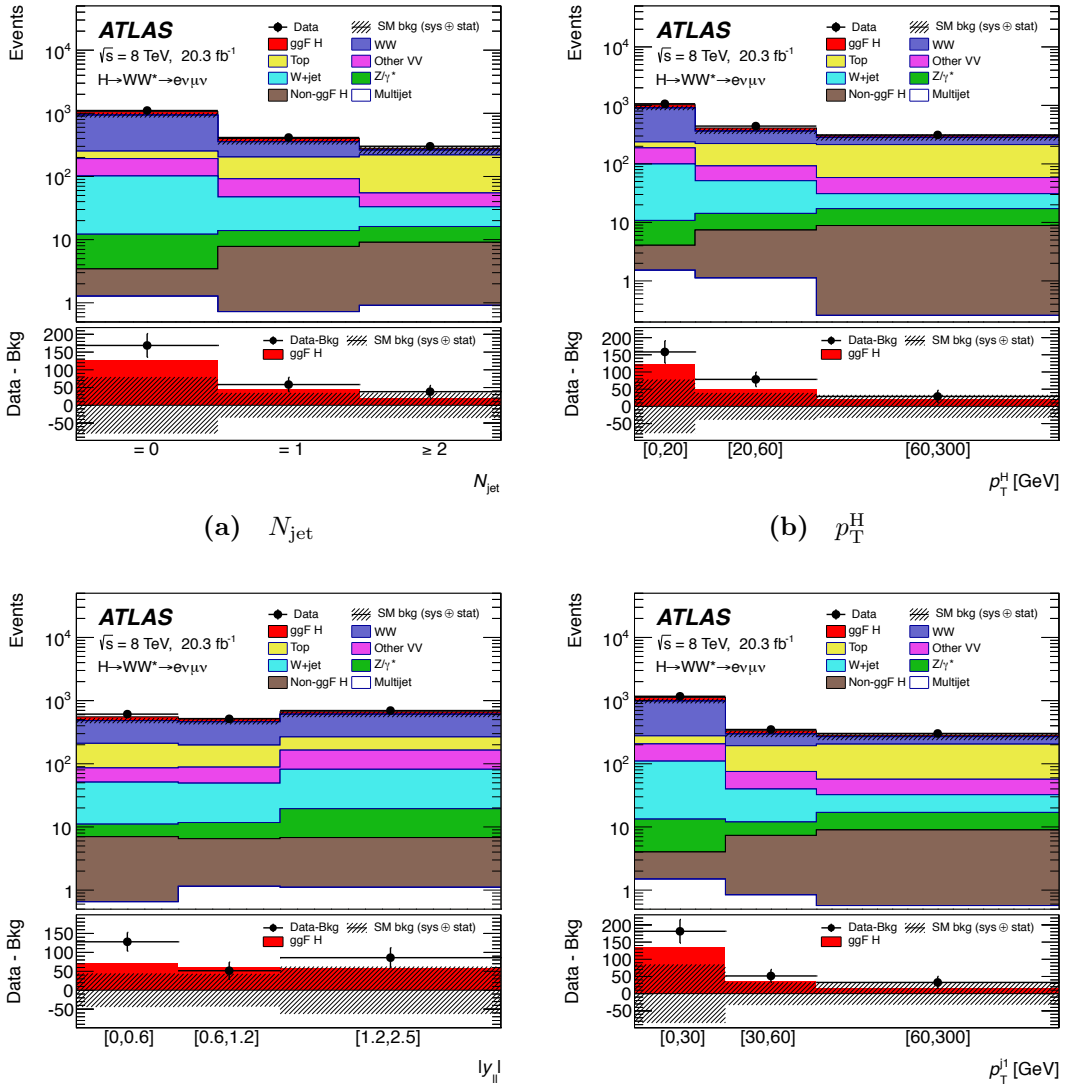

(a) N_{jet} **(b)** p_{T}^{H}

(c) $|y_{\ell\ell}|$ **(d)** $p_{\text{T}}(j_1)$

Figure A.11 Observed distributions of (a) N_{jet}, (b) p_{T}^{H}, (c) $|y_{\ell\ell}|$, and (d) $p_{\text{T}}(j_1)$ with signal and background expectation, combined over the $N_{\text{jet}} = 0$, $= 1$, and ≥ 2 signal-region categories. The background processes are normalised as described in Section 8.6. The hatched band shows the sum in quadrature of statistical and systematic uncertainties on the sum of the backgrounds.

Appendix B: VH Prospects

B.1 WH Channel Results

Event yields for the 2 lepton channel are presented in Section 9.7. Analogous results for the 1-lepton which were used in combination in Section 9.10 are given here. Table B.1 shows the WH event yields for signal and background for an integrated luminosity of 300 fb^{-1}, assuming the appropriate smearing and efficiency functions for pile-up of $\langle\mu\rangle = 60$. Table B.2 show the event yields for 3000 fb^{-1}, assuming the appropriate smearing and efficiency functions for pile-up of $\langle\mu\rangle = 140$.

Figures B.1 and B.2 show the di-b-jet mass distributions for all the WH signal regions

One-lepton, 2-jet signal region				
Process	$p_{\mathrm{T}}^{\mathrm{W}}$[GeV]			
	$90-120$	$120-160$	$160-200$	>200
WH	114.1 ± 3.1	118.6 ± 3.1	130.8 ± 3.2	216 ± 4
ZH	7.11 ± 0.18	3.79 ± 0.13	2.89 ± 0.11	2.28 ± 0.11
VH total	121.2 ± 3.1	122.4 ± 3.1	133.7 ± 3.2	218 ± 4
W+*jets*	6780 ± 273	5189 ± 199	4359 ± 166	7996 ± 184
Z+*bb*	1130 ± 60	470 ± 40	224 ± 29	164 ± 25
single top	9180 ± 85	4330 ± 64	2293 ± 44	2155 ± 52
$t\bar{t}$	62700 ± 400	32570 ± 290	16470 ± 210	10180 ± 160
Multijet	1181 ± 15	146.5 ± 3.4	71.1 ± 2.3	35.7 ± 1.8
WW	46 ± 13	25 ± 10	18 ± 8	60 ± 15
VZ	369 ± 19	413 ± 19	464 ± 20	597 ± 22
Total bkg	81400 ± 500	43200 ± 400	23930 ± 270	21190 ± 250
S/B ($\times 10^{-3}$)	1.49 ± 0.04	2.84 ± 0.08	5.59 ± 0.15	10.28 ± 0.23
$S/\sqrt{B}$	0.43 ± 0.01	0.59 ± 0.02	0.86 ± 0.02	1.50 ± 0.03
One-lepton 3-jet signal region				
Process	$p_{\mathrm{T}}^{\mathrm{W}}$[GeV]			
	$90-120$	$120-160$	$160-200$	>200
WH	24.9 ± 1.4	27.0 ± 1.5	33.1 ± 1.6	72.2 ± 2.3
ZH	2.79 ± 0.11	1.80 ± 0.09	2.00 ± 0.09	2.26 ± 0.11
VH total	27.7 ± 1.4	28.8 ± 1.5	35.1 ± 1.6	74.4 ± 2.3
W+*jets*	3006 ± 186	1811 ± 110	1880 ± 106	4149 ± 121
Z+*bb*	490 ± 40	206 ± 28	110 ± 20	48 ± 14
single top	6540 ± 72	2972 ± 56	1901 ± 42	2647 ± 51
$t\bar{t}$	101000 ± 500	42810 ± 340	21430 ± 240	17200 ± 200
Multijet	370 ± 9	49.3 ± 1.9	26.4 ± 1.3	13.7 ± 1.1
WW	11 ± 6	11 ± 6	18 ± 8	25 ± 9
VZ	73 ± 9	85 ± 9	92 ± 8	177 ± 1
Total bkg	111500 ± 500	48000 ± 400	25500 ± 270	24260 ± 250
S/B ($\times 10^{-3}$)	0.25 ± 0.01	0.60 ± 0.03	1.38 ± 0.07	3.07 ± 0.11
$S/\sqrt{B}$	0.083 ± 0.004	0.131 ± 0.007	0.22 ± 0.01	0.48 ± 0.02

Table B.1 Estimated event yields for signal and background, for the one-lepton channel in $p_{\mathrm{T}}^{\mathrm{W}}$ bins. The yields are for $\sqrt{s} = 14$ TeV, $\langle\mu\rangle = 60$ and an integrated luminosity of 300 fb^{-1}, before the fit model has been applied. The uncertainties correspond to limited Monte Carlo statistics.

One-lepton 2-jet signal region				
Process	$p_{\mathrm{T}}^{\mathrm{W}}$[GeV]			
	$90-120$	$120-160$	$160-200$	>200
WH	928 ± 28	950 ± 28	986 ± 28	2030 ± 40
ZH	71.1 ± 1.8	39.7 ± 1.3	28.1 ± 1.1	26.5 ± 1.1
VH total	1000 ± 28	990 ± 28	1014 ± 28	2060 ± 40
W+*jets*	46800 ± 2345	40920 ± 2046	37002 ± 1521	89950 ± 2195
Z+*bb*	10900 ± 600	4700 ± 400	3110 ± 340	3200 ± 400
single top	73500 ± 707	36540 ± 605	22510 ± 457	23300 ± 528
$t\bar{t}$	483000 ± 4000	260000 ± 2600	157300 ± 2000	122500 ± 1800
Multijet	11800 ± 150	1465 ± 34	711 ± 23	356 ± 18
WW	390 ± 120	280 ± 100	210 ± 90	600 ± 150
VZ	2820 ± 160	3200 ± 170	3940 ± 190	6630 ± 240
Total bkg	629400 ± 4400	348100 ± 3400	224800 ± 2600	246500 ± 2900
S/B ($\times 10^{-3}$)	1.59 ± 0.05	2.84 ± 0.09	4.51 ± 0.14	8.34 ± 0.19
$S/\sqrt{B}$	1.26 ± 0.04	1.68 ± 0.05	2.14 ± 0.06	4.14 ± 0.08
One-lepton 3-jet signal region				
Process	$p_{\mathrm{T}}^{\mathrm{W}}$[GeV]			
	$90-120$	$120-160$	$160-200$	>200
WH	213 ± 13	212 ± 13	288 ± 15	720 ± 23
ZH	28.1 ± 1.1	21.6 ± 0.9	20.0 ± 0.9	26.5 ± 0.9
VH total	241 ± 13	234 ± 13	308 ± 15	746 ± 23
W+*jets*	18470 ± 1304	16470 ± 1093	16090 ± 1040	45430 ± 1423
Z+*bb*	5200 ± 400	1730 ± 250	1230 ± 210	780 ± 180
single top	55400 ± 721	27440 ± 568	18070 ± 431	26900 ± 519
$t\bar{t}$	825000 ± 5000	379900 ± 3200	221800 ± 2400	199400 ± 2300
Multijet	3710 ± 80	490 ± 20	264 ± 13	137 ± 11
WW	140 ± 70	70 ± 50	70 ± 50	280 ± 100
VZ	700 ± 70	810 ± 90	890 ± 80	1840 ± 120
Total bkg	908600 ± 4900	426900 ± 3400	258500 ± 2700	274800 ± 2800
S/B ($\times 10^{-3}$)	0.27 ± 0.02	0.55 ± 0.03	1.20 ± 0.06	2.72 ± 0.09
$S/\sqrt{B}$	0.25 ± 0.01	0.36 ± 0.02	0.61 ± 0.03	1.42 ± 0.05

Table B.2 Estimated event yields for signal and background, for the one-lepton channel in $p_{\mathrm{T}}^{\mathrm{W}}$ bins. The yields are for $\sqrt{s} = 14$ TeV, $\langle\mu\rangle = 140$ and an integrated luminosity of 3000 fb^{-1}, before the fit model has been applied. The uncertainties correspond to limited Monte Carlo statistics.

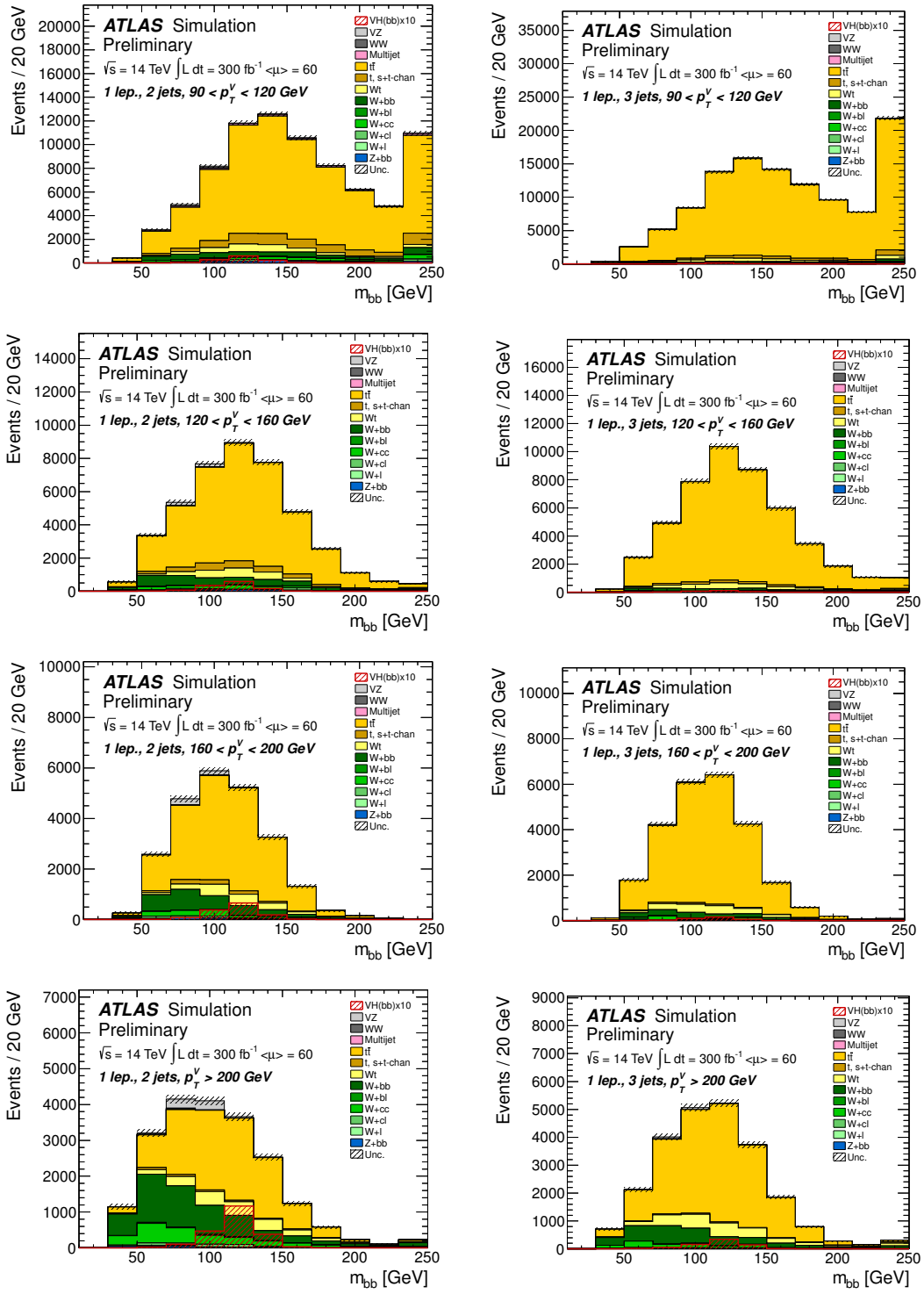

Figure B.1 Di-b-jet (m_{bb}) distribution for the 2-jet (left) and 3-jet (right) bins of the one-lepton channel for $\sqrt{s} = 14$ TeV, $\langle\mu\rangle = 60$ and an integrated luminosity of 300 fb^{-1}. The entries in overflow are included in the last bin. The Higgs boson signal cross section has been multiplied by a factor of 10. The dashed band corresponds to the statistical uncertainties only.

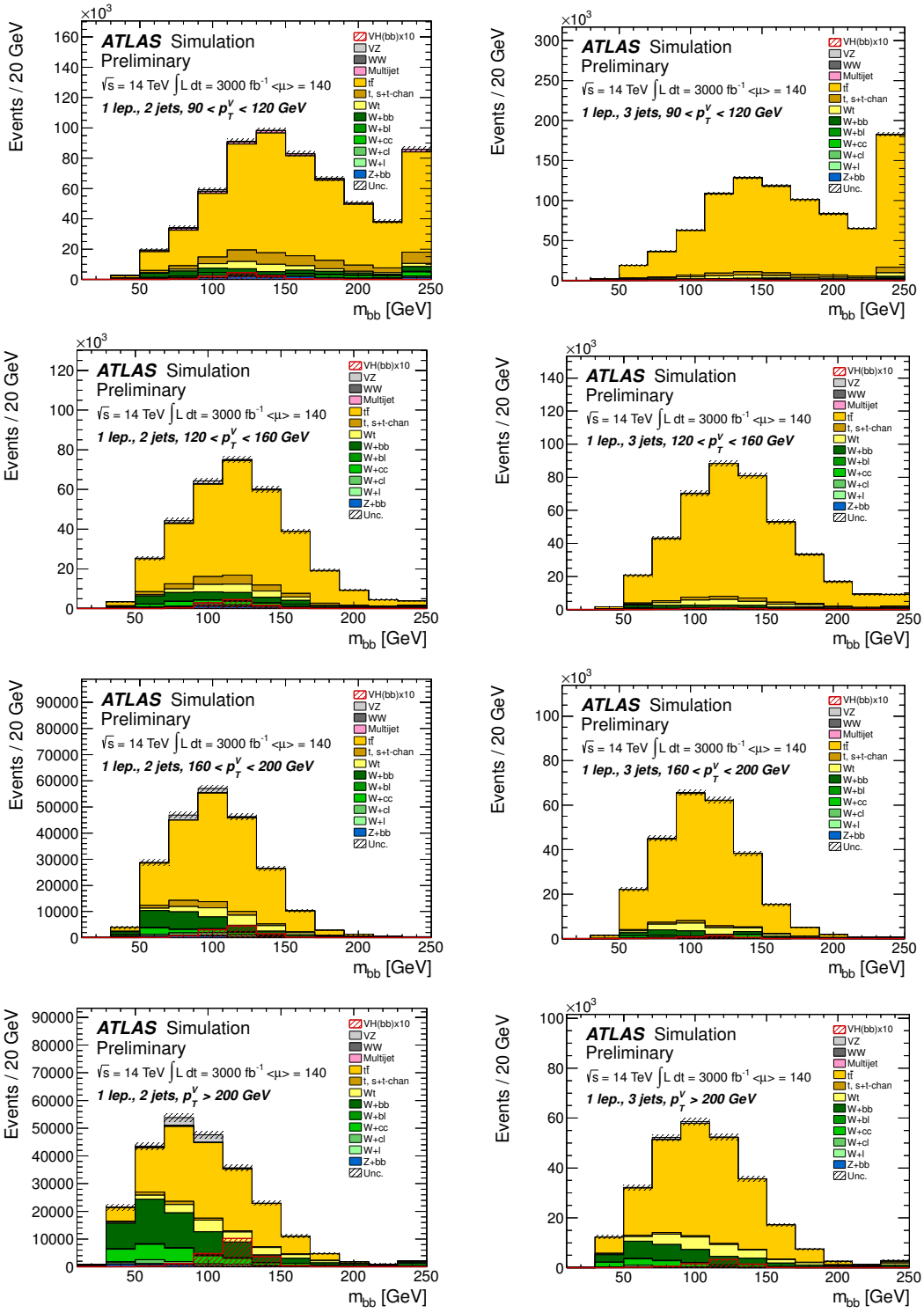

Figure B.2 m_{bb} distribution for the 2-jet (left) and 3-jet (right) bins of the one-lepton channel for $\sqrt{s} = 14$ TeV, $\langle\mu\rangle = 140$ and an integrated luminosity of 3000 fb^{-1}. The entries in overflow are included in the last bin. The Higgs boson signal cross section has been multiplied by a factor of 10. The dashed band corresponds to the statistical uncertainties only.

B.2 Systematic Uncertainty Ranking Plots for One and Two-Lepton Analyses

The fit model presented in Section 9.9 takes systematic uncertainties in the form of nuisance parameters into account. The impact of each nuisance parameter on the fit results is given below for the 300 and 3000 fb^{-1} 2-lepton cases.

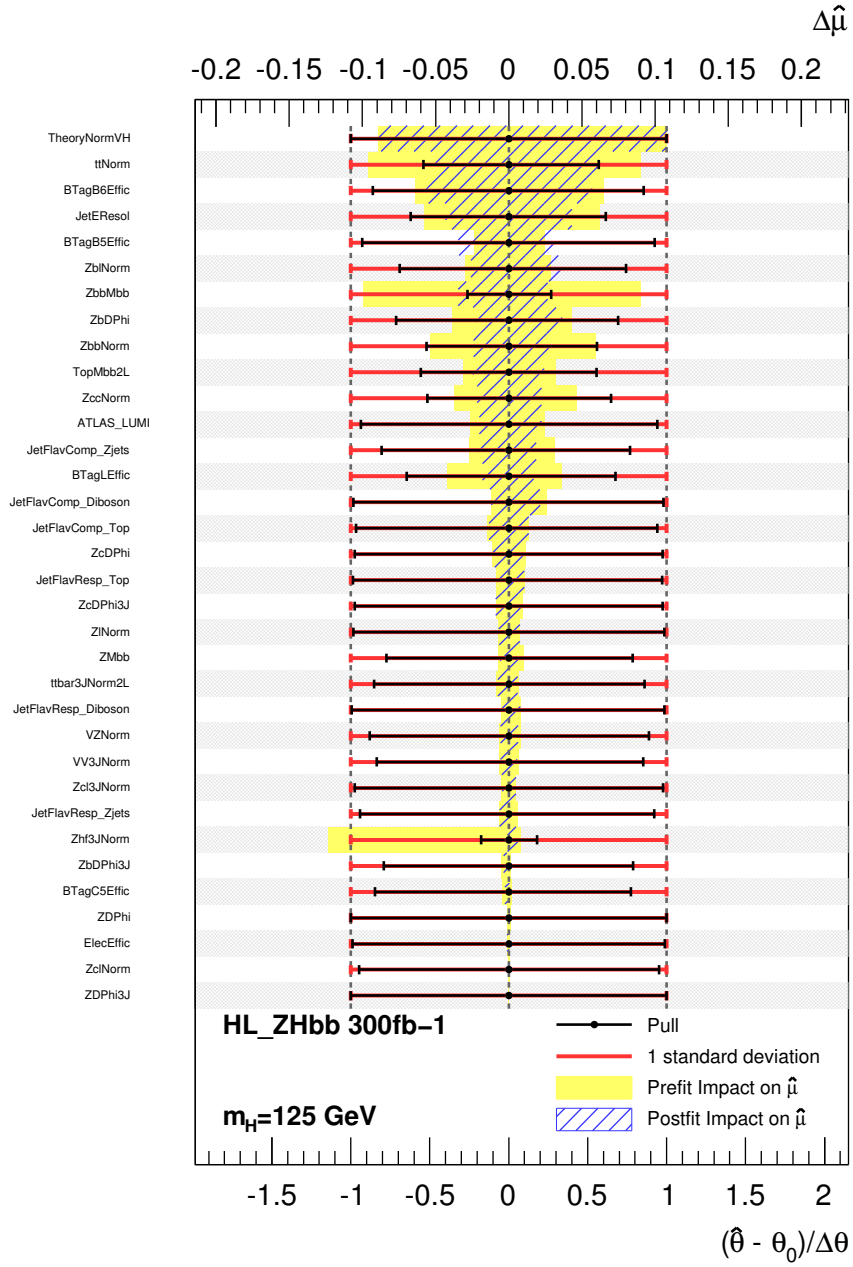

Figure B.3 Impact of the nuisance parameters on $\hat{\mu}$, in decreasing order of post-fit effect in the 2-lepton channel for the particle level plus smearing 14 TeV, $\langle\mu\rangle = 60$ and 300 fb^{-1} analysis. The x axis at the top represents the fractional variation on $\hat{\mu}$ caused by each of the nuisance parameters on the y axis. Around each pull point both post (in blue) and pre-fit (in solid yellow) one sigma errors are shown, highlighting the eventual constraints.

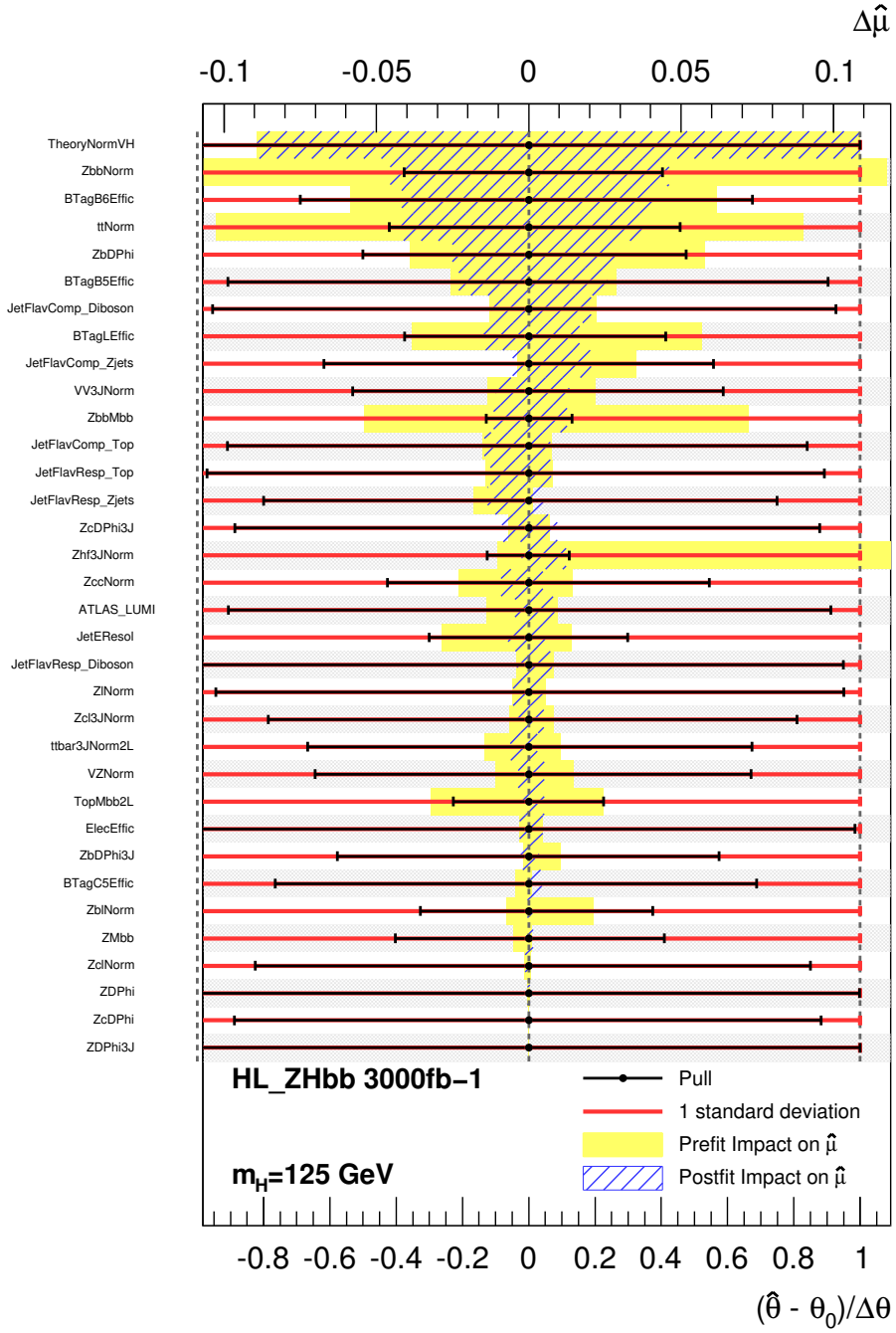

Figure B.4 Impact of the nuisance parameters on $\hat{\mu}$, in decreasing order of post-fit effect in the 2-lepton channel for the particle level plus smearing 14 TeV, $\langle\mu\rangle = 140$ and 3000 fb^{-1} analysis. The x axis at the top represents the fractional variation on $\hat{\mu}$ caused by each of the nuisance parameters on the y axis. Around each pull point both post (in blue) and pre-fit (in solid yellow) one sigma errors are shown, highlighting the eventual constraints.

Appendix C: SCT Sensor Depletion Voltage from Track Data at the end of Run 1

As part of my ATLAS authorship qualification task, I evaluated the depletion voltage of the SCT Barrel 3 sensors at the end of Run 1 at 110 ± 10 V using collision tracks, collected in end-of-run fills with varying sensor bias voltage. This result disagrees with the predicted value of the depletion voltage of up to 50 V for the given fluence.

Introduction

The SCT is made up of p in n silicon strip sensors [114]. The majority carriers are holes and electrons in the p- and n-type silicon respectively. When a junction between the p- and n-type silicon is formed, free carriers from either side diffuse across the junction; holes move to the n- side of the junction, resulting in a net negative charge on the p-side and electrons diffuse into the p-side, leaving the n-side with a positive charge. This transfer leaves a region around the junction with no free charge carries, called the depletion region, which exhibits a small potential [267]. A charged particle traversing through the depleted region can excite an electron-hole pair. The absence of an electron called a hole, can be treated as a particle with an effective mass and charge equal and opposite to the electron [268]. Both the electron and hole then drift to either side of the depleted region due to the potential and induce a measurable current. This effect is enhanced by applying an external reverse bias to the silicon junction, thus increasing the drift potential and subsequently the amplification of the induced signal, but also increasing the width of the depletion zone and therefore the active area of the silicon sensor. An asymmetry in dopant concentration of the SCT sensors makes them p^+ n junctions, with a wide n-side as a common bulk and thin micro-strip p-sides, as in Figure C.1.

The SCT sensors have an average thickness of about 290 μm and were fully depleted with a bias of around 65 V at the time of commissioning in 2007 [114].

In practice the SCT is operated at 150 V, which reduces noise and facilitates readout. The SCT will be exposed to high radiation levels during the LHC running and will suffer radiation damage. This manifests itself as type-inversion of the silicon, where the n-type is gradually converted to p-type silicon due to the change of effective dopant concentrations by ionising radiation. Subsequently, the p-n junction will shift towards the bottom side of the sensor and a higher bias voltage must be applied to fully deplete the sensor. Predictions of the change in depletion voltage due to radiation damage have been made, see Figure C.7. The radiation dosage is measured as Φ_{eq}, the equivalent flux of 1 MeV neutrons per cm^{-2}. It is expected that the SCT sensors will undergo type inversion after exposure to $\Phi_{eq} \approx 2 \cdot 10^{12}\,\mathrm{cm}^{-2}$.

Additionally, crystal defects in the silicon can be cause by radiation damage, introducing local recombination and generation centres, which increase the leakage current and thus decrease the signal to noise. Furthermore, the creation of charge trapping centres by radiation damage leads to a reduction in charge collection efficiencies [269].

The SCT is made up of 3 barrel layers, with barrel 1 having the smallest radius and barrel 3 the largest. The different proximities to the collision point means that each barrel experiences different radiation dosages.

For my authorship qualification task I performed an evaluation of how the depletion depth of the current Semiconductor Tracker sensors have been affected by radiation damage. In January 2013, multiple end-of-fill runs were recorded with non-standard SCT bias voltage settings. The bias voltage of all modules on barrel 3 was varied from 30 to 150 V. This voltage scan allows the determination of the depletion voltage from the relationship between track angles and SCT cluster sizes. For a given track incidence angle the number of strips above threshold is determined by the bias voltage, until saturation is reached when the sensor is fully depleted. The depletion depth is proportional to the slope of the average cluster size versus ϕ_{local}. From plotting this slope versus bias voltage, the depletion depth can be indirectly determined. The depletion voltage is then given by the bias voltage above which the depletion depth plateaus.

Results were compared to findings by C. Oropeza Berrera [270], who in 2008 performed identical studies using cosmic data, evaluating the depletion voltage of the un-irradiated SCT sensors at approximately 65 V. My results suggest a current depletion voltage of about 110 V. However, trusted models for the fluence received by barrel 3 and for the development of the depletion voltage as a function of fluence predict a current depletion voltage of less than 50 V. Further investigation is needed to explain this large discrepancy.

Method

When a charged particle traverses a SCT sensor, as in Figure C.1, it excites free charge carriers in the sensor bulk that travel towards the micro strips on the top surface of the sensor. For a fully depleted sensor the entire depth of the sensor is active and the number of strips n (or cluster size), that measure an above threshold signal is given by $n = \tan(\phi)\, d\, p^{-1}$, where d is the sensor depth, p is the strip pitch and ϕ is the local incidence angle. On average $d = 290\,\mu$m and for the barrel $p = 80\,\mu$m. For a sensor that is not fully depleted, the active depth is reduced and liberated electron-hole pairs will recombine with free charge carriers.

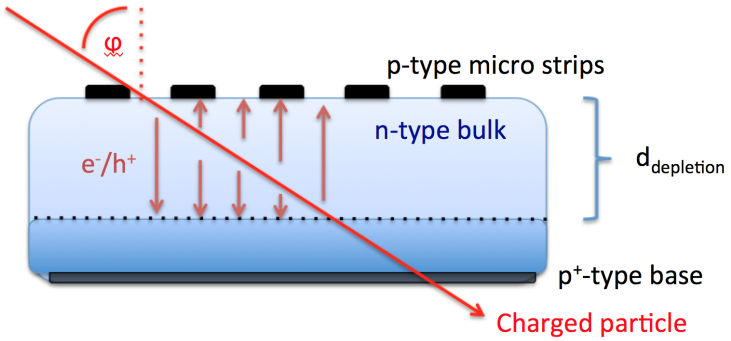

Figure C.1 Sketch of SCT module, showing the micro strips (black) onto of the sensor bulk (blue). An incident charged particle liberates charge carries in the sensor that are recorded by the strips. The number strips that measure a signal depends on the incidence angle of the particle and the depletion depth of the sensor.

Thus, for a given incidence angle the cluster size increases with the bias voltage, until saturation is reached when the sensor is fully depleted. In a small angle approximation, the derivative of the average cluster size n versus ϕ_{local} is proportional to the deletion depth d. (Here ϕ_{local} is angle in ϕ an incident track makes to the sensor normal.) The depletion voltage is then given by the bias voltage above which the cluster size as a function of bias voltage plateaus. A straight line fit to one side of the cluster size versus ϕ_{local} distribution, as in Figure C.2, gives a good and simple approximation of the slope in the range of low ϕ. The optimal fit range and whether to include the minimum or not, was tested. It was found that the measurements of the slopes were sensitive to the fit range, introducing a roughly constant offset to the slope vs voltage plot, but not changing the point of saturation.

The choice of fit range in ϕ_{local} to obtain the straight line slope is not obvious. Figure C.3(a-c) shows examples of the distribution for 70 V with a straight line fit in different ranges which can be well approximated by a straight line.

The relationship between depletion depth d and bias voltage V_{bias} is given by $d \propto \sqrt{V_{bias}}$ [271], and the modulus of the slope was thus plotted against $\sqrt{V_{bias}}$,

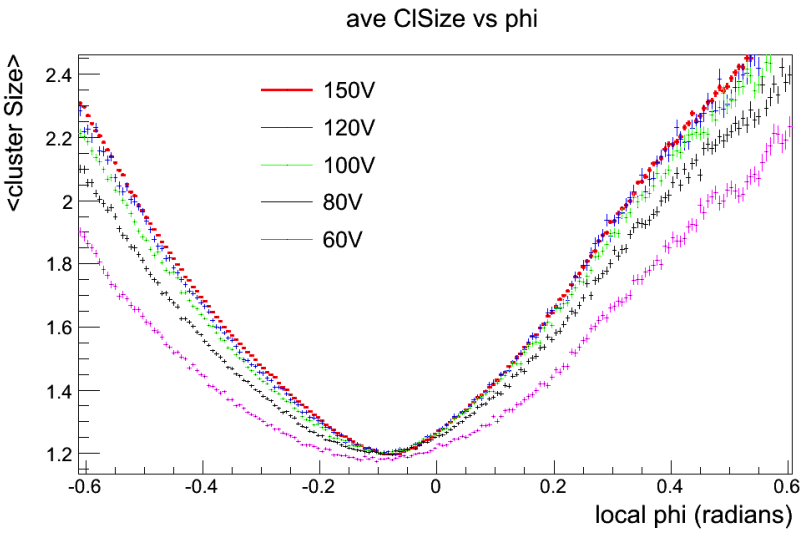

Figure C.2 The average cluster size was recorded against the local track incidence angle in ϕ for different bias voltages. All hits recorded on Barrel 3 were selected.

as in Figure C.4(a) for various fit ranges. It can be seen that the choice of fit range introduces a constant offset in the slope calculation. As we are after the bias voltage at which the slope calculation plateaus, it can be assumed that, within the scope of tested fit ranges, the search is insensitive to the fit range. Similarly, the sensitivity to applying the fit to different bin sizes of the average cluster size distributions was tested, seen in Figure C.4(b).

It was decided that the data used for Figures C.3 and C.4 had too low statistics. In response to this additional end-of-fill runs were collected. Initially, it was assumed to observe plateauing at voltages lower than 100V, however this was not the case and the bias voltage scan was increased to 60V - 130V.

To study the dependence of the cluster size on track η and therefore on the local incidence angle parallel to the strips, θ_{local}, hits were selected depending on which η-module they were recorded, as in Figure C.5.

This splitting resulted in improved fit results with smaller errors and shows that plateauing is more prominent for small track η. At the same time the average cluster size increases with η, with this trend converging for η module and 4, 5 and 6. These findings suggest that with higher θ_{local} the ionising particle travels "along" or "under" a given strip in the bulk, thus increasing the chance of liberating more charge carriers and putting this strip above threshold.

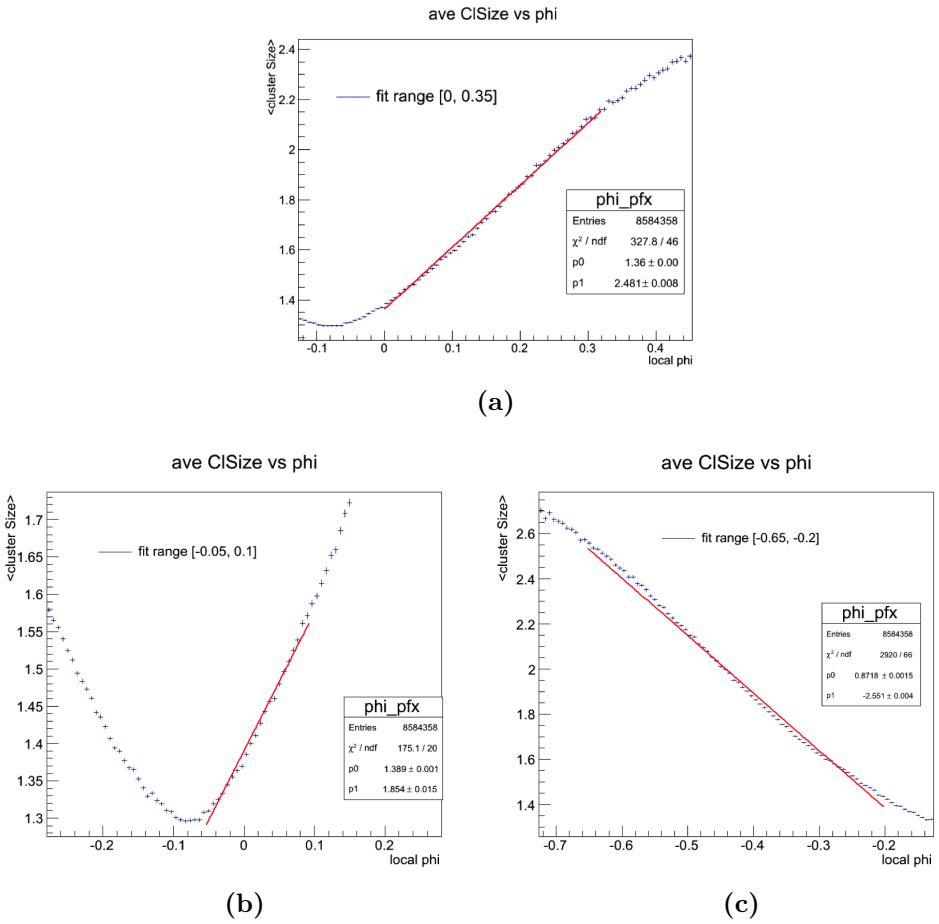

Figure C.3 Examples of different fit ranges of (a) [0, 0.35] rad, (b) [-0.05, 0.1] rad and (c) [-0.65, -0.2] rad.

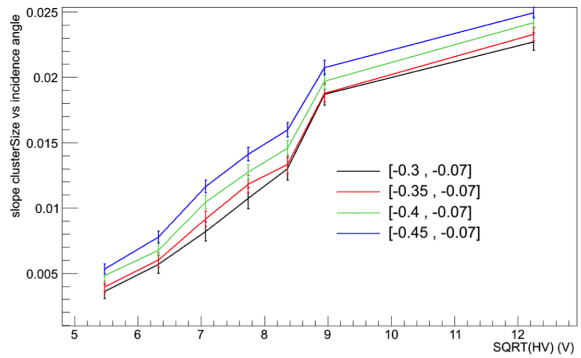

(a)

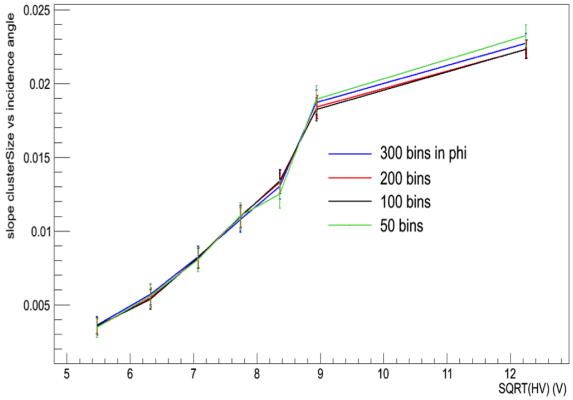

(b)

Figure C.4 (a) Modulus of slopes evaluated for different fit ranges. (b) Slopes evaluated at fixed fit range but different bin sizes.

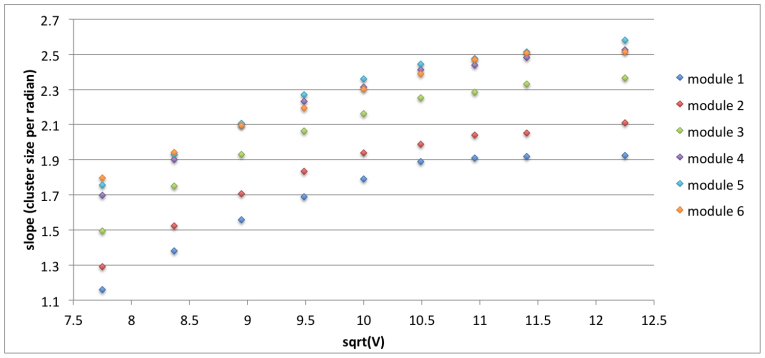

Figure C.5 Results split by SCT η-module the hit was recorded. Error bars obtained from error on fit are too small to see on this scale, but increase as you go up in η.

Comparison of Results

A stricter $|\eta_{track}| < 0.05$ cut was applied to ensure a near zero θ_{local} but preserving statistics at the same time. A very low η scenario is also comparable to the cosmic runs, where the cosmic muons primarily come straight down. My results are compared to a 2008 cosmic study [270], where the depletion voltage was determined by essentially the same method, in Figure C.6. In 2008 the depletion voltage was measured at approximately 65V in agreement with the design specifications [114].

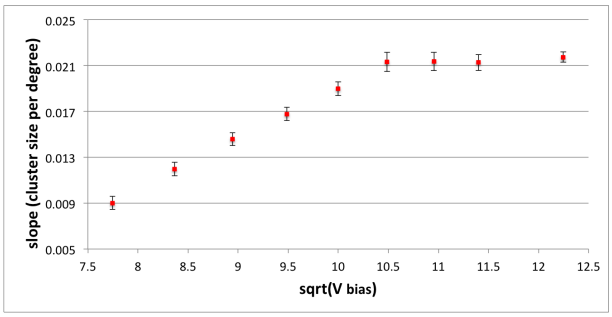

(a)

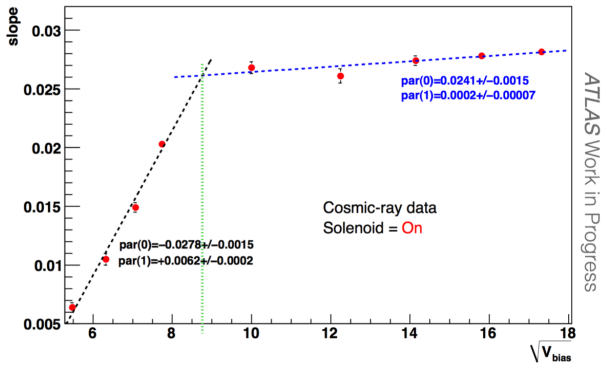

(b)

Figure C.6 The straight line slope of SCT cluster size against track incidence angle as function of $\sqrt{V_{bias}}$ for (a) 2013 Collision data and (b) 2008 cosmic data. The data rises in a linear fashion and then plateaus. The depletion voltage is given by the bias voltage at which the data plateaus. Data here in degrees.

By comparison to Figure C.7 and the estimated fluence of $\Psi_{eq} = 0.5 \cdot 10^{13} cm^{-2}$ [272] [273] for barrel 3 at end of Run 1 one would expect the current depletion voltage to be in the range of 10 - 50V, not the about 110 V my findings suggest. According to my results the SCT barrel 3 has already undergone type inversion and shows a depletion voltage equivalent to a 10 times higher radiation fluence than currently assumed.

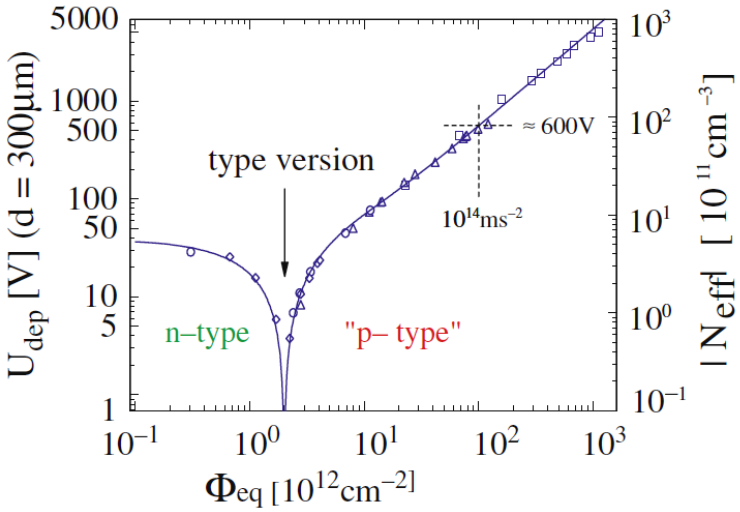

Figure C.7 Predicted depletion voltage of the silicon sensors as a function of radiation exposure. The radiation dosages measured in units of 1 MeV neutron equivalent fluence, Φ_{eq} [274].

Conclusion

The average SCT cluster size as a function of track incidence angle and η was studied. The SCT cluster size was found to increase with $|\eta|$. The current depletion voltage at the end of Run 1 of the Barrel 3 sensors was evaluated at 110 ± 10 V and compared to calculations made in 2008 with cosmic ray data. The results however disagrees with simulations of the fluence and its affect to the sensors, which predict a depletion voltage of maximum 50 V. The reason for this discrepancy is yet unknown. This study should be repeated with more recent cosmic ray data to bring clarification.

Appendix D: FE-I4 Front-end Readout Chip for ATLAS Inner Detector Upgrade

In preparation of the ATLAS Inner Detector upgrade I contributed to the commissioning of a probe-station for the new FE-I4 readout chips which in part will be tested at the University of Edinburgh before installation in the detector. A short description of the FE-I4 chip and initial results are presented here.

During the 2013/2014 shutdown a new silicon pixel layer was installed between the beam pipe and the currently inner most layer of the Pixel Detector. The Insertable B-Layer (IBL) [275] increased the tracking capabilities for hadronised b-quarks. It will bring enhanced b-jet tagging, beneficial for example to the $ZH \rightarrow \ell^+\ell^-b\bar{b}$ searches. The IBL consists of silicon sensors that are bump bonded to front-end read-out chips. The current FE-I3 front end chips used in the pixel detector are not capable of processing the expected hit rate of the IBL, which will have a higher hit occupancy than the current pixel detector, due to its proximity to the interaction point. Together with new silicon sensors, the new FE-I4 [276] can bear a higher hit-occupancy that the current FE-I3 and is less susceptible to radiation damage [277]. A single FE-I4 chip has 80 x 336 pixels. The per-pixel circuit diagram is shown in Figure D.1.

Silicon sensor pixels will be DC coupled to the FE-I4 pixels, which each have independent amplification and shaping, followed by a tuneable threshold, separating noise from particle hits. One important measurement of the front end chip is the Time over Threshold (ToT) of the amplified and shaped signal. The ToT measurement has a 4bit resolution in units of bunch crossing intervals, normally 25 ns. The ToT response of a pixel is a measure of the injected charge Q_{in}, provided by a charged particle passing through the sensor; it must therefore be uniform and calibrated across all pixels. The same holds for the threshold value itself. This calibration is performed for each pixel individually by tuning different parameters that control the ToT response.

The charge sensitive amplifier, *Preamp* together with C_{f1}, as in Figure D.1 produces an output voltage proportional to Q_{in} and inversely proportional to the potential of the feedback capacitor C_{f1}. In order to reset the amplifier, C_{f1}

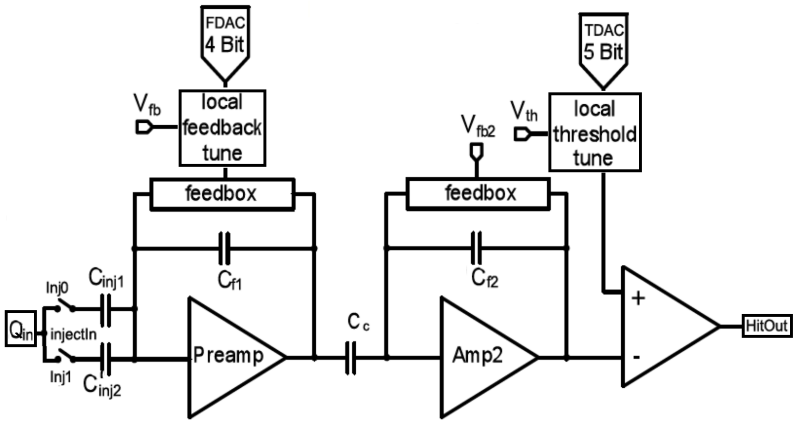

Figure D.1 An injected charge is passed through two amplifier and discriminator stage in the FE-I4.

must be discharged. This is done by the $feedbox$, which is a source of constant feedback current. A second amplifier stage is used to ensure sufficient gain for a large dynamic range. Using two stages also allows to correct for imperfections of the feedback capacitors and amplifiers.

The output of the 2nd amplifier stage is compared to the threshold voltage in the discriminator. The resultant signal is shown in Figure D.2.

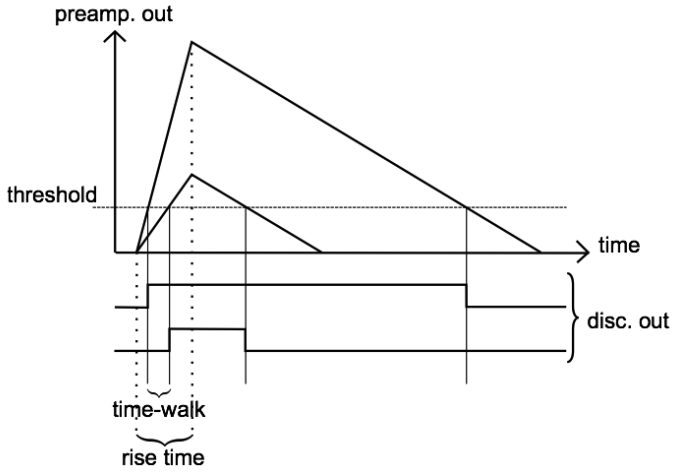

Figure D.2 The discriminator counting the time over threshold of the signal from two different charges. The threshold is varied by the TDAC and the downwards slope is determined by the FDAC tune.

The down slope of the signal is given by the $feedbox$, see Figure D.1, which is configured by the $FDAC$. The 4 bit setting of the $FDAC$ alters the slope of the signal. The threshold is the sum of the global threshold voltage V_{th} and the 5 bit $TDAC$ value applied to the discriminator. The threshold and ToT are thus calibrated to a common value, for a given amount of injected charge, across all

pixels by individually tuning the *FDAC* and *TDAC* of each.

The FE-I4 exhibits a constant rise time, that is the time the signal takes to reach its maximum, is independent of Q_{in}. This facilitates a defined ToT measurement. As a result, the rise slope is proportional to Q_{in}, called "time walk effect".

The FE-I4 will also be used for the upgrade of Pixel Barrel and Endcaps. Significant failure rates in the order of 20% have been reported in the manufactured FE-I4 chips [278]. Multiple stages of quality control must be performed before any chip is installed in the ATLAS detector. Testing the FDAC and TDAC tuning functionalities is a relatively high level test, which must be performed on every pixel of every chip to ensure a calibrated injected charge to ToT response.

FE-I4 Characterisation

The Edinburgh silicon lab is responsible for testing the performance of FE-I4 chips before they are used in the R&D programme of the ATLAS pixel end caps upgrade. 50 wafers, of 60 FE-I4 chips were tested, starting in August 2013. My task was to help commissioning the new lab equipment and setup an automated testing procedure for wafer testing.

After delivery I set up the Agilent B1500 Source-Measuement-Unit, which is used for silicon characterisation. It can apply small test signals to a device under test and measure its response. It is capable of operating at currents as low as 1 fA. I performed various types of measurements on discrete electrical components to gain knowhow on operating this unit. It was used to measure the injection capacitors of the FE-I4 chips. In order to perform large scale wafer testing I interfaced the B1500 to a PC, which allowed for automated and programmable remote control. The connection to the PC was made via GBIP using the VISA C++ library in Visual Studio. During the installation of this, several driver conflicts between the Agilent and NI software had to be overcome.

Using a USBpix test board, an ATLAS wide standard testing platform for the FE-I4 [279], I characterised a single FE-I4 chip to evaluate a list of primitive tests that will later be performed on the wafers. I contributed to the commissioning the USBpix readout system, that connects the FE-I4 to a PC, in preparation of these tests. This single chip has a 3D sensor bump bonded to it. Initial scans showed an unexpected pattern in test scans, which could be solved by applying a sensor bias, revealing the particular behaviour of the sensor, which was bonded to the readout chip only with every other column. It is believed that the injected test charge was being drained into the unbiased sensor. By applying various bias voltages V and measuring the sensor current I, I obtain an I/Vcurve for the sensor, from which the correct depletion voltage can be found, see Figure D.3.

With the correct sensor bias voltage, scans were performed to tune the FDAC and TDAC of the single FE-I4 chip, shown in Figure D.4. Both distributions

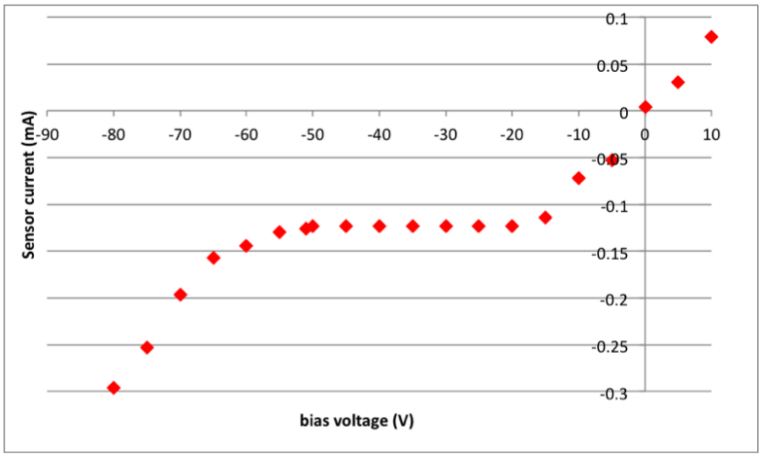

Figure D.3 Ohmic behaviour is observed for a bias greater -20V and a break down voltage of -60V. I chose to bias the sensor with -50V.

should follow a Gaussian. In Figure D.4(a) the FDAC values peak at the limit of the range, which is counting all overflow entires. This is an indication that some pixels are not correctly tuned due to the limited range of the FDAC. In Figure D.4(b) one can see a high count at zero of the TDAC distribution, which correspond to set of masked columns at the end of the chip. These were masked as they showed irregular behaviour.

The discriminator threshold as well as the ToT were found to become more uniform after tuning, see Figure D.5. The threshold was tuned to 3000 electrons, which is sufficiently higher than the noise level of about 150 electrons, in order to discriminate between hits and noise. The ToT was tuned to 7 bunch crossings, which for the expected hit occupancy is short enough to avoid overlapping signals of two separate particle hits.

The width of the threshold distribution is limited by the noise of the chip and is satisfactorily small after tuning. The ToT uniformity still needs improving. This is achieved by running multiple iterations of FDAC and TDAC tune scans until the ToT converges, but still needs to be implemented.

In preparation of Run 2, the IBL was successfully installed in the ATLAS detector using the FE-I4 chip, adding 12 million channels to the existing Pixel Detector. The performance evaluation of the IBL modules is given in Ref. [280].

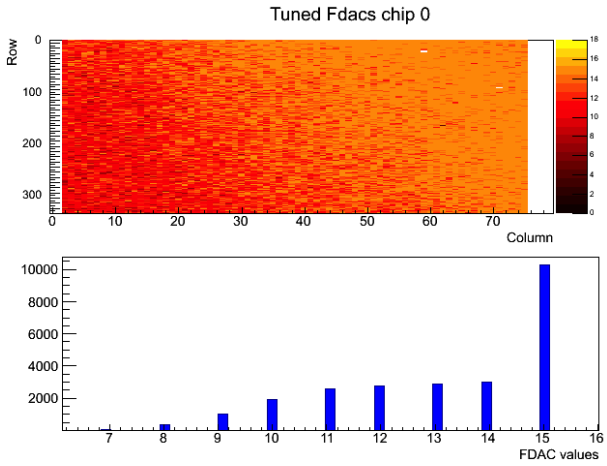

(a)

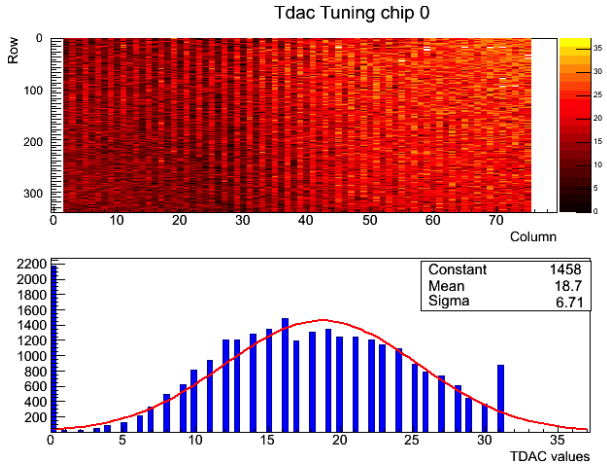

(b)

Figure D.4 A map of the pixels showing the 80 columns and 336 rows. The FDAC and TDAC settings are shown for each pixel as well as a histogram summarising the results. (a) The FDAC tuning values range form 0 to 16. (b) The TDAC values range form 0 to 32.

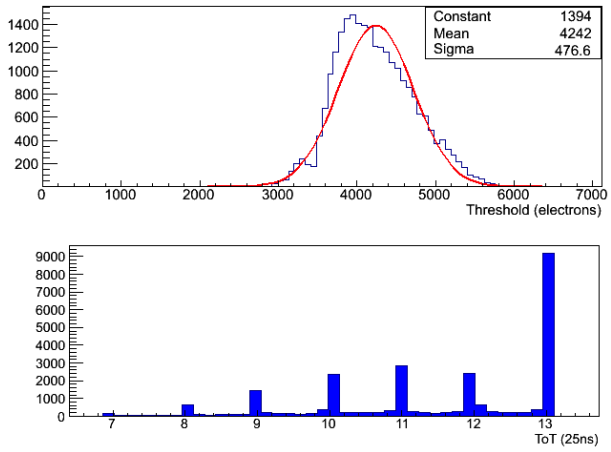

(a)

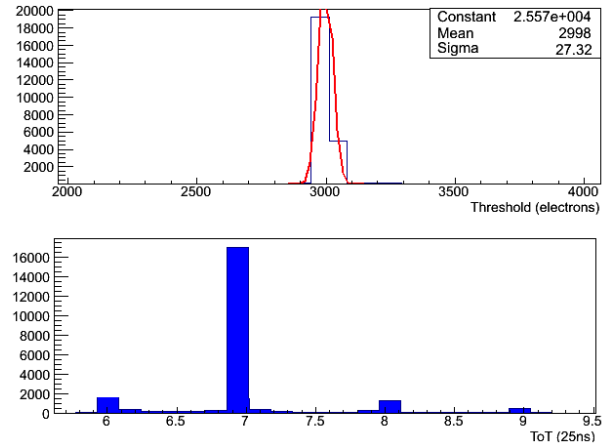

(b)

Figure D.5 Discriminator threshold and time over threshold for a given test charge for all pixels of the chip. The results are show for before (a) and after (b) chip tuning.